

Dissertation zur Erlangung des Doktorgrades
der Fakultät für Chemie und Pharmazie
der Ludwig-Maximilians-Universität München



Insights into the function of DNA repair factors MRN and ATM

Matthias Ralf Rotheneder

aus

Weißenburg in Bayern, Deutschland

2022

Erklärung

Diese Dissertation wurde im Sinne von §7 der Promotionsordnung vom 28. November 2011 von Herrn Prof. Dr. Karl-Peter Hopfner betreut.

Versicherung an Eides statt

Diese Dissertation wurde eigenständig und ohne unerlaubte Hilfe erarbeitet.

München, am 9. August 2022

Matthias Rotheneder

Dissertation eingereicht am:	10. August 2022
1. Gutachter:	Prof. Dr. Karl-Peter Hopfner
2. Gutachter:	Prof. Dr. Roland Beckmann
Mündliche Prüfung am:	5. Oktober 2022

This thesis has been prepared from December 1st 2017 to August 9th 2022 in the laboratory of Prof. Dr. Karl-Peter Hopfner at the Gene Center of the Ludwig-Maximilians-University in München, Germany.

This is a cumulative thesis based on the following publications:

Matthias Rotheneder*, Kristina Stakyte*, Katja Lammens, Joseph D. Bartho, Erik van de Logt, Aaron Alt, Brigitte Kessler, Christophe Jung, Wynand P. Roos, Barbara Steigenberger, Karl-Peter Hopfner, **Cryo-EM structure of the Mre11-Rad50-Nbs1 complex reveals the molecular mechanism of scaffolding functions**, *Manuscript in revision (09.08.2022)*

Kristina Stakyte*, Matthias Rotheneder*, Katja Lammens*, Joseph D. Bartho*, Ulrich Grädler, Thomas Fuchß, Ulrich Pehl, Aaron Alt, Erik van de Logt, Karl-Peter Hopfner, **Molecular basis of human ATM kinase inhibition**, *Nature Structural and Molecular Biology*, Volume 28, October 2021, Pages 789-798

* these authors contributed equally

Table of contents

Erklärung	III
Versicherung an Eides statt	III
Abstract.....	1
1. Introduction	3
1.1. DNA damage and its effect on life	3
1.1.1. Exogenous sources of DNA damage	3
1.1.2. Endogenous sources of DNA damage	4
1.1.3. DNA strand breaks	6
1.2. DNA damage repair pathways	6
1.2.1. Repair of damaged nucleobases	6
1.2.1.1. Direct reversal of DNA damage.....	7
1.2.1.2. Base excision repair (BER).....	8
1.2.1.3. Nucleotide excision repair (NER)	8
1.2.1.4. Translesion synthesis (TLS).....	9
1.2.1.5. Mismatch repair (MMR).....	9
1.2.2. Single strand break (SSB) repair	10
1.2.3. Double strand break (DSB) repair pathways.....	11
1.2.3.1. Canonical non-homologous end joining (C-NHEJ)	12
1.2.3.2. Alternative end-joining (A-EJ) and Microhomology-mediated end-joining (MMEJ) ..	13
1.2.3.3. Homologous recombination (HR)	13
1.2.3.4. DSB repair pathway choice in mammalian cells	14
1.2.3.5. The Mre11-Rad50-Nbs1 (MRN) complex in DSB repair	16
1.2.3.5.1. Structure and functions of the MRN subunits	16
1.2.3.5.2. Biological functions of the MRN complex.....	21
1.3. DNA damage response (DDR)	23
1.3.1. The PIKK family of signaling kinases.....	24
1.3.2. ATM is a key player in DDR	26
1.3.2.1. ATM structure and function.....	26
1.3.2.2. Targeting ATM in cancer therapy.....	28
1.4. Objectives.....	30

2. Publications.....	32
2.1. Cryo-EM structure of the Mre11-Rad50-Nbs1 complex reveals the molecular mechanism of scaffolding functions.....	32
2.2. Molecular basis of human ATM kinase inhibition.....	77
3. Discussion.....	103
3.1. Cryo-EM structure of the Mre11-Rad50-Nbs1 complex.....	103
3.1.1. The Mre11-Nbs1 interface.....	103
3.1.2. The Nbs1 N-terminal domain and higher order oligomers.....	105
3.1.3. Dynamics within the MRN catalytic head.....	106
3.1.4. DNA-binding activities.....	108
3.1.5. MRN apex domain tethering.....	109
3.2. Molecular basis of human ATM kinase inhibition.....	111
3.2.1. The N-terminal solenoid domain.....	111
3.2.2. The kinase domain and its regulation.....	112
3.2.3. Molecular basis of ATM-inhibitor potency and selectivity.....	114
Literature.....	116
Danksagung.....	131

Abstract

DNA double strand breaks (DSB) are a particularly deleterious threat to genomic integrity throughout all domains of life. DSBs can cause chromosomal aberrations, tumorigenesis and cell death if left unrepaired and are caused by either endogenous or exogenous sources. Cells rely on efficient detection, repair and response upon occurrence of DSBs. In eukaryotes, DSBs are mostly repaired by either end joining pathways or homologous recombination (HR). HR, in contrast to the end joining pathways, enables error-free DSB repair in presence of a template sister chromatid. The Mre11-Rad50-Nbs1 (MRN) complex recognizes and tethers DNA ends, even if they are obstructed by proteins to initiate HR. In order to respond to DSBs, the MRN complex recruits and activates the signaling kinase Ataxia-telangiectasia mutated (ATM), that belongs to the phosphatidylinositol 3-kinase-related protein kinase (PIKK) family. Activated ATM in turn initiates the cellular DNA damage response (DDR). Mre11 and Rad50 are highly conserved and form a topology-specific, ATP-dependent nuclease complex that processes DNA ends but leaves genomic DNA intact. The eukaryote specific Nbs1 subunit finetunes MRN's endonuclease activity by providing interaction with proteins (e.g. CtIP). Apart from its nucleolytic activity, MRN has a scaffolding function that promotes DNA end tethering, repair foci formation and possibly signal amplification.

Although the complex has been studied for more than two decades, a model that integrates both MRN's enzymatic and scaffolding functions has not yet been established. In the first part of the thesis, such a model was elaborated by combining both structural and biochemical data from this and previous studies. A cryo-electron microscopy (cryo-EM) structure of the *Chaetomium thermophilum* (Ct)MRN catalytic head domain in its ATPγS-bound state not only clarifies its atomic architecture but also reveals how a core part of Nbs1 stabilizes and possibly locks the Mre11 dimer. In this structure significant parts of the Rad50 coiled-coils were resolved in a rod configuration, stabilized by several interaction points. A previously uncharacterized C-terminal Mre11 domain, denoted bridge could further stabilize the rod configuration. The rod configuration and the bridge domain restrict access to the Rad50 DNA binding site. Biochemical analysis revealed the Rad50 DNA binding site is extremely specific for DNA ends. However, an additional, eukaryote-specific DNA binding site at the C-terminus of Mre11 enables binding to internal DNA. The Rad50 coiled-coil domains are linked at the apex via a zinc hook dimerization motif to form a large proteinaceous ring/rod. Cryo-EM data and crystal structures explained how two MRN complexes can tether DNA ends via dimerization of these apical domains. *In vivo* assays indicate that mutation of the apex tethering element negatively impacts DSB repair.

Mutations in DDR pathways allow cancer cells to cope with increased replication and genotoxic stress. For this reason, proteins involved in DDR were described to be promising targets in cancer therapy. Due to its central role in DSB induced DDR, ATM is an auspicious target for drug development. However, lack of ATM high-resolution structures, as well as atomic details of small molecule inhibitor binding modalities hampered the application of structure-based drug design. In the second part of the thesis, the binding modalities of two ATP-competitive ATM-inhibitors were described. This project was a collaborative work with Merck KGaA, that provided a novel inhibitor (M4076) with improved pharmacokinetics. Comparison of the inhibitor-bound kinase active sites with the likewise resolved ATPγS-bound active site explains the high affinities that were determined in biochemical assays. Superposition and sequence alignment of the

ATM kinase active site with other PIKK active sites enables to rationalize the molecular reasons for selectivity. In biochemical assays, IC_{50} values of the inhibitors for ATM, PIKKs and CHK2 showed high selectivity towards ATM. The binding of the inhibitors stabilized the N-terminal solenoid domain of ATM, this enabled the generation of a high-resolution structure of the entire ATM protein. The quality of the map allowed the identification of two zinc binding sites that possibly stabilize loops and the generation of a near-complete ATM structure. Taken together, the structural data provides the framework for structure-based ATM inhibitor design and allows mapping of cancer mutation as well as functionally important protein interaction sites.

1. Introduction

1.1. DNA damage and its effect on life

The deoxyribonucleic acid (DNA) encodes for the genetic instructions that enable all processes of life. DNA itself is a highly complex biological macromolecule that organisms store, maintain, transcribe, replicate and transmit in order to ensure survival and propagation of their species. In eukaryotes, the DNA molecule is a linear polymer, formed by two strands with opposite polarity, but complementing genetical information that twist around each other to form a double helix. A polymeric strand is comprised of monomeric nucleotide subunits, which consist of a phosphate, a deoxyribose sugar and a nucleobase. The phosphates and sugars form the polyphosphoester backbone that coils around the stacked, hydrophobic nucleobases that encode for the genetic information. In intact DNA, there are purine (adenine, guanine) and pyrimidine (thymine, cytosine) nucleobases. Via complementary base pairing, each type of nucleobase forms specific hydrogen bonds across the double helix (Watson-Crick base pair)¹.

In contrast to other biological macromolecules (ribonucleic acid (RNA), proteins, lipids, polysaccharides), DNA molecules have a long lifetime and are represented by one maternal/paternal copy in most cells², ^a. Damaged DNA would accumulate quickly if not repaired efficiently. In fact, aging and impaired cellular or organ functions are associated with time-dependent accumulation of damaged DNA³. Through errors in DNA repair or during replication, DNA damage can lead to mutagenic alternations of the genetic information². A mutation is not only permanent during a cells lifetime but also transferred to decedent cells or organisms (in case of a germline mutation). For these reasons, organisms exposed to DNA damaging environments or with defect DNA repair mechanisms are prone to tumorigenesis, genetic instability, impaired growth rates, premature ageing and other degenerative diseases^{4,5}.

1.1.1. Exogenous sources of DNA damage

Even before understanding the molecular details, scientists described certain exogenous sources such as ionizing (IR) and ultraviolet (UV) radiation or certain chemicals promote genetic alterations and cancer formation^{6,7}. IR causes ionization of molecules which can lead to direct bond breakage or formation of free radicals that further react with surrounding biomolecules. Albeit less energetic than IR, UV radiation still transfers enough energy to excite molecular bonds, especially to π -conjugated chromophores, such as DNA nucleobases. After photon-absorption, excited chromophores can either react directly or the energy can be transferred to molecular oxygen to form DNA-damaging reactive oxygen species (ROS)⁸. ROS can cause single-strand breaks (SSB), double-strand breaks (DSB) or oxidation of DNA bases. Oxidation of guanine for instance leads to formation of 8-oxo guanine that can form a non-canonical (Hoogsteen) base pair with adenine and introduces a T-A transversion if misrepaired⁹. Similarly, adenine can be oxidized to form 8-oxo adenine (Figure 1.1). ROS also react with other nucleophilic molecules (e.g. unsaturated fatty acids, proteins) to form reactive species (e.g. aldehydes) that can form mutagenic adducts with nucleobases¹⁰. Another common UV photoproduct is the cyclo-butane pyrimidine dimer (CPD), a covalent linkage

^a This is obviously a simplification, as most eukaryotic cells contain mitochondria which harbor mitochondrial DNA-genomes (mtDNA). mtDNA has interesting properties, remarkably distinct from that of the eukaryotic genome²⁰⁸.

between consecutively stacked pyrimidine bases (Figure 1.5)². A day of exposure to sunlight can induce up to 10⁵ UV photoproducts in each keratinocyte². It is not surprising that UV exposure and resulting DNA damage in melanocytes is the primary cause of melanoma development in humans¹¹.

A major class of DNA damaging molecules are DNA alkylating agents. Commonly, an electrophilic intermediate is formed that reacts with nucleophilic DNA base amines leading to alkylation or even covalent crosslinking¹². Alkylating agents include N-mustards (e.g. Cyclophosphamide), nitrosoureas (e.g. Carmustine, see Figure 1.6), platin-based antineoplastics (e.g. Cisplatin, Carboplatin) and alkyl sulfonates (e.g. Busulfan) and find application in cancer chemotherapy¹²⁻¹⁴. Intercalators interact reversibly with DNA and interfere with cellular processes such as transcription, which has been exploited to treat certain types of cancer¹⁵. These molecules are often planar, polycyclic compounds (e.g. Daunorubicin, see Figure 1) that are able to insert in between the stacked DNA bases, thereby they locally alter the DNA structure. Naturally occurring carcinogenic molecules are often fungal secondary metabolites. Relevant examples include the *Aspergillus sp.* Aflatoxins, a family of carcinogenic poisons that form alkylating and intercalating intermediates upon metabolization in the liver¹⁶. Interestingly, also *Penicillium roqueforti* a mold that is used for the manufacturing of blue cheese, produces DNA damaging mycotoxins that cause toxic DNA-protein crosslinks (DPC)¹⁷.

1.1.2. Endogenous sources of DNA damage

Exposure towards exogenous DNA damaging agents is partially avoidable, however DNA integrity is also threatened from various endogenous sources. Even though DNA is a relatively stable molecule^b, it is mostly synthesized by condensation reactions that can be hydrolyzed. Spontaneous acid-catalyzed hydrolysis reactions result in purine/pyrimidine-loss (abasic sites, AP-site) or can cause deamination (Figure 1.3)¹⁸. Intriguingly, base deamination reactions occur more frequently in single-stranded (ss)DNA, as opposed to double-stranded (ds)DNA, so during processes with transient ssDNA intermediates (transcription, recombination, replication) the deamination rate is increased¹⁰.

Apart from generation by IR or UV, ROS are also produced by certain endogenous events, such as cellular respiration in mitochondria, catabolic reactions in peroxisomes, protein folding reactions in the endoplasmic reticulum (ER), immune response by the NADPH oxidase and stress reaction, that lead to dysfunctions in the respective organelles/enzymes^{9,19}. In order to minimize self-inflicted ROS damage to DNA (and other biomolecules) organisms rely on compartmentalization (ER, peroxisome, mitochondria) and ROS quenching enzymes (e.g. superoxide dismutase, catalase, peroxiredoxin)¹⁰. Even more, the dsDNA structure itself and its tight association with nucleosomes contributes to its stability and protection. Nevertheless, ROS cause an estimated 2300 SSBs per cell each day¹⁰.

^b DNA is a stable biomolecule, the half-life time of mitochondrial (mt)DNA in bone was estimated to be 521 years²⁰⁹. Storage in perma-frost conditions massively increased the longevity of DNA samples and allowed the recovery of genome-wide data from a 700 000 years old horse and more than 1 million year old mammoth specimen^{210,211}.

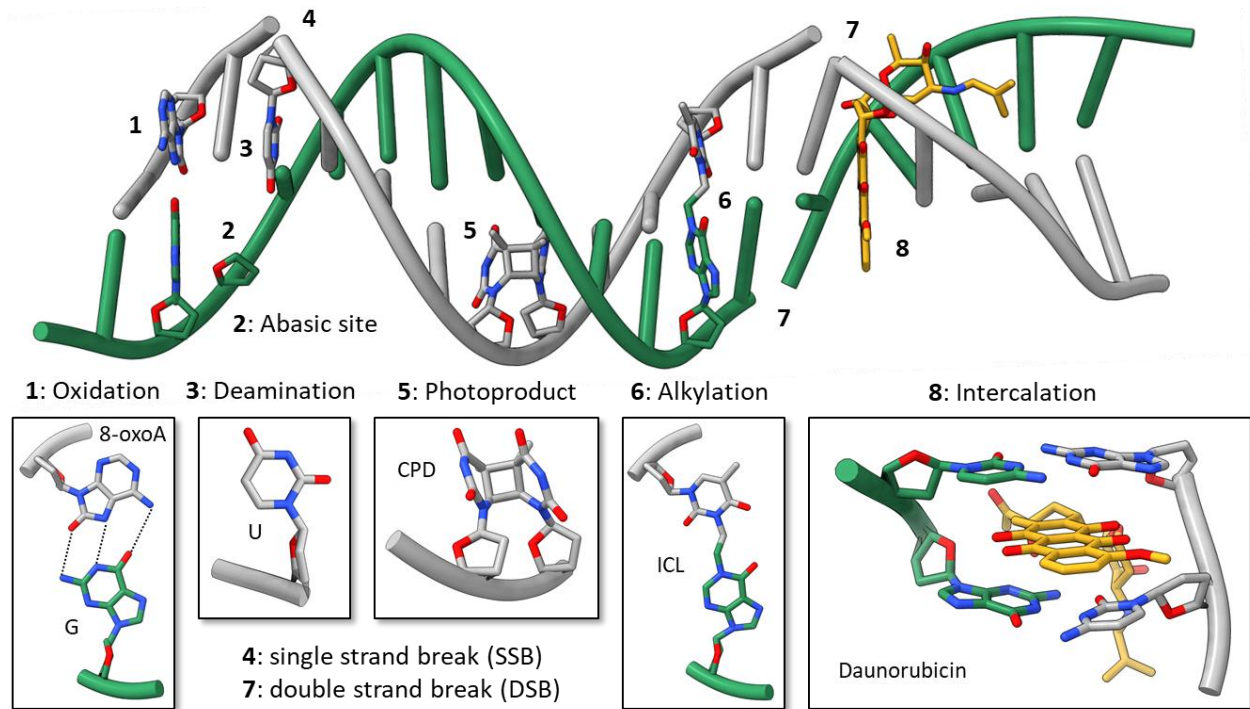


Figure 1: Different types of DNA damage. The graphic illustrates the results of events that cause DNA damage. 1: Reactive oxygen species (ROS) caused oxidation of adenine (A) to form 8-oxoA that can form a Hoogsteen base-pair with guanine (G) (PDB D75); 2: Spontaneous hydrolysis causes abasic sites (AP sites); 3: Deamination of cytosine (C) generates uracil (U); 4: Single-strand break (SSB); 5: UV radiation causes formation of a cyclo-butane pyrimidine dimer (CPD), a common photoproduct; 6: Bifunctional alkylating agents like Carmustine can cause interstrand crosslinks (ICL) (PDB 2MH6); 7: Double-strand break (DSB); 8: planar, polycyclic intercalating agents like Daunorubicin change the DNA structure (PDB 1AGL).

Aside from antecedently listed ROS-dependent alkylation events and exogenous alkylating agents, certain endogenous metabolites can alkylate DNA. Most frequently, nucleobases get methylated non-specifically by the cellular methyl-donor *S*-adenosyl methionine (SAM) at nucleophilic non-carbon atoms^{20, c}. Other endogenous alkylating metabolites include choline, trimethyl glycine (TMG), and nitrosated bile salts¹⁰.

During cell division the whole genome is replicated by high fidelity replicative polymerases (Pol) δ and ϵ . Pol δ and ϵ ensure correct base pairing and removal of incorrectly inserted nucleotides via their 3'-5' exonuclease activity²¹. In healthy cells, the replicative machinery, coupled with DNA mismatch repair (MMR) factors, has an extremely low error rate of 10^{-7} - 10^{-9} ^{10, d}. Nevertheless, base substitutions, insertions and deletion errors accumulate, especially at repetitive sequences. Lower fidelity polymerases are required for replication initiation (Pol α), DNA repair (Pol β ζ η ι κ μ ν σ θ , REV1, PrimPol, Tdt) and mitochondrial replication (Pol γ)^{10,21}. Replication and transcription processes causes topological stress to chromosomes that can be dissolved by topoisomerases. Topoisomerases act by introducing transient SSBs

^c Unspecific, mutagenetic methylation events (e.g. at O⁴-thymine, O⁶-guanine) have to be differentiated from specific, epigenetic methylation events (5-methylcytosine, N⁶-methyladenine, N⁴-methylcytosine). Methylation at e.g. CpG sites is a stable, epigenetic marker that is involved in regulation of gene expression²¹². These methylation events are catalyzed by specific DNA methyltransferases that use SAM as cofactor.

^d A haploid human genome contains around 3.2⁹ base pairs that have to be replicated²¹³. Taken together during each replication round only 3-300 errors are introduced per cell.

(type I) or DSBs (type II), thus abortive telomerase reactions cause SSBs or DSBs respectively¹⁰. This can happen if DNA/RNA polymerases collide with DNA-bound topoisomerase or due to topoisomerase poisons (e.g. Camptothecin, Quinolone antibiotics). Some intercalating agents (e.g. Daunorubicin, see Figure 1) or DNA distortions can trap topoisomerases to form covalent DNA-protein crosslinks (DPCs)^{17,22}.

1.1.3. DNA strand breaks

SSBs arising from various sources (see previous sections) are common types of DNA lesions, often accompanied by nucleotide loss and/or damaged backbone termini²³. As the complementary DNA strand can be used as a template, SSB repair (SSBR) is an efficient and rapid process. However, if SSBs are not repaired appropriately in proliferating cells, SSBs cause stalling and collapsing of DNA replication forks that eventually can lead to DSB formation²³. In dividing cells, around 1% of endogenous SSB lesions lead to formation of approx. 50 DSBs per cell per cell cycle²⁴.

Although DSBs are a relative rare form of DNA damage, the effects on the cells can be extremely detrimental as they cause chromosome breakage or rearrangements that are associated with tumorigenesis or impaired gene function^{2,4}. DSBs can be one-ended if they occur at collapsed replication forks or deprotected telomers or two-ended if linear chromosomes break^{4,25}. Despite the danger that DSBs imply, intentional DSB introduction and subsequent, recombination repair is an important source of genetic variation. The adaptive immune system relies on constant variation of the variable domain in antibodies to enable specific binding to antigens. This diversity can be partially attributed to somatic V(D)J recombination that occurs in the primary lymphoid organs²⁶. In Meiosis, DSB induction and subsequent repair enhances the genetic recombination in sexual reproduction. Therefore, the topoisomerase-related Spo11 intentionally introduces DSBs in order to increase meiotic recombination events²⁷.

1.2. DNA damage repair pathways

To counteract DNA damage, cells rely on specific repair mechanisms for different types of DNA lesions. The repair is performed by a complex network of interacting proteins that include nucleases, helicases, polymerases, topoisomerases, recombinases, ligases, glycosylases, demethylases, kinases, phosphatases and non-enzymatic scaffolding enzymes⁵. As all these proteins act on DNA, precise regulation, activation and coordination of all these factors is of utter importance. Initially, lesion-specific sensor enzymes initiate adequate DNA damage response (DDR) and promote subsequent repair¹⁰.

1.2.1. Repair of damaged nucleobases

An overview of nucleobase repair pathways is depicted in Figure 2. Commonly, a DNA lesion is sensed directly or indirectly (e.g. via helix distortion), the damaged bases are removed by tightly regulated nucleases and the complementary strand is used as a template for DNA polymerases to fill the gap.

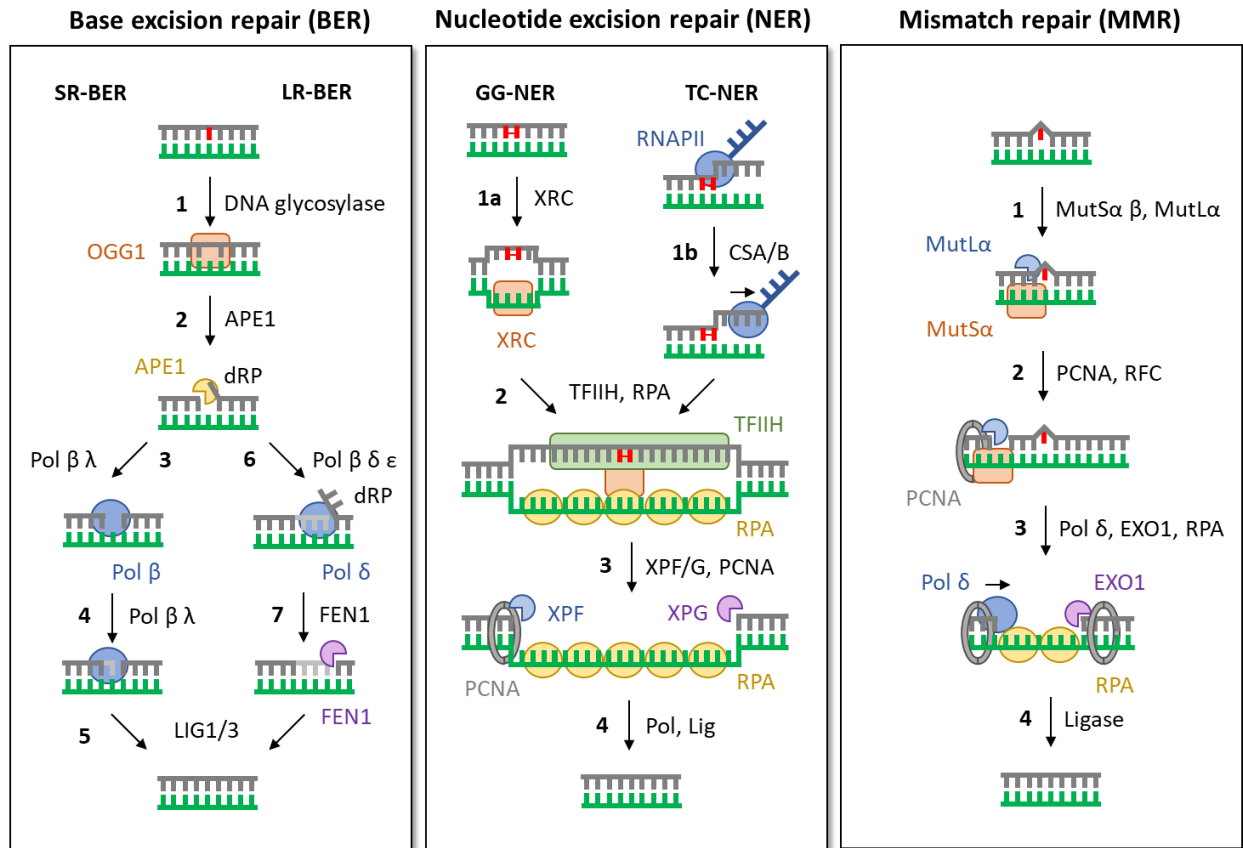


Figure 2: Schematic overview of nucleobase damage repair pathways. **Base excision repair (BER)** (graphic adapted²⁸) 1: Recognition and removal of damaged nucleobase by specific DNA glycosylases. 2: DNA strand incision generates a deoxyribose phosphate (dRP) flap. 3,4: In short-range (SR-)BER, DNA Pol β or λ lyase activity create a gap that is filled by their DNA polymerase activity 5: The gap is sealed by ligases LIG1/3. 6: Bifunctional DNA glycosylases initiate long-range (LR-)BER, Pol β δ ε perform strand displacement synthesis. 7: Flap endonuclease (FEN1) removes the dRP flap. **Global genome nucleotide-excision repair (GG-NER)** (graphic adapted²⁹) 1a: A helix-distorting nucleobase damage enables binding of XRC complex to exposed ssDNA. Transcription-coupled (TC-)NER 1b: Lesion-stalled RNA polymerase II (RNAPII) gets backtracked by CSA-CSB heterodimer. 2: Damage verification by association of TFIIH complex, protection of ssDNA by RPA. 3: Removal of damaged DNA by endonucleases XPF and XPG. 4: Gap-filling and Ligation. **Mismatch repair (MMR)** 1: Mismatch recognition by MutSα or MutSβ, recruitment of endonuclease MutLα. 2: PCNA mediated cleavage by MutLα and (4) Exo1. Pol δ fills the gap, RPA protects ssDNA. 4: Ligation by LIG1.

1.2.1.1. Direct reversal of DNA damage

Some types of nucleobase damage can be repaired directly via error-free reversal. Single-step reversal reactions are catalyzed by specific enzymes that work on certain types of alkylated bases¹⁰. In mammals, O⁶-alkylguanine DNA alkyltransferase (AGT) acts on O⁶-alkylguanine and O⁴-alkylthymine and α-ketoglutarate-dependent dioxygenases (AlkBH1-8, FTO) act on N-alkylated base adducts^{10,30}. The one-step reversal reactions do not require advanced regulation networks. Despite its simplicity, AGT repair plays an important role in the cancer field. Varying tumoral expression levels of AGT correlate with the therapeutic response to DNA damaging chemotherapy (e.g. with Carmustine)³¹.

1.2.1.2. Base excision repair (BER)

BER is responsible for repair of small, mostly non-helix-distorting base lesions. Single nucleotide-lesions are repaired by short-patch BER, while lesions that involve multiple nucleotides are repaired by long-patch BER²⁸. Both BER variants are initiated by lesion-specific DNA glycosylases that recognize oxidized bases, uracil bases, mis-pairing, and flipped-out bases^{10,28}. Monofunctional DNA glycosylases catalyze base extrusion and hydrolysis of the N-glycosidic nucleobase-sugar bond to form an AP site²⁸. These single AP sites (and others formed by spontaneous hydrolysis, see section 1.1.2) are further processed in short range BER as substrate of AP endonuclease 1 (APE1). APE1 catalyzes hydrolysis of the DNA backbone 5' to the AP site, thereby generating a nick¹⁰. Poly (ADP-ribose) polymerase 1 (PARP-1) and X-ray repair cross-complementing protein 1 (XRCC1) bind at these single-stranded nicks to promote further repair²⁸. PARP-1 adds poly-ADP ribose (PAR) moieties to itself and chromatin, to promote chromatin decondensation³². The remaining abasic 5'-deoxyribose phosphate (dRP) flap is exchanged with an intact nucleotide by Pol β or λ , in a two-step lyase-polymerase reaction^{28,33}. Eventually, the remaining nick is sealed by DNA ligase 1 (LIG1) or a complex of DNA ligase 3 (LIG3) and X-ray repair cross-complementing protein 1 (XRCC1)¹⁰.

Certain lesion-specific bifunctional DNA glycosylases (NTHL1, NEIL1-3, OGG1) catalyze glycosylase and lyase reactions to initiate long-patch BER²⁸. The resulting gaps are again processed by APE1, before either Pol β (in resting cells) or Pol δ/ϵ (in proliferating cells) fill the gap¹⁰. These DNA polymerases synthesize a replacement stretch in a strand-displacing manner to create a poly-nucleotide flap¹⁰. Upon removal of the dRP flap by flap endonuclease1 (FEN1) and nick ligation by LIG1, the damage is repaired.

1.2.1.3. Nucleotide excision repair (NER)

More bulky nucleotide lesions, such as UV-induced CPDs (Figure 1) or Cisplatin induced 1,2-intrastrand d(GpG) adducts, are repaired via NER pathways^{10,34}. NER is subdivided in global genome (GG-)NER and transcription-coupled (TC-)NER. In GG-NER the complete genomic DNA is screened for distortions in the helical geometry caused by aforementioned lesions. The damage sensor is the XPC-Rad23B-CETN2 (XRC) complex^e that binds to ssDNA opposing a lesion thereby recognizing a broad range of DNA damage²⁹. The UV-DDB complex consisting of DNA damage-binding protein 1 and 2 (DDB1, DDB2) enhances recruitment of XPC-XRC at UV induced, mildly helix-distorting CPD-lesions¹⁰. Lesion-bound XPC is the substrate of the transcription initiation factor IIH (TFIIH) complex, a ten protein subunit complex that works in NER and transcription initiation¹⁰. The assembly of XRC with TFIIH serves the verification of the DNA damage before in the next step potentially dangerous DNA incisions are made²⁹. Endonucleolytic incisions are performed by structure-specific endonucleases XPF-ERCC1 and XPG slightly up- and downstream from the DNA lesion²⁹. The resulting 22-30 nucleotide long ssDNA stretch is protected by single-strand binding protein RPA (replication protein A) until eventually gap-filling DNA synthesis and ligation fill and seal the gap²⁹. Depending on the cell proliferation status different DNA polymerases (Pol δ κ in non-replicating cells, Pol ϵ in replicating cells) and ligases (LIG1 in non-replicating cells, XRCC1-LIG3 in replicating cells) together

^e Xeroderma Pigmentosum, complementation group C (XPC); UV excision repair protein Radiation sensitive 23B (Rad23B); Centrin 2 (CETN2)

with processivity factor PCNA (proliferating cell nuclear antigen) and replication factor C (RFC) perform these reactions²⁹.

Recognition of CPDs is a slow process and persisting CPDs interfere with replication and transcription that can even lead to DSB formation (section 1.1.3). In replication such lesions can be bypassed via homologous recombination dependent template switching or translesion DNA synthesis (TLS) (section 1.2.1.4)¹⁰. In transcription however, no RNA polymerase is known to bypass helix-distorting lesions so cells rely on TC-NER to avoid stalling of transcription²⁹. TC-NER pathway is initiated by recruitment of CSA and CSB (Cockayne syndrome WD repeat protein A/ERCC6, B/ERCC8) to lesion-stalled RNA polymerase II¹⁰. The core NER factors are then being recruited together with other TC-NER specific proteins. This leads to reverse translocation of the stalled RNA polymerase (backtracking), exposure and subsequent repair of the lesion site¹⁰. Incision based removal of the damaged site, gap-filling DNA synthesis and ligation is assumed to be similar in TC-NER and GG-NER¹⁰.

1.2.1.4. Translesion synthesis (TLS)

Dividing cells rely on TLS in order to avoid DNA strand breaks and long-term DNA polymerase stalling. During replication, dsDNA is unwound and attempts to excise the lesion would lead to replication fork collapse and asymmetrical DSBs³⁵. Conclusively, TLS is not a repair mechanism but enables cells to (temporarily) tolerate DNA damage. This implies that incorporation of incorrect nucleotides by the lower fidelity TLS polymerases is potentially mutagenic¹⁰. All described TLS polymerases (Pol β ζ η ι κ λ μ ν σ θ , REV1, PrimPol) synthesize DNA with lower fidelity than the high-fidelity replicative DNA polymerases (Pol δ ϵ)¹⁰. To tolerate bulky or distorted DNA templates, TLS polymerases have a large active site and lack a 3'-5' proofreading ability³⁵. The domains that detect correct base pairing to the template base are generally shorter and bind both template and nucleotide base weaker³⁵. For TLS polymerases to function a two-step process was proposed, in which an inserter TLS Pol (η ι κ ζ REV1) incorporates a nucleotide opposing the lesion and an extender Pol (κ ζ) extends the termini¹⁰. Additionally, TLS polymerases function in other cellular pathways, including BER, NER and interstrand crosslink repair (ICL)¹⁰.

1.2.1.5. Mismatch repair (MMR)

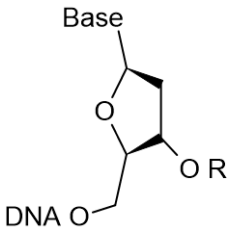
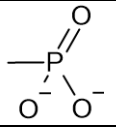
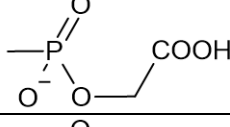
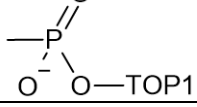
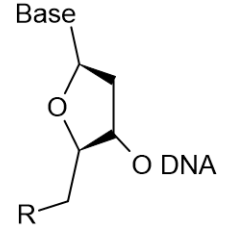
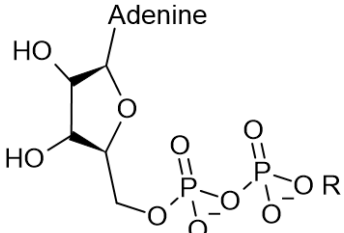
MMR increases the replication fidelity by correcting mismatching nucleobases and insertion/deletion loop (IDL) mispairs³⁶. In human cells, the MutS α complex recognizes base mismatches and small IDLs, the MutS β complex recognizes large IDLs¹⁰. Upon damage recognition, the respective MutS complex slides along the DNA to enable interaction of MutL α ¹⁰. MutL α regulates the nucleolytic removal of the mismatch by interacting with Exonuclease 1 (EXO1) and PCNA/RFC³⁶. This creates a gap and a ssDNA strand that is protected by the single-strand binding protein RPA. Similar to other nucleobase repair pathways, the gap is filled by DNA polymerases (POL δ , RFC, HMGB1) and the DNA ends are connected by ligases (LIG1)¹⁰.

1.2.2. Single strand break (SSB) repair

SSBs are a frequent type of DNA damage and commonly repaired via global SSBR. SSBs are rapidly detected and bound by PARP family members, most dominantly by PARP1³². PARP1 has an N-terminal DNA binding domain, a central BRCT-domain for self-modification and the C-terminal catalytic domain³⁷. Upon SSB binding, PARP1 activates itself by auto-PARylation which leads to synthesis of long, branched PAR-chains on chromatin proteins³². Thus, PARP1 generates a scaffold to recruit SSBR proteins to sites of DNA damage. These target proteins contain PAR-binding modules that frequently activate adjacent functional domains upon PAR binding³². PARylation is highly transient and rapid PAR catabolism by PAR glycohydrolase (PARG) was shown to be crucial for efficient DNA repair³⁸. PARP1 also gets activated indirectly during BER (see section 1.2.1.2). Furthermore, PARP1 activation leads to changes in the chromatin structure, mostly to chromatin relaxation³². PAR binding chromatin remodelers (e.g. ALC1, SMARCA5, CHD2) reposition the nucleosomes to increase accessibility or change histone composition^{39,40}. XRCC1 is recruited to PAR-sites and acts as a scaffolding protein to assemble and coordinate the SSBR machinery²³.

The termini of most SSBs are chemically altered and attached moieties need to be removed before the DNA gap can be filled. A variety of enzymes are able to process very different types of damaged DNA ends (Table 1). It is noteworthy that topoisomerase-DNA DPC repair does not rely solely on TDP1 (Tyrosyl-DNA phosphodiesterase, see Table 1) but also on preceded proteasomal degradation of the trapped topoisomerase¹⁷. After the termini are restored to their conventional configuration (3'-hydroxyl, 5'-phosphate), the resulting gap can be filled. This can either happen as a single-nucleotide insertion (short-patch SSBR) or in strand displacement synthesis for multiple nucleotides (long-patch SSBR)²³. Hereby, the displaced single-stranded dRP flap is removed by FEN1 (aided by PARP1 and PCNA)¹⁰. In short-patch SSBR, the gap is filled by Pol β , followed by LIG3-catalysed ligation¹⁰. In long-patch SSBR, the final steps are catalyzed by Pol β together with Pol δ ϵ and the PCNA/PARP1 dependent LIG^{10,23}.

Table 1: Common types of damaged DNA strand breaks and corresponding repair enzymes.

Terminus	Modification (R =)	Enzyme	Abbreviation (Activity)
3' hydroxyl end (R = H) 		PNKP	<i>Bifunctional polynucleotide phosphatase/kinase</i> (3' phosphate removal)
		APE1	<i>Apurinic–apyrimidinic endonuclease I</i> (Removal of 3' glycolates or aldehydes upon sugar disintegration/alkylation)
		TDP1	<i>Tyrosyl-DNA phosphodiesterase</i> (removes covalently bound Topoisomerases)
5' phosphate end (R = OPO ₃ ²⁻) 	—OH	PNKP	<i>Bifunctional polynucleotide phosphatase/kinase</i> (5' kinase activity)
		APTX	<i>Aprataxin</i> (Removal of adenylated 5' DNA ends, produced during abortive ligase activity)

1.2.3. Double strand break (DSB) repair pathways

DSBs arising from various sources are a substantial threat to genomic integrity (section 1.1.3). To counteract the danger that DSBs impose on life, cells rely on different, conserved DNA repair mechanisms. Canonical non-homologous end joining (C-NHEJ), alternative end-joining (A-EJ), and homologous recombination (HR) have been distinguished. Each pathway has different advantages and requirements and pathway choice varies between different organisms and cell types⁴. Given the diversity of DSBs these pathways tend to be complex and potentially interchangeable processes. A graphical overview of the important DSB repair pathways is shown in Figure 2.

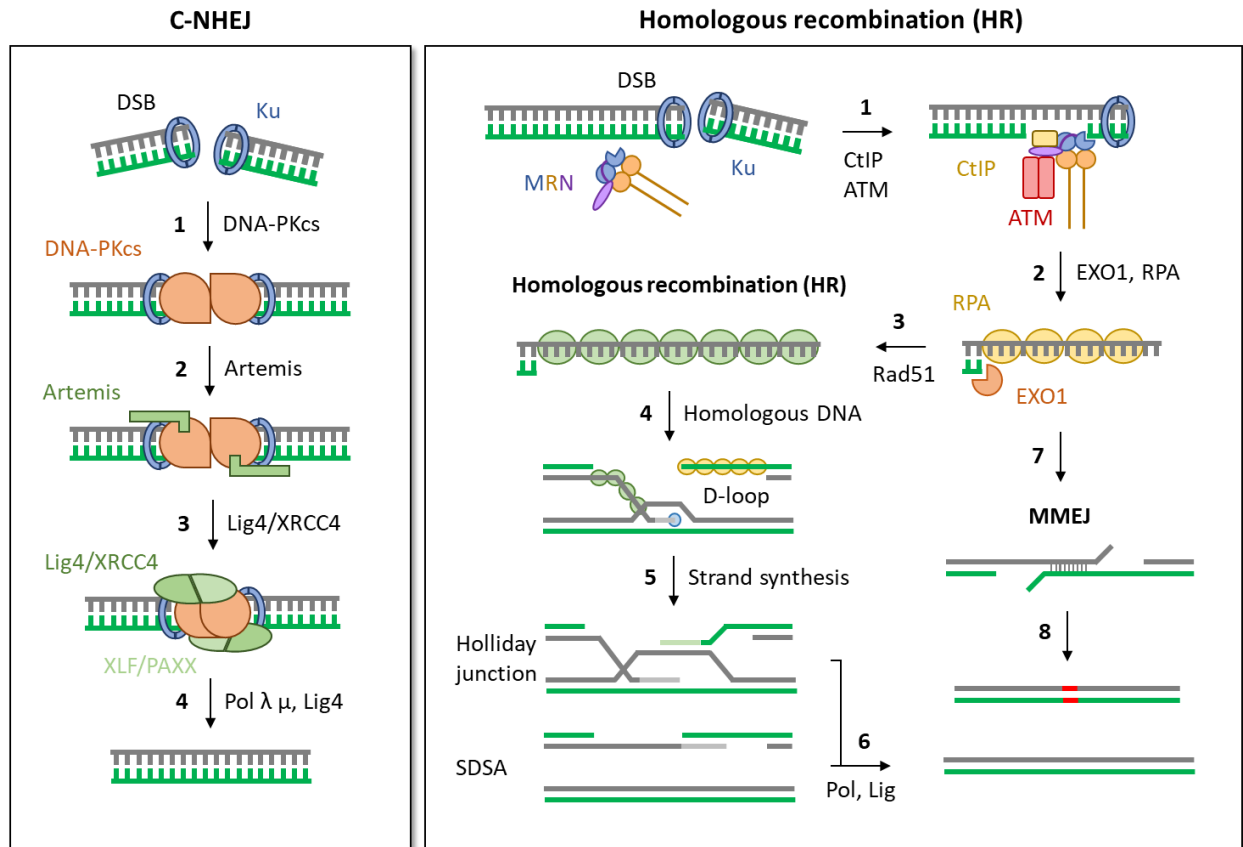


Figure 3: Schematic overview of DSB repair pathways (graphic adapted⁴). **Canonical non-homologous end joining (C-NHEJ):** Ku70/80 rapidly binds DNA DSBs. 1: Recruitment of DNA-PKcs to form the DNA-PK holoenzyme complex which provides long-range tethering. 2: Artemis processes structurally altered DNA ends. 3: The factors Lig4/XRCC4 and XLF/PAXX work together to closely align DNA ends. 4: The gap is filled by Pol λ or μ and sealed by Lig4. **Homologous recombination (HR):** The MRN complex recognizes (Ku70/80-bound) DNA ends. 1: MRN performs short-range end resection upon activation by CtIP to remove Ku70/80 or other blocked ends. MRN recruits and activates the kinase ATM to activate the cellular DNA damage response (DDR) and to alter the chromatin structure. 2: EXO1 or BLM/DNA2 perform long-range resection to generate long 3' ssDNA overhangs, protected by RPA. 3: DNA recombinase Rad51 is loaded by BRCA2 and PALB2 to remove RPA and create a nucleoprotein filament. 4: The nucleoprotein filament can invade homologous donor DNA which is used as a template for DNA synthesis. 5: The D-loop gets dissolved by formation of either a double Holliday-junction or by synthesis-dependent strand annealing (SDSA). The Holliday-junction can be dissolved by topoisomerase complexes. 6: Gaps are filled by Pol δ κ ν and nicks are sealed by Lig1. **Microhomology-mediated end joining (MMEJ)** 7: Upon MRN-dependent short-range resection and possibly long-range resection, microhomologies on the same DNA strand are used for strand annealing. 8: Upon flap removal, gaps are filled by Pol θ and ligation is catalyzed by LigIII α .

1.2.3.1. Canonical non-homologous end joining (C-NHEJ)

C-NHEJ does not rely on a template sister-chromatid, so it can be used to directly religate DSBs in haploid cells throughout the cell cycle⁴¹. However, if the DNA ends are damaged (Table 1), their nucleolytic clearance leads to loss of genetic information. The highly abundant Ku70-Ku80 (Ku70/80) heterodimer binds DNA ends with extremely high affinity to nucleate the assembly of the C-NHEJ core-machinery and to protect DNA ends^{4,42}. Ku70/80 bound DNA ends serve as platform to recruit the DNA-dependent protein kinase catalytic subunit (DNA-PKcs) to form the DNA-PK holoenzyme complex⁴¹. Structural work revealed how the Ku80 C-terminal region mediates DNA-PK dimerization and thus long-range tethering of DNA

ends⁴³. Upon formation of the dimeric tethering complex, DNA-PK is activated and undergoes autophosphorylation⁴⁴. The DNA ligase IV (LIG4) and its essential stabilizer XRCC4 assemble on DNA-PK together with scaffolding factors XRCC4-life factor (XLF) and paralogue of XRCC4 and XLF (PAXX)⁴. Eventually, all these factors work together to closely align the DNA ends which enables DNA end processing by the nuclease Artemis and specialized Pol λ and μ ⁴. Artemis is recruited and activated by DNA-PK phosphorylation and processes each DNA end to form clean ends^{45,46}. Pol λ and μ activity is required to avoid extensive loss of genetic information and to create a 3' OH and 5' phosphate end that can be used in ligation⁴¹. The final ligation reaction is catalyzed by LIG4-XRCC4⁴. Apart from the aforementioned classical NHEJ-components more factors regulate C-NHEJ. Interestingly, the multifunctional HR complex Mre11-Rad50-Nbs1 (MRN) promotes efficient C-NHEJ, possibly by DNA end tethering⁴⁷.

1.2.3.2. Alternative end-joining (A-EJ) and Microhomology-mediated end-joining (MMEJ)

In absence of Ku70/80 proteins or in C-NHEJ deficient cells, DSBs can be repaired via HR (see 1.2.3.3) or alternative (A-)EJ pathways. A subset of A-EJ pathways relies on genetic microhomologies to enable DNA end connection and has been described as microhomology-mediated end joining (MMEJ)⁴⁸. MMEJ is a highly mutagenic repair pathway that enables tumors to survive defective HR pathways⁴⁸. However, it is topic of current scientific research whether MMEJ is a main repair pathway or a mere backup. Other A-EJ pathways (single-strand annealing (SSA), end-joining) were defined based on the amount of DNA sequence complementarity used and factors involved⁴⁹. As A-EJ pathways are often enhanced in malignant cells they appear to be a promising target in cancer cells with defects in other repair pathways⁴⁹.

All A-EJ pathways share factors with the major DSB repair pathways (HR, C-NHEJ) and are initiated by DNA end resection, however it most likely that not all factors that contribute to A-EJ were described yet⁴⁹. The A-EJ end resection is initiated by the MRN complex and CtBP-interacting protein (CtIP), possibly followed by the more processive nucleases Exo1 and DNA2⁵⁰⁻⁵². Juxtaposition and/or annealing of the DNA ends is a requirement for further repair. In SSA, Rad52 anneals complementary RPA-coated strands upon resection, in the other A-EJ pathways DNA end bridging is dependent on PARP-1 and/or MRN⁵³⁻⁵⁵. In MMEJ, the majority of gaps resulting from annealing of processed ends is filled by Pol θ and ligation is catalyzed by LigIII α ^{49,56}.

1.2.3.3. Homologous recombination (HR)

In vegetative cells, HR is used to faithfully repair DSBs, while during meiosis functional HR promotes chromosome segregation and exchange of genetic material⁵⁷. This illustrates how HR is not a linear process but rather a complex network of pathways with different outcomes dependent on cell state and type. DNA end resection initiates HR and prevents ligation by C-NHEJ⁵⁷. The functional core of HR is a ATP-dependent DNA recombinase (Rad51 in eukaryotes) that enables pairing of resected ends with homologous template DNA⁵⁸. The requirement for homologous template DNA is the reason why HR is only activated when cells enter the S-phase⁵⁹.

Initially, the multifunctional MRN complex recognizes and resects free and structurally altered DNA ends (e.g. DNA-protein crosslinks (DPCs), compare Table 1)⁵⁸. The MRN complex acts as a ATP-dependent nuclease that catalyzes an endonucleolytical incision next to the DNA end, followed by short-range 3'-5' resection towards the DNA end to generate a 3' overhang⁵⁰. Efficient short-range resection is dependent on MRN's interaction with CtIP (Sae2 in yeast) and blocked DNA ends^{50,60}. CtIP is recruited by MRN only upon CDK-dependent phosphorylation at T847 to promote HR and inhibit NHEJ during S/G2-phase^{59,61,62}. Similarly, CKD-dependent phosphorylation of CtIP at S327 is required to recruit BRCA1^f, which also stimulates HR by preventing assembly of the HR-inhibiting 53BP1-RIF1 complex at DNA ends⁶³. Short-range resection and incision on both DNA strands removes terminal DPCs or bound Ku70/80 heterodimers from the end and provides an entry-point for long range resecting factors^{4,64,65}. Recent structural work revealed how the prokaryotic MR complex forms a gate that enables unspecific, topological recognition of diverse DNA ends and subsequently undergoes ATP-dependent rearrangement to initiate resection⁶⁶. Upon recognition and loading to DNA ends the MRN complex recruits and activates the signaling kinase ataxia-telangiectasia mutated (ATM) via a mechanism that requires Rad50's ATPase activity and (nucleosome-free) DNA⁶⁷. Activated ATM mediates checkpoint signaling to delay the progression of the cell cycle and activate the DDR⁶⁸. Activated ATM also phosphorylates the histone variant H2AX at S139 to form γ H2AX foci that can extend well beyond the site of the DSB and subsequently alter the chromatin structure⁴. The adaptor protein mediator of DNA damage checkpoint 1 (MDC1) binds γ H2AX chromatin and further recruits MRN-ATM complexes and thus contributes to ATM signal amplification⁴.

Initial short-range resection is followed by processive EXO1 or BLM/DNA2 catalyzed long-range resection to generate long 3' ssDNA overhangs¹⁰. The overhang is initially protected by RPA that gets displaced by the DNA recombinase Rad51 to generate a nucleoprotein filament¹⁰. Rad51 loading on ssDNA is a highly regulated process, mainly aided by BRCA2 and PALB2 (partner and localizer of BRCA2)⁵⁸. The nucleoprotein filament invades nearby DNA to scan for annealing regions and forms a displacement(D)-loop¹⁰. Eventually, the D-loop is dissolved to a four-way junction intermediate (double Holliday-junction) which can be resolved by various different topoisomerase complexes (e.g. BLM-TOPOIII-RMI1-RMI2)⁶⁹. Alternatively, the newly synthesized strand can also dissociate from the D-loop and anneal to the resected DNA end at the other side of the DSB⁶⁹. This process has been named synthesis-dependent strand annealing (SDSA) and is most prominent in somatic cells, as it avoids potential chromosomal rearrangements caused by resolution of the Holliday-junction¹⁰. Eventually, Rad51 is removed by Rad54 to allow gap filling synthesis by Pol δ κ ν as well as LIG1-catalyzed ligation¹⁰.

1.2.3.4. DSB repair pathway choice in mammalian cells

As the main DSB repair pathways C-NHEJ and HR have specific advantages and requirements. Cells rely on mechanisms to direct repair towards one pathway, based on DSB end structure, repair time, cell cycle state, and chromatin context^{4,25}. Even though the pathways are conserved from yeast to mammals,

^f BRCA1: Breast cancer type 1 susceptibility protein, is a tumor suppressor. Mutations in BRCA1 can greatly increase breast and ovarian cancer risk.

different organism and cell types can have different pathway preferences. For this reason, the following analysis focuses on somatic mammalian cells.

Specific DSB end structures result in specific pathway decisions. Long sticky-ends for instance prevent efficient Ku70/80 binding and hence efficient C-NHEJ repair⁷⁰. Similarly, chemically blocked or inaccessible DNA ends may require HR-dependent end processing and/or chromatin remodelling⁴. Problematic one-ended DSBs (e.g. at sites of broken replication forks, see section 1.1.3) require HR suppression to prevent break-induced replication (BIR, processively migrating D-loop that produces long stretches of ssDNA)⁴. The time it takes to repair the lesion influences pathway choice too. As a general trend rapid DSB repair (few minutes) is usually assigned to C-NHEJ and slower repair phases to HR⁴. For example, IR/UV-induced breaks that occur throughout the cell-cycle in a genome-wide manner are quickly repaired, mostly via C-NHEJ⁷¹. Because of the efficient early response by Ku70/80 and quick repair times it is assumed that C-NHEJ acts as the default DSB repair pathway in non-dividing, mammalian somatic cells⁴. HR on the other hand is favored (and restricted to) S/G2-phase and to complex DNA breaks through C-NHEJ inhibition.

C-NHEJ is inhibited by endonuclease-mediated end resection to remove bound Ku70/80 and targeted Ku70/80 degradation (by specific E3 ligases)^{4,72}. To restrict endonuclease activity and therefore C-NHEJ inhibition/HR initiation to S/G2 phase, HR activation is controlled by the activity of cyclin-dependent kinases (CDKs)^{73,74}. CDKs are periodically turned on and off to regulate protein expression in a cell cycle-dependent manner. Phosphorylation of CtIP, EXO1 and DNA2 by S-CDK promotes efficient end resection while impaired EXO1 phosphorylation reduces end resection⁷⁵. Another example is CDK2 phosphorylation of CtIP and BRCA1 in S/G2 phase. This enables CtIP/BRCA1 interaction with the MRN complex and its subsequent activation⁶¹. Other post-translational modifications (PTMs) (e.g. acetylation, SUMOylation, polyribosylation) were shown to finetune pathway choice⁷⁵. An important example is BRCA1 that gets PARylated by PARP1 to reduce its function and subsequently impair HR⁷⁶.

Regulation of pathway choice is dependent on the cell cycle state to ensure that C-NHEJ dominates in G1 phase and HR is favored only upon late S-phase⁴. An important mechanism is the balance between BRCA1 and 53BP1 that influences pathway choice based on cell cycle state and chromatin context (Figure 4). In G1 phase, the MRN complex recognizes DNA ends and recruits/activates the kinase ATM, which in turn phosphorylates many targets (Table 2)^{63,77}. Phosphorylated MDC1 is recruited to γ H2AX and in turn recruits ubiquitin-ligases (RNF8 which recruits RNF168) to further modify the chromatin by ubiquitination^{4,77}. Phosphorylated 53BP1 senses this chromatin context (H2AK15ub; H4K20me2)⁸ and recruits RIF1 to DSB site which prevents BRCA1 from accessing DNA ends^{4,63,75}. Hence, 53BP1 and RIF1 form a complex that protects the DNA ends from long-range resection and thereby promote C-NHEJ in G1/early S-phase⁴. In late S-phase, rising CDK-activity promotes phosphorylation of CtIP and Nbs1 (among others)⁷⁷. Phosphorylated CtIP interacts with BRCA1 and strongly antagonizes RIF1 binding⁶³. Moreover, phosphorylated CtIP/Nbs1 stimulate MRNs endonuclease activity to initiate end resection and subsequent HR repair⁵⁰.

⁸ Monomethylated H4K20 was shown to enhance chromatin accessibility and promote transcription of housekeeping genes²¹⁴.

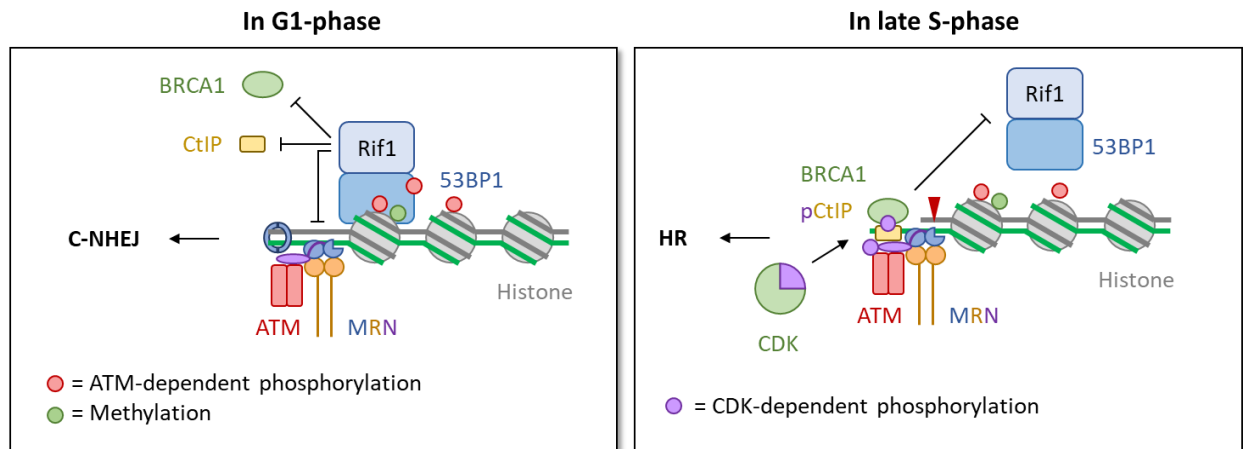


Figure 4: The balance of Rif1-53BP1 and BRCA1-CtIP influences the pathway choice depending on cell cycle state (adapted from⁷⁷). In G1-phase, phosphorylated 53BP1 senses the chromatin state and prevents association of BRCA1-CtIP at DNA ends to promote C-NHEJ. Upon late S-phase, CDK-phosphorylated (p)CtIP and Nbs1 stimulate MRNs endonuclease activity (red triangle). BRCA1 interacts with pCtIP and antagonizes Rif1 binding to promote HR repair.

1.2.3.5. The Mre11-Rad50-Nbs1 (MRN) complex in DSB repair

The MRN complex acts in multiple cellular processes, among them most importantly repair of DSBs (section 1.2.3.5.2). In DSB repair, the MRN complex is a multifunctional key player and has important roles in DDR, meiotic recombination and telomere maintenance. The complex most importantly initiates HR but it also functions in NHEJ and A-EJ⁷⁵. How MRN acts on DNA ends by combining sensor, scaffolding and enzymatic functions is not yet fully understood, especially in eukaryotic organisms. Mre11 and Rad50 are highly conserved throughout all domains of life and their functional deficiency leads to developmental issues or embryonic lethality^{78,79}. Nbs1 is the eukaryote-specific non-enzymatic subunit that modulates DNA damage signaling and MRN activation^{50,60,80}. Similar to Mre11 and Rad50, its deletion is lethal in mice, however a small fragment of Nbs1 was shown to rescue embryonic viability⁸¹. The conserved core complex forms a M₂R₂ heterotetrameric assembly that in eukaryotes binds one or two Nbs1 subunits^{82,83}.

1.2.3.5.1. Structure and functions of the MRN subunits

Mre11 is the Mn²⁺-dependent nuclease subunit that has a 3' to 5' exonuclease activity on its own^{54,84}. This activity is stimulated within the MR complex^{54,84}. However, as part of the MRN complex and stimulated by CtIP, Mre11 acts as an endonuclease that cleaves around 20 bp from a blocked DNA end followed by processive 3' to 5' resection towards the block^{50,60}. Mre11 consist of a N-terminal phosphodiesterase domain that harbors the highly conserved Mn²⁺-binding site in which binding and hydrolysis of the DNA backbone is catalyzed (see Figure 5)⁸⁵. Together with the adjacent capping domain, the well-ordered nuclease is formed⁸⁵⁻⁸⁷. The nuclease forms a tight dimer via conserved helical bundle structure⁸⁵⁻⁸⁷. A conserved Nbs1-motif binds asymmetrically across the dimer interface possibly to further stabilize the Mre11 dimer (see also Figure 8)⁸². The nuclease is followed by a flexible linker region that connects the Rad50-interacting helices with the nuclease^{86,88}. These helices form a short helix-loop-helix (HLH) motif in

prokaryotes and a more complex helical, Rad50-binding domain (RBD) in eukaryotes that interacts with the base of the Rad50 coiled-coils (CC)^{66,86,88-90}. The C-terminus in eukaryotes forms a large (around 200 amino acids in human Mre11), flexible domain that has DNA binding activity^{91,92}.

As the Mre11 dimer formation is required for functional HR repair, it was suggested that the dimeric nuclease domains tether two DNA ends to form a synaptic complex⁹³. Several Mre11-DNA structures show its capabilities to bind different DNA end architectures⁹³. However, it remains unclear how Mre11 could combine nuclease and tethering functions especially in complex with Rad50, where its DNA binding sites are blocked by the Rad50 nucleotide binding domain (NBD)^{66,90}. In synaptic Mre11-DNA crystal structures, the DNA is localized in a position distant from the active site, it is unclear how Mre11 on its own could tether DNA ends and process DNA ends in an unified mechanism (Figure 5C)^{85,93}.

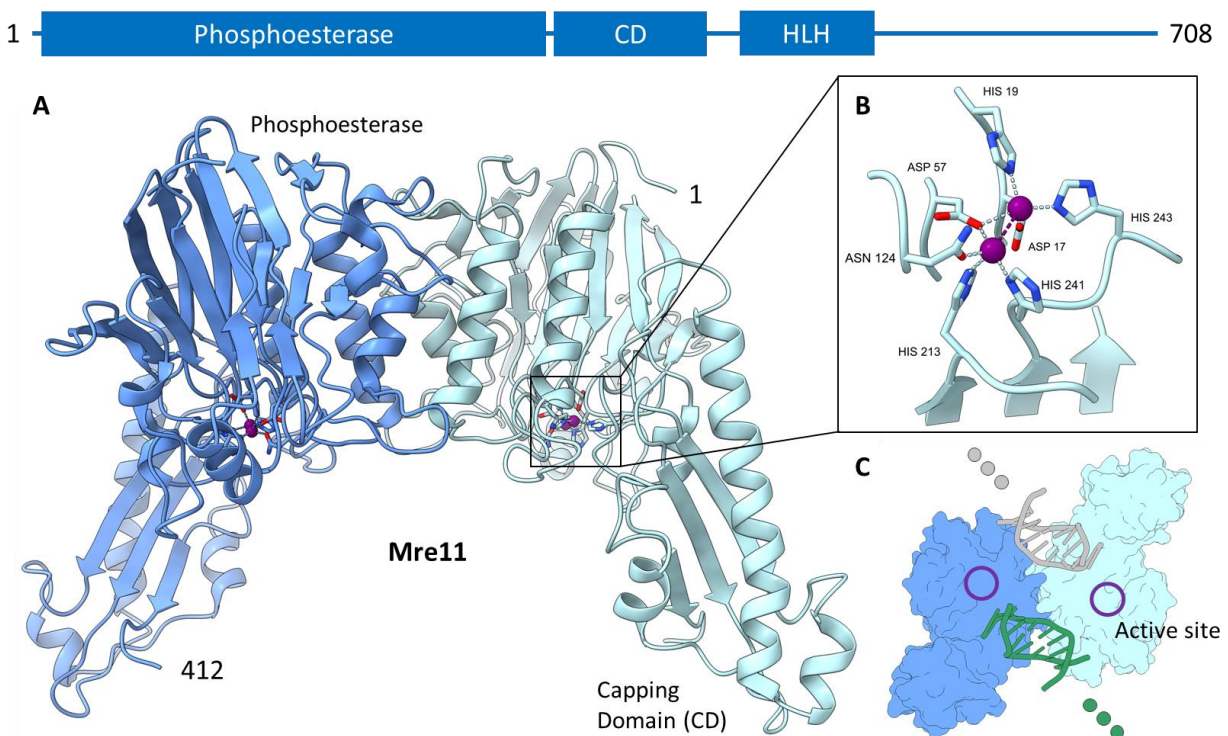


Figure 5: Structure of the eukaryotic Mre11 nuclease. Illustration of Mre11 domain organization: 4-325 phosphoesterase domain, 328-420 capping domain (CD), 438-521 helix-loop-helix interaction site, 521-708 flexible eukaryote specific C-terminus. A: Crystal structure of *Chaetomium thermophilum* (Ct)Mre11 nuclease dimer (PDB-ID: 4YKE), inset B shows catalytic site. C: DNA-bound Mre11 nuclease crystal structure shows a possible end tethering complex (PDB-ID: 3DSC)⁹³.

Rad50 has a structure resembling that of the structural maintenance of chromatin (SMC) protein family. In Rad50, the N- and C-terminus interact to form a globular ABC-type ATPase domain (nucleotide binding domain, NBD) (Figure 6)⁹⁴. Common to ABC-type ATPases, the globular NBDs dimerize and bind two ATP molecules with highly conserved motifs (Figure 6B)⁹⁴. The N-terminal part of the NBD contains the β -phosphate binding Walker A motif and the C-terminal part contains the signature (senses γ -phosphate) and Walker B motif involved in γ -phosphate and Mg^{2+} binding, respectively^{88,94}. Upon ATP-dependent dimerization, a DNA binding groove is formed at the base of the NBDs (Figure 6)^{86,94,95}. Eukaryotic Rad50 shows

a slow basal ATPase rate that is stimulated by DNA and Nbs1⁹⁶. Rad50 mutants with impaired ATPase activity lead to dramatic phenotypes, similar to that of completely deleted Rad50^{97,98}. A set of Rad50 mutations, located at the exposed β -sheets showed strong defects in meiotic recombination but not in DNA repair⁹⁸. The majority of Rad50s protein mass protrudes as an elongated, antiparallel CC domain from the globular NBDs. The length of the CCDs is remarkably different between different domains of life and varies between 10 nm (viral) and 60 nm (higher eukaryotes)⁹⁹. The variations in CC length possibly correlates with the complexity of chromatin organization and inherent inter-chromosomal distances⁹⁹. The CC domains are absolutely indispensable for the function of the MRN complex and truncations of the CC domains severely impaired MRN's function¹⁰⁰. At the apex, the Rad50 protein folds back onto itself to form a homo-dimerization domain, denoted zinc hook or apex domain. A conserved CXXC motif from each of the dimerizing Rad50 proteins coordinates a single Zn^{2+} ion¹⁰¹.

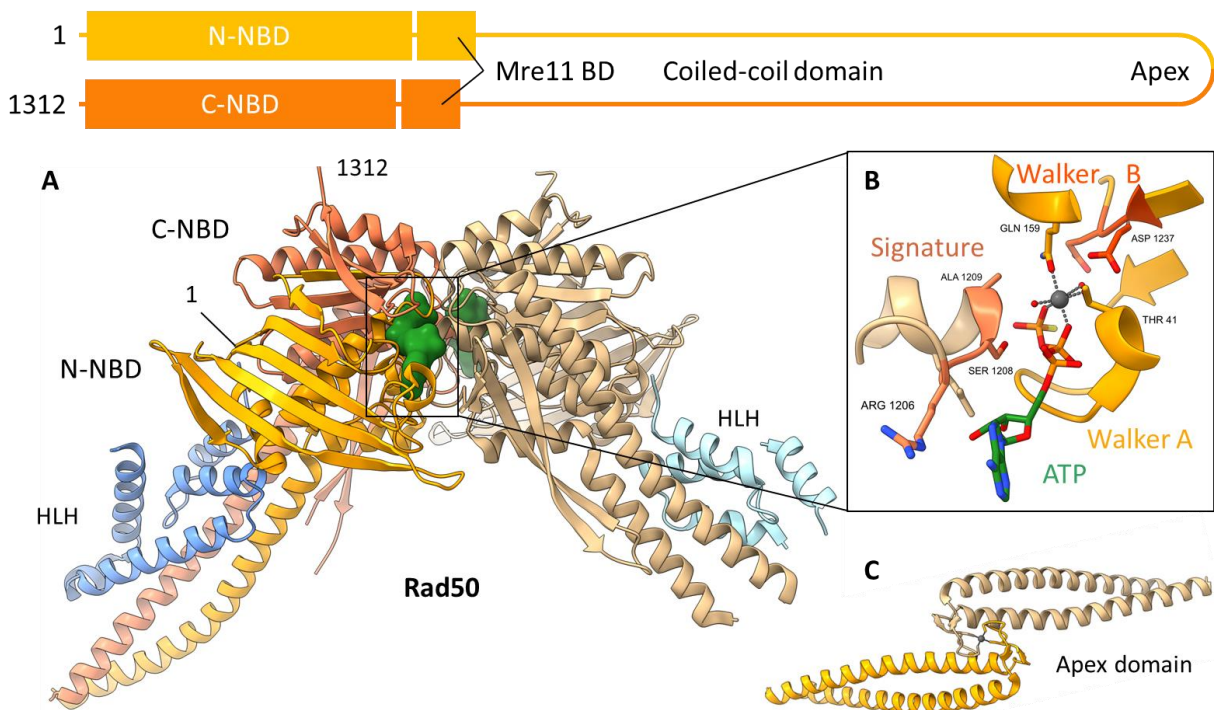


Figure 6: Structure of the eukaryotic Rad50 ATPase. Illustration of the Rad50 domain organization: 3-117 N-terminal nucleotide binding domain (N-NBD), 181-216 and 1104-1140: Mre11 binding domain (Mre11 BD), 217-686 and 708-1139: Coiled-coil domain 687-707: Apex domain, 1159-1311: C-terminal (C)-NBD. A: Crystal structure of *Chaetomium thermophilum* (Ct)Rad50 NBD dimer (N-NBD: orange, C-NBD dark orange, Dimer: Tan) bound to Mre11 helix-loop-helix (HLH) domain (blue) (PDB-ID: 5DA9)⁸⁸. ATP is contoured in green. B: Detailed view of the nucleotide binding mode at the dimer interface: Walker A motif orange loop, Walker B motif highlighted orange/dark orange, signature motif highlighted orange, Mg^{2+} is colored grey. C: Crystal structure of the prokaryotic apex domain (zinc hook) in an open conformation (PDB-ID: 1L8D)¹⁰¹.

Rad50 and Mre11 together form the evolutionary conserved MR core complex. The dynamics of the MR core complex and the interplay between the different domains are not yet fully understood. A mechanistic working model is visualized to integrate different research results, mostly on the prokaryotic complex (Figure 7). The core complex consists of two Mre11 and two Rad50 subunits with a distinct head domain and the CCs that adopt either a ring or a rod shape¹⁰²⁻¹⁰⁴.

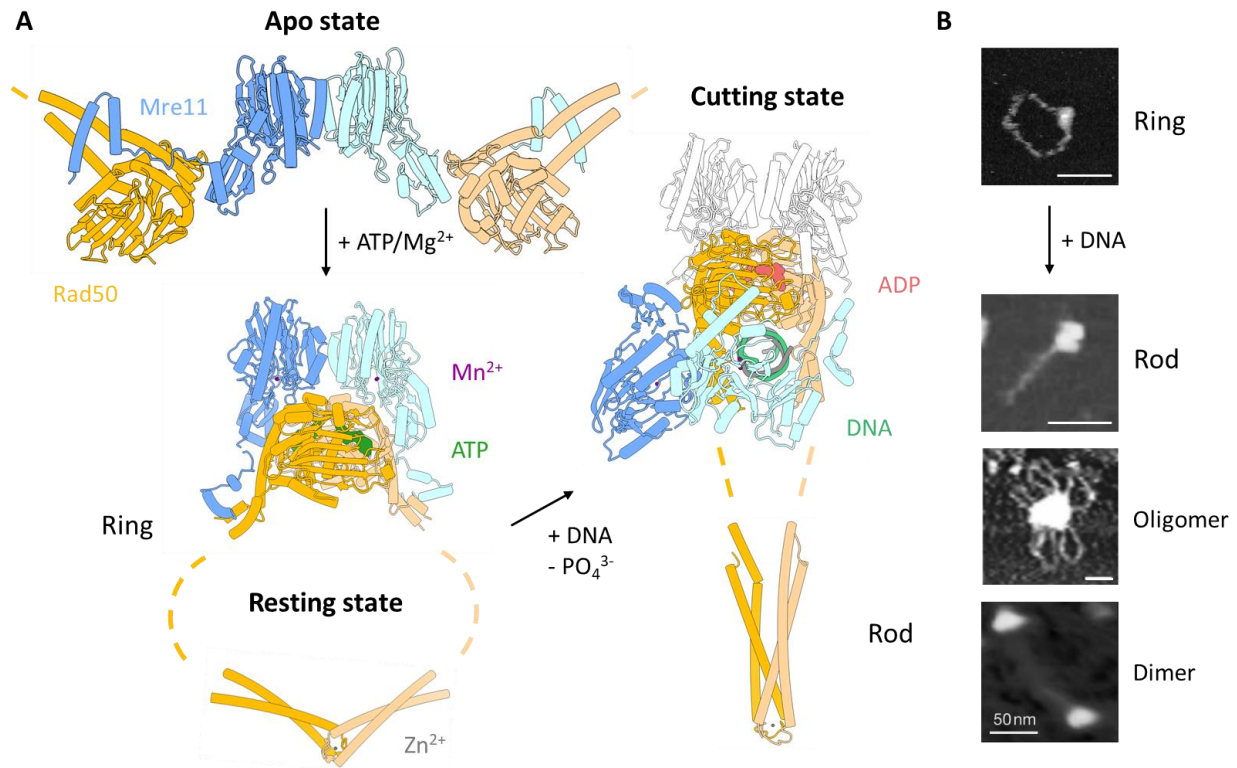


Figure 7: Dynamics of the core Mre11-Rad50 complex. A: Structural model of the prokaryotic MR complex. In the apo state, Mre11 (blue) Rad50 (orange) adopts an open, elongated conformation (PDB-ID: 3QG5)⁸⁶. Upon ATP (green) binding, the Rad50 NBDs dimerize to form a DNA binding site. In the resting state the coiled-coils (CC) adopt a ring-shaped conformation (PDB-ID: 3QG5, 1L8D)^{86,101}. Upon DNA (green/grey) binding, the MR complex adopts a closed rod-shaped conformation, in the catalytic site ADP (red) is bound (PDB-ID: 6S85, 6ZFF)⁶⁶. B: AFM data of eukaryotic MR complexes. Without DNA, the complex adopts a ring shape, similar to prokaryotic MR. Upon DNA binding, rod-shaped structures, oligomers and dimers were observed^{102–104}.

Structural data revealed how the Rad50 NBDs dimerizes upon ATP binding, while the Mre11 subunit rests in a conformation in which the phosphoesterase site is blocked by the NBDs^{66,86,90}. The ATP-bound conformation has been described as resting state and seems to resemble the normal physiological state of MR^{66,h}. The MR complex in resting state was shown to bind DNA via an exposed binding site at the base of the Rad50 NBDs^{86,90,95}. In this state the two Rad50 CCs protrude from the head in an open conformation and dimerize at the apex domain to form a closed, ring-shaped structure^{66,102–104}. A crystal structure of the archaeal Rad50 apex domain in an open conformation fits very well to this model¹⁰¹. Single-molecule studies revealed how the MRN complex binds to linear DNA and diffuses until it detects DNA ends⁶⁴. MRN was shown to be able to bypass nucleosomes while scanning for DNA ends⁶⁴. Intriguingly, truncation of the Rad50 CC domains did not change the DNA binding life times and the diffusion rates of MRN was ATP-independent⁶⁴. Thus, MRN in the resting state most likely scans for DNA ends without encircling the DNA in a mechanism that is also independent of ATP-induced conformational changes of the Rad50 subunits. However, a detailed mechanism that explains how DNA scanning is performed in the resting state has not

^h Under physiological conditions, ATP is always available at concentrations from 0.5-5 mM depending on cell types²¹⁵. The ATP binding affinity of Rad50 was measured to be at around 1.5 μ M and independent of whether Rad50 was associated with Mre11²¹⁶. Consequently, it can be assumed that the equilibrium is shifted towards the ATP-bound resting state.

been published yet. Cryo-EM and AFM data revealed how the MR core complex undergoes large scale conformational changes upon DNA end recognition in order to process the DNA end^{66,104}. For this reason, this state has been labelled cutting state⁶⁶. The CCs switch from an open, ring-shaped to a closed, rod-shaped conformation to embrace and tightly bind the DNA end⁶⁶. Other crystal structures of the Rad50 apex domain revealed a rod-shaped conformation that can be interpreted as part of the rod-shaped MR complex¹⁰⁵. The Mre11-dimer rotates from a blocked position in the resting state to the side of one Rad50 NBD⁶⁶. The Rad50 NBDs and one of the Mre11 subunits form a DNA binding channel in which a DNA end protrudes into the Mre11 active site⁶⁶. In a cryo-EM structure of the cutting state, ADP was bound by the Rad50 NBDs and in biochemical assays it was observed that DNA stimulates the Rad50 ATPase rate^{65,66}. It seems the energy for these mesoscale rearrangements are provided by ATP-hydrolysis. Nuclease experiments illustrated that the MR complex only degraded linear but not circular DNA⁶⁶. As previously mentioned (section 1.2.3.3), MRNs nuclease activity is enhanced by protein blocks at the DNA end^{50,60}. To conclude, in order to adopt the cutting state, the MR complex requires a (blocked) DNA end which is recognized by its topology and not by specific chemical properties⁶⁶.

Nbs1 (Xrs2 in yeast) is present only in eukaryotes and acts as an adaptor protein to coordinate DSB repair and DDR signaling. The way Nbs1 regulates the MR core complex has not yet been conclusively understood. Nbs1 does not have any catalytic activity on itself, it acts solely as scaffolding protein. Therefore, Nbs1 has a structured N-terminal region that consists of a Fork-head associated (FHA) and tandem-BRCA1 carboxy-terminal (BRCT) domains that are each directly linked (Figure 8)^{106,107}. This modular configuration is atypical for FHA/BRCT domain containing proteins, as each of these domains could bind phosphopeptides on its own¹⁰⁸. However, structural data revealed that binding of pCtIP to FHA modifies the configuration of the tandem-BRCT domain and most likely its phosphopeptide binding capacities (Figure 8)^{107,108}. The Nbs1 N-terminus binds and recruits phosphorylated proteins, among them CtIP, BLM, BRCA1 and Mdc1^{106,107,109,110}. Depending on the interactor, the MRN complex is activated at DSB sites only in certain phases of the cell cycle (CtIP/BRCA1-mediated) and recruited to γ H2AX (Mdc1-mediated)^{106,107,109,110}. Adjacent to the N-terminus, an unstructured region functions more like a flexible tether¹⁰⁷. This flexible region is followed by a mostly unstructured 108 amino region that was characterized as a minimal Nbs1-fragment capable of rescuing the Δ Nbs1 phenotype⁸¹. This region is responsible for nuclear localization and stabilization of the MR complex⁸¹. Structural data revealed how a conserved NFKxFxK motif within this region bridges the Mre11-interface and a less conserved N-terminal part binds to the sides of the Mre11 phosphoesterase domain⁸². Further at the C-terminus a region was shown to interact with ATM¹¹¹.

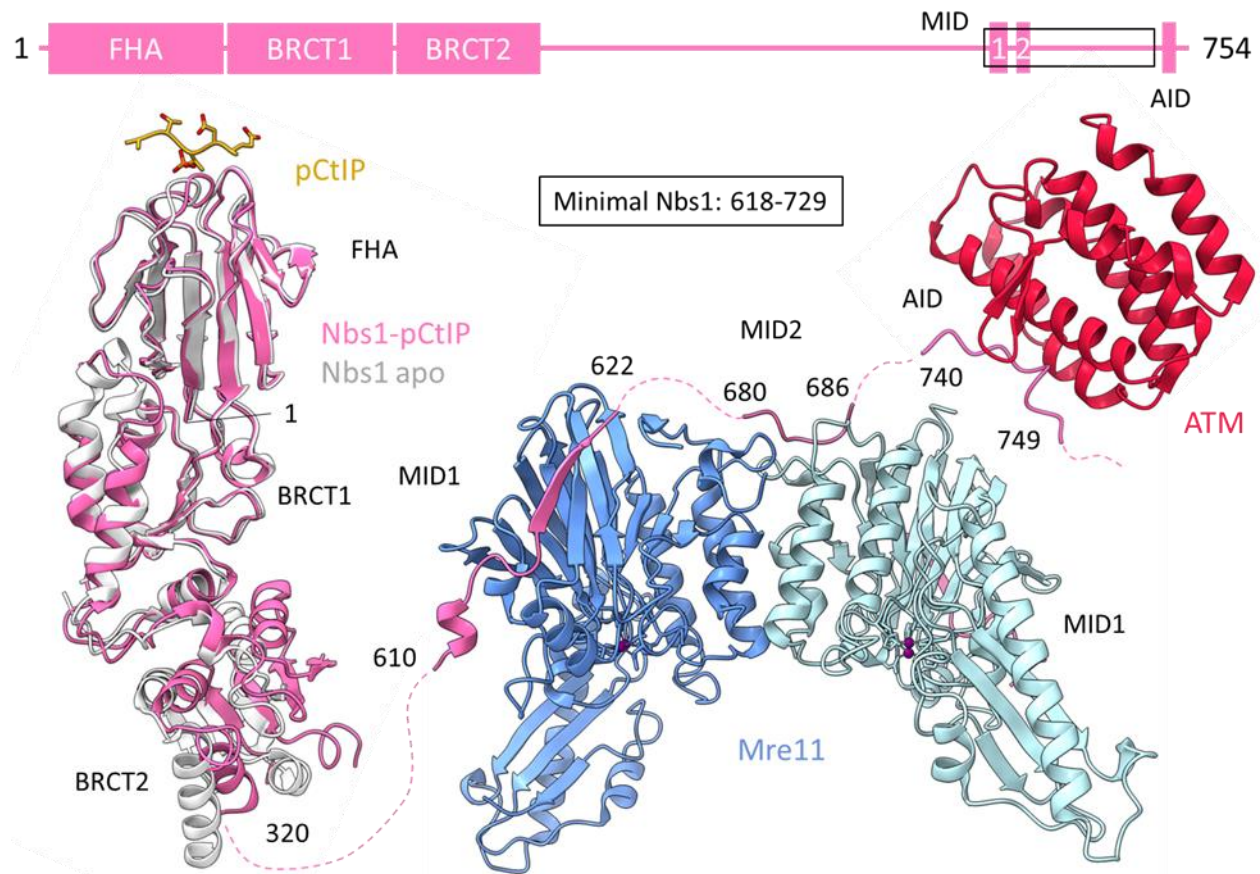


Figure 8: Structural data of eukaryotic Nbs1. Illustration of Nbs1 domain organization (amino acid numbering for human Nbs1): 1-115 FHA, 117-225 and 226-320 tandem-BRCT domain, 610-622 and 680-686 Mre11-interacting domains (MID1, MID2), 740-749 ATM-interacting domain (AID), the minimal Nbs1 fragment able to rescue the Δ Nbs1 phenotype is highlighted with a black frame⁸¹. Structures of Nbs1: Apo Nbs1 (Grey, PDB-ID: 3HUE) undergoes conformational change upon phosphor-(p)CtIP (yellow) binding (pink, PDB-ID: 3HUF), MID1 and MID2 interact with Mre11 phosphoesterase domain (shades of blue, PDB-ID: 4FBW) and an N-terminal region of ATM (red, PDB-ID: 7SID)^{82,111}.

1.2.3.5.2. Biological functions of the MRN complex

As discussed earlier, MRN recognizes DNA ends and its DNA resection activity initiates HR repair and inhibits NHEJ (section 1.2.3.4). However, the observation that knockdown of Mre11 results in decreased efficiency of both C-NHEJ and A-EJ pathways indicates the DNA repair pathways are not isolated, they rather seem to function as a tightly coupled web of pathways¹¹². As described, Mre11 catalyzes the initial nucleolytic resection in A-EJ (section 1.2.3.2)⁴⁸. The exact function of MRN in C-NHEJ remains elusive, possibly it has a more structural rather than enzymatic function. This is indicated by research in *S. cerevisiae* where nuclease-dead Mre11 could partially rescue the effects of Mre11 deletion in C-NHEJ-dependent repair of incompatible DNA ends¹¹³. MRN initiates repair of Spo11-initiated DSBs (section 1.1.3) and thus promotes meiotic recombination events⁵². In the adaptive immune system, MRN enables efficient somatic V(D)J recombination by initiating the repair of RAG-induced DSBs¹¹⁴. Mre11 on itself acts as a Mn²⁺-dependent and ATP-independent 3'-5' exonuclease that can also open hairpin structures⁸⁴. However, in

eukaryotic cells Mre11 is most likely associated with Rad50 and Nbs1, as its nuclear localization is dependent on Nbs1 and the HLH motif is a strong hydrophobic interface^{88,115}. *In vitro* studies on eukaryotic and prokaryotic MR(N) revealed that the complex cleaves both DNA strands next to a blocked DNA end^{50,116-118}. Eukaryotic MRN requires stimulation by phosphorylated CtIP to show a robust endonuclease activity^{50,116}. Strikingly, MRN showed also endonuclease activity adjacent to a nucleosome¹¹⁸. However, it is possible that the terminal nucleosome substrate used in this study is simply recognized as blocked DNA end because MRN does not cut on internal nucleosomes, it simply bypasses them⁶⁴. Upon a 5' endonucleolytic incision, the MRN complex catalyzes a short range 3' to 5' resection towards the DNA end resulting in a 3' ssDNA tail that is a substrate for further HR⁵². The processive short-range endonuclease activity is interpreted as nucleolytic cleansing of blocked DNA ends to remove aggregated or bound DPCs and to initiate HR.

Apart from nucleolytic processing of DNA ends, MRN also recruits ATM to initiate DDR signaling in response to DSBs (section 1.3). The MRN complex is uniformly distributed within the nucleus. However, upon DSB formation, the complex relocates and aggregates very fast to the site of DNA lesions¹¹⁹. DNA-bound MRN was shown to physically associate with and activate ATM to initiate further signaling⁶⁷. This process might be enhanced via MRN-dependent cooperative oligomerization^{64,120}. Apart from actively activating ATM, a role of MRN in ATR activation has been proposed. The complex binds several ATR-activating DNA structures (e.g. dsDNA-ssDNA junctions) and recruits the ATR-activator TOPBP1¹²¹.

Lastly, the MRN complex has important functions in telomere maintenance. The transition from circular to linear chromosomes in eukaryotes gave rise to two main challenges that had to be addressed in order to maintain genome integrity. Firstly, the end replication problem was solved by introduction of repetitive end sequences (TTAGGGn in mammalian cells) and the ribonucleoprotein telomerase¹²². In every round of replication of linear DNA, the lagging strand is shortened as no new primers can be synthesized towards the end. Telomerase is a reverse transcriptase enzyme that can elongate the telomers by adding repetitive sequences to prevent end shortening¹²². Secondly, the DSB recognition problem arises from exposed DNA ends that resemble DSBs. This problem is solved by the end structure of telomers that prevents unintentional DDR activation by masking the DNA end. In telomers, a (T-)loop is formed in which the chromosome end invades repetitive telomeric dsDNA further downstream¹²². This structure is stabilized by telomeric proteins denoted shelterins. Loss of shelterin proteins leads disruption of the T-loop structure and attempted repair and DDR at telomers¹²³. The functional role of MRN in telomere maintenance was discovered in yeast, where deletion of MRN components led to shortened telomeres and cellular senescence^{124,125}. In human meiocytes, Mre11 is recruited by Nbs1 to telomeres, where the proteins are found to be concentrated. Thus, MRN most likely promotes recruitment of telomere proteins during telomere replication in late S-phase¹²⁶. Following replication, the blunt ended telomere is processed by Mre11 (to prevent attempted C-NHEJ) and to enable T-loop formation. MRN was shown to physically interact with the shelterin protein telomeric repeat-binding factor (Trf)2¹²⁷. Trf2 prevented ATM activation and subsequently DDR initiation at telomers¹²⁷. The interaction of Nbs1 and Trf2 is disrupted by a CDK2-dependent phosphorylation and thus coupled to the cell cycle¹²⁸. To prevent MRN nuclease activity at intact telomeres, in yeast Rif2 inhibits MRN's activity to capture DNA ends by a physical interaction with the Rad50

β -sheets¹²⁹. To summarize, MRN is required to establish the formation of functional telomeres upon replication, later in the cell cycle MRN is inhibited by Rif2 and ATM activation is prevented by Trf2.

1.3. DNA damage response (DDR)

The previously described mechanisms and pathways (section 1.2) ensure efficient repair of various types of DNA lesions (section 1.1). However, cells also rely on robust response to DNA lesions to sense damage, enable activation of DNA repair factors, cell cycle arrest and chromatin modification. Therefore, cells rely on the DNA damage response (DDR). The DDR is a signaling pathway that is primarily mediated by members of the phosphatidylinositol 3-kinase (PI3K)-like protein kinase (PIKK) and PARP family⁵. PARP1 and PARP2 catalyze the addition of PAR chains to chromatin proteins to create a scaffold that enables recruitment of other DDR proteins (compare section 1.2.2)^{5,32,40}. The PIKKs ATM and/or ATR are recruited to DNA lesions by sensors (e.g. Ku70/80, MRN, RPA) and initially phosphorylate mediator proteins (e.g. H2AX, Mdc1) in order to amplify the DDR⁵.

ATM and/or ATR activity leads to activation of checkpoint kinases (Chk)1 and 2, which then results in cell cycle arrest and DNA repair (Figure 9)¹³⁰. Persistent checkpoint signaling forces cells into apoptosis to prevent damaged cells from dividing¹³⁰. Chk1 is expressed in S/G2 phase and gets mostly activated in response to single-stranded DNA structures (e.g. DSB, stalled replication forks resected DSBs) by activated ATR¹³¹. ATR relies on ATR interacting protein (ATRIP) to bind RPA-coated ssDNA¹³². RPA-coated ssDNA also stimulates binding of the RAD9-HUS1-RAD1 (9-1-1) complex which recruits TopBP1 to activate ATR¹³¹. Chk2 is a stable protein that is expressed throughout the cell cycle and mostly functions in response to DSBs¹³⁰. ATM is recruited to DSBs by the MRN complex and activates (among others) Chk2 to initiate the DDR. It is generally accepted that ATM is the principle mediator of the G1/S cell cycle checkpoint, while ATR primarily induces intra-S and G2/M checkpoints¹³¹. However, even though ATM and ATR act mostly on different, non-redundant signaling pathways, they have partially overlapping functions. Chk1 for example gets also phosphorylated by ATM in response to IR¹³³. Due to the overlapping functions of ATM and ATR, defects in either pathway can be partially compensated for by the respective other pathway¹³¹.

G1/S cell cycle check point activation prevents cells with damaged DNA from entering S-phase¹³¹. Activation of G1/S checkpoint signaling is mediated by phosphorylation of tumor suppressor p53 by ATM and Chk2^{131,134}. Phosphorylation of p53 prevents its Mdm2-mediated ubiquitinylation and degradation, ATM also directly phosphorylates Mdm2 to render it less active^{131,135}. This leads to accumulation of p53 in the nucleus, where it acts as transcription factor to induce expression of genes involved in cell cycle checkpoint activation¹³¹. An important p53-regulated gene is CDK2-inhibiting protein p21, which prevents CDK- and PCNA-activity and thus cell cycle progression and DNA synthesis¹³¹. Progression through S-phase is promoted by the phosphatase Cdc25A through activation of CDK2 which is required for DNA synthesis¹³¹. Chk1 or Chk2 activity (depending on the DNA damage type) mediates Cdc25A degradation to prolong DNA synthesis and enforce intra-S checkpoint signalling¹³¹. Entry into mitosis requires the activation of nuclear CDK2 through dephosphorylation by the phosphatase Cdc25C. To activate G2/M checkpoint signaling, Cdc25C is phosphorylated by Chk1 and subsequently sequestered into the cytoplasm¹³¹.

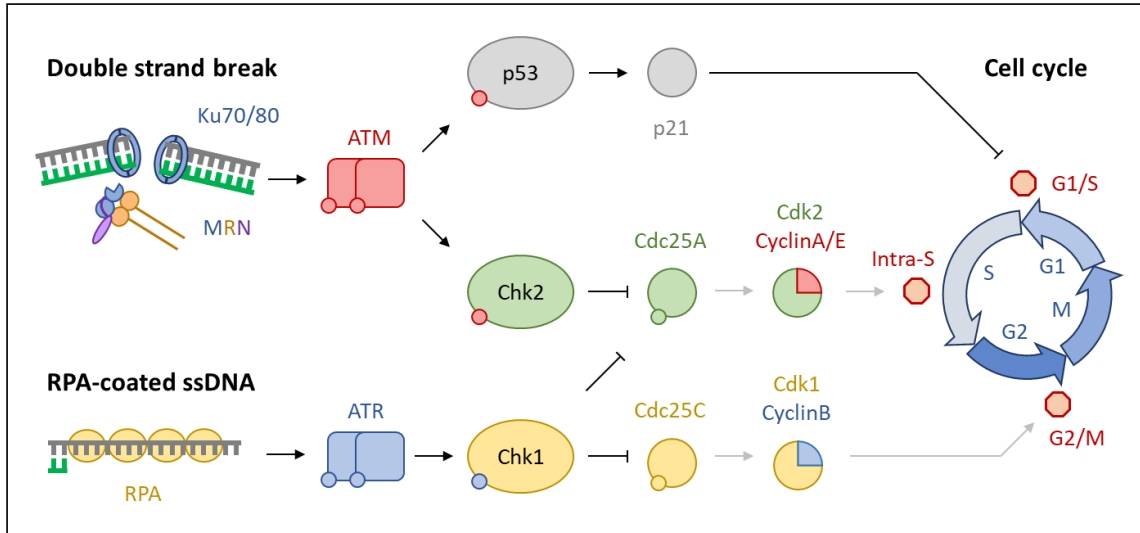


Figure 9: ATM and ATR-dependent DNA damage induced cell cycle checkpoint signaling (graphic adapted¹³¹). ATM and ATR are activated by DSBs or RPA-coated ssDNA stretches and signaling induces cell cycle arrest. Activated ATM phosphorylates (small circles) p53 to prevent its degradation. Accumulated p53 leads to expression of p21 (among others) which mainly inhibits Cyclin-dependent kinase (CDK)2 activity to inhibit cell cycle progression mainly via inhibition of G1/S checkpoint. Main targets of ATM and ATR are checkpoint kinases Chk1 and Chk2. Central targets of Chk1/2 are the Cdc25 phosphatases that control the activity of specific CDK1/CDK2 which in turn regulate the progression through the cell cycle. Chk1/2 activity leads to inhibition of Cdc25 activity and subsequent cell cycle arrest at G2/M or Intra-S phase checkpoints.

1.3.1. The PIKK family of signaling kinases

PIKK family members ATM, ATR and DNA-PKcs respond to DSBs, however as established earlier (section 1.2.3.1) DNA-PKcs acts on a smaller group of proteins involved in C-NHEJ and is not found in lower eukaryotes^{5,45,46}. ATM and ATR have overlapping functions as the main signaling kinases of DNA damage. ATM leans more towards response to DSBs, while ATR acts more as a responder to SSBs and binds to RPA coated ssDNA stretches⁵. Other PIKK family members are mTOR (mammalian target of rapamycin), TRRAP (Transformation/transcription domain-associated protein) and SMG1 (Suppressor with morphogenetic effect on genitalia 1). The mTOR kinase has been identified as target of the immunosuppressive drug rapamycin/sirolimus and was shown to sense certain metabolic parameters and subsequently regulates translation of cell cycle proteins¹³⁶. SMG1 is involved in regulation of non-sense mediated RNA decay¹³⁷. TRRAP is the only PIKK member that does not have any kinase activity, it is part of protein complexes that regulate transcription and modify chromatin^{138,139}.

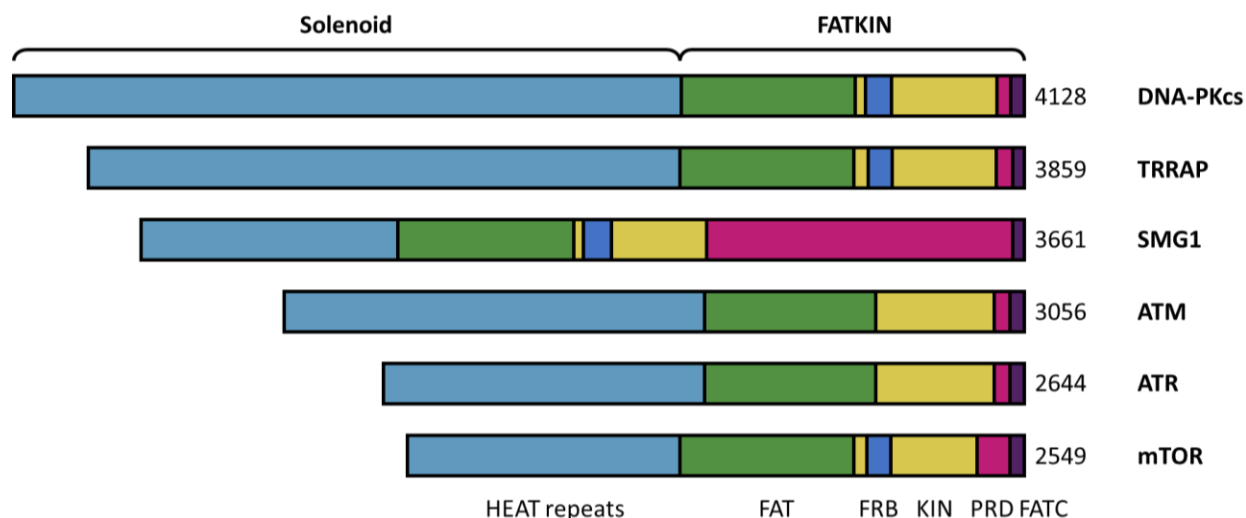


Figure 10: Domain architecture of members of the PIKK family. PIKKs have N-terminal solenoid domain consisting of HEAT repeats (light blue) with low conservation and C-terminal FATKIN domain. FATKIN consists of the FRAP-ATM-TTRAP (FAT, green), kinase (KIN, yellow), PIKK regulatory domain (PRD, pink), C-terminal FAT (FATC, purple) domain. Some PIKKs also contain a fragment rapamycin binding (FRP, dark blue). The number of amino acids of human proteins is indicated.

All PIKK family members are large proteins (up to 465 kDa for DNA-PKcs) and share a similar domain architecture (Figure 10). In order to function, all PIKKs rely on accessory proteins¹³⁹. The PIKK kinase domain (KIN) near the C-terminus (around 400 residues) is highly conserved and shares homology with the phosphoinositide 3-kinase (PI3K) family. The kinase active site within the KIN domain is typically blocked by either access restriction or locking of the active site loop¹³⁹. The active site is principally in a catalytic competent conformation and is regulated by certain PIKK-specific elements¹³⁹. Similar to many kinases, the KIN consist of an N-terminal (N-)lobe and a larger C-terminal (C-)lobe that form an ATP-binding cleft, a conserved motif (absent in TRRAP) catalyzes the kinase reaction^{136,139}. The FRAP-ATM-TTRAP (FAT) domain (around 700 residues) tightly wraps around the KIN domain and together the domains form a functional unit, denoted FATKIN. FAT and the smaller, C-terminal FATC domain are important for the regulation of kinase activity¹³⁹. A PIKK regulatory domain (PRD) was initially discovered in ATR to be an important regulatory element that blocks the substrate channel in some PIKKs (ATM, mTOR)¹³⁹. Most PIKKs (DNA-PKcs, mTOR, TRRAP, SMG1) have a FRB (fragment rapamycin binding) insertion at the beginning of the KIN domain¹³⁹. A complex of FKBP12 and rapamycin were shown to bind the mTOR-FRB with extremely high affinity¹⁴⁰. The N-terminal part of all PIKKs consists of a huge, α -helical solenoid domain with low sequence conservation. The solenoid domain is mostly comprised of a protein tandem repeat structural motif denoted HEAT-repeatⁱ. HEAT repeat domains are highly flexible, even elastic, amphiphilic arrays that serve as a protein-protein interaction hub¹⁴¹. Very little is known about the mechanism of HEAT repeat, especially under physiological, crowded conditions¹⁴¹. In PIKKs, the N-terminal domain serves as a binding platform, that enables recruitment of the various different interaction partners¹³⁹.

ⁱ The acronym HEAT is derived from proteins that contain this motif: **H**untingtin **E**longation factor 3, protein phosphatase 2A subunit **A**, **T**OR1 kinase¹⁴¹.

1.3.2. ATM is a key player in DDR

ATM mostly acts in response to DSBs to activate the DDR (see section 1.3). Due to its central role in DDR signaling and its therapeutic potential it has been object of intensive research. Mutation of the ATM gene causes defective cell cycle checkpoint activation, reduced DSB repair capacity and dysfunctional apoptosis¹⁴². Mutated ATM gene in humans causes the rare autosomal recessive disease Ataxia–telangiectasia (AT), which manifests in genomic instability, increased cancer risk and neurodegeneration¹⁴².

As previously described, ATM is recruited by the MRN complex to DSB sites (section 1.2.3.5). The exact mode of how ATM is activated remains unclear, however autophosphorylation and the presence of nucleosome-free DNA as well as the MRN complex play an important role^{142–144}. The current hypothesis assumes that ATM is in an autoinhibited, dimeric state and undergoes monomer transition upon activation^{142,145}. Observations that ATM has a low basal kinase activity could explain the existence of a constitutively active population of ATM kinases also in unperturbed cells^{146,147}. Upon activation, ATM phosphorylates itself and a plethora of substrates (more than 700 putative substrates have been identified in a genomic screen) in order to activate the cellular DDR¹⁴². Among the substrates that ATM phosphorylates are DNA damage sensors (e.g. ATM, Nbs1), mediator proteins (e.g. Mdc1, 53BP1, BRCA1, CtIP), downstream transducers (e.g. Chk1, Chk2, p53) and most notably downstream effectors (e.g. BLM, SMC1, Artemis). A non-conclusive summary of relevant ATM targets and the effect of their phosphorylation is summarized in Table 2.

It is noteworthy that ATM can also be activated outside of the nucleus in mechanisms independent of DSBs. It was shown that ATM is also localized to peroxisomes, mitochondria, and the cytoplasm¹⁴⁸. An emerging function of ATM is that it reacts in response to oxidative stress. A C-terminal cysteine (2991) was shown to form a disulfide bond with the other protomer to promote its activation in response to ROS¹⁴⁹.

1.3.2.1. ATM structure and function

Structural work on ATM was hampered due to its size, complex fold and flexible N-terminus. The first structures of intact, full-length ATM dimers were obtained using cryo-EM. Structures of fungal and human ATM were resolved at low to medium resolution and exclusively showed an autoinhibited dimer in a butterfly shape (Figure 11)^{150–154}. In all these structures, the FATKIN domain forms a tight dimer with hydrophobic interactions. The kinase active site is in a properly folded state and was shown to be able to bind ATP also in the absence of ligands. However, access to the active site was restricted by the PRD domain that acts as a pseudo-substrate.

The FAT consists of multiple parts denoted TRD (tetratricopeptide repeats domain). In the autoinhibited state, the TRD3 domain interacts with the PRD domain from the symmetry-related molecule. Thus, the PRD from each protomer inhibits the active site from the opposing protomer^{150–154}. This supports the assumption that ATM undergoes dimer to monomer transition upon activation¹⁵⁵. In favor of this hypothesis a cryo-EM structure of monomeric ATM albeit with low resolution has been published¹⁵⁶. However, another study found that in an open conformation the FATKIN dimer interface is limited and the PRD is in

an unordered conformation that would allow substrate access¹⁵⁰. The authors suggested an equilibrium dynamic between an open and a closed conformation that could be influenced via interactors to regulate the ATM activation¹⁵⁰.

Table 2: Important substrates of the ATM kinase (adapted from¹⁴²).

Substrate	Phosphate site	Function
DNA damage sensors		
ATM	367, 1893, 1981	PIKK in DDR, autophosphorylation, ATM activation ¹⁴²
Mre11	676, 678	MRN complex, influences function in DNA repair ^{157,158}
Rad50	635	MRN complex, adapter in signaling for cell cycle/DNA repair ¹⁵⁹
Nbs1	278, 343	MRN complex, FHA/BRCT domain, Telomere maintenance ¹⁴²
DNA-PKcs	2609	PIKK in NHEJ, Inactivation and dissociation from DNA ¹⁶⁰
Mediators		
H2AX	139	Histone, signals DNA damage, chromatin relaxation ¹⁴²
53BP1	25	Tumor suppressor, BRCT domain, DSB pathway choice ¹⁶¹
BRCA1	1423, 1524	Tumor suppressor, BRCT domain, DSB pathway choice ¹⁴²
Mdc1	168	BRCT/FHA domain, recruits DSB repair factors to γ H2AX ¹⁴²
CtIP	664, 745	Scaffold, DSB pathway choice, MRN activation ^{142,162}
Transducers		
Chk1	317, 345	Checkpoint kinase, activation ¹⁶³
Chk2	19, 33, 35, 68	Checkpoint kinase, activation ^{164,165}
Effectors		
p53	15	Tumor suppressor, transcription factor, activation ¹⁴²
Mdm2	395	p53 E3-ligase, inactivation, results in p53 activation ¹³⁵
MdmX	342, 367, 403	Mdm2 homolog, cooperates with Mdm2, inactivation ¹⁶⁶
BLM	99	Helicase, complex with DNA2, G2/M checkpoint ¹⁴²
SMC1	957, 966	SMC protein, cohesin and centromere complex, Intra-S ¹⁶⁷
Artemis	503, 516, 645	Endonuclease, DNA-repair, G2/M checkpoint ¹⁴²

The C-terminal part of the solenoid domain has been denoted pincer, and connects the N-terminal solenoid domain with the C-terminal FATKIN region^{150–154}. This connection was shown to be rather flexible contributing to the overall complexity of the dynamics within the ATM molecule. In studies on fungal ATM that resolved the solenoid to a higher resolution, it was reported that in a compact conformation the solenoid can form another interface with the FATKIN. In this compact conformation the solenoids also contribute to the dimer formation via a ionic spiral-spiral interface (Figure 11)¹⁵². The conserved FxY motif in Nbs1 was shown to bind to a conserved hydrophobic, while ATM retains its inactive dimer conformation (Figure 8)¹¹¹.

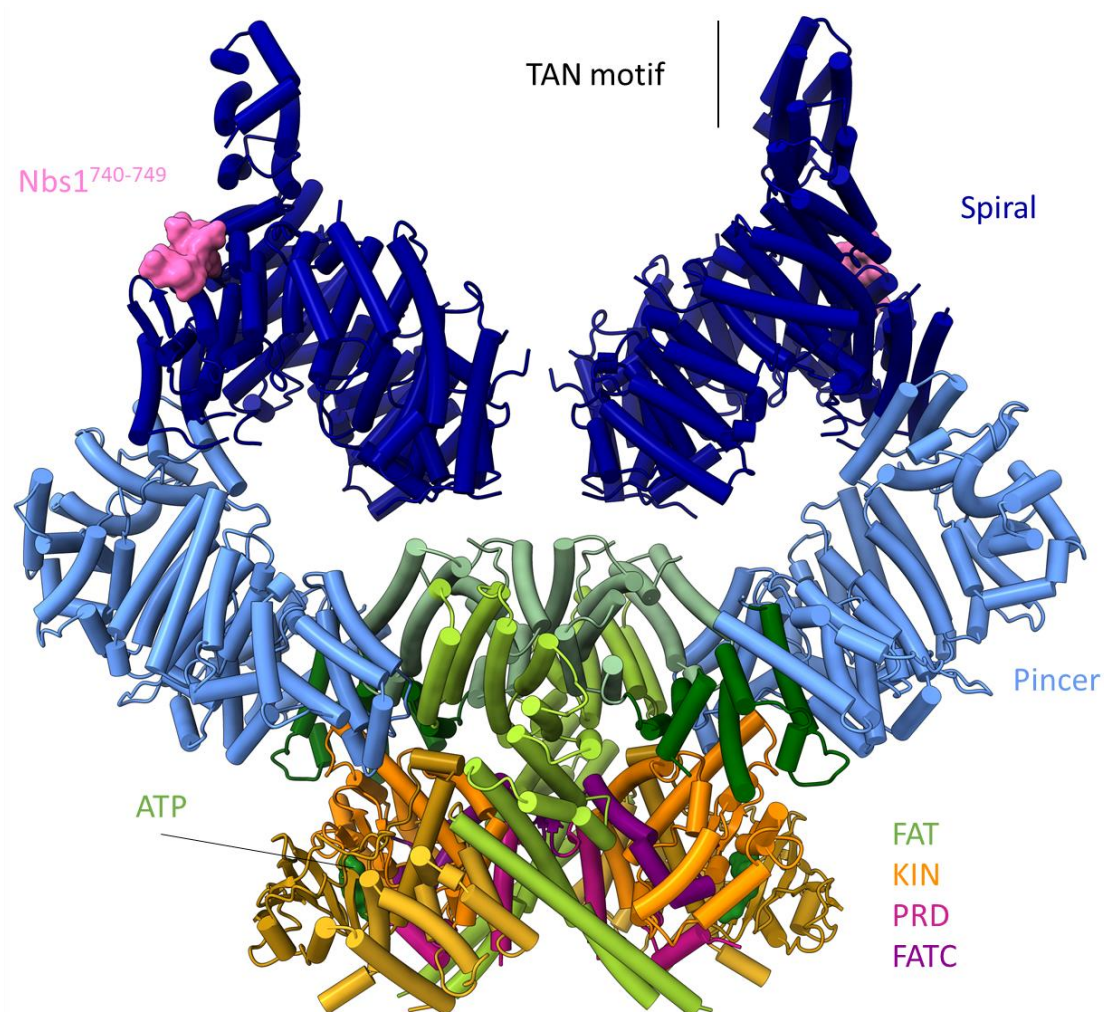


Figure 11: Autoinhibited ATM kinase bound to Nbs1 (PDB: 7SID). Domain coloring similar to Figure 10. Access to KIN (yellow) domain is restricted by PRD (pink). FAT (shades of green) domain consist of TRD domains (1-3). A dimer is formed via two interaction sites: N-FAT (darker green), C-FAT (lighter green). Nbs1 C-terminal fragment 740-749 (FxF/Y motif, pink) binds to the N-terminal spiral domain (dark blue).

1.3.2.2. Targeting ATM in cancer therapy

Cancer cells acquire mutations in DDR genes to ensure survival and to avoid checkpoint activation and subsequent cell-cycle arrest and/or apoptosis¹⁶⁸. This leads to increased mutation rate and genomic instability, both fundamental characteristics of cancer^{169,170}. Altered DDR enables cancer cells to cope with increased amounts of replication and genotoxic stress¹⁴⁸. The increased levels of genotoxic stress in cancer cells can emerge from internal sources (e.g. high replication rate) but also from DNA-damaging cancer chemotherapy and radiotherapy (e.g. Daunorubicin, see also section 1.1)¹³¹. Altered DDR and DNA-repair pathways enable certain cancer cells to develop resistance against DNA-damaging drugs or radiotherapy¹⁴⁸. Thus, targeting DDR proteins showed promising effects in cancer chemotherapy.

ATM is an outstanding target for cancer therapy as its function enables cells to respond to DNA damage and protects from oxidative stress (section 1.3.2). Cancer cells usually have an increased proliferative capacity which renders them susceptible to DNA damaging agents or radiotherapy¹⁴⁸. However, to survive under DNA damaging conditions, cancer cells rely on DSB repair. AT-patients with defective ATM gene are sensitive to ionizing radiation and suffer from genomic instability¹⁴². AT-cells still manage to repair DSBs, however breaks persisted over long time periods¹⁴⁸. Consequently, even transient inhibition of ATM increased the sensitivity of cancer cells to IR and DNA-damaging drugs (e.g. Etoposide, Camptothecin, Doxorubicin)^{171,172}. The rationale for the pharmacological inhibition of ATM is increase the genotoxic stress by maintaining high levels of unrepaired DSBs which leads to tumor cell death^{131,148}.

Another strategy relies on the observation that cancer cells accumulate mutations in DDR pathways. Often certain pathways (e.g. ATM signaling, HR) are shut down and compensated for by alternative, often up-regulated pathways (e.g. ATR signaling, MMEJ). PARP inhibitors are a promising, novel group of anti-cancer drugs that exploit the fact that certain cancer types rely more heavily on PARP-dependent DNA repair functions¹⁷³. ATM deficiency and/or reduced expression levels was identified as a biomarker of sensitivity towards PARP or ATR inhibitors^{174,175}. However, as not all cancers are deficient in ATM signaling and thus PARP-inhibitor sensitive, selective inhibition of ATM could increase the spectrum of PARP and ATR inhibitors. Indeed, ATM inhibitors in combination with PARP inhibitors induced synthetic lethality in proliferating cancer cells as a result of replication stress and persistent DSBs¹⁷⁶. The first generation of high-affinity ATM inhibitors (e.g. KU-55933, CP466722, AZD0156, AZD1390) was identified in compound library screens and optimized to improve their pharmacokinetic properties^{171,172,177,178}.

1.4. Objectives

The MRN complex is a key player in DSB repair that combines enzymatic activities with scaffolding functions to enable efficient HR repair. The MRN complex and its components have been studied since over 25 years and many important biochemical and structural properties were determined. However, there is no conclusive model that integrates the enzymatic and non-enzymatic scaffolding functions. Considering its many unique properties, studying the MRN complex always has been a challenge. Especially noteworthy are the elongated, flexible Rad50 CC domains, the many cofactors (Zn^{2+} , Mn^{2+} , Mg^{2+} , ATP), unstructured regions (Nbs1 middle section, Mre11 C-terminus), the high DNA-binding affinity and high oligomerization tendency. Most of the structural data on the MR(N) complex was obtained by X-ray crystallography. However, in order to crystallize the proteins all flexible regions had to be removed, so the structural data on MR(N) is mostly comprised of separated, more or less artificial pieces. Recently, it was shown that the flexible domains, especially the CCs, provide a functional connection between different domains (e.g. apex domain and catalytic head)^{102,105,159}. Intriguingly, the CCs adopted a previously unseen rod conformation in the DNA-bound cryo-EM structure of prokaryotic full-length MR⁶⁶.

The aim of the first study was to obtain insights into the structure and function of the full-length eukaryotic MRN complex. Due to the aforementioned challenges the MRN complex imposes, structural work relied on high-quality protein material from the thermophilic, eukaryotic model-organism *Chaetomium thermophilum*. However, to verify that functional findings, expression and purification of both *Chaetomium thermophilum* and human MRN complexes had to be established. Biochemical characterization required the implementation of biochemical *in vitro* assays to quantify MRN's ATPase rate, DNA binding activity and nuclease activity. For structural investigations it was necessary to optimize the cryo-EM sample preparation, data generation and processing. To overcome cryo-EM resolution limitations with low-molecular weight domains, the apex domain was additionally crystallized. Various constructs had to be produced and screened in order to generate crystals suitable for X-ray diffraction experiments. To obtain *in vivo* data and crosslinking mass-spectrometry (XL/MS) data, collaborations were established and initial experiments had to be conducted.

Based on the first structure of eukaryotic, full-length MRN obtained in this study, unexpected details on the architecture of the complex were revealed and a model was established that explains how eukaryotic MRN specifically detects DNA ends. Additional structural and *in vivo* data explain how MRN complexes are able to multimerize via their apex-domains to enable DNA end tethering.

The kinase ATM is a central signaling kinase in the DDR that phosphorylates hundreds of protein substrates. The activation of ATM at DSBs relies on the MRN complex, but also other modes of activation (e.g. by ROS) were described. To interact within the aforementioned network of substrates and interactors, ATM possess a huge (almost 2000 amino acids) solenoid domain, mainly consisting of HEAT-repeats. The biological importance of ATM is reflected in the severity of symptoms that (AT-)patients with dysfunctional *ATM* gene suffer from. Functional DDR impedes cancer development by promoting DNA repair as well as forcing severely damaged cells into apoptosis. For this reason, AT-patients have an increased risk to develop cancer and also cancer cells have mutated and altered DDR pathways. Recently, DDR proteins

have been successfully targeted in cancer chemotherapy. Due to its central signaling role, ATM is a promising target in cancer therapy. Specific ATM inhibitors were used as sensitizers to enhance the effect of IR-radiation therapy or DNA-damaging chemotherapy or to induce synthetic lethality in combination with other DDR targeting inhibitors. Structural and functional research on ATM has been hampered due to its large size and complex fold as well as its inherent flexibility. With recent advances in cryo-EM, the first structures of ATM showed its architecture in an autoinhibited, dimeric state^{150–154}. However, especially in the flexible, N-terminal solenoid domain, the resolution is low, which prevents confident model building. Further, there are no high-resolution human ATM structures to enable structure-based drug design.

The aim of the second study was to obtain a high-resolution structure of the human ATM kinase. Therefore, a robust expression and purification method had to be implemented. Due to the complex fold and size of ATM, recombinant expression was only possible in human cells. To verify the quality and biological activity of the purified protein, *in vitro* kinase and thermo shift assays had to be designed. Structural investigation required the optimization of the cryo-EM grid preparation, cryo-EM data collection and processing as well as model building. A priority of structural work on ATM was to generate a high-resolution map of the N-terminal solenoid domain. An ATM specific inhibitor (KU-55933) was used to increase the overall rigidity of the protein. A collaboration with Merck KGaA was initiated to test the novel M4076 inhibitor and to obtain affinity and *in vivo* data. To understand the binding modalities of ATM-specific inhibitors, high-resolution structures of ATP-competitive ATM-inhibitors (KU-55933, M4076) were obtained. As no structure of human ATM bound to ATP was available, an ATM structure with ATPyS was collected, too.

Based on the high-quality map a confident model of the complete ATM kinase, including the N-terminal region, was built. This revealed novel structural features and two zinc-binding sites that enable further understanding of the structural assembly of the N-terminal solenoid. Structures of the ATM kinase domain, bound to ATPyS, KU-55933, M4076 enable comparison and understanding of the structural reason for their selectivity and set a basis for future structure-based drug design.

2. Publications

2.1. Cryo-EM structure of the Mre11-Rad50-Nbs1 complex reveals the molecular mechanism of scaffolding functions

Matthias Rotheneder*, Kristina Stakyte*, Katja Lammens, Joseph D. Bartho, Erik van de Logt, Aaron Alt, Brigitte Kessler, Christophe Jung, Wynand P. Roos, Barbara Steigenberger, Karl-Peter Hopfner, **Cryo-EM structure of the Mre11-Rad50-Nbs1 complex reveals the molecular mechanism of scaffolding functions**, *Manuscript in revision process*

* these authors contributed equally

Summary

In this manuscript we present the first cryo-EM structure of full-length eukaryotic MRN complex in a $M_2R_2N_1$ stoichiometry. The catalytic head of the CtMRN complex adopts a globular conformation in which ATPyS is bound to the Rad50 NBDs. The Nbs1 subunit wraps around the Mre11 nuclease dimer and introduces asymmetry in the complex. From the catalytic head, the long CCs protrude in rod-shaped conformation, possibly stabilized via a novel Mre11 bridge domain. Biochemical analysis of the DNA-binding of CtMRN revealed two DNA binding modes. The eukaryote-specific N-terminus of Mre11 binds internal DNA in an ATP-independent manner, while the conserved DNA binding site at the base of the Rad50 NBDs binds DNA ends dependent of ATP with very high affinity and specificity.

Author contribution

Matthias Rotheneder, Kristina Stakyte, Brigitte Kessler and Aaron Alt established expression of MRN complex from human *Chaetomium thermophilum*. Protein purification for assays and grid preparation was conducted by Matthias Rotheneder, Kristina Brigitte Kessler, Erik van de Logt and Yilan Fan. Matthias Rotheneder, Kristina Stakyte, Erik van de Logt and Yilan Fan performed biochemical assays. Matthias Rotheneder and Kristina Stakyte prepared grids. Cryo-EM data collection and processing were conducted by Matthias Rotheneder, Kristina Stakyte, Katja Lammens, Joseph Bartho, and Karl-Peter Hopfner. I cloned constructs for *in vivo* assays together with Kristina Stakyte, Brigitte Kessler and Erik van de Logt. Wynand P. Roos performed *in vivo* DNA repair and homologous recombination assays. Christophe Jung collected and processed DNA anisotropy data on a custom designed fluorescence microscope. CtRad50 apex domain was crystallized by Matthias Rotheneder, Kristina Stakyte and Brigitte Kessler. X-ray crystallography data was collected and processed by Matthias Rotheneder, Kristina Stakyte, Katja Lammens and Karl-Peter Hopfner. Model building for cryo-EM and X-ray data was conducted by Matthias Rotheneder, Kristina Stakyte, Katja Lammens, Joseph Bartho, and Karl-Peter Hopfner. The manuscript was written and edited by Matthias Rotheneder, Kristina Stakyte, Katja Lammens, Joseph Bartho, and Karl-Peter Hopfner.

Cryo-EM structure of the Mre11-Rad50-Nbs1 complex reveals molecular mechanism of scaffolding functions

Matthias Rotheneder^{1,+}, Kristina Stakyte^{1,+}, Katja Lammens¹, Joseph D. Bartho¹, Erik van de Logt¹, Aaron Alt^{1,2}, Brigitte Kessler¹, Christophe Jung¹, Wynand P. Roos⁴, Barbara Steigenberger³, Karl-Peter Hopfner^{1,*}

¹ Gene Center, Ludwig-Maximilians-Universität, Munich, Germany, Department of Biochemistry,

² Present address: CureVac AG, Tübingen, Germany

³ Mass Spectrometry Core Facility, Max-Planck-Institute of Biochemistry, Martinsried, Germany

⁴ Institute for Toxicology, Johannes-Gutenberg-Universität, Mainz, Germany

+ These authors contributed equally

* Correspondence:

Prof. Dr. Karl-Peter Hopfner

Gene Center

Feodor-Lynen-Str. 25

81377 Munich, Germany

Tel: +49(0)89 2180 76953

Email: hopfner@genzentrum.lmu.de

Summary

The MRN (Mre11-Rad50-Nbs1) complex is a central DNA double-strand break repair factor that detects and nucleolytically processes DNA ends, activates the ATM kinase, and tethers DNA at break sites. The integrative mechanism how MRN can act both as nuclease and scaffold protein is not well understood. Here we provide a cryo-EM structure of MRN from *Chaetomium thermophilum* which takes shape as a 2:2:1 complex with a single Nbs1 wrapping around the autoinhibited Mre11 nuclease dimer. MRN has two DNA binding modes, one ATP independent for binding intact DNA through Mre11's C-terminus, along with an ATP dependent mode for loading onto DNA ends, suggesting how it may interact with DSBs and intact DNA. MRNs two 60 nm long segmented coiled-coil domains protrude from the catalytic head as linear rod, the apex of which is assembled by two joined zinc-hook motifs. Apices from two MRN complexes can further dimerize through a new interface, forming 120 nm spanning MRN-MRN structures. Our results provide a near-atomic resolution architecture of MRN and suggest how it mechanistically integrates catalytic and tethering functions.

Introduction

DNA double strand breaks (DSBs) are a threat for genomic integrity throughout life. Un- or misrepaired DSBs can lead to cell death, gross chromosomal aberrations, aneuploidy, and tumorigenesis (Carbone et al., 2020). DSBs can be caused by ionizing radiation and genotoxic chemicals, and frequently arise during DNA replication (Tubbs and Nussenzweig, 2017). In addition, "programmed" DSBs are physiological intermediates in immunoglobulin gene rearrangements and meiotic chromosome recombination (Johnson et al., 2021; Zhang et al., 2022). To maintain genomic stability, cells have evolved potent DSB sensing, signaling and repair pathways, which are generally grouped into two major branches. In end joining reactions, such as non-homologous end joining (NHEJ) or microhomology mediated end joining (MMEJ), broken DNA ends are ligated without or with various amounts of limited processing, a procedure that can be potentially mutagenic (Chaplin et al., 2021; Zhao et al., 2020). In homologous recombination (HR), DNA ends are resected into long 3' single strand overhangs, which pair with the homologous template for template dependent DNA synthesis (Chen et al., 2018; Haber, 2018; Wright et al., 2018). In eukaryotic cells, the usage of the different pathways is tightly regulated in the cell cycle (Scully et al., 2019).

DSBs can be structurally very diverse and feature chemical alterations, hairpins or covalently attached proteins. Latter arise during abortive type II topoisomerase reactions and are the physiological source of DSBs in meiosis (Johnson et al., 2021; Morimoto et al., 2019). Detection and repair of chemically diverse and obstructed DNA ends, in particular protein-blocked DNA ends, requires the Mre11-Rad50-Nbs1 (MRN, Mre11-Rad50-Xrs2 in yeast) complex (Cejka, 2015; Paull, 2018; Syed and Tainer, 2018). Current models suggest that MRN cuts the 5' strand in the vicinity of the DNA end, followed by exonucleolytic back-resection in 3' to 5' direction (Deshpande et al., 2016; Garcia et al., 2011). The resulting ssDNA can act in strand annealing in end-joining reactions or can be further extended by 5' to 3' long-range resection in HR. MRN or bacterial MR homologs can also cleave the second strand, thereby inducing a DSB near the blocked end, which will clip off the blocked DNA termini (Connelly et al., 2003; Deshpande et al., 2016; Myler et al., 2017). The evolutionary conserved core complex is formed by two copies of each Mre11 and Rad50, with a globular ATP dependent DNA binding and nuclease module (catalytic head) and up to 60 nm long flexible coiled-coil (CC) domains (de Jager et al., 2001; Hopfner et al., 2001; Lammens et al., 2011; Lim et al., 2011). The Rad50 CC domains are joined apically via a zinc-hook dimerization motif to form a proteinaceous ring (Hohl et al., 2015; Hopfner et al., 2002; Park et al., 2017). Recent structural data on *E. coli* Mre11-Rad50 (EcMR, also denoted SbcCD) suggest that the CC domains act as gate and chemo-mechanical sensor via ring to rod transitions to promote ATP dependent loading and cleavage of linear but not circular DNA (Kashammer et al., 2019).

In eukaryotes, Mre11 and Rad50 bind a third protein, Nijmegen breakage syndrome 1 (Nbs1, denoted Xrs2 in yeast) (Carney et al., 1998), which regulates MRs nuclease activity and acts as a scaffold for interactions with chromatin and DNA repair and signaling factors. Genetic inactivation of Mre11, Rad50 or Nbs1 is lethal in mammals, while hypomorphic mutations lead to several genome instability syndromes, like Nijmegen breakage syndrome and Ataxia-telangiectasia-like disorder, characterized by cancer predisposition, neurodegeneration and/or immunological defects (Bian et al., 2019; Buis et al., 2008; Luo et al., 1999; Zhu et al., 2001). The eukaryotic MRN complex has both enzymatic and structural functions in DSB

repair. It is involved in HR and end joining pathways, meiotic and replication associated recombination, chromatin architecture as well as telomere maintenance (Marie and Symington, 2022; Paull, 2018; Syed and Tainer, 2018). The various activities of MRN/X are tightly orchestrated and regulated by the cell cycle state and additional factors, such as ATM/Tel1, CtIP/Sae2 and Rif2 (Cejka and Symington, 2021). CtIP/Sae2 functions as DNA scaffold protein (Andres et al., 2019) and MRN/X coactivator (Cannavo and Cejka, 2014, Wang, 2017; Deshpande et al., 2016; Reginato et al., 2017) and is critical for DSB processing (Mimitou and Symington, 2008; Sartori et al., 2007). At *S. cerevisiae* telomeres, on the contrary, Sae2's coactivator function is counteracted by telomeric factor Rif2, which prevents endonucleolytic cleavage by MRX (Khayat et al., 2021; Martina et al., 2012; McGee et al., 2010; Roisne-Hamelin et al., 2021).

MRN/X also recruits and activates the Ataxia telangiectasia mutated (ATM, Tel1 in yeast) at DSBs (Cassani et al., 2019; Lee and Paull, 2005; You et al., 2005). ATM/Tel1 phosphorylates a large number of target proteins, thereby orchestrating the DNA damage response, a complex set of events that involves chromatin reorganization, DNA repair, cell cycle arrest, transcriptional responses and apoptosis (Lee and Paull, 2021). An important but particularly poorly understood function of MRN/X is tethering of DNA (Cassani et al., 2018; Mojumdar et al., 2019; Seeber et al., 2016), and more generally chromatin organization (Delamarre et al., 2020; Forey et al., 2021; Salifou et al., 2021). MRN/X forms large clusters in vitro and repair foci in vivo, and both catalytic head complexes as well as CC domains are observed in low resolution EM or atomic force microscopy (AFM) to engage in cluster formation (Frame et al., 2006; Hopfner et al., 2002; Vera et al., 2022; Zabolotnaya et al., 2020). Such clusters might be involved in generating multiple cleavage events at DSBs as well (Cannavo et al., 2019). The mechanism how MRN integrates enzymatic and structural tethering functions, and the molecular basis for the roles of the CCs in clustering has not been established and remains unclear. A particular conundrum is how the CC domain and zinc-hook can be involved in both intra-complex and inter-complex interactions, to act as gate in DSB sensing on one hand, or bridge MRN complexes in tethering functions on the other hand.

Here we report the cryo-electron microscopy (cryo-EM) structure of *Chaetomium thermophilum* (Ct)MRN complex bound to ATP γ S. Our structure not only clarifies the atomic architecture of eukaryotic MRN but reveals several unexpected features that rationalize enzymatic and tethering functions in a single framework. A 3.8 Å reconstruction of MRN's catalytic head shows that 75 amino acids of Nbs1 wrap as an extended chain around both Mre11 subunits. This portion of Nbs1 agrees well with that of the minimal core of murine Nbs1 necessary to maintain embryonic viability (Bian et al., 2019). Our data thus clarify CtMRN as a M2R2N1 complex and suggest that a key function of Nbs1 is to stabilize the Mre11 dimer. The Rad50 CC domains are in a rod configuration, stabilized by several points of interactions along their entire lengths. Unexpectedly, we not only observe zinc-hook mediated dimerization of the two CC domains in a rod-configuration, but the apices of two MRN CC domains further dimerize to form joined MRN-MRN assemblies. Supported by cell based and biochemical studies, the structure provides a molecular basis for the transient tethering of DNA ends and/or chromatids by MRN.

Results

Cryo-EM structure of the Mre11-Rad50-Nbs1 complex

Recombinant expression of the MRN proteins from *Chaetomium thermophilum* (Ct) in insect cells resulted in a homogeneous MRN complex with a 2:2:1 stoichiometry (Figure S1A). We vitrified the protein in the presence of ATP γ S, which we found to stabilize the complex for cryo-EM. Since CtMRN's ATPase is 10-fold stimulated by DNA (see below), similar to human (Hs)MRN and *Escherichia coli* (Ec)MR (Deshpande et al., 2017; Saathoff et al., 2018), the resulting ATP γ S bound structure resembles an autoinhibited “resting” state of the complex between occasional ATP hydrolysis events.

In the micrographs, we observed homogenous particles along with large, clustered oligomers, entangled Rad50 coiled-coils (CCs) and partially dissociated complexes (Figure S1B). For structure determination, we focused on isolated particles that typically showed a globular head module (i.e., Rad50^{NBDs} bound to the Mre11 dimer and Nbs1) along with straight or curved protruding CCs. The highly elongated, flexible nature of the particles prevented us to obtain a cryo-EM map of the entire complex, however we could reconstruct a structure covering the head and approx. 50% of the proximal CCs, and another structure covering 25% of the distal CCs around the zinc-hook.

We first focused on the head module and adjacent CCs. Several rounds of automated particle picking, 2D classification, training of the TOPAZ neural network-based particle picker, followed by extensive 3D classification, refinement and polishing led to a 4.0 Å C1-reconstruction of the catalytic head module (Figure 1A, Figure S1C, D, Figure S2, Table 1). By further selecting for straight CCs and re-extracting the particles with bigger box sizes, we obtained a C2-symmetrical density with 4.8 Å overall resolution in which around 30 nm of the Rad50 CCs were resolved (Figure 1A, Figure S2, S3A-E). Different regions of the C1 map were improved by further classification through variability analysis, masking, and focused refinement, which brought out features like the path of Nbs1 around the Mre11 dimer and parts of the Mre11 extended C-terminus. We generated a composite map by combining the higher resolution maps of different regions, using the C2-map with long CCs as a reference and scaffold (Figure S1D). The EM density maps enabled us to build an atomic model for the catalytic head domain and 30 nm of the Rad50 CCs, using various crystal structures and AlphaFold2 models for subunits as starting models (Figure 1A, Figure S3F).

The catalytic head model consists of two Mre11, the two Rad50^{NBD} subunits and an extended portion of Nbs1 that wraps around both Mre11 protomers (Figure 1A). The Mre11 nuclease domain, composed of the phosphodiesterase and capping domains (CD), forms the characteristic dimer structure with a prominent DNA binding cleft. The Mre11 nuclease active sites are blocked by both Rad50^{NBDs}, which are situated in the DNA binding cleft to prevent unspecific DNA degradation. Following the nuclease domain, the helix-bundle Rad50-binding domain (RBD) attaches Mre11 to the Rad50 CCs. Overall, the architecture of the M₂R₂ head module is related to that of EcMR bound to ATP γ S, showing the autoinhibited “resting” state (Kashammer et al., 2019).

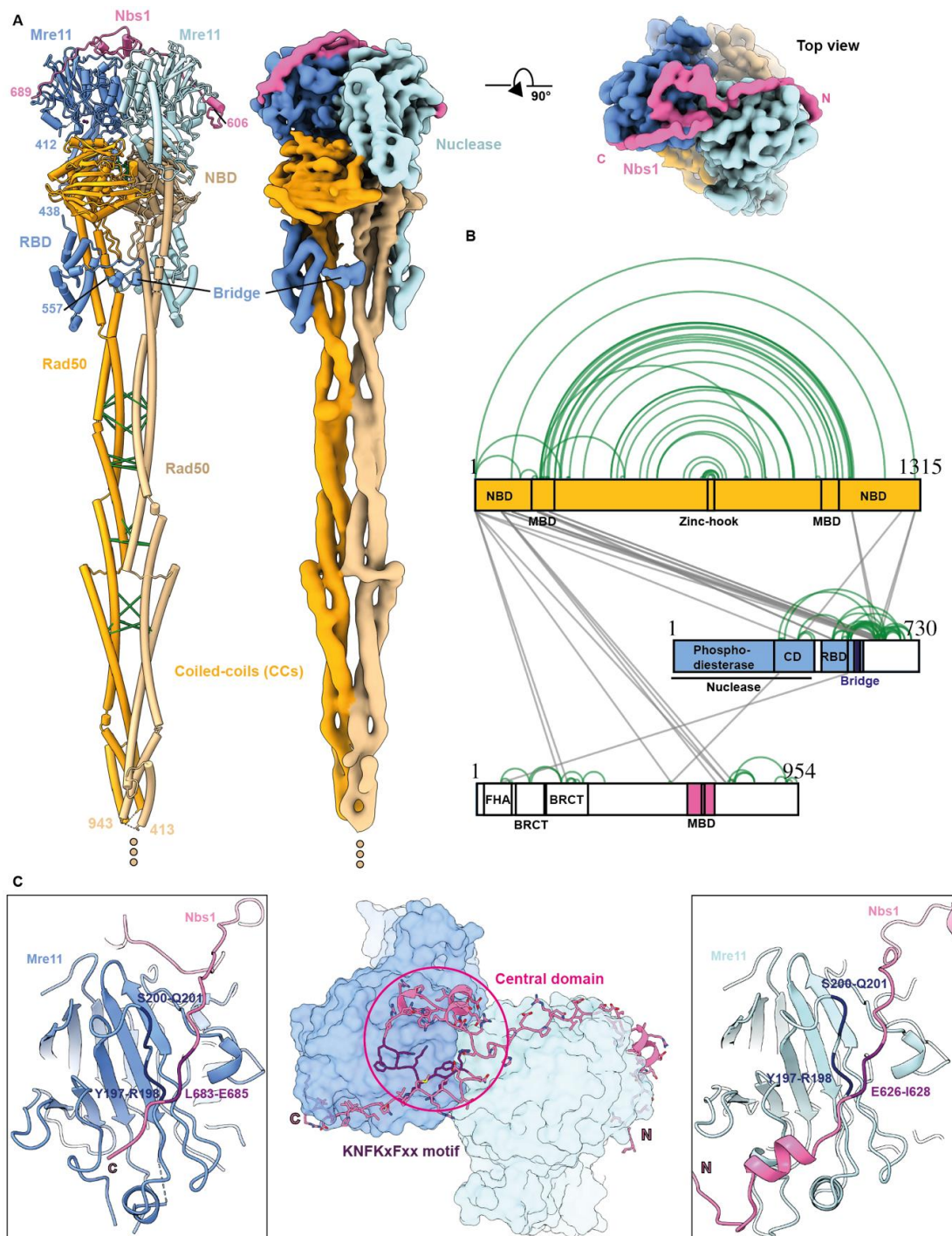


Figure 1: Structure of the MRN complex in resting state. (A): Cryo-EM structure and composite map of the MRN complex with CCs in closed conformation. The map was created by combining the higher resolution maps of different regions. The atomic model of the catalytic head domain and 30 nm of the Rad50 CCs region is shown, whereas Mre11 is colored blue, Rad50 orange and NBS1 pink, respectively. Crosslink restraints obtained by CX-MS are labeled green in the Coiled-coil domain. **(B): Graphical overview of the Lysine-specific chemical cross-linking mass spectrometry results (CX-MS).** The crosslinks are highly consistent with the model and validate the fitting of the AlphaFold2 predicted CC part. Colored portions indicate structurally characterized parts of each protein. **(C): A single Nbs1 polypeptide (colored pink) binds asymmetrically across both Mre11 phosphodiesterase domains (colored blue).** The interfaces of the N- and C-terminal region, which bind with reverse polarity to equivalent regions on Mre11, as well as the central core region harboring the conserved KNFKxFxx motif are shown.

The CC-domains have a highly segmented nature with interspersed loops (CC segment joints). CtMRN-ATPyS CCs are parallel and tightly engaged (rod configuration), in contrast to the EcMR-ATPyS resting state complex, where the CCs protrude at an angle of approx. 60° from the head (ring configuration) (Figure S4A). Both CCs interact with each other predominantly via contacts at the segment joints. Additionally, the CCs are held together by a bridge element formed by Mre11 that spans the CCs in the vicinity of the Rad50NBDs and is absent in the prokaryotic MR complex (Figure 1A, Figure S4A). Imaging CtMRN in the presence of ATP, we observed a small fraction of particles that showed open CCs, similar to the structure observed in the EcMR-ATPyS resting state complex (Figure S4B) (Kashammer et al., 2019). This indicates that ATP, like in the bacterial complex, can induce CC opening.

To generally validate the structural model and obtain additional architectural information, we performed lysine-specific chemical cross-linking followed by LC-MS/MS (XL-MS), which provides in-solution distance restraints of <30 Å between C α atoms (Figure 1B, Figure S4C). In general, the obtained crosslinks are highly consistent with the model and especially validate the low-resolution parts of the map in the CCs and the fitting of the AlphaFold2 predicted CC segments (Figure 1A). The crosslinks also agree well with a highly extended conformation of the CCs as observed in the micrographs. Out of 40 crosslinks mapped to our model, 35 fulfill the distance restraints. The remaining crosslinks are all located within the catalytic head and could be explained by its flexibility (Video S1). This does not argue for elbow elements and folding of the CCs as observed for the structurally related class of SMC proteins (Burmann et al., 2019).

A single Nbs1 wraps around the Mre11 dimer

A single Nbs1 polypeptide binds asymmetrically to both Mre11 phosphodiesterase domains with an S shaped double turn across the Mre11 dimerization interface (Figure 1C). In total the Mre11 interacting region of CtNbs1 comprises 75 residues. Binding is centered on the highly conserved KNFKxFxx motif (K659-F664), which binds right across the two-fold symmetry axis of the M₂R₂ head module with the pseudo-symmetric KxFxR region (Figure 1C, Figure S5A). This interaction was previously observed in a crystal structure of *S. pombe* (Sp)Mre11 catalytic domain bound to a small fragment of SpNbs1, showing a high structural conservation of this central interaction mode (Figure S5B) (Schiller et al., 2012). However, the cryo-EM map, in conjunction with AlphaFold2 multimer analysis, enables us to trace the entire interaction region of Nbs1 around the Mre11 dimer (Figure 1A top view, Figure S3E).

A series of coordinated turns, N-terminal of the KNFKxFxx motif form a small, compact central domain that further bridges the Mre11:Mre11 interface (Figure 1C). The central domain is reasonably well ordered with many contacts to Mre11, and has a predicted local resolution range from 3.8 Å to 4.3 Å. The size of the central domain structure appears to be a species-specific feature of Nbs1 homologs, as alignment with other species shows a significantly shorter sequence neighboring the KNFKxFxx motif (Figure S5A). The N- and C-terminal chains of CtNbs1 turn and extend back past this central domain in both directions to wrap across the entire Mre11 phosphodiesterase dimer (Figure 1C, insets). Both extensions bind with reverse polarity to equivalent regions of the two Mre11 phosphodiesterase domains. This extended part of a single Nbs1 polypeptide interacts with and breaks the symmetry of the Mre11 dimer. Beyond this core Mre11 interaction region, the Nbs1 C-terminal chain branches away into the solvent, while the N-terminal chain

forms a short helix, overall resulting not only in an asymmetric Mre11-Nbs1 complex, but also asymmetries in the interactions between Mre11 and Rad50 (Figure S5C). The asymmetric elements of Mre11 and Rad50 directly correlate with the orientation of Nbs1, suggesting the symmetry breaking orientation of Nbs1 influences the behavior of the entire MRN complex. This may be driven by the Mre11 loop H213-L225, which alternately interacts with N-terminal strand of Nbs1 in a conformation matching the crystal structure (Figure S5C, left), or swings 15 Å to interact with Rad50 (Figure S5C, right). One Rad50 appears stabilized by this interaction, while the other shows a more flexible conformation, deviating up to 8 Å from the symmetry related position (Video S1).

The strong interactions of the central domain are present in most observed particles, while the weaker interactions of the N- and C-terminal chains with Mre11 allows their release into the solvent. 3D classification of the Mre11-Nbs1 interaction showed that particles could be divided into 5 classes: central domain with N-terminal chain bound (27%), central domain with C-terminal chain bound (27%), central domain with both chains bound (25%), central domain with neither chain bound (13%), and no Nbs1 bound (8%) (Figure S5D). This indicates that the interaction of Nbs1 with MRN could be locally quite dynamic, perhaps to allow for conformational changes or respond to interaction partners. Finally, we note that the 75-residue long Mre11 interaction region of Nbs1 more or less precisely corresponds to the minimal fragment of Nbs1 required to maintain embryonic viability. This highlights the importance of the asymmetric wrapping of the Mre11 dimer by Nbs1 as revealed by work for MRN core functionality in mammals (Kim et al., 2017).

Rad50 is in a pre-engaged ATP state

Closer inspection of the head module reveals one Mg^{2+} -ATP γ S moiety bound to each of the two Walker A motif regions of the Rad50 dimer (Figure 2A, B). Mg^{2+} is properly coordinated by Walker B and Q-loop residues. However, the signature motifs, a conserved motif characteristic for the ABC-type ATPase family, are approx. 10 Å away from the γ -(thio)phosphate of ATP γ S. In the fully engaged state of ABC-type ATPases, the signature motif binds the γ -(thio)phosphate of the “trans” ATP, inducing a “powerstroke” in the ABC-type ATPase dimer when transiting from apo to ATP-bound states (Figure 2C). We took advantage of two crystal structures of the isolated CtRad50^{NBD}, bound to ATP γ S and either DNA or the Mre11^{RBD}, respectively, to compare with the cryo-EM structure of CtMRN and reveal structural differences (Seifert et al., 2016). Both structures show the same conformation with the signature motifs fully engaged with the trans γ -(thio) phosphates (Figure 2C). Comparison with the cryo-EM structure reveals a approx. 30° rotation of each of the two NBDs, driven via signature motif γ -(thio)phosphate interactions. Accompanying are corresponding movements of the CC domains (truncated in the crystal structures) (Video S1). Thus, in the full-length CtMRN cryo-EM structure, the adhesion of the CC domains and possibly the Mre11 bridge, likely prevents full engagement of the Rad50^{NBDs}, by obstructing the necessary rotation of the NBDs, which remain in a partially engaged state. Even in the presence of ATP, only a subset of particles showed an open CC conformation, altogether pointing to a tighter autoinhibition of MRN as compared to MR in the absence of DNA (Figure S4B).

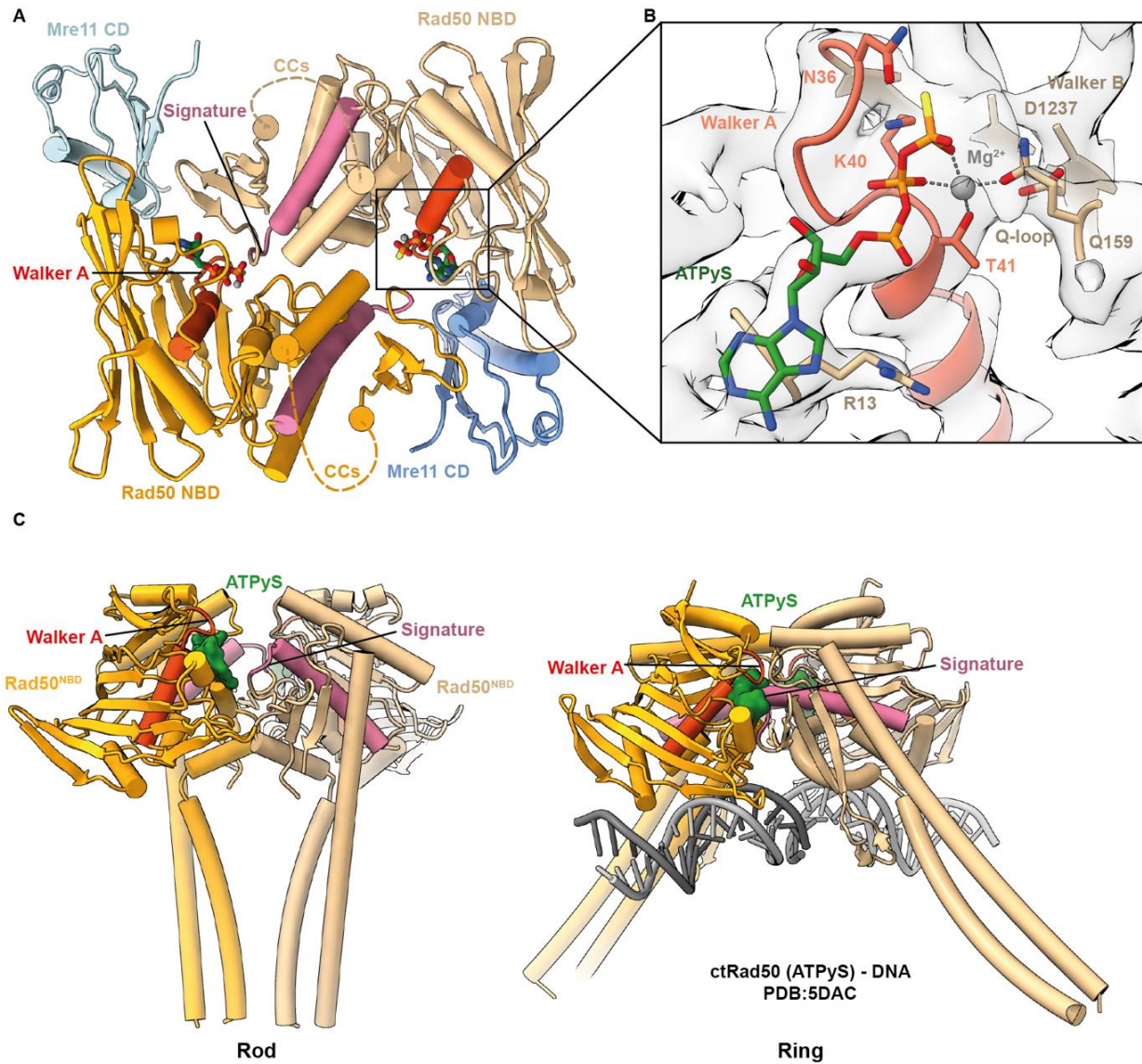


Figure 2: Rad50 in a pre-engaged ATP state. (A): Bottom view of Rad50 NBDs with ATP γ S bound. Enzymatically important elements are highlighted. **(B):** Close-up view of the coordinated Mg²⁺ and ATP γ S in the NBD of Rad50. The Mg²⁺ ion is depicted in gray and enzymatically important residues are annotated and illustrated as sticks. The atomic model is overlaid by the cryo-EM map. **(C):** Comparison of the cryo-EM structure with the ATP γ S bound Rad50 crystal structure (PDB code: 5DAC) illustrates the differences in Rad50NBD dimerization and the pre-engaged state of Rad50 in the MRN complex. In the cryo-EM structure the signature motifs are ~10Å away from the γ -(thio)phosphate of ATP γ S. In the fully engaged crystal structure the signature motif interacts with the γ -(thio)phosphate of the "trans" ATP inducing a "powerstroke" to the Rad50 and the CC domain.

ATP dependent and independent DNA binding by MRN

The rod structure of the CCs raises the question whether the canonical DNA binding site on the Rad50NBDs remains accessible to DNA (Figure 2C, crystal structure) and what role ATP plays in DNA binding. To assay ATP dependent and independent DNA binding, we used a fluorescence polarization anisotropy (FA)-based assay (Materials and Methods). Wild-type CtMRN complex binds to 80-mer dsDNA oligonucleotide with K_d of 53 ± 5 nM and 30 ± 2 nM in the presence of ATP and ATP γ S, respectively (Figure 3A). We attribute the higher K_d for ATP to hydrolysis dependent turnover since DNA robustly stimulates ATP hydrolysis (see below). Surprisingly, MRN also binds DNA in absence of ATP with a somewhat higher K_d of 73 ± 7 nM (Figure 3A). Robust DNA binding in the absence of ATP was also seen for human MRN and appears to be a preserved feature of eukaryotic MRN/X, which is in contrast to the strictly ATP dependent DNA binding of prokaryotic MR (Hopfner et al., 2000; Lammens et al., 2011; Paull and Gellert, 1999; Rojowska et al., 2014).

Interestingly, the binding curves converge to higher FA plateau values than in presence of ATP and ATP γ S (97 mP and 92 mP, respectively) compared to the curve with no nucleotide (56 mP) (Figure 3A). This approx. 2-fold FA increase in presence of ATP and ATP γ S is a strong hint for the binding of a second DNA molecule to the MRN complex. Apart from the canonical binding site at the Rad50^{NBDs}, we hypothesized that the eukaryote-specific Mre11 C-terminal extension could bind an additional DNA molecule (Usui et al., 1998). We generated a mutant MRN complex (M ^{Δ CRN}), where this Mre11 extension (568-730) was removed (Figure 3B, top). The truncation still retains the bridge, as removal of the bridge resulted in an instable complex that was not characterized further. Our truncation site coincides with a recently described SPARTN protease cleavage site in human Mre11 in certain cancers cells that reduced the affinity of HsMre11 to DNA (Na et al., 2021). CtM ^{Δ CRN}'s ability to bind DNA in the absence of ATP/ATP γ S was nearly abolished, confirming both binding caused by the Mre11 C-terminal tail and ATP dependence for binding to Rad50^{NBD}. (Figure 3B) As expected, DNA binding to Rad50^{NBDs} in the presence of ATP/ATP γ S remained nearly unaltered (K_d values 51 ± 5 nM, 28 ± 2 nM, respectively). Moreover, the levels of the FA plateaus (50 mP and 27 mP) are consistent with FA increase caused by one DNA oligomer, as seen above for the wt CtMRN. In addition, sigmoidal DNA binding curves for CtMRN and CtM ^{Δ CRN} with and without ATP with Hill coefficients >1 (ranging from 1.3 to 3.0, see Material and Methods) indicate cooperative binding modes possibly arising from protein oligomerization, similar to what was observed for *S. cerevisiae* MRX (Vera et al., 2022). In support for this interpretation, we noticed that DNA-bound CtM ^{Δ CRN} complexes were significantly less prone to oligomer formation than CtMRN, observed by visualization of fluorescently labeled DNA (Figure S6A, B).

Next, to investigate the preference of CtMRN and CtM ^{Δ CRN} for DNA ends, we performed competition assays by adding increasing amounts of unlabeled circular or linearized plasmid DNA to the solution containing a fixed amount of protein and labelled 80-mer dsDNA. For CtMRN, the linearized DNA competed approx. 3-fold better than the circular DNA, showing an only moderate preference for DNA ends (Figure 3C). This could be due to the presence of the Mre11's C-terminal tail containing the second binding site exhibiting no preference for DNA ends. However, for CtM ^{Δ CRN}, linear DNA competed ~ 35 -fold better than circular DNA (Figure 3D), demonstrating the strong dependence for DNA ends of the Rad50^{NBDs}.

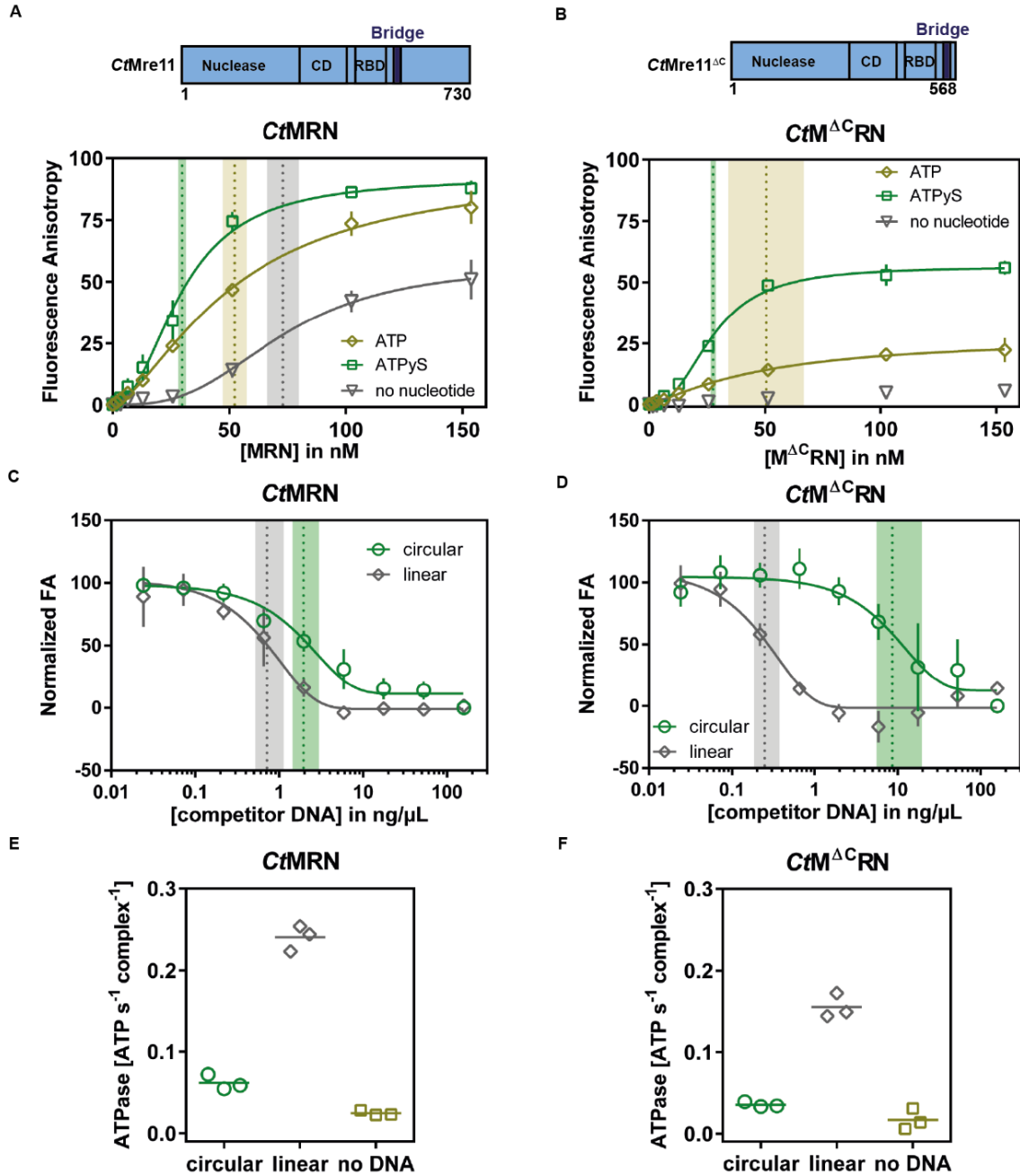


Figure 3: ATP dependent and independent DNA binding by MRN. (A): DNA binding assay with CtMRN. Top, depiction of full length CtMre11 construct used in the DNA binding and ATPase assays. Fluorescence anisotropy-based assay documenting the effect of ATP and ATPyS on CtMRN binding towards 80-mer dsDNA. The wild type complex binds cooperatively to dsDNA also in the absence of ATP. **(B): DNA binding assay with CtM^{ΔC} RN.** Top, Depiction of CtMre11^{ΔC} construct used in the DNA binding and ATPase assays. Similar Fluorescence anisotropy assay as in (A) using the C-terminal truncated CtM^{ΔC} RN complex. CtM^{ΔC} RN binding to DNA was nearly abolished in the absence of ATP/ATPyS, while it retained DNA binding in the presence of ATP or ATPyS. **(C): CtMRN DNA binding specificity.** DNA binding competition assay utilizing the FA-based experiment as in (A and B) and adding increasing amounts of unlabeled circular or linearized plasmid DNA to the experiment. The results reveal that CtMRN binds linear and circular DNA with a similar affinity. **(D): CtM^{ΔC} RN DNA binding specificity.** DNA binding competition assay as in (C) showing that CtM^{ΔC} RN complex has a strong preference for linear DNA. **(E): ATPase assays of CtMRN** showing the stimulation of the ATP hydrolysis rate by addition of linearized DNA. **(F): ATPase assays of CtM^{ΔC} RN** showing the stimulation of the ATP hydrolysis rate by addition of linearized DNA, as for CtMRN.

Finally, to test the effect of DNA stimulated ATP hydrolysis on DNA binding properties, we performed ATPase assays. Similar to studies on human MRN, we find that linear DNA stimulated CtMRN's ATPase approx. 10-fold, while circular DNA stimulated MRN only 2-fold (Figure 3E) (Deshpande et al., 2017). ATPase rates of CtM^ΔCtRN were generally reduced to 2/3 of wt MRN's ATPase levels but showed a similar 10-fold (linear) and 2-fold (circular) stimulation by DNA (Figure 3F). The lower ATPase rate might be caused by a less stable protein. However, the strong increase of M^ΔCtRN's preference for ATP dependent binding of linear vs circular DNA are unlikely caused by the moderate reduction in ATPase activity, especially because the same increase in preference for linear over circular DNA is observed in the presence of ATPγS.

We conclude that MRN possesses two DNA binding components. The first binds DNA in an ATP dependent manner via the evolutionary conserved head module. Much like bacterial MR, a strong preference for specific binding at DNA ends is exhibited through this mode. The second DNA binding mode is ATP independent and lies within the CtMre11 C-terminal tail. These additional interactions further increase binding of internal DNA elements.

MRN-MRN tethering via zinc-hook tetramerization

During cryo-EM data processing we noted 2D classes that resembled Rad50 zinc-hook dimers in the “closed” rod configuration (Figure S1C). We denote the tips of the dimerized CCs of a single MRN complex as CC apex. 2D class averages did not show single apices but depicted apex dimers: two Rad50 zinc-hooks, joined via Zn²⁺ coordination to form the canonical apex in rod configuration, further dimerize in an anti-parallel fashion. As a result, these apex-apex interactions tether two MRN complexes. Selecting and training for those particles enabled us to reconstruct a cryo-EM density at an overall resolution of 4.9 Å, which resolved another 14 nm of the total CCs (Figure 4A, Figure S7, Table 1). To obtain a higher resolution and independently verify this apex-apex interaction, we crystallized a fragment of the CC region around the zinc-hook (CtRad50⁵⁸⁹⁻⁷⁸²). We obtained crystals in space group P1 and determined a structure to 2.5 Å resolution by molecular replacement, using a corresponding CtRad50 AlphaFold2 model (Figure 4B) (Jumper et al., 2021). Data collection and model statistics are listed in Table 2. The asymmetric unit of the crystal consists of a dimer of zinc-hook dimers, i.e., two tethered apices, in the same arrangement as observed by cryo-EM (Figure 4B).

Zooming in, we find that the primary interface between the CCs of a single M₂R₂N₁ complex through joint coordination of a Zn²⁺ ion is very similar to that observed in crystal structures of archaeal and human Rad50 zinc-hook regions (Hopfner et al., 2002; Park et al., 2017; Soh et al., 2021). Conserved C691 and C694 from each of the two protomers jointly bind Zn²⁺ in a tetrahedral fashion (Figure 4C). In both cryo-EM and crystal structure, the two CCs are arranged in the same rod configuration, stabilized by small confined, hydrophobic contact points along the two CC protomers.

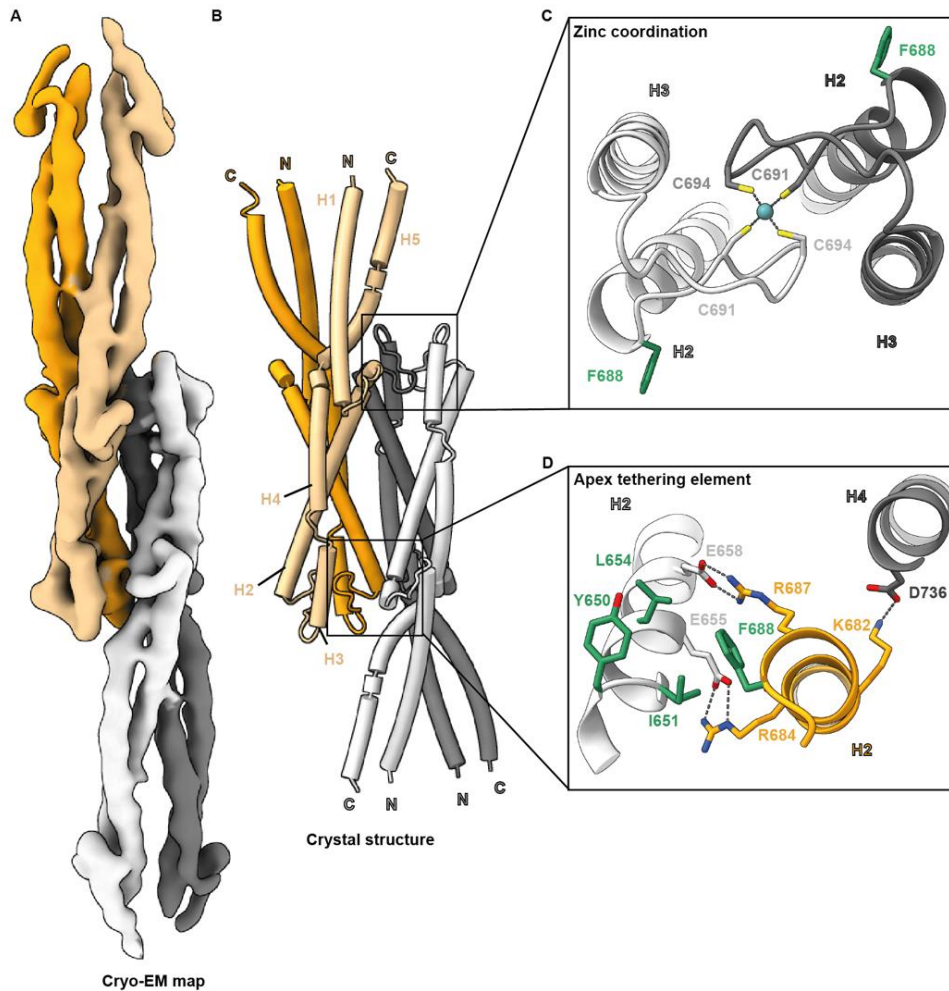


Figure 4: Structure of the CtRad50 zinc-hook tetramer. (A): Cryo-EM map of zinc-hook tetramer at 4.9 Å resolution, whereas each Rad50 monomer belonging to one MRN complex is depicted in related color. (B): Atomic model of the zinc-hook tetramer crystal structure shown in comparison to the cryoEM map. (C): Close-up view of the Zn²⁺ binding site. (D): Rad50 apex tethering element with the residues involved in the interaction shown in stick representation.

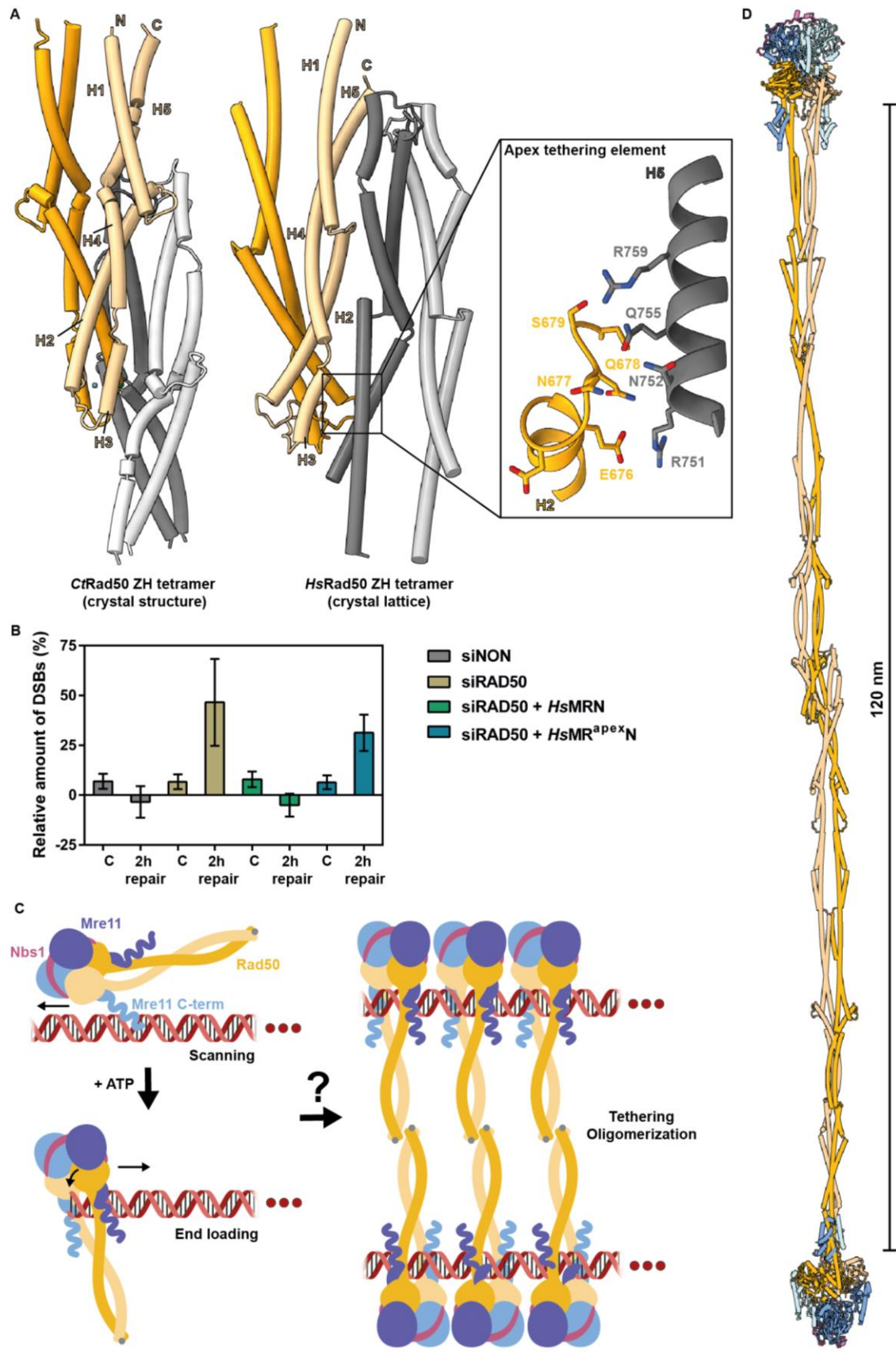
The rod state, as opposed to the originally observed open state, enables an antiparallel interaction of two apices through formation of a secondary interface (Figure 4D) (Hopfner et al., 2002). Hereby, F688 of one Rad50 dimer binds into a hydrophobic pocket (I651 and L654) at the last CC segment joint of the other Rad50 dimer. Flanking this hydrophobic interaction are salt bridges between R684 and E655, R687 and E658, and K686 and D736. Altogether, these contacts are formed twice in the secondary interface. Furthermore, due to the dimeric nature of the CC rods, the tethering interactions can form on both sides of a given apex, thus leading to formation of two-dimensional sheets of antiparallel tethered apices in the crystal lattice (Figure S8A). Interestingly, we observe apex multimers in cryo-EM, supporting the idea of higher-order apex interactions (Figure S8B). Due to the low number of particles, we could not obtain higher resolved 3D maps at this stage. Nevertheless, crystal packing and the cryo-EM classes raise the possibility that CC apex tethering might go beyond MRN-MRN dimer interactions towards higher order oligomerization.

Since the CtRad50 zinc-hook shows structural conservation to the previously published crystal structure of the HsRad50 zinc-hook (Park et al., 2017), we wondered whether HsRad50 could also form these antiparallel tethering interactions and inspected the underlying crystal lattice (PDB: 5GOX). Intriguingly, the HsRad50 apices adopt related, compared to CtRad50 longitudinally shifted, tethered structures within the crystal lattice (Figure 5A). Like in CtRad50, the same region at the tip of the CC helix mediates this interaction to the neighboring apex and we denote this region as apex tethering element. The apex tethering element does not interact with the first loop insertion element of the CCs, as observed for CtRad50, but with a CC segment just beyond (Figure 5A, inset). Nevertheless, the overall mode of antiparallel interactions of both human and *C. thermophilum* CC apices suggest that apex-apex interactions might be a conserved feature to tether two or more MRN complexes.

Zinc-hook tetramerization is required for efficient DNA repair in human cells

To assess the functional significance of MRN-MRN tethering on recombinational DNA damage repair in living cells, we mutated the HsRad50 apex tethering element (DENQS675-679AAAAA; Rad50^{apex}). Purified HsMR^{apex}N complex has a M₂R₂N₁ stoichiometry and a thermal stability profile similar to that of wt HsMRN complex, suggesting that the overall complex formation and folding is not affected by the mutations (Figure S9A, B). We analyzed the capability of HsMR^{apex}N to repair reactive oxygen species (ROS) mediated DNA damage through comet assays in U2OS cells. Endogenous Rad50 was knocked down via siRNAs and the cells were transfected with wt or mutated Rad50, along with wtMre11 and wtNbs1 to have all components expressed at the same level. Knock-down of endogenous Rad50 without supplementing plasmid expressed MRN caused impaired DNA repair upon ROS induced stress (Figure 5B). Residual repair capacity may be attributed to remaining levels of endogenous Rad50 after siRNA knock down. Transfection with wt MRN fully rescued the repair deficiency (Figure 5B). Transfection with MR^{apex}N only led to a partial rescue, despite robust overexpression of the proteins (Figure S9C). The rescue level is in a similar range, slightly better than in the absence of MRN transfection, indicating that the mutant has a residual but substantially affected repair capacity. Taken together, these data suggest that the apex tethering element mutation compromises MRN function in DSB repair and that the structurally observed tethering interaction is an important feature of MRN in human cells.

Figure 5: Zinc-hook mediated MRN-MRN tethering. (A): Comparison of CtRad50 and HsRad50 zinc-hook tetramers. Crystal structure of CtRad50 zinc-hook tetramer and crystal lattice of HsRad50 zinc-hook (PDB:5GOX) tetramer indicates conserved zinc-hook tethering mechanism. Inset illustrates the apex tethering element (orange Rad50 side chains) and its interactions. **(B): Mutation of apex tethering element in human MRN impairs DNA repair *in cellulo*.** DNA comet assay shows relative amount of DNA double strand breaks (DSBs) after 2h following the treatment (or control without the treatment) of U2OS cells with tert-Butyl hydroperoxide. Cells treated with siRAD50 show high levels of DNA damage. Transfection with wild type human MRN decreases DNA damage to control levels, while transfection with MR^{apex}N does not. **(C): Proposed model of DNA scanning, end detection and DNA tethering by eukaryotic MRN.** MRN complex scans DNA via the C-terminus of Mre11. Upon DNA end detection, MRN loads onto DNA in an ATP dependent mechanism and binds DNA via the canonical Rad50 binding site. Further oligomerization may occur via Rad50 NBDs and zinc-hook leading to DNA end tethering. Details of DNA binding in the tethering mode need to be addressed in future work. **(D): Model of Rad50 zinc-hook mediated MRN dimer.** This structure could bridge DNA ends that are up to 120 nm apart.



Discussion

The MRN complex is a tightly regulated, multifunctional DNA double-strand break (DSB) repair factor that senses and processes DSBs (Cejka, 2015; Paull, 2018; Syed and Tainer, 2018). In addition to its nuclease activity, MRN has functions in DNA damage signaling (via ATM recruitment and activation), DNA tethering, telomere maintenance and chromatin organization (Cannavo and Cejka, 2014; de Jager et al., 2001; Deshpande et al., 2016; Khayat et al., 2021; Lamarche et al., 2010; Lee and Dunphy, 2013; Lee and Paull, 2005; Salifou et al., 2021; You et al., 2005). Many mechanistical aspects of the activation and regulation, but especially also the scaffold functions remain unclear up to date. Using cryo-EM analysis and crystallography, we determined the structure of the MRN complex in a resting state, providing an architectural framework and mechanism for the unresolved question how MRN combines catalytic and structural tethering functions.

Our structure of the full-length MRN clarifies the complex stoichiometry as $M_2R_2N_1$ and provides a molecular basis for the symmetry breaking by Nbs1. Parts of Nbs1 wrap as elongated chain around the Mre11 nuclease domain dimer, binding to the same surface regions of both Mre11 protomers via different Nbs1 elements. The observed wrapping mode argues that an essential function of Nbs1 is to stabilize the Mre11 dimer and head architecture, which might be critical for ATM activation and other functions of the complex. For instance, the *S. cerevisiae* Nbs1/Xrs2 provides nuclear localization, is required for ATM/Tel1 recruitment and canonical end-joining activities, while it is dispensable for nuclease associated functions of MRN/X (Oh et al., 2016). In mice, Nbs1 deletions cause embryonic lethality, however a minimal Mre11 binding fragment that more or less precisely correlates with the portion of Nbs1 that we visualize here, was shown to restore viability and enable ATM activation (Kim et al., 2017). These data indicate that the observed wrapping of the Mre11 dimer by Nbs1 would be particularly important for roles in DNA tethering and Tel1 activation.

An unexpected observation was that the CtMRN-ATP γ S CCs adopt a closed rod state, rather than the open, flexible ring structure that was observed for the EcMR-ATP γ S complex (Kashammer et al., 2019). We attributed the open state with loading onto DNA ends, especially those that carry a proteinaceous block. The relatively narrow opening between the CC domains at the head complex could help clamp down DNA once it is loaded, as observed in the EcMR cutting state, but it is difficult to envision how a blocked DNA end could enter between the CCs in this configuration. The structure may indicate that eukaryotic MRN is more autoinhibited than bacterial MR, which makes sense considering the much more complex functional spectrum of eukaryotic MRN and the perhaps even greater cytotoxic threat that unregulated DNA cleavage by MRN might pose on eukaryotic genomes. However, the CCs might also be more dynamic than presented by the cryo-EM analysis. For instance, atomic force microscopy (AFM) studies generally show a more dynamic nature of the CC domains (Moreno-Herrero et al., 2005; Tatebe et al., 2020; Zabolotnaya et al., 2020). We also observe a subpopulation of open CC domains exclusively in the presence ATP, in line with the idea that ATP binding is needed to open the CCs (Lee et al., 2013). Comparison with the crystal structures of CtRad50^{NBD} in complex with ATP γ S reveals that a full engagement of the NBDs with the signature motif binding to the γ -phosphate of ATP needs an approx. 60° rotation of NBDs with respect to the other, a movement that would pry the CCs open (Figure 2C, Video S1) (Seifert et al., 2016). A switch

between a semi-engaged NBD (this study) and engaged NBD (Rad50^{NBD} crystal structures) would be consistent with studies that show partially open and closed conformations of NBDs on archaeal MR (Canny and Latham, 2022). It is likely that cooperative ATP and DNA binding may help to stabilize the open CC conformation with fully engaged NBDs, since linear DNA triggers ATP hydrolysis approx. 10-fold in both *C. thermophilum* (Figure 3F) and human MRN (Deshpande et al., 2017). Thus, it is reasonable to assume that DNA interacts with MRN after ATP dependent loading on DSBs such that DNA is bound at Rad50's NBDs between the CC, consistent with prior crystallographic analysis of CtRad50 and crystal as well as cryo-EM structures of prokaryotic MR in complex with DNA (Kashammer et al., 2019; Liu et al., 2016; Seifert et al., 2016).

However, the spectrum of DNA binding activities by MRN is arguable more complex than for bacterial MR, which only displayed DNA binding activities that were highly specific for DNA ends and fully dependent on ATP (Saathoff et al., 2018). We identify here the C-terminal extension of eukaryotic Mre11 as responsible for the additional nucleotide independent DNA binding activity, as well as the increased capacity to bind circular compared to linear DNA. A DNA binding site in the C-terminus of *S. cerevisiae* Mre11 has been identified early on and found to be specifically important for formation of meiotic breaks and chromatin organization at DSBs, but otherwise showed almost wt phenotypes in meiosis (Furuse et al., 1998). Thus, our identified separation of DNA binding modes into one that involves the core head complex and is highly specific for DNA ends and ATP, and another that is ATP independent and extends DNA binding also to undamaged DNA regions could be particularly useful to dissect the pleiotropic enzymatic and scaffolding functions of MRN in genome biology. We envision that MRN, like bacterial MR, is loaded onto DBSs in a configuration where the DNA end passes through the CCs, while internal DNA is recognized in a more peripheral fashion via the Mre11's C-terminus (Figure 5C). However, the molecular details of the different modes of DNA binding to MRN must await future studies.

The separation of binding modes is consistent with and useful to interpret several recent studies. The presence of two modes fit very well to the DNA binding dynamics observed in single-molecule DNA curtain experiments (Myler et al., 2017). The canonical, ATP-dependent Rad50 DNA binding site seems to be responsible for binding to DNA ends, where HsMRN was observed to cleave Ku and itself off in a process that requires ATP. However, prior to DNA end recognition, MRN was observed to diffuse along linear DNA in an ATP independent fashion. These and our data suggest that MRN binds to internal DNA via a mechanism that involves the Mre11 C-terminus that allows sliding along DNA. Upon engagement of DNA ends MRN is then properly loaded in an ATP dependent process to form a cutting state.

Furthermore, a physiologically occurring truncation of the HsMre11 C-terminus at a site that matches the one analyzed biochemically by us in CtMRN was identified in human cancer cells and attributed to cleavage by the SPRTN protease (Na et al., 2021). The biochemical analysis showed loss of DNA binding and nuclease activities of MRN in vitro, consistent with our work. However, in that study in vitro nuclease and DNA binding activities were only assessed in the absence of ATP. As a result, the conclusion that truncation of the Mre11 C-terminus benefits these cancer cells due to loss of all MRN DNA binding should be further studied, as MRNs ATP dependent interaction with DNA ends might still be intact. For instance, the Mre11 truncation could be beneficial to cancer cells because some DSB sensing capacity might still be present,

while MRNs poorly understood role in chromosome organization or transcription, process that could require specifically interaction with intact DNA, could be affected (Forey et al., 2021; Salifou et al., 2021).

The perhaps most important result of our work is the discovery of the apex dimerization, since this provides an integrated mechanistic framework for both head-associated DNA binding, nuclease and zinc-hook associated tethering. Numerous studies, starting from early low-resolution negative stain electron microscopy to AFM and cell-based studies show that CC apices from different MR/MRN complexes can associate to form large DNA tethering assemblies in vitro and that MRN has functions in tethering or cohesion of different DNA elements (de Jager et al., 2001; He et al., 2012; Hohl et al., 2015; Hopfner et al., 2002; Moreno-Herrero et al., 2005; Park et al., 2017; Seeber et al., 2016; Vera et al., 2022; Zabolotnaya et al., 2020). Based on structural work on the zinc-hook regions, which showed nearly antiparallel (Hopfner et al., 2002) and parallel (Park et al., 2017; Soh et al., 2021) conformations, up to date it was assumed that the dimerization of two zinc-hooks can occur between the CCs of a single MRN complex (intra-complex) or between the CCs from different MRN complexes (inter-complex), thus tethering MRN. However, the stability of the zinc-hook dimers, the emerging role of the CC domains as critical chemo-mechanical element, rather than a mere linker element, made it unlikely that zinc-hooks switch from intra- to inter-complex interaction modes. Rather they act as stably associated hinge that can switch between ring and rod states of the CCs of a single MRN complex.

Our cryo-EM data now resolves this prevailing conundrum, showing that two apex regions in the rod configuration can further dimerize to join two MRN-MRN complexes (Figure 5D). We believe this clarifies the mode how MRN-MRN dimers are tethered generating large structures spanning up to approx. 120 nm (Figure 5D). Apparently, the tethering interaction requires the CC domain to be in the rod configuration. Thus, it is possible that ATP dependent dynamics and DNA loading at head have a functional crosstalk with the state of tethering.

The mode of this tether, with a very small hydrophobic anchor surrounded by salt bridges might be quite transient on a single MRN-MRN level. Since, MRN complexes have the property to form large clusters at DNA ends, likely through head-head interactions (Vera et al., 2022), multiple protruding CC rods from those clusters could form a molecular velcro through multivalent interactions (de Jager et al., 2001; Zabolotnaya et al., 2020), which could be an interesting way to regulate tethering strength through the size of such clusters (Figure 5C). Likewise, such a cluster could interact with MRN complexes on the sister-chromatid, providing a possible mechanism for the role of MRX in sister-chromatid cohesion at DSBs in *S. cerevisiae* (Seeber et al., 2016). Of note, the type of interface with a small hydrophobic parts and ion pairs is characteristic for the types of interactions found in liquid-liquid phase separated condensates (Banani et al., 2017). Furthermore, inspection of the crystal lattice of CtRad50apex shows that even 1D-lattice like interactions between multiple apices might form, which fit very well to the 1D-lattice geometry of the Rad50NBD dimers bound to DNA. It is therefore possible that DNA tethering by MRN proceeds via multivalent interactions much like those proposed for phase separated condensates.

The HsRad50hook crystal lattice revealed a similar tetrameric arrangement with predominantly ionic interactions (Figure 5A) (Park et al., 2017). Mutating the apex tethering interface impaired repair of ROS

mediated DNA damage in human cells, showing its functional significance. Part of the apex-apex interface is also a loop insertion element in the segmented CC that carries a SQ-motif (S635, Q636). This site has been noticed and studied before and it was found to be phosphorylated by both ATM and ATR (Gatei et al., 2011; Gatei et al., 2014). Mutations in S635 affected DSB repair, checkpoint activation and survival, but cohesin loading at sites of replication restart (Gatei et al., 2011; Gatei et al., 2014), while the mutated purified HsMRN had unaltered nuclease activity (Gatei et al., 2011). From a structural point of view, phosphorylation could increase the stability of the tethering through interactions with nearby basic amino acids on the opposing apex protomer, but it could also alter the geometry of the apex and reduce tethering. While these results mirror the effect of the Rad50^{apex} mutants of our study, they show that tethering may be subject to regulation by ATM and ATR in human cells. However, the functional importance of MRN-MRN tethering and its regulation probably differs in different species, since replacement of the zinc-hook region with the hinge domain of the bacterial SMC protein MukB did not result in increased Camptothecin and hydroxyurea sensitivity in *S. pombe* (Tatebe et al., 2020).

In summary, we provide the framework for the molecular architecture of the eukaryotic MRN complex. We reveal an unexpected, closed conformation of the MRN CCs that enables topology sensitive binding of DNA ends as well as DNA end tethering.

References

- Andres, S.N., Li, Z.M., Erie, D.A., and Williams, R.S. (2019). Ctp1 protein-DNA filaments promote DNA bridging and DNA double-strand break repair. *The Journal of biological chemistry* 294, 3312-3320. 10.1074/jbc.RA118.006759.
- Banani, S.F., Lee, H.O., Hyman, A.A., and Rosen, M.K. (2017). Biomolecular condensates: organizers of cellular biochemistry. *Nature reviews. Molecular cell biology* 18, 285-298. 10.1038/nrm.2017.7.
- Bepler, T., Kelley, K., Noble, A.J., and Berger, B. (2020). Topaz-Denoise: general deep denoising models for cryoEM and cryoET. *Nature communications* 11, 5208. 10.1038/s41467-020-18952-1.
- Berger, I., Fitzgerald, D.J., and Richmond, T.J. (2004). Baculovirus expression system for heterologous multiprotein complexes. *Nature biotechnology* 22, 1583-1587. 10.1038/nbt1036.
- Bian, L., Meng, Y., Zhang, M., and Li, D. (2019). MRE11-RAD50-NBS1 complex alterations and DNA damage response: implications for cancer treatment. *Molecular cancer* 18, 169. 10.1186/s12943-019-1100-5.
- Bradford, M.M. (1976). A rapid and sensitive method for the quantitation of microgram quantities of protein utilizing the principle of protein-dye binding. *Analytical biochemistry* 72, 248-254. 10.1006/abio.1976.9999.
- Buis, J., Wu, Y., Deng, Y., Leddon, J., Westfield, G., Eckersdorff, M., Sekiguchi, J.M., Chang, S., and Ferguson, D.O. (2008). Mre11 Nuclease Activity Has Essential Roles in DNA Repair and Genomic Stability Distinct from ATM Activation. *Cell* 135, 85-96. 10.1016/j.cell.2008.08.015.
- Burmann, F., Lee, B.G., Than, T., Sinn, L., O'Reilly, F.J., Yatskevich, S., Rappsilber, J., Hu, B., Nasmyth, K., and Lowe, J. (2019). A folded conformation of MukBEF and cohesin. *Nature structural & molecular biology* 26, 227-236. 10.1038/s41594-019-0196-z.
- Cannavo, E., and Cejka, P. (2014). Sae2 promotes dsDNA endonuclease activity within Mre11-Rad50-Xrs2 to resect DNA breaks. *Nature* 514, 122-125. 10.1038/nature13771.
- Cannavo, E., Reginato, G., and Cejka, P. (2019). Stepwise 5' DNA end-specific resection of DNA breaks by the Mre11-Rad50-Xrs2 and Sae2 nuclease ensemble. *Proc Natl Acad Sci U S A* 116, 5505-5513. 10.1073/pnas.1820157116.
- Canny, M.D., and Latham, M.P. (2022). LRET-derived HADDOCK structural models describe the conformational heterogeneity required for DNA cleavage by the Mre11-Rad50 DNA damage repair complex. *Elife* 11. 10.7554/eLife.69579.

Carbone, M., Arron, S.T., Beutler, B., Bononi, A., Cavenee, W., Cleaver, J.E., Croce, C.M., D'Andrea, A., Foulkes, W.D., Gaudino, G., et al. (2020). Tumour predisposition and cancer syndromes as models to study gene-environment interactions. *Nature reviews. Cancer* 20, 533-549. 10.1038/s41568-020-0265-y.

Carney, J.P., Maser, R.S., Olivares, H., Davis, E.M., Le Beau, M., Yates, J.R., 3rd, Hays, L., Morgan, W.F., and Petrini, J.H. (1998). The hMre11/hRad50 protein complex and Nijmegen breakage syndrome: linkage of double-strand break repair to the cellular DNA damage response. *Cell* 93, 477-486. 10.1016/s0092-8674(00)81175-7.

Cassani, C., Gobbin, E., Vertemara, J., Wang, W., Marsella, A., Sung, P., Tisi, R., Zampella, G., and Longhese, M.P. (2018). Structurally distinct Mre11 domains mediate MRX functions in resection, end-tethering and DNA damage resistance. *Nucleic acids research* 46, 2990-3008. 10.1093/nar/gky086.

Cassani, C., Vertemara, J., Bassani, M., Marsella, A., Tisi, R., Zampella, G., and Longhese, M.P. (2019). The ATP-bound conformation of the Mre11-Rad50 complex is essential for Tel1/ATM activation. *Nucleic acids research* 47, 3550-3567. 10.1093/nar/gkz038.

Cejka, P. (2015). DNA End Resection: Nucleases Team Up with the Right Partners to Initiate Homologous Recombination. *The Journal of biological chemistry* 290, 22931-22938. 10.1074/jbc.R115.675942.

Cejka, P., and Symington, L.S. (2021). DNA End Resection: Mechanism and Control. *Annual review of genetics* 55, 285-307. 10.1146/annurev-genet-071719-020312.

Chaplin, A.K., Hardwick, S.W., Liang, S., Kefala Stavridi, A., Hnizda, A., Cooper, L.R., De Oliveira, T.M., Chirgadze, D.Y., and Blundell, T.L. (2021). Dimers of DNA-PK create a stage for DNA double-strand break repair. *Nature structural & molecular biology* 28, 13-19. 10.1038/s41594-020-00517-x.

Chen, C.C., Feng, W., Lim, P.X., Kass, E.M., and Jasin, M. (2018). Homology-Directed Repair and the Role of BRCA1, BRCA2, and Related Proteins in Genome Integrity and Cancer. *Annu Rev Cancer Biol* 2, 313-336. 10.1146/annurev-cancerbio-030617-050502.

Connelly, J.C., de Leau, E.S., and Leach, D.R. (2003). Nucleolytic processing of a protein-bound DNA end by the E. coli SbcCD (MR) complex. *DNA Repair (Amst)* 2, 795-807.

de Jager, M., van Noort, J., van Gent, D.C., Dekker, C., Kanaar, R., and Wyman, C. (2001). Human Rad50/Mre11 Is a Flexible Complex that Can Tether DNA Ends. *Molecular Cell* 8, 1129-1135. 10.1016/s1097-2765(01)00381-1.

Delamarre, A., Barthe, A., de la Roche Saint-Andre, C., Luciano, P., Forey, R., Padioleau, I., Skrzypczak, M., Ginalski, K., Geli, V., Pasero, P., and Lengronne, A. (2020). MRX Increases Chromatin Accessibility at Stalled Replication Forks to Promote Nascent DNA Resection and Cohesin Loading. *Mol Cell* 77, 395-410 e393. 10.1016/j.molcel.2019.10.029.

Deshpande, R.A., Lee, J.H., Arora, S., and Paull, T.T. (2016). Nbs1 Converts the Human Mre11/Rad50 Nuclease Complex into an Endo/Exonuclease Machine Specific for Protein-DNA Adducts. *Mol Cell* 64, 593-606. 10.1016/j.molcel.2016.10.010.

Deshpande, R.A., Lee, J.H., and Paull, T.T. (2017). Rad50 ATPase activity is regulated by DNA ends and requires coordination of both active sites. *Nucleic acids research* 45, 5255-5268. 10.1093/nar/gkx173.

Forey, R., Barthe, A., Tittel-Elmer, M., Wery, M., Barrault, M.B., Ducrot, C., Seeber, A., Krietenstein, N., Szachnowski, U., Skrzypczak, M., et al. (2021). A Role for the Mre11-Rad50-Xrs2 Complex in Gene Expression and Chromosome Organization. *Mol Cell* 81, 183-197 e186. 10.1016/j.molcel.2020.11.010.

Frame, F.M., Rogoff, H.A., Pickering, M.T., Cress, W.D., and Kowalik, T.F. (2006). E2F1 induces MRN foci formation and a cell cycle checkpoint response in human fibroblasts. *Oncogene* 25, 3258-3266. 10.1038/sj.onc.1209352.

Furuse, M., Nagase, Y., Tsubouchi, H., Murakami-Murofushi, K., Shibata, T., and Ohta, K. (1998). Distinct roles of two separable in vitro activities of yeast Mre11 in mitotic and meiotic recombination. *The EMBO journal* 17, 6412-6425. 10.1093/emboj/17.21.6412.

Garcia, V., Phelps, S.E.L., Gray, S., and Neale, M.J. (2011). Bidirectional resection of DNA double-strand breaks by Mre11 and Exo1. *Nature* 479, 241-244.

Gatei, M., Jakob, B., Chen, P., Kijas, A.W., Becherel, O.J., Gueven, N., Birrell, G., Lee, J.H., Paull, T.T., Lenthal, Y., et al. (2011). ATM protein-dependent phosphorylation of Rad50 protein regulates DNA repair and cell cycle control. *The Journal of biological chemistry* 286, 31542-31556. 10.1074/jbc.M111.258152.

Gatei, M., Kijas, A.W., Biard, D., Dork, T., and Lavin, M.F. (2014). RAD50 phosphorylation promotes ATR downstream signaling and DNA restart following replication stress. *Human molecular genetics* 23, 4232-4248. 10.1093/hmg/ddu141.

Grimm, M., Zimniak, T., Kahraman, A., and Herzog, F. (2015). xVis: a web server for the schematic visualization and interpretation of crosslink-derived spatial restraints. *Nucleic acids research* 43, W362-369. 10.1093/nar/gkv463.

Haber, J.E. (2018). DNA Repair: The Search for Homology. *BioEssays : news and reviews in molecular, cellular and developmental biology* 40, e1700229. 10.1002/bies.201700229.

He, J., Shi, L.Z., Truong, L.N., Lu, C.S., Razavian, N., Li, Y., Negrete, A., Shiloach, J., Berns, M.W., and Wu, X. (2012). Rad50 zinc hook is important for the Mre11 complex to bind chromosomal DNA double-stranded breaks and initiate various DNA damage responses. *The Journal of biological chemistry* 287, 31747-31756. 10.1074/jbc.M112.384750.

Hohl, M., Kochanczyk, T., Tous, C., Aguilera, A., Krezel, A., and Petrini, J.H. (2015). Interdependence of the rad50 hook and globular domain functions. *Mol Cell* 57, 479-491. 10.1016/j.molcel.2014.12.018.

Hopfner, K.P., Craig, L., Moncalian, G., Zinkel, R.A., Usui, T., Owen, B.A., Karcher, A., Henderson, B., Bodmer, J.L., McMurray, C.T., et al. (2002). The Rad50 zinc-hook is a structure joining Mre11 complexes in DNA recombination and repair. *Nature* 418, 562-566. 10.1038/nature00922.

Hopfner, K.P., Karcher, A., Craig, L., Woo, T.T., Carney, J.P., and Tainer, J.A. (2001). Structural biochemistry and interaction architecture of the DNA double-strand break repair Mre11 nuclease and Rad50-ATPase. *Cell* 105, 473-485.

Hopfner, K.P., Karcher, A., Shin, D.S., Craig, L., Arthur, L.M., Carney, J.P., and Tainer, J.A. (2000). Structural biology of Rad50 ATPase: ATP-driven conformational control in DNA double-strand break repair and the ABC-ATPase superfamily. *Cell* 101, 789-800.

Johnson, D., Crawford, M., Cooper, T., Claeys Bouuaert, C., Keeney, S., Llorente, B., Garcia, V., and Neale, M.J. (2021). Concerted cutting by Spo11 illuminates meiotic DNA break mechanics. *Nature* 594, 572-576. 10.1038/s41586-021-03389-3.

Jumper, J., Evans, R., Pritzel, A., Green, T., Figurnov, M., Ronneberger, O., Tunyasuvunakool, K., Bates, R., Zidek, A., Potapenko, A., et al. (2021). Highly accurate protein structure prediction with AlphaFold. *Nature* 596, 583-589. 10.1038/s41586-021-03819-2.

Jung, C., Bandilla, P., von Reutern, M., Schnepf, M., Rieder, S., Unnerstall, U., and Gaul, U. (2018). True equilibrium measurement of transcription factor-DNA binding affinities using automated polarization microscopy. *Nature communications* 9, 1605. 10.1038/s41467-018-03977-4.

Jung, C., Schnepf, M., Bandilla, P., Unnerstall, U., and Gaul, U. (2019). High Sensitivity Measurement of Transcription Factor-DNA Binding Affinities by Competitive Titration Using Fluorescence Microscopy. *J Vis Exp*. 10.3791/58763.

Kashammer, L., Saathoff, J.H., Lammens, K., Gut, F., Bartho, J., Alt, A., Kessler, B., and Hopfner, K.P. (2019). Mechanism of DNA End Sensing and Processing by the Mre11-Rad50 Complex. *Mol Cell* 76, 382-394 e386. 10.1016/j.molcel.2019.07.035.

Khayat, F., Cannavo, E., Alshmary, M., Foster, W.R., Chahwan, C., Maddalena, M., Smith, C., Oliver, A.W., Watson, A.T., Carr, A.M., et al. (2021). Inhibition of MRN activity by a telomere protein motif. *Nature communications* 12, 3856. 10.1038/s41467-021-24047-2.

Kim, J.H., Grosbart, M., Anand, R., Wyman, C., Cejka, P., and Petrini, J.H.J. (2017). The Mre11-Nbs1 Interface Is Essential for Viability and Tumor Suppression. *Cell reports* 18, 496-507. 10.1016/j.celrep.2016.12.035.

Klykov, O., Steigenberger, B., Pektas, S., Fasci, D., Heck, A.J.R., and Scheltema, R.A. (2018). Efficient and robust proteome-wide approaches for cross-linking mass spectrometry. *Nature protocols* 13, 2964-2990. 10.1038/s41596-018-0074-x.

Kosinski, J., von Appen, A., Ori, A., Karius, K., Muller, C.W., and Beck, M. (2015). Xlink Analyzer: software for analysis and visualization of cross-linking data in the context of three-dimensional structures. *Journal of structural biology* 189, 177-183. 10.1016/j.jsb.2015.01.014.

Kulak, N.A., Geyer, P.E., and Mann, M. (2017). Loss-less Nano-fractionator for High Sensitivity, High Coverage Proteomics. *Mol Cell Proteomics* 16, 694-705. 10.1074/mcp.O116.065136.

Lamarche, B.J., Orazio, N.I., and Weitzman, M.D. (2010). The MRN complex in double-strand break repair and telomere maintenance. *FEBS letters* 584, 3682-3695. 10.1016/j.febslet.2010.07.029.

Lammens, K., Bemeleit, D.J., Mockel, C., Clausing, E., Schele, A., Hartung, S., Schiller, C.B., Lucas, M., Angermuller, C., Soding, J., et al. (2011). The Mre11:Rad50 structure shows an ATP-dependent molecular clamp in DNA double-strand break repair. *Cell* 145, 54-66. 10.1016/j.cell.2011.02.038.

Lee, J., and Dunphy, W.G. (2013). The Mre11-Rad50-Nbs1 (MRN) complex has a specific role in the activation of Chk1 in response to stalled replication forks. *Mol Biol Cell* 24, 1343-1353. 10.1091/mbc.E13-01-0025.

Lee, J.H., Mand, M.R., Deshpande, R.A., Kinoshita, E., Yang, S.H., Wyman, C., and Paull, T.T. (2013). Ataxia telangiectasia-mutated (ATM) kinase activity is regulated by ATP-driven conformational changes in the Mre11/Rad50/Nbs1 (MRN) complex. *The Journal of biological chemistry* 288, 12840-12851. 10.1074/jbc.M113.460378.

Lee, J.H., and Paull, T.T. (2005). ATM activation by DNA double-strand breaks through the Mre11-Rad50-Nbs1 complex. *Science* 308, 551-554. 10.1126/science.1108297.

Lee, J.H., and Paull, T.T. (2021). Cellular functions of the protein kinase ATM and their relevance to human disease. *Nature reviews. Molecular cell biology* 22, 796-814. 10.1038/s41580-021-00394-2.

Lim, H.S., Kim, J.S., Park, Y.B., Gwon, G.H., and Cho, Y. (2011). Crystal structure of the Mre11-Rad50-ATPgammaS complex: understanding the interplay between Mre11 and Rad50. *Genes & development* 25, 1091-1104. 10.1101/gad.2037811.

Liu, Y., Sung, S., Kim, Y., Li, F., Gwon, G., Jo, A., Kim, A.K., Kim, T., Song, O.K., Lee, S.E., and Cho, Y. (2016). ATP-dependent DNA binding, unwinding, and resection by the Mre11/Rad50 complex. *The EMBO journal* 35, 743-758. 10.15252/embj.201592462.

Luo, G., Yao, M.S., Bender, C.F., Mills, M., Bladl, A.R., Bradley, A., and Petrini, J.H. (1999). Disruption of mRad50 causes embryonic stem cell lethality, abnormal embryonic development, and sensitivity to ionizing radiation. *Proc Natl Acad Sci U S A* 96, 7376-7381.

Marie, L., and Symington, L.S. (2022). Mechanism for inverted-repeat recombination induced by a replication fork barrier. *Nature communications* 13, 32. 10.1038/s41467-021-27443-w.

Martina, M., Clerici, M., Baldo, V., Bonetti, D., Lucchini, G., and Longhese, M.P. (2012). A balance between Tel1 and Rif2 activities regulates nucleolytic processing and elongation at telomeres. *Molecular and cellular biology* 32, 1604-1617. 10.1128/MCB.06547-11.

McGee, J.S., Phillips, J.A., Chan, A., Sabourin, M., Paeschke, K., and Zakian, V.A. (2010). Reduced Rif2 and lack of Mec1 target short telomeres for elongation rather than double-strand break repair. *Nature structural & molecular biology* 17, 1438-1445. 10.1038/nsmb.1947.

Mimitou, E.P., and Symington, L.S. (2008). Sae2, Exo1 and Sgs1 collaborate in DNA double-strand break processing. *Nature* 455, 770-774. 10.1038/nature07312.

Mojumdar, A., Sorenson, K., Hohl, M., Toulouze, M., Lees-Miller, S.P., Dubrana, K., Petrini, J.H.J., and Cobb, J.A. (2019). Nej1 Interacts with Mre11 to Regulate Tethering and Dna2 Binding at DNA Double-Strand Breaks. *Cell reports* 28, 1564-1573 e1563. 10.1016/j.celrep.2019.07.018.

Moreno-Herrero, F., de Jager, M., Dekker, N.H., Kanaar, R., Wyman, C., and Dekker, C. (2005). Mesoscale conformational changes in the DNA-repair complex Rad50/Mre11/Nbs1 upon binding DNA. *Nature* 437, 440-443. 10.1038/nature03927.

Morimoto, S., Tsuda, M., Bunch, H., Sasanuma, H., Austin, C., and Takeda, S. (2019). Type II DNA Topoisomerases Cause Spontaneous Double-Strand Breaks in Genomic DNA. *Genes (Basel)* 10. 10.3390/genes10110868.

Myler, L.R., Gallardo, I.F., Soniat, M.M., Deshpande, R.A., Gonzalez, X.B., Kim, Y., Paull, T.T., and Finkelstein, I.J. (2017). Single-Molecule Imaging Reveals How Mre11-Rad50-Nbs1 Initiates DNA Break Repair. *Mol Cell* 67, 891-898 e894. 10.1016/j.molcel.2017.08.002.

Na, J., Newman, J.A., Then, C.K., Syed, J., Vendrell, I., Torrecilla, I., Ellermann, S., Ramadan, K., Fischer, R., and Kiltie, A.E. (2021). SPRTN protease-cleaved MRE11 decreases DNA repair and radiosensitises cancer cells. *Cell death & disease* 12, 165. 10.1038/s41419-021-03437-w.

Nikolova, T., Marini, F., and Kaina, B. (2017). Genotoxicity testing: Comparison of the gammaH2AX focus assay with the alkaline and neutral comet assays. *Mutat Res Genet Toxicol Environ Mutagen* 822, 10-18. 10.1016/j.mrgentox.2017.07.004.

Oh, J., Al-Zain, A., Cannavo, E., Cejka, P., and Symington, L.S. (2016). Xrs2 Dependent and Independent Functions of the Mre11-Rad50 Complex. *Mol Cell* 64, 405-415. 10.1016/j.molcel.2016.09.011.

Park, Y.B., Hohl, M., Padjasek, M., Jeong, E., Jin, K.S., Krezel, A., Petrini, J.H., and Cho, Y. (2017). Eukaryotic Rad50 functions as a rod-shaped dimer. *Nature structural & molecular biology* 24, 248-257. 10.1038/nsmb.3369.

Paull, T.T. (2018). 20 Years of Mre11 Biology: No End in Sight. *Mol Cell* 71, 419-427. 10.1016/j.molcel.2018.06.033.

Paull, T.T., and Gellert, M. (1999). Nbs1 potentiates ATP-driven DNA unwinding and endonuclease cleavage by the Mre11/Rad50 complex. *Genes & development* 13, 1276-1288.

Pettersen, E.F., Goddard, T.D., Huang, C.C., Couch, G.S., Greenblatt, D.M., Meng, E.C., and Ferrin, T.E. (2004). UCSF Chimera--a visualization system for exploratory research and analysis. *J Comput Chem* 25, 1605-1612. 10.1002/jcc.20084.

Punjani, A., Rubinstein, J.L., Fleet, D.J., and Brubaker, M.A. (2017). cryoSPARC: algorithms for rapid unsupervised cryo-EM structure determination. *Nature methods* 14, 290-296. 10.1038/nmeth.4169.

Reginato, G., Cannavo, E., and Cejka, P. (2017). Physiological protein blocks direct the Mre11-Rad50-Xrs2 and Sae2 nuclease complex to initiate DNA end resection. *Genes & development* 31, 2325-2330. 10.1101/gad.308254.117.

Rohou, A., and Grigorieff, N. (2015). CTFFIND4: Fast and accurate defocus estimation from electron micrographs. *Journal of structural biology* 192, 216-221. 10.1016/j.jsb.2015.08.008.

Roisne-Hamelin, F., Pobiega, S., Jezequel, K., Miron, S., Depagne, J., Veaute, X., Busso, D., Du, M.L., Callebaut, I., Charbonnier, J.B., et al. (2021). Mechanism of MRX inhibition by Rif2 at telomeres. *Nature communications* 12, 2763. 10.1038/s41467-021-23035-w.

Rojowska, A., Lammens, K., Seifert, F.U., Drenth, C., Feldmann, H., and Hopfner, K.P. (2014). Structure of the Rad50 DNA double-strand break repair protein in complex with DNA. *The EMBO journal* 33, 2847-2859. 10.15252/embj.201488889.

Saathoff, J.H., Kashammer, L., Lammens, K., Byrne, R.T., and Hopfner, K.P. (2018). The bacterial Mre11-Rad50 homolog SbcCD cleaves opposing strands of DNA by two chemically distinct nuclease reactions. *Nucleic acids research* 46, 11303-11314. 10.1093/nar/gky878.

Salifou, K., Burnard, C., Basavarajiah, P., Grasso, G., Helmsmoortel, M., Mac, V., Depierre, D., Franckhauser, C., Beyne, E., Contreras, X., et al. (2021). Chromatin-associated MRN complex protects highly transcribing genes from genomic instability. *Sci Adv* 7. 10.1126/sciadv.abb2947.

- Sartori, A.A., Lukas, C., Coates, J., Mistrik, M., Fu, S., Bartek, J., Baer, R., Lukas, J., and Jackson, S.P. (2007). Human CtIP promotes DNA end resection. *Nature* 450, 509-514. 10.1038/nature06337.
- Scheltema, R.A., Hauschild, J.P., Lange, O., Hornburg, D., Denisov, E., Damoc, E., Kuehn, A., Makarov, A., and Mann, M. (2014). The Q Exactive HF, a Benchtop mass spectrometer with a pre-filter, high-performance quadrupole and an ultra-high-field Orbitrap analyzer. *Mol Cell Proteomics* 13, 3698-3708. 10.1074/mcp.M114.043489.
- Schiller, C.B., Lammens, K., Guerini, I., Coordes, B., Feldmann, H., Schlauderer, F., Mockel, C., Schele, A., Strasser, K., Jackson, S.P., and Hopfner, K.P. (2012). Structure of Mre11-Nbs1 complex yields insights into ataxia-telangiectasia-like disease mutations and DNA damage signaling. *Nature structural & molecular biology* 19, 693-700. 10.1038/nsmb.2323.
- Scully, R., Panday, A., Elango, R., and Willis, N.A. (2019). DNA double-strand break repair-pathway choice in somatic mammalian cells. *Nature reviews. Molecular cell biology* 20, 698-714. 10.1038/s41580-019-0152-0.
- Seeber, A., Hegnauer, A.M., Hustedt, N., Deshpande, I., Poli, J., Eglinger, J., Pasero, P., Gut, H., Shinohara, M., Hopfner, K.P., et al. (2016). RPA Mediates Recruitment of MRX to Forks and Double-Strand Breaks to Hold Sister Chromatids Together. *Mol Cell* 64, 951-966. 10.1016/j.molcel.2016.10.032.
- Seifert, F.U., Lammens, K., Stoehr, G., Kessler, B., and Hopfner, K.P. (2016). Structural mechanism of ATP-dependent DNA binding and DNA end bridging by eukaryotic Rad50. *The EMBO journal* 35, 759-772. 10.15252/embj.201592934.
- Soh, Y.M., Basquin, J., and Gruber, S. (2021). A rod conformation of the *Pyrococcus furiosus* Rad50 coiled coil. *Proteins* 89, 251-255. 10.1002/prot.26005.
- Syed, A., and Tainer, J.A. (2018). The MRE11-RAD50-NBS1 Complex Conducts the Orchestration of Damage Signaling and Outcomes to Stress in DNA Replication and Repair. *Annual review of biochemistry* 87, 263-294. 10.1146/annurev-biochem-062917-012415.
- Tatebe, H., Lim, C.T., Konno, H., Shiozaki, K., Shinohara, A., Uchihashi, T., and Furukohri, A. (2020). Rad50 zinc hook functions as a constitutive dimerization module interchangeable with SMC hinge. *Nature communications* 11, 370. 10.1038/s41467-019-14025-0.
- Tubbs, A., and Nussenzweig, A. (2017). Endogenous DNA Damage as a Source of Genomic Instability in Cancer. *Cell* 168, 644-656. 10.1016/j.cell.2017.01.002.
- Usui, T., Ohta, T., Oshiumi, H., Tomizawa, J., Ogawa, H., and Ogawa, T. (1998). Complex formation and functional versatility of Mre11 of budding yeast in recombination. *Cell* 95, 705-716.

Vera, K., Giordano, R., Eliana, B., Kristina, K., Janny, T., Gea, C., Sung Sik, L., Raphaël, G., Ralf, S., Petr, C., and Matthias, P. (2022). Nature Portfolio. 10.21203/rs.3.rs-811984/v1.

Wright, W.D., Shah, S.S., and Heyer, W.D. (2018). Homologous recombination and the repair of DNA double-strand breaks. *The Journal of biological chemistry* 293, 10524-10535. 10.1074/jbc.TM118.000372.

You, Z., Chahwan, C., Bailis, J., Hunter, T., and Russell, P. (2005). ATM activation and its recruitment to damaged DNA require binding to the C terminus of Nbs1. *Molecular and cellular biology* 25, 5363-5379. 10.1128/MCB.25.13.5363-5379.2005.

Zabolotnaya, E., Mela, I., Williamson, M.J., Bray, S.M., Yau, S.K., Papatziadou, D., Edwardson, J.M., Robinson, N.P., and Henderson, R.M. (2020). Modes of action of the archaeal Mre11/Rad50 DNA-repair complex revealed by fast-scan atomic force microscopy. *Proceedings of the National Academy of Sciences* 117, 14936-14947.

Zhang, Y., Zhang, X., Dai, H.Q., Hu, H., and Alt, F.W. (2022). The role of chromatin loop extrusion in antibody diversification. *Nature reviews. Immunology*. 10.1038/s41577-022-00679-3.

Zhao, B., Rothenberg, E., Ramsden, D.A., and Lieber, M.R. (2020). The molecular basis and disease relevance of non-homologous DNA end joining. *Nature reviews. Molecular cell biology* 21, 765-781. 10.1038/s41580-020-00297-8.

Zheng, S.Q., Palovcak, E., Armache, J.P., Verba, K.A., Cheng, Y., and Agard, D.A. (2017). MotionCor2: anisotropic correction of beam-induced motion for improved cryo-electron microscopy. *Nature methods* 14, 331-332. 10.1038/nmeth.4193.

Zhu, J., Petersen, S., Tessarollo, L., and Nussenzweig, A. (2001). Targeted disruption of the Nijmegen breakage syndrome gene NBS1 leads to early embryonic lethality in mice. *Current biology : CB* 11, 105-109.

Zivanov, J., Nakane, T., Forsberg, B.O., Kimanius, D., Hagen, W.J., Lindahl, E., and Scheres, S.H. (2018). New tools for automated high-resolution cryo-EM structure determination in RELION-3. *Elife* 7. 10.7554/eLife.42166.

Material and Methods

Expression and purification of the CtMRN complex

Codon-optimized synthetic genes (Genscript, Piscataway, USA) encoding CtMre11, CtRad50, CtNbs1 were PCR amplified and cloned into pACEBac1 (CtMre11, CtRad50) and pIDK (CtNbs1) using MultiBac expression system (Berger et al., 2004). Recombination steps were carried out in *Escherichia coli* XL1Blue cells (Stratagene) under addition of Cre-recombinase (NEB). Baculoviruses were generated in *Spodoptera frugiperda* (SF21) insect cells (IPLB-Sf21AE) and virus titers were determined by small scale test expression. 1 L of *Trichoplusia ni* High Five cells (Invitrogen), seeded to 1 mio/mL, were infected with 1:1000 of baculovirus and cultured for 72 h at 27°C. Cells were harvested by centrifugation.

Fresh cell pellet was suspended in 50 mL of Lysis buffer (50 mM HEPES pH 7.0, 250 mM NaCl, 10% glycerol, 0.5 mM TCEP, 5 µL TURBO DNase (Thermo-Fisher Scientific), supplemented with a SIGMAFAST Protease Inhibitor Cocktail Tablet, EDTA free (Merck) on ice. All further purification steps were performed on ice or in an 8°C cold room. The cells were lysed using a dounce homogenizer followed by sonication for 1 min (50% duty cycle, 5 output control). The lysate was cleared by centrifugation at 17000 rpm for at least 1 h using a SS-34 rotor. The soluble supernatant was prefiltered with a Millex fiber-glass filter (Roth) and filtered using 0.45 µm PVDF membrane filters (Merck Millipore).

The lysate was applied onto a 5 mL HiTrap Heparin HP column (GE Healthcare) attached to an AKTA Pure system (GE Healthcare) and equilibrated in Buffer A (50 mM HEPES pH 7.0, 250 mM NaCl, 10% glycerol, 0.5 mM TCEP). The column was washed with 5 CV Buffer A, 5 CV of 7% Buffer B (50 mM HEPES pH 7.0, 1 M NaCl, 10% glycerol, 0.5 mM TCEP). Protein was eluted with 33% Buffer B, pooled, and dialyzed for 8 h in SEC buffer (20 mM HEPES 7.0, 200 mM NaCl, 10% Glycerol, 0.5 mM TCEP). 1 g (dry mass) cellulose phosphate (CP) fine mesh resin (Merck) was prepared according to protocol and equilibrated in SEC buffer. The dialyzed protein was applied to CP resin, which was washed until no DNA eluted anymore. Protein was eluted by addition of CP elution buffer (20 mM HEPES 7.0, 400 mM NaCl, 10% glycerol, 0.5 mM TCEP) to a total of 10 CV. The CP eluate was concentrated and applied to size exclusion chromatography (SEC; Superose 6, 10/300, GE Healthcare) in SEC buffer (No glycerol was added for cryo-EM grid preparation). Stoichiometric CtMRN complex eluted at 0.4 CV.

Crosslinking mass spectrometry

Freshly purified MRN complex was diluted in compensation buffer to obtain a protein concentration of 0.25 mg/mL in 20 mM HEPES (pH 7.0), 200 mM NaCl, 5 mM MgCl₂, 1 mM MnCl₂, 0.2 mM TCEP, 1 mM ATPγS. The complex was incubated for 15 min at 21°C, then a 6.2 mM solution of bissulfosuccinimidyl suberate (BS3), dissolved in 20 mM HEPES (pH 8.5) buffer, was added to obtain a final concentration of 31.1 µM BS3. The protein was crosslinked for 30 min @ 35°C before it was quenched by addition of 1 M Tris-HCl (pH 8.0) to a final concentration of 62 mM.

To the crosslinked proteins, 4 M Urea and 50 mM Tris (pH 8.0) was added. The mixture was sonicated using a Bioruptor Plus sonication system (Diogenode) for 10x 30 s at high intensity. Thereafter, 40 mM 2-chloroacetamide (CAA, Sigma-Aldrich) and 10 mM tris(2-carboxyethyl) phosphine (TCEP; Thermo Fisher Scientific) were added for the reduction and alkylation of disulfide bonds. After incubation for 20 min at 37°C, the samples were diluted 1:2 with MS grade water (VWR). Crosslinked proteins were digested overnight at 37°C by addition of 0.5 µg of LysC and 1 µg of trypsin (Promega). Afterwards, the mixture was acidified with 10% trifluoroacetic acid (TFA; Merck) in water to a final concentration of 1%, followed by desalting of the peptides using Sep-Pak C18 1cc vacuum cartridges (Waters). Desalted peptides were vacuum-dried.

Vacuum-dried peptides were dissolved in buffer A (0.1% formic acid). For nano LC separation of the peptides at a flow rate of 250 nL/min, the Thermo Easy-nLC 1000 (Thermo Fisher Scientific) equipped with a 30-cm analytical column (inner diameter: 75 microns; packed in-house with ReproSil-Pur C18-AQ 1.9-micron beads, Dr. Maisch GmbH) was used. Through the nano electrospray interface, eluting peptides were sprayed into the benchtop Orbitrap Q Exactive HF (Thermo Fisher Scientific) (Scheltema et al., 2014). As gradient, the following steps were programmed with increasing addition of buffer B (80% acetonitrile, 0.1% formic acid): linear increase from 8 to 30% over 60 minutes, followed by a linear increase to 60% over 5 minutes, a linear increase to 95% over the next 5 minutes, and finally maintenance at 95% for another 5 minutes. The mass spectrometer was operated in data-dependent mode with survey scans from m/z 300 to 1650 Th (resolution of 60k at m/z = 200 Th), and up to 15 of the most abundant precursors were selected and fragmented using stepped Higher-energy collisional Dissociation (HCD with a normalized collision energy of value of 19, 27, 35). The MS2 spectra were recorded with dynamic m/z range (resolution of 30k at m/z = 200 Th). AGC target for MS1 and MS2 scans were set to 3 x 10⁶ and 105, respectively, within a maximum injection time of 100 and 60 ms for the MS1 and MS2 scans, respectively. Charge state 2 was excluded from fragmentation to enrich the fragmentation scans for cross-linked peptide precursors.

The acquired raw data were processed using Proteome Discoverer (version 2.5.0.400) with the XlinkX/PD nodes integrated (Klykov et al., 2018). To identify the crosslinked peptide pairs, a database search was performed against a FASTA containing the sequences of the proteins under investigation as well as a contaminant database. DSS was set as a crosslinkers. Cysteine carbamidomethylation was set as fixed modification and methionine oxidation and protein N-term acetylation were set as dynamic modifications. Trypsin/P was specified as protease and up to two missed cleavages were allowed. Furthermore, identifications were only accepted with a minimal score of 40 and a minimal delta score of 4. Otherwise, standard settings were applied. Filtering at 1% false discovery rate (FDR) at peptide level was applied through the XlinkX Validator node with setting simple.

The crosslinks were analyzed and visualized using the xVis Crosslink Analyzer Webserver and the Xlink Analyser software for UCSF Chimera (Grimm et al., 2015; Kosinski et al., 2015; Pettersen et al., 2004).

Cryo-EM grid preparation

Freshly purified MRN complex was diluted in compensation buffer to obtain a protein concentration of 0.27 mg/mL in 20 mM HEPES (pH 7.6), 200 mM NaCl, 5 mM MgCl₂, 1 mM MnCl₂, 20 µM ZnCl₂, 0.2 mM

TCEP, 2 mM ATPγS. The complex was incubated for at least 10 min at 21°C to bind ions and nucleotide. Just before plunging, Octyl β-D-glucopyranoside (β-OG) was added to a final concentration of 0.05%. Grids were prepared using a Leica EM GP plunge freezer (Leica). β-OG containing sample (4.5 μl) was deposited onto plasma cleaned (GloQube, Quorum) copper grid (Cu 200, R2/1, Quantifoil). Sample was applied to the grids at 15°C and 95% humidity and blotted for 2.7 s before plunge-freezing the grid in liquid ethane.

Cryo-EM data acquisition

Six datasets of CtMRN-ATPγS (total 29349 micrographs) were acquired on a Titan Krios transmission electron microscope (Thermo Fisher Scientific) operated at 300 kV, with a K2 summit direct electron detector (Gatan) operated in counting mode and energy filter (Gatan). Data acquisition was automated with the EPU (Thermo Fisher Scientific) software package. Images were recorded at a nominal magnification of 130,000x (1.059 Å/pix) with a defocus range of 1.0 μm to 2.8 μm, and total dose of 45 e⁻/Å² over 40 frames.

Cryo-EM image processing

Motion correction with MotionCor2 and CTF estimation with CTFFind4 were performed on-the-fly for all datasets using an in-house developed pipeline (Rohou and Grigorieff, 2015; Zheng et al., 2017). Initially, particles were picked in CryoSPARC v3.2.0 using the implemented blob picker (Punjani et al., 2017). After 2D classification, selected particles were used to train the TOPAZ deep picker (Bepler et al., 2020). TOPAZ was trained iteratively until no further increase in particle numbers and particles were extracted using box sizes of 768 pix (Long CC map), 352 pix (Catalytic head map), 352 pix (ZH tetramer).

The particles for the Catalytic head map were transferred to Relion v3.0, further sorted by 2D classification and subjected to focused 3D refinement with masking the catalytic head (Zivanov et al., 2018). This resulted in the C1 map of the catalytic head at 4.0 Å. Further focused 3D classification resulted in three different classes that showed different degrees of Nbs1 binding to the catalytic head. Non-uniform (NU) refinement of the Long CC particles in CryoSPARC led to a C2 map with 4.8 Å overall resolution. Further local refinements of the C2 maps led to two maps of the CCs with 6.8 Å and 7.6 Å, respectively.

The ZH particles were processed in CryoSPARC. An ab-initio reconstruction was created from the particles picked in TOPAZ. Particles were repicked and sorted via heterogenous refinement with 5 references from a ZH tetramer, ZH octamer, Mre11, MRN catalytic head, and a part of the CCs. The ZH particles were pooled and sorted via iterative rounds of 2D classification. In NU refinement, followed by local refinement a 4.9 Å C2 map of the ZH were calculated. To avoid over-sharpening, the map was eventually filtered to 7 Å.

DNA-stimulated ATPase assays

We used a NADH-coupled assay to monitor the rate of ATP hydrolysis by CtMRN. The ATPase rate was assayed in reaction buffers containing 250 nM MRN complex, 20 mM HEPES pH 7.0, 80 mM NaCl; 5 mM

MgCl₂, 1 mM MnCl₂, 0.1 mg/mL BSA, 0.2 mM TCEP, 0.25 mM NADH, 20 U/ml PK, 30 U/ml LDH, 2 mM Phosphoenolpyruvate (PEP), the reaction was started by addition of 1 mM ATP and 52 ng/μL DNA. The measurements were started immediately after ATP addition for 2 h at 37 °C. The oxidation rate of NADH was assayed fluorometrically by measuring the fluorescence at 460 nm (excitation 340 nm) on a Tecan microplate reader (Infinite M1000).

The linear decrease in fluorescence between 200 s and 800 s was fitted to a linear regression and the slope was used to calculate the ATPase rate using the following formula. The NADH slope was calculated using a calibration curve which was recorded by titrating ADP to a constant NADH solution in reaction buffer without MRN/DNA.

$$ATPase\ rate\ [ATP\ complex^{-1}s^{-1}] = \frac{slope\ [FU\ s^{-1}]}{NADH\ slope\ \left[-587.9\ \frac{FU}{\mu M\ ATP}\right] c_{MRN}\ [\mu M\ complex]}$$

Direct fluorescence polarization anisotropy (nucleotide dependence)

Fluorescence polarization anisotropy was used to monitor CtMRN and CtM^{ΔC}RN binding to 80 bp dsDNA. 5 nM of 3' 6-FAM-labeled DNA was incubated with increasing amounts of MRN in ATP (20 mM HEPES pH 7.0, 100 mM NaCl, 5 mM MgCl₂, 0.2 mg/ml BSA, 1 mM ATP, 0.5 mM TCEP), ATPyS (20 mM HEPES pH 7.0, 100 mM NaCl, 5 mM MgCl₂, 0.2 mg/ml BSA, 1 mM ATPyS, 0.5 mM TCEP) and no nucleotide (20 mM HEPES pH 7.0, 100 mM NaCl, 5 mM MgCl₂, 0.2 mg/ml BSA, 0.5 mM TCEP) assay buffers. All DNA binding reactions were done without addition of MnCl₂ to avoid DNA degradation. After 15 min incubation at 37 °C, the fluorescence anisotropy was measured at an excitation wavelength of 488 nm and an emission wavelength of 520 nm using an automated polarization microscope (Jung et al., 2018; Jung et al., 2019). Each sample was measured at twelve different z-planes to reduce the effect of potential fluorescing protein-DNA aggregates that could lead to erroneous FA values, these measurements were repeated three times for each of the 3-4 replicates. The FA values were calculated for each image using the following formula, requiring the parallel (I⁼) and perpendicular (I⁺) fluorescence intensities and the instrumental G-factor (G = 1.15 for our setup, as determined by measuring free dye in solution). Regions of interest (ROI) were defined as equal-sized regions around the maxima in the respective channels.

$$FA(z, t) = \frac{I^=(z, t) - GI^+(z, t)}{I^=(z, t) + 2I^+(z, t)}$$

Finally, we calculated for each sample the median FA value of all images acquired from a given well to reduce variability, namely the contribution to FA of images containing potential Protein-DNA aggregates. Data was analyzed using Prism (GraphPad) and K_D values derived by fitting the anisotropy data to a Specific binding with Hill slope model, using the following formula:

$$FU = \frac{B_{max}\ [MRN\ in\ nM]^h}{K_D^h\ [MRN\ in\ nM]^h}$$

Competitive fluorescence polarization anisotropy (topology dependence)

Fluorescence polarization anisotropy was used to monitor CtMRN and CtM^{AC}RN binding to linear and circular DNA. 5 nM of 3' 6-FAM-labeled 80 bp dsDNA was incubated with 45 nM MRN in ATPyS containing assay buffer (20 mM HEPES pH 7.0, 100 mM NaCl, 5 mM MgCl₂, 0.2 mg/ml BSA, 1 mM ATP, 0.5 mM TCEP). After 10 min incubation, increasing amount of either circular or linear (obtained by digesting of circular DNA with PvuII-HF NEB) pUC19 plasmid DNA was added. After 15 min incubation at 37 °C, the fluorescence anisotropy was measured using the same setup as described above.

Data was analyzed using Prism (GraphPad) by fitting the anisotropy data to a One phase decay model, using the following formula, K_D was calculated as ln(2)/K.

$$FU = (FU_{max} - FU_{min}) e^{-K[DNA\ in\ ng/\mu l]} + FU_{min}$$

Fluorescence imaging and segmentation of protein-DNA aggregates

To characterize the relative amount of aggregates between samples, we acquired for each sample z-stacks of widefield fluorescence images. Image segmentation of the aggregates was performed using a custom-written Definiens XD 2.0 script (Munich, Germany). The image analysis procedure was the following. The individual aggregates appear in bright, relatively round objects within a heterogeneous background arising from the inhomogeneous widefield illumination. To facilitate the detection of the contour of the objects, we applied a 3D-Gaussian filter with a kernel size of 5 × 5 × 3 pixels, followed by a second 3D-Gaussian filter with the same kernel size. We then subtracted the latter image from the previous one. This procedure resulted in a background-subtracted image. Then, we applied a global threshold and carried out segmentation using an algorithm implemented in the Definiens XD 2.0 software platform. Briefly, the Multi-Threshold Segmentation algorithm splits the image domain and classifies the resulting image objects based on a defined pixel value threshold. This results in segmented patterns classified as “aggregates” or “background”. We then extracted for each frame the total number of aggregate particles, their size (in a 2D projection within our optical resolution of about approx. 0.5 μm) and their average fluorescence intensity. The latest parameter can be assumed to be proportional to the number of protein-DNA aggregating in a single particle. Data was plotted using Prism (GraphPad).

Crystallization of the CtRad50 Zn-hook domain

Codon-optimized synthetic DNA (Genscript, Piscataway, USA) encoding CtRad50⁵⁹⁸⁻⁷⁸² was PCR amplified and cloned into pET47b (6xHis-HRV3C-CtRad50⁵⁹⁸⁻⁷⁸²). The construct was expressed in *Escherichia coli* BL21 Rosetta cells (Novagen). 0.5 L of *E. coli* culture were grown in TURBO Broth™ medium (Molecular Dimensions) containing Kanamycin (50 μg/mL) and Chloramphenicol (34 μg/mL) at 37°C to an OD₆₀₀ of 2.0 before induction with 0.4 mM IPTG. Upon induction, further cultivation was performed at 18°C, until the cells reached an OD₆₀₀ of 7.0.

The cells were harvested via centrifugation (10 min, 3000 g, 4°C) and resuspended in 150 mL Lysis buffer (50 mM HEPES 7.5, 250 mM NaCl, 10 % Glycerol, 5 mM β -Mercaptoethanol, 2 μ L TURBO DNase (Thermo-Fisher Scientific), supplemented with a SIGMAFAST Protease Inhibitor Cocktail Tablet, EDTA free (Merck). The cells were lysed via sonication for 3x 3 min (50% duty cycle, 5 output control) and cleared lysate was prepared by centrifugation at 17 000 rpm for 1 h using a SS-34 rotor.

5 mL Ni-NTA beads (Macherey-Nagel) were equilibrated in Buffer A (50 mM HEPES 7.5, 250 mM NaCl, 10 % Glycerol, 5 mM β -mercaptoethanol) and incubated with cleared lysate for 1h at 8°C on a rolling incubator. The beads were washed with 3 CV of Buffer A, 3 CV Buffer A and 20 mM Imidazole, followed by 3 CV Buffer A. 5 mL of Buffer A containing 50 μ L HRV3C protease (Cytiva) were added, and the beads were incubated over night at 8°C on a rolling incubator. On the next day the eluate was applied to a fresh 5 mL of Ni-NTA, equilibrated in Buffer A and the flow-through was collected. EDTA was added to a final concentration of 1 mM and the protein was concentrated to 30 mg/ml. A Superose 200 16/60 HiLoad column (Cytiva) was equilibrated in SEC buffer (20 mM HEPES 7.5, 150 mM NaCl, 1 mM EDTA, 5% Glycerol, 0.5 mM TCEP) and 3 mL of the concentrated protein sample was injected. The eluate was fractionated and analysed on SDS PAGE.

Crystals of CtRad50⁵⁹⁸⁻⁷⁸² were grown in hanging drops by mixing 1.5 μ L protein at 4.5 mg/mL and 1.5 μ L reservoir solution (0.1 M MES pH 6.8, 0.6 M NaCl, 18% PEG4000). The crystals were soaked in a reservoir solution supplemented with 10% 1,4-butanediol and frozen in liquid Nitrogen. Data was collected to 2.5 Å at the P14 beamline (EMBL Hamburg).

Comet assay

Cells and culture conditions: The human osteosarcoma cell line U2OS (RRID:CVCL_0042) was cultivated in DMEM containing 10% fetal bovine serum (FBS) and penicillin/streptomycin at 37°C in a humidified 5% CO₂ atmosphere.

Protein extracts and Western blot analysis: Whole-cell protein extracts were prepared by disrupting cell pellets in Lysis Buffer (20 mM tris, 1 mM EDTA, 1 mM β -mercaptoethanol, 5% glycerine, pH 8.5) supplemented with various protease and phosphatase inhibitors (0.02 M β -glycerophosphate, 1 mM Na₃VO₄, 0.1 mM phenylmethylsulfonyl fluoride, 0.01 mM MG-132, 0.01 M dithiothreitol, 0.01 M NaF and cOmplete™) using sonication. The protein concentration was determined using the Bradford method as described (Bradford, 1976). 30 μ g of protein were separated by sodium dodecyl sulphate polyacrylamide gel electrophoresis (SDS-PAGE) and transferred overnight at 100 mA in blotting buffer (0.025 M tris, 0.192 M glycine, 20% methanol) onto a nitrocellulose membrane. All primary antibodies were used at 1:1000 dilution in 5% BSA in tris buffered saline (TBS) containing 0.1% Tween and 1% Na-Azide. The antibodies used were anti-RAD50 (Cell Signalling, #3427) and anti-Vinculin (Santa Cruz, sc-73614). The secondary antibodies (LI-COR Bioscience) were diluted (1:10000) in TBS containing 0.1% Tween and the proteins were visualized using the Odyssey® Infrared Imaging System (LI-COR Biotechnology).

Transfections: For RAD50 knockdown, U2OS cells were transfected with siRNA targeting RAD50 (s792, Silencer®Select, ThermoFisher Scientific) and negative control siRNA (#AM4611; Life Technologies) using Lipofectamine RNAiMAX (Invitrogen), according to the manufacturer's instructions. The siRNA mediated knockdown of RAD50 was confirmed on protein level using Western blot analysis.

For RAD50 wild-type and mutant expression, the plasmids pACEMam1_pMDC_HsMRN and pACE-Mam1_pMDC_HsMR^{ΔPEX}N were transfected into U2OS cells using Polyethylenimine Hydrochloride (PEI) (#24765; Polysciences). 1 µg plasmid DNA was mixed with 4 µg PEI in 200 µl serum and antibiotic free DMEM medium, 45 min later the DNA/PEI complex was added to the cells dropwise. The RAD50 expression was confirmed by Western blot analysis.

Neutral comet assay: DNA double-strand breaks (DSBs) and their repair was monitored by single-cell gel electrophoresis under neutral conditions. RAD50 was knocked down in U2OS cells, 8 hours later the cells were transfected with the MR123, MR132 or MR133 expression plasmids. 16 h later the knockdown and transfected cells were reseeded into three Petri dishes, designated untreated, tert-Butyl hydroperoxide (t-BuOOH) treated and t-BuOOH treated with 2 h repair. The next day, the cells were exposed to 150 µM t-BuOOH for 1 h. The comet assays were performed, as described (Nikolova et al., 2017). Shortly, cells were embedded in 0.5 % low melting point agarose in PBS and spread onto glass slides coated with 1.2 % agarose. All following steps were performed at 4°C, unless stated otherwise. Cells were lysed in lysing solution (2.5 M NaCl, 100 mM EDTA, 10 mM Tris, 1% Na-Laurylsarcosinate, 1% Tryton X-100) at a pH of 7.5. Slides were electrophoresed for 25 min in electrophoresis buffer (90 mM Tris, 90 mM boric acid, 2 mM EDTA, pH= 7.5) at 7.4 V/cm, fixed in 100% methanol and then dried. All following steps were performed at room temperature. DNA was stained using propidium iodide (50 µg/ml) and 50 cells per slide were evaluated using a fluorescence microscope and the Comet IV software (Perceptive Imaging, Liverpool, UK). Data are expressed as tail intensity, which denotes the percentage of DNA in the tail multiplied by the length between the center of the head and tail.

Acknowledgements

EM data were collected at the Cryo-EM Core Facility of the Gene Center, Department of Biochemistry, LMU, Munich. We are grateful for support by G. Witte for help in collection of X-ray diffraction data. We gratefully thank S. Woike for providing his experience in rendering of structural movies. Funding was provided by the Deutsche Forschungsgemeinschaft (CRC1361, Gottfried Wilhelm Leibniz-Prize, SFB1361 and GRK1721 to K.P.H., CRC1054 to K.L.) and a PhD fellowship from Boehringer Ingelheim Fonds (BIF) to E.v.d.L.

Author contributions

M.R., K.S., E.v.d.L., A.A., B.K., were involved in protein production, crystallization, and *in vitro* assays. M.R., K.S., K.L., J.D.B, A.A., and K.P.H. carried out structural studies. C.J. performed fluorescence anisotropy measurements and segmentation of protein-DNA aggregates. W.P.R. contributed the *in cellulo* comet assays to quantify the DNA repair efficiency. B.S. processed crosslinked complexes and performed mass spectrometry analysis. K-P.H designed overall research and provided funding. All authors were involved in interpretation of data, final manuscript preparation and approval.

Competing interests

None of the authors declares competing interests. A.A. contributed as an employee at the Gene Center, Department of Biochemistry, LMU at the time of the study and is currently an employee of CureVac, Tübingen, Germany.

Supplementary Figures

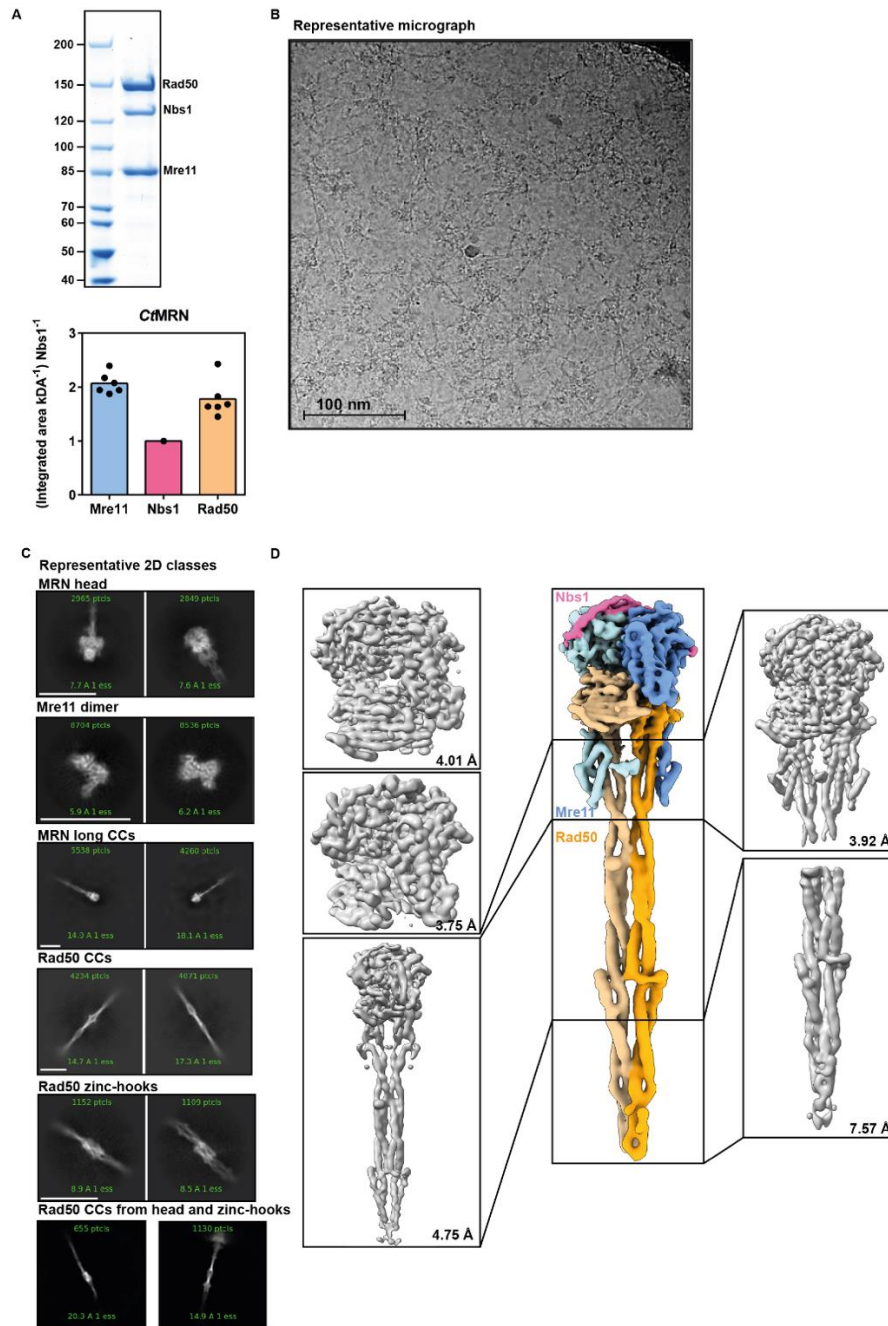


Figure S1: CtMRN complex cryo-EM preparation. (A): Representative SDS-PAGE of purified CtMRN complex and gel quantification (N=6). (B): Representative Micrograph of CtMRN-ATPyS. (C): Representative 2D classes of particles picked within the CtMRN-ATPyS datasets. (D): Composite map (colored) composition. The highest resolved areas from the depicted LAFTEr filtered maps were used to generate a composite map.

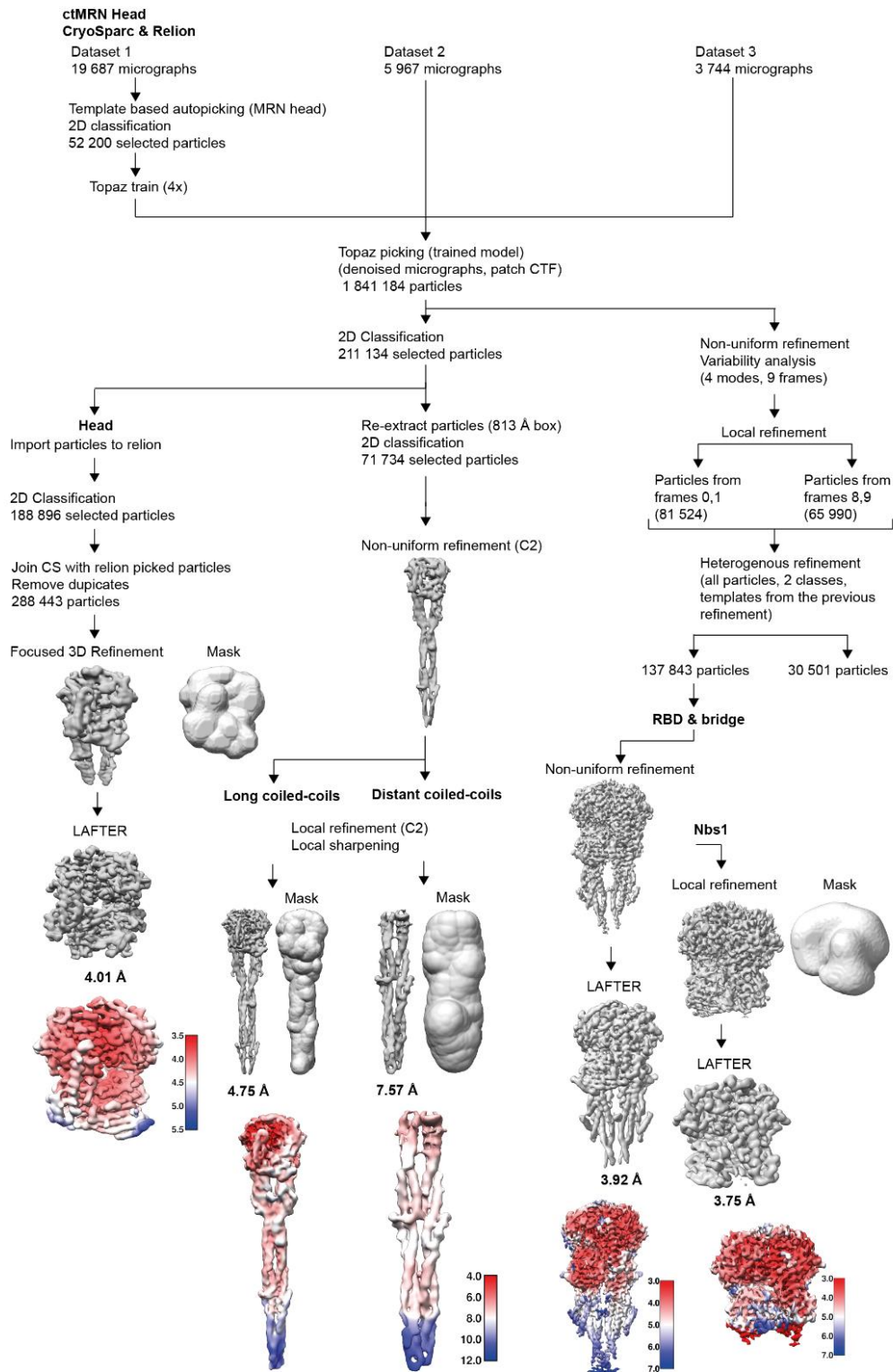


Figure S2: Processing schemes for the CtMRN catalytic head and CC maps. Processing schemes of CtMRN-ATPys head, long coiled-coils, distant coiled-coils and RBD & bridge with local resolution estimates at the end of each processing branch.

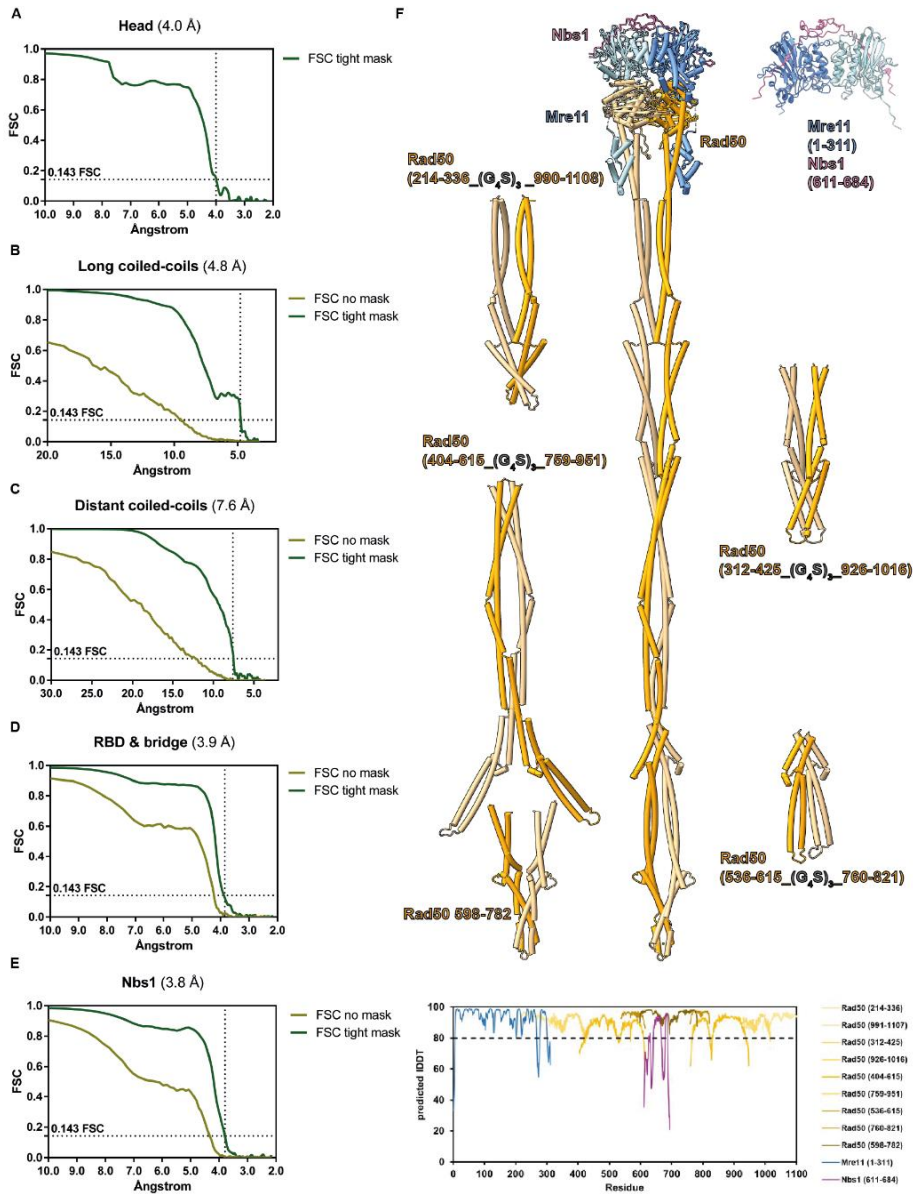


Figure S3: FSC curves and AlphaFold2 models. (A): FSC curves of the Head maps (Relion v3.0). **(B):** FSC curves of the long coiled-coils map (CryoSPARC v3.2.0). **(C):** FSC curves of the distant coiled-coils map (CryoSPARC v3.2.0). **(D):** FSC curves of the RBD & bridge map (CryoSPARC v3.2.0). **(E):** FSC curves of the Nbs1 map (CryoSPARC v3.2.0). **(G):** AlphaFold2 models used to build a full-length MRN model and predicted IDDT scores (>80 indicates high confidence models).

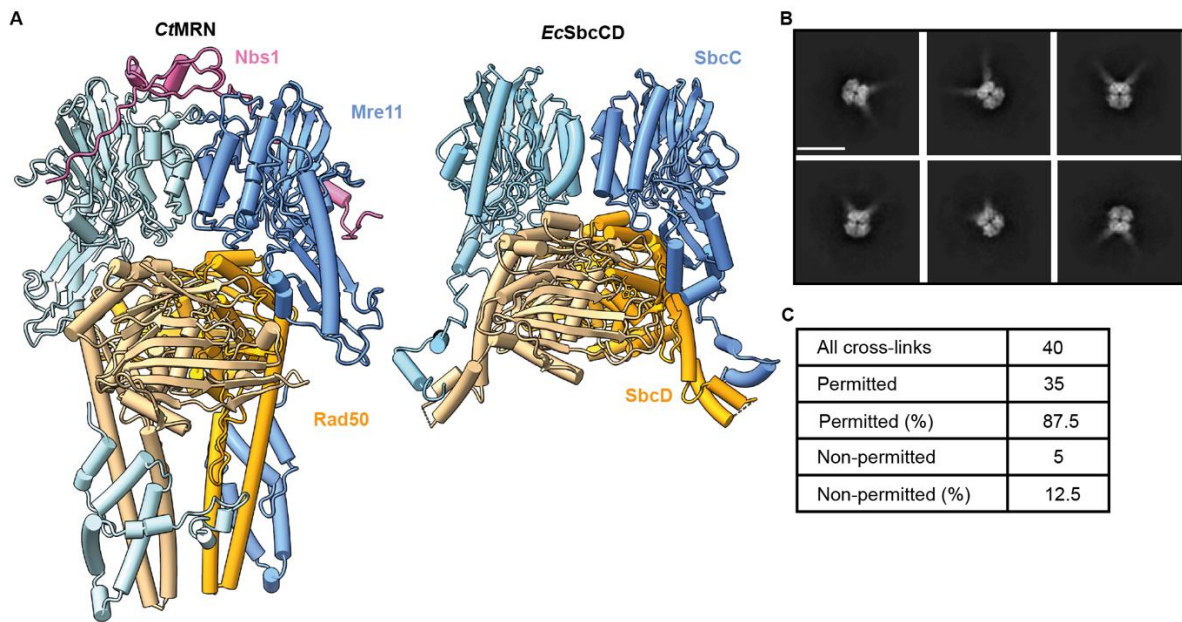


Figure S4: Conformations of Rad50 CCs and crosslinking MS statistics. (A): Comparison of the Cryo-EM structures of the eukaryotic CtMRN complex and the prokaryotic EcMR/SbcCD complex bound to ATP γ S. Mre11/SbcD colored in blue, Rad50/SbcC colored orange, Nbs1 colored pink. (B): 2D classes of CtMRN particles bound to ATP showing open coiled-coils. Scale bar 10 nm. (C): Statistics of XL-MS restraints fitted to cryo-EM model.

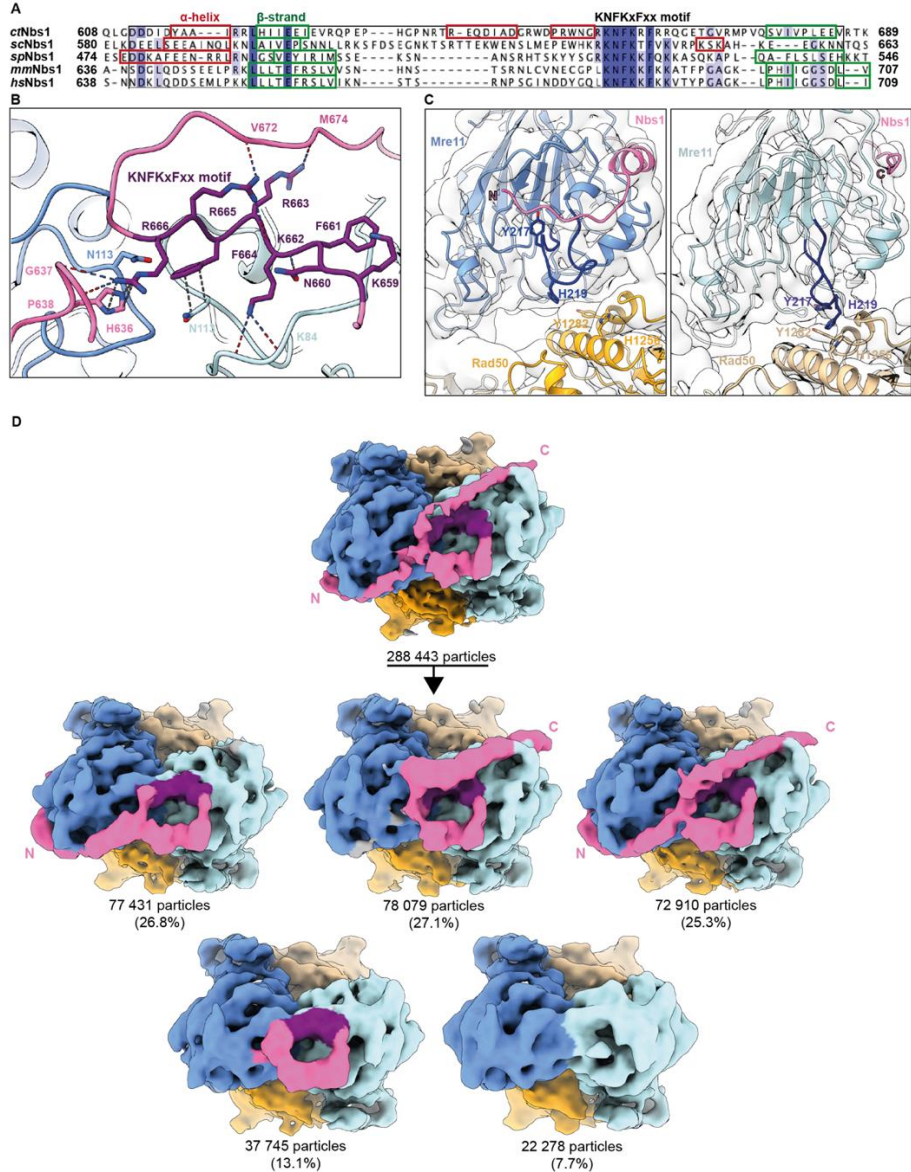


Figure S5: Structural characterization of Nbs1. (A): Sequence alignment of Nbs1 from different species. Conserved residues were highlighted in shades of blue, predicted α -helices were framed in red, predicted β -strands were framed in green. Alignments were calculated with Clustal Ω , secondary structure predictions with JPred4. **(B): Side view of the KNFKxFxx motif (purple) interactions with Mre11 (shades of blue).** **(C): Side-by-side comparison of N- and C-termini of resolved Nbs1 peptide interacting with Mre11.** Longer N-terminus of Nbs1 interacts with Mre11 loop containing Y217 and H219 residues affecting Mre11-Rad50 interaction at this site. **(D): Heterogeneity of Nbs1-Mre11/Rad50 interactions.** 3D classification revealed full interaction (25.3%), CD/N-terminal interaction (26.8%), CD/C-terminal interaction (27.1%), CD interaction (13%), no Nbs1 present (7.7%). Rad50 highlighted in shades of orange, Mre11 in shades of blue, Nbs1 in pink, KNFKxFxx motif in purple.

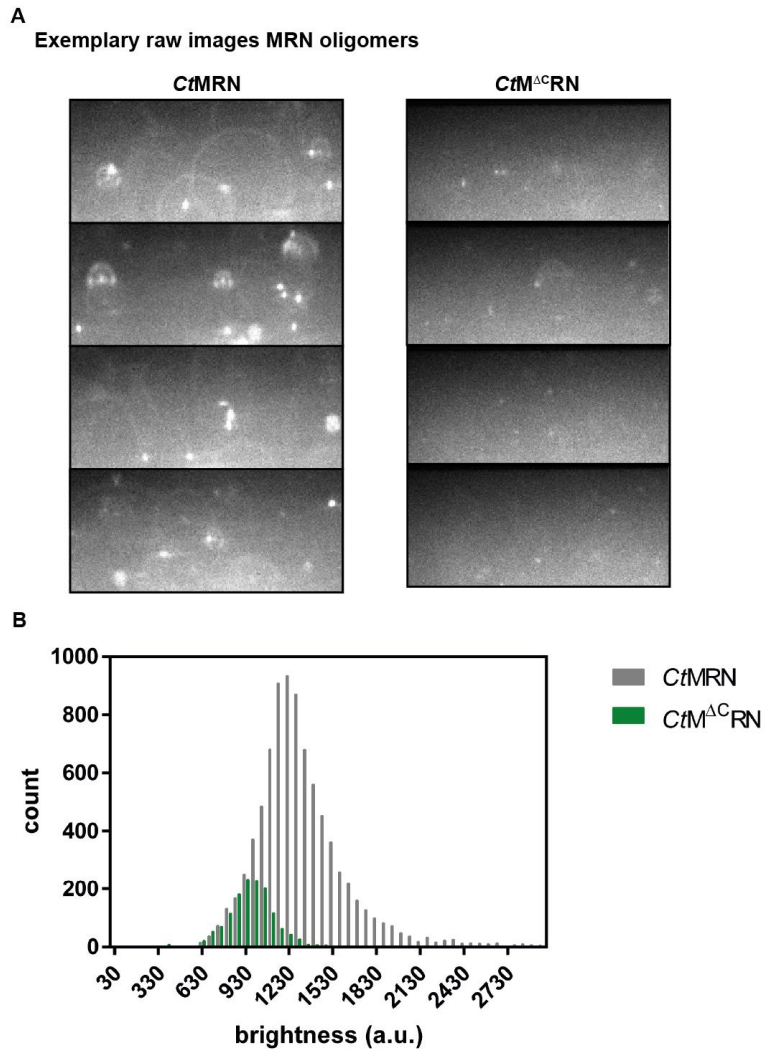


Figure S6: Quantification of CtMRN clustering. (A): Exemplary fluorescence images of CtMRN/ CtM^{ΔC}RN with FAM-labeled DNA. (B): Histogram of CtMRN-DNA and CtM^{ΔC} RN-DNA cluster formation. Fluorescence images were collected and clusters grouped based on their size.

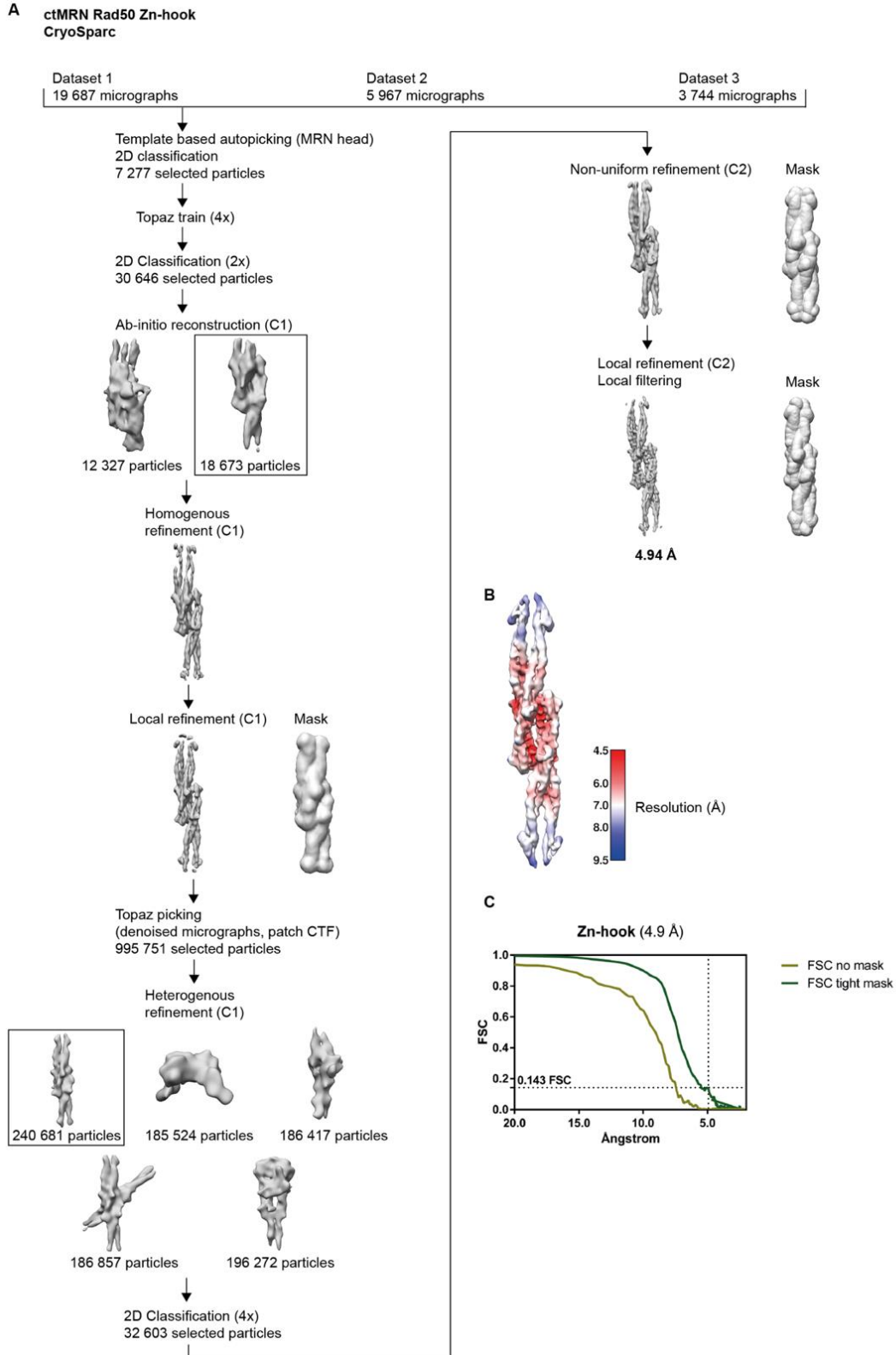


Figure S7: Processing schemes for the CtMRN zinc-hook map. (A): Cryo-EM processing scheme for the CtRad50 Zn-hook in CryoSPARC v3.2.0. (B): Local resolution estimation of the CtRad50 Zn-hook Cryo-EM map. (C): FSC curve of the Cryo-EM Zn-hook map (CryoSPARC v3.2.0).

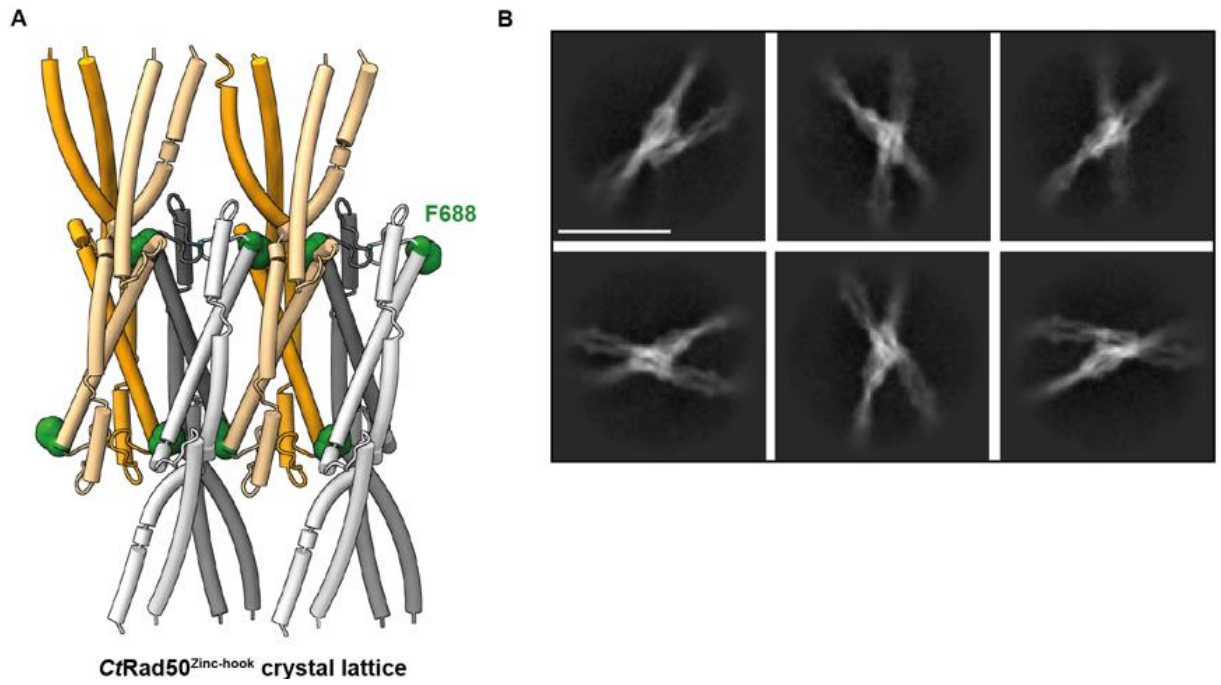


Figure S8: Higher order CtMRN zinc-hook structures. (A): Crystal lattice of *CtRad50*^{zinc-hook} with F688 residue hidden in the lattice arrangement. **(B):** 2D classes of *CtRad50* zinc hook octamers. Scale bar 10 nm.

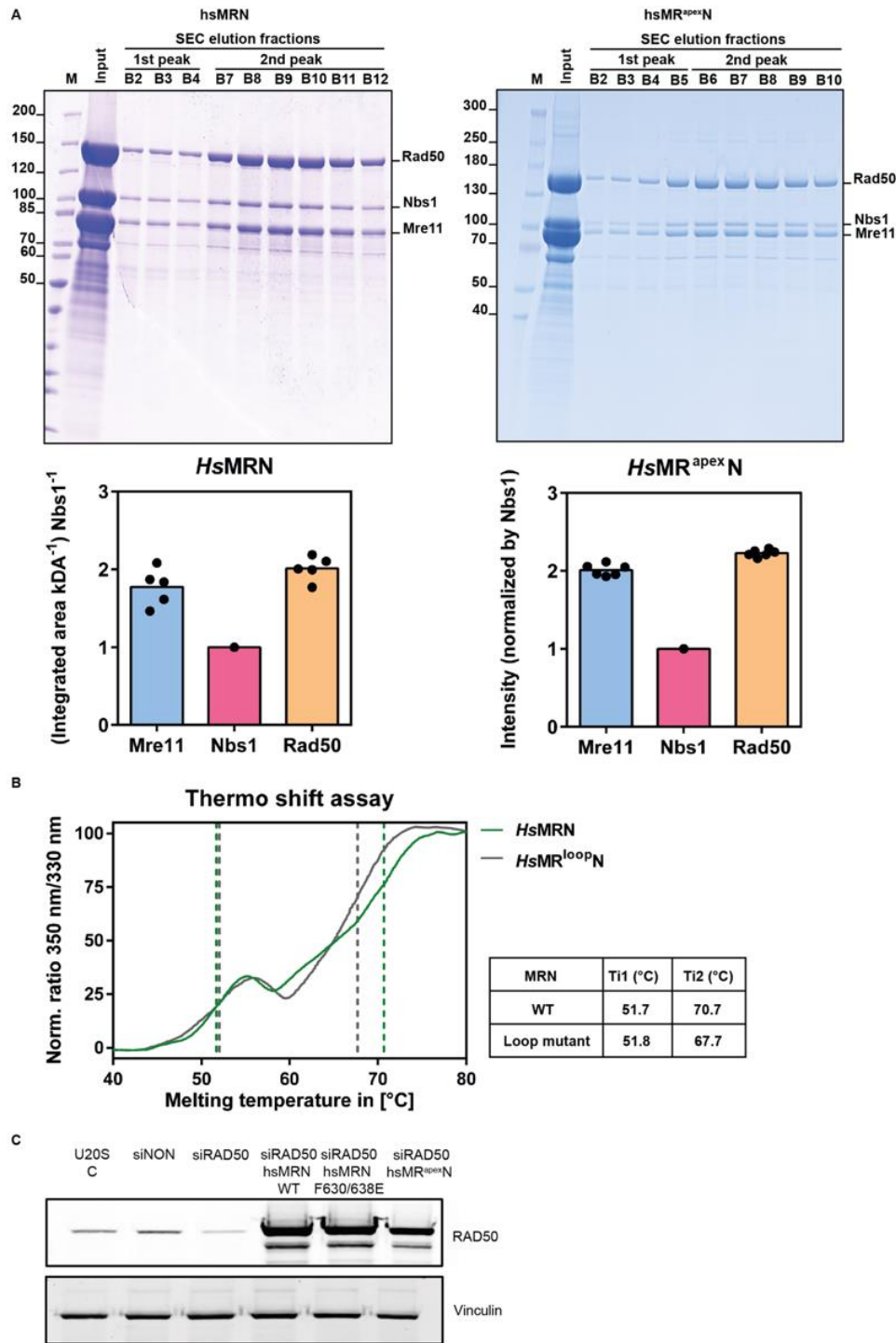


Figure S9: Quality assessment of purified *HsMRN* and *HsMR^{loopN}* complexes and siRNA knock-down of *HsRad50*. (A): Representative SDS-PAGE of purified *HsMRN* and *HsMR^{loopN}* complexes. Below, normalized gel quantification of complex stoichiometry (N = 5). (B): Microscale thermophoresis thermo-shift assay with purified *HsMRN* and *HsMR^{loopN}* complexes. Melting points are indicated. (C) Knock-down of Rad50 and overexpression of mutated *HsMRN* complex. Western blot stained with anti-Rad50 antibody and Vinculin loading control. U2OS C: untreated cells, siNON: non-targeting siRNA; siRad50: siRNA targeting Rad50; siRad50 *HsMRN* WT: siRNA targeting Rad50, transfection with codon-optimized WT *MRN* genes; siRad50 *HsMRN* F630/638E: siRNA targeting Rad50, transfection with codon-optimized mutant *MRN* genes; siRad50 *HsMR^{loopN}*: siRNA targeting Rad50, transfection with codon-optimized mutant *MRN* genes.

2.2. Molecular basis of human ATM kinase inhibition

Kristina Stakyte*, [Matthias Rotheneder](#)*, Katja Lammens*, Joseph D. Bartho*, Ulrich Grädler, Thomas Fuchß, Ulrich Pehl, Aaron Alt, Erik van de Logt, Karl-Peter Hopfner, **Molecular basis of human ATM kinase inhibition**, *Nature Structural and Molecular Biology*, Volume 28, October 2021, Pages 789-798

<https://doi.org/10.1038/s41594-021-00654-x>

* these authors contributed equally

Summary

In this publication we report high-resolution structures of human ATM kinase bound to inhibitors and ATP γ S. High-quality cryo-EM densities enabled us to build a near-complete atomic model that includes the more flexible N-terminal solenoid. Even though the overall dimer architecture is similar to previously published structures, our model is significantly better and allowed us to correctly assign the registry in the N-terminal region. We identified two previously uncharacterized zinc-binding sites that are not required for basal kinase activity but stabilize the overall fold and a loop that contains cancer mutations as well as an important auto-phosphorylation site. In accordance to previous structures, we observed different HEAT-repeat conformations that did change the kinase domain conformation. Mapping of cancer mutations indicated functionally important elements. The kinase domains of ATM bound to KU-55933, M4076 and ATP γ S was determined at 2.8 Å, 2.8 Å and 3.0 Å resolution, respectively. Access to the kinase active site was restricted by the PIKK regulatory domain (PRD) which confirm its autoinhibitory function. Our models set the molecular basis to understand why M4076 has increased affinity towards ATM compared to KU-55933. Comparing our structures with that of other PIKK kinase active sites enables us to identify non-conserved residues that interact with the inhibitors and to understand the molecular basis for the inhibitors' selectivity profile. Altogether, our structural data enables to design and improve ATM-specific inhibitors for cancer therapy

Author contributions

Kristina Stakyte, Matthias Rotheneder, Aaron Alt established expression and purification of the human ATM kinase. Together with Kristina Stakyte I purified ATM protein for cryo-EM and for assays. Erik van de Logt established the production of a CtIP fragment used as a substrate for ATM kinase assays. Kristina Stakyte, Matthias Rotheneder performed ATM kinase assays. Together with Kristina Stakyte I generated grids for cryo-EM data collection. All first authors were involved in the cryo-EM data collection and processing. Model building was performed by Kristina Stakyte, Matthias Rotheneder, Katja Lammens, Joseph D. Bartho, Karl-Peter Hopfner. Thomas Fuchß was principal inventor of M4076 at Merck KGaA, Darmstadt, Germany. Ulrich Grädler was involved in the structure-based design of M4076. Thomas Fuchß and Ulrich Pehl contributed biochemical assay and kinase selectivity results and graphs. All authors were involved in the data interpretation and manuscript preparation.



Molecular basis of human ATM kinase inhibition

K. Stakyte^{1,4}, M. Rotheneder^{1,4}, K. Lammens^{1,4}✉, J. D. Bartho^{1,4}, U. Grädler², T. Fuchß², U. Pehl², A. Alt^{1,3}, E. van de Logt¹ and K. P. Hopfner^{1,4}✉

Human checkpoint kinase ataxia telangiectasia-mutated (ATM) plays a key role in initiation of the DNA damage response following DNA double-strand breaks. ATM inhibition is a promising approach in cancer therapy, but, so far, detailed insights into the binding modes of known ATM inhibitors have been hampered due to the lack of high-resolution ATM structures. Using cryo-EM, we have determined the structure of human ATM to an overall resolution sufficient to build a near-complete atomic model and identify two hitherto unknown zinc-binding motifs. We determined the structure of the kinase domain bound to ATP γ S and to the ATM inhibitors KU-55933 and M4076 at 2.8 Å, 2.8 Å and 3.0 Å resolution, respectively. The mode of action and selectivity of the ATM inhibitors can be explained by structural comparison and provide a framework for structure-based drug design.

Cells rely on an efficient DNA damage response (DDR) to maintain genomic stability. Cancer cells, on the other hand, acquire defects in DDR genes to increase the genomic instability and mutation rate while ensuring cancer cell survival. The DDR comprises complex chains of events that result in the efficient repair of various types of DNA damage, including DNA double-strand breaks (DSBs)¹. DSBs are a hallmark of cancer and particularly harmful to the cell if left unrepaired. Initiation of the DDR leads to activation of checkpoint responses, cell-cycle arrest, recruitment of the DNA repair machinery and chromatin remodeling^{2–4}. Persistent DSBs and DDR trigger cellular senescence or apoptosis, thereby helping to remove potentially abnormal cells. However, misrepaired DSBs can result in gross chromosomal aberrations, aneuploidy or loss of genetic information and are linked to cancer development^{1,5–7}.

Ataxia telangiectasia-mutated (ATM) is a ~350-kDa Ser/Thr kinase that initiates a DDR following DSB formation. On activation, ATM phosphorylates a multitude of downstream transducers and effector proteins at SQ/TQ motifs. Target proteins include the DSB repair factor CtIP, histone variant H2AX, tumor suppressors BRCA1 and p53, and the checkpoint transducing kinase CHK2⁴. ATM belongs to a family of related surveillance kinases known as phosphatidylinositol 3-kinase-related protein kinases (PIKKs). Members of this kinase family also include ATR, the DNA-dependent protein kinase catalytic subunit (DNA-PKcs), mTOR, SMG1 and TRRAP^{8,9}. ATM, ATR and DNA-PKcs monitor the cell for DNA damage by sensing DSBs (ATM and DNA-PKcs) or single-stranded DNA (ssDNA; ATR). SMG1 triggers nonsense-mediated messenger RNA (mRNA) decay. TRRAP is involved in epigenetic control of transcription regulation, while mTOR is part of distinct complexes that regulate metabolism, translation and cell growth^{10–13}. PIKKs share a fairly conserved domain structure^{14–16}. The N-terminal parts of the polypeptide chains are generally composed of HEAT repeats and form 100–300-kDa α -solenoid structures, which are interaction modules for nucleic acids and/or protein cofactors¹⁷. The C-terminal region known as FATKIN contains the kinase (KIN) domain along with regulatory domains. The latter are denoted as FAT (FRAP, ATM and TRRAP) domain, PRD (PIKK regulatory domain) and FATC (C-terminal

part of the FAT domain). The FAT, PRD and FATC wrap around the kinase, regulating substrate recognition.

Cryo-EM provided the first structures of human ATM along with its fungal homologs at low to medium resolution^{16,18–21}. ATM resides in the cell as an autoinhibited dimer in all organisms studied. The FATKIN is tightly associated through a fairly hydrophobic interface and keeps the kinase domains side by side in an inactive state^{16,18–21}. The structure of human ATM at 4.7 Å showed how the PRD restricts kinase active site access by acting as a pseudo-substrate¹⁶. More highly resolved fungal Tel1 (ATM ortholog) structures showed details of the kinase active site^{19,21}. They also revealed that Tel1 can bind ATP and possesses a properly folded active site geometry, even in the absence of activating ligands^{19,21}. Current models of active site access postulate either ligand-induced conformational changes in the ATM dimer, or a dimer-to-monomer transition^{22–24}.

Although the DDR is important for genome integrity maintenance of healthy cells, it also helps cancer cells to cope with increasing amounts of replication and genotoxic stress, and to develop resistance against DNA-damaging chemo- and/or radiotherapy, thereby favoring tumor growth and survival²⁵. Consequently, targeting of proteins involved in the DDR has shown promising effects in cancer therapy^{26,27}. Owing to its prominent role in DDR signaling, ATM represents an auspicious target for drug development, predominately as an anticancer therapeutic. Inhibition of ATM increases the sensitivity of cancer cells to DNA-damaging agents and/or ionizing radiation^{28–31}. DSB repair is crucial for the survival of malignant tumor cells, especially under DNA-damaging conditions. Thus, the rationale for transient pharmacological ATM inhibition is to impair DSB repair and maintain the extent of unrepaired tumor DNA damage for several hours so as to drive tumor cells ultimately to cell death^{27,32,33}. Moreover, based on genetic and pharmacological evidence, inhibition of ATM kinase activity is considered to ameliorate mutant huntingtin (mHTT) toxicity as a potentially novel clinical intervention to treat Huntington's disease³⁴. ATM deficiency or reduced expression levels have been identified as a biomarker of sensitivity for selective poly adenosine diphosphate-ribose polymerase (PARP) or ATR inhibition in the treatment of solid tumors^{35–38}. ATM inhibitors in combination with ATR or PARP inhibitors induce synthetic lethality in proliferating cancer cell lines as a result of mitotic

¹Gene Center, Department of Biochemistry, Ludwig-Maximilians-Universität, Munich, Germany. ²Merck KGaA, Darmstadt, Germany. ³Present address: Proteros Biostructures GmbH, Martinsried, Germany. ⁴These authors contributed equally: K. Stakyte, M. Rotheneder, K. Lammens, J. D. Bartho. ✉e-mail: klammens@genzentrum.lmu.de; hopfner@genzentrum.lmu.de

replication stress and unrepaired DSBs³⁹. Initial high-affinity ATM inhibitors (KU-55933 and CP466722) were identified by compound library screens and served as lead structures for the development of compounds with improved pharmacokinetic properties (KU-60019 and KU-59403)^{28,29,40,41}. More recently, next generations of inhibitors (AZ31, AZ32, AZD0156 and AZD1390) with up to subnanomolar half-maximum inhibitory concentration (IC₅₀) potencies and suitable pharmacokinetic profiles were identified, demonstrating preclinical *in vivo* efficacy in rodent cancer models^{42–44}. Both ATM inhibitors, AZD0156 and AZD1390, had been selected to enter clinical trials either in combination with cytotoxic chemotherapy, as well as targeted anticancer agents such as the PARP1/2 inhibitor olaparib (Lynparza, AZD2281) for the treatment of solid tumors, or with radiotherapy in the treatment of brain cancers^{43–45}. M4076, a subnanomolar potent, ATP-competitive and orally bioavailable ATM inhibitor with excellent human kinase selectivity and physicochemical and pharmacokinetic properties was developed at Merck KGaA⁴⁶. Currently, M4076 is in a phase I clinical trial for the treatment of cancer (ClinicalTrials.gov ID NCT04882917)³¹.

Structure-based approaches are an important source of information for the optimization of selective inhibitors, and progress in the resolution capabilities of cryo-EM has opened up this technique to structure-based drug design⁴⁷. Despite the fact that several cryo-EM structures of eukaryotic ATM/Tel1 have been published, high-resolution structures of human ATM enabling structure-based drug design are not yet available^{16,18–21}. In this Article, we use cryo-EM to investigate the detailed binding modes of ATM-specific kinase inhibitors KU-55933 and M4076 comprising chemically diverse scaffolds. We present cryo-EM structures of human ATM in complex with KU-55933, M4076 and the non-hydrolysable ATP analog ATP γ S at resolution below 3 Å, permitting the distinct fitting of all three compounds. The protein structures provide a detailed view of the kinase domain and the active site conformation in its inhibited state, and clearly explain the distinct ATM kinase inhibition and selectivity profiles of KU-55933 and M4076 based on their binding modes. The quality of the maps allowed us to generate a near-complete atomic model of human ATM, including the more flexible spiral and pincer domains, where we identified two zinc-binding motifs.

Results

Near-complete atomic structure of human ATM. Human ATM was expressed in Expi293F cells and purified using FLAG affinity followed by anion exchange chromatography. Biochemical analysis indicates that the purified protein is an enzymatically active kinase that is capable of phosphorylating its natural substrate, the C-terminal fragment of human CtIP (Fig. 1a). Basal kinase activity was reduced in the presence of the widely used ATM inhibitor KU-55933 (Fig. 1a). To reduce protein flexibility within the kinase domain of human ATM, we incubated the protein sample with KU-55933 before cryo-EM grid preparation¹. Consistent with the published human ATM cryo-EM structure, which showed distinct dimeric states, we still observed conformational flexibility in the N-terminal α -solenoid domain, but, in contrast, did not observe conformationally 'open' C-terminal domains or monomers in the micrographs (Extended Data Fig. 1a and Supplementary Video 2)³. We reconstructed a full-length human ATM structure by using a 2.8-Å-resolution pincer-FATKIN map in combination with 3.0–3.3-Å maps for the spiral and pincer domains (Supplementary Figs. 1 and 2 and Table 1). The overall domain organization is illustrated in Fig. 1b. The quality of the map enabled us to build full side chain models for all secondary structural elements, along with large parts of the loop regions within the FATKIN and pincer domains. We also corrected the sequence assignments at the N-terminal 1,932 residues of earlier structures that were modeled based on lower-resolution maps (Fig. 1b, insets and Extended Data Fig. 1e)^{2,3}.

Intriguingly, analysis of the sequence and EM density revealed the presence of a zinc-binding motif in the pincer domain (Fig. 1b, top inset and Supplementary Video 1). This motif also validates a newly assigned registry. The zinc-binding site belongs to the classical Cys2 His2 motif zinc finger type and consists of residues H1876, H1895, C1899 and C1900 in a loop region at the C-terminal end of the pincer domain. The zinc-binding motif is pointing towards the spiral domain, which mediates the recruitment of DNA, binding partners such as NBS1 and substrates such as p53⁴⁵. The loop stabilized by this motif contains the important cancer mutation T1880R⁴⁸. Because all four zinc coordinating residues are only conserved in certain mammals, an essential, evolutionarily conserved role of this motif for kinase activity is not likely, but it could play an important function in mammalian-specific regulation and ligand or substrate recognition (Extended Data Fig. 1b)³⁴. Mutation of the two zinc coordinating cysteine residues did not diminish kinase activity (Extended Data Fig. 1c). However, addition of zinc-specific chelating agents decreased the thermal stability of the ATM (Extended Data Fig. 1d).

To model the N-terminal α -solenoid structure, this region of the density was processed independently by subtracting the density for the C-terminal domains and the other protomer of the dimer to create a map of the N terminus alone (Supplementary Fig. 2). This workflow permitted classification of the structural variation within the N terminus, resulting in a map with an overall resolution of 3.15 Å that allowed atomic modeling of the N terminus. The map displays defined side chain densities until the two most N-terminal helices and indicates a different sequence assignment than previously published (Fig. 1c). This area is of particular interest because the HEAT repeats are believed to provide an interaction hub for components of the DNA repair machinery, such as NBS1, and substrates like p53^{49,50}. In the center of the solenoid structure, the HEAT repeat pattern is broken where the loop (amino acids 549–570) between helices 24 and 25 extends to interact with the FATKIN domain loops (residues 2084–2092 and 2107–2123; Extended Data Fig. 2a,d). We note the direct contact between the N-terminal region of the α -solenoid and the FATKIN domain that was not observed in the previously published human ATM structures. However, the equivalent inter-domain interaction was observed in ctTel1¹⁹. After this FATKIN interacting loop, three short helices 25–28 break the HEAT repeat pattern in the center of the solenoid ring, followed by the 'plug' loop (residues 630–643) which bridges through the center of the solenoid (Extended Data Fig. 2c). This loop is tethered to the edge of the solenoid in a structure that may represent a second zinc-binding motif (Fig. 1c and Supplementary Video 1). The local resolution is insufficient to resolve all residues with confidence, but the density represents a turn-like structure bringing in close proximity two histidines (H635 and H636) with two cysteines (C633 and C790), with an additional density sufficient for a zinc atom. Helix 29 then sits on the opposite side of the solenoid, running nearly parallel to the junction between the N- and C-terminal sections of the solenoid structure, before loop 657–683 passes back across the bottom of the solenoid ring, connecting to helix 30 on the far outer side of the solenoid (Extended Data Fig. 2c). The solenoid then continues with regular HEAT repeats until the hinge region.

The functionally important Tel1/ATM N-terminal (TAN) motif (residues 15–27) and essential residues 91–97 form a continuous interaction site on the solenoid-facing side of the N terminus^{48,49}. The proline and hydrophobic residues within this interaction site are more probably conserved for their role in protein folding rather than for ligand interaction. P37 caps helix 3, while the hydrophobic residues form internal contacts between HEAT repeats. The long, unstructured loop (residues 825–879) interacts with R35 of helix 2, directly neighboring the TAN motif. This loop contains the cancer-associated mutation F858L and may be involved in signal transduction or ligand binding at the N terminus (Extended Data Fig. 3)⁴⁸.

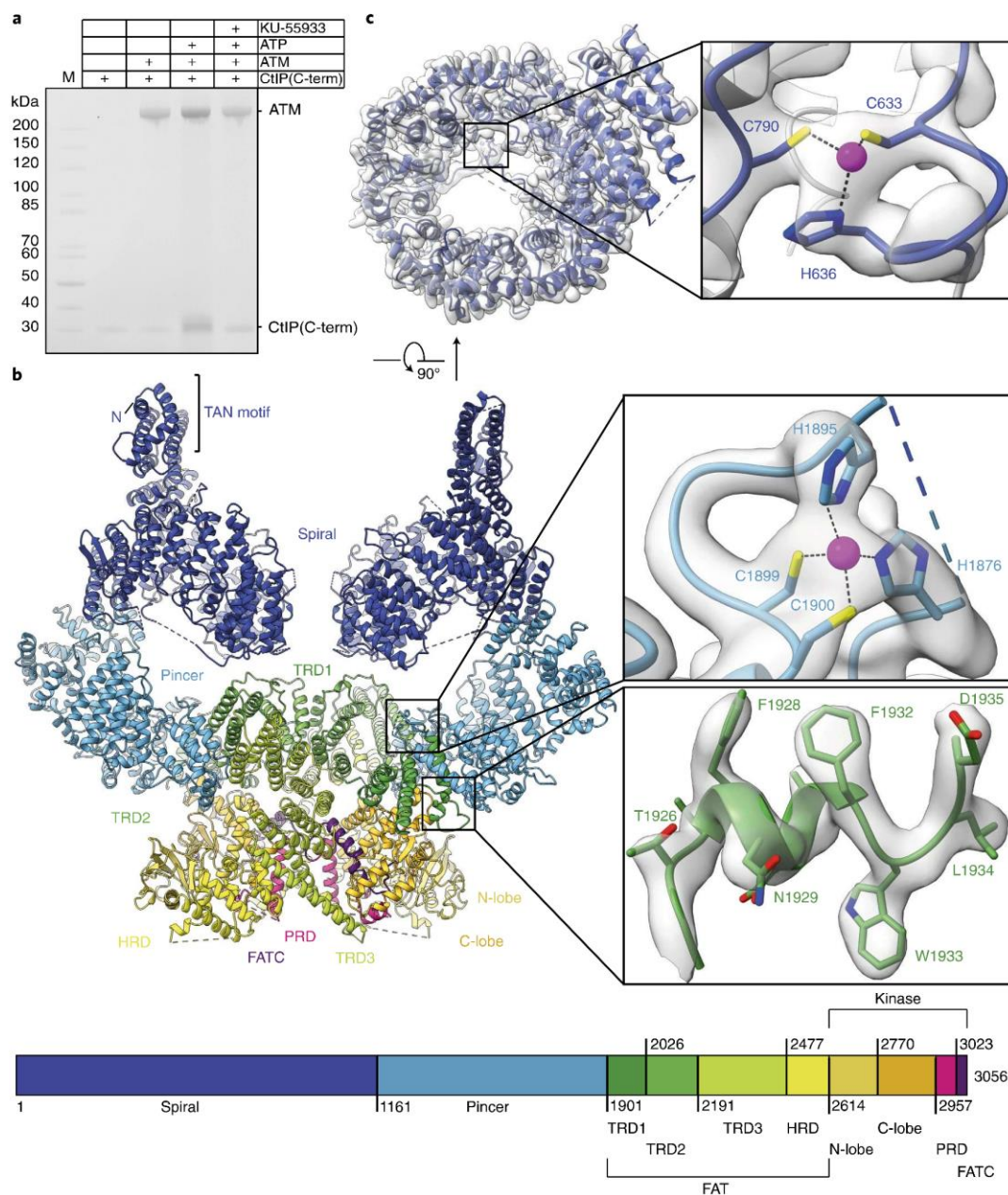


Fig. 1 | Cryo-EM structure and activity of dimeric human ATM. **a**, Inhibition of basal ATM kinase activity by KU-55933. Phosphorylation of human CtIP C terminus (650–897, phosphomimetic mutant T847E) visualized by phosphoprotein SDS-PAGE staining. The experiment was repeated twice with similar results. The uncropped gel image is available as source data. **b**, Model of KU-55933-bound human ATM. The structural domains are colored according to the schematic shown below the model. This domain color coding will be used throughout this Article. Top inset: pincer zinc-binding motif and map quality in the region. Bottom inset: map quality of the representative region (residues 1926–1935) in TRD1. **c**, Cryo-EM density map of the N-terminal spiral domain at 3.06 Å resolution (contoured at 0.017) with the fitted model in top view. Inset: spiral zinc-binding motif and map quality in the region.

To analyze the orientation of the region N-terminal to the FATKIN domain, we conducted focused three-dimensional (3D) classification on the spiral and pincer domain of all ATM particles (Supplementary Fig. 1). This indicated the presence of three different dimeric classes of ATM (Extended Data Fig. 1a and Supplementary Video 2). The main class, comprising 45% of the particles, belongs to a symmetrically related dimer with a small gap between the two opposing spiral domains, while 31% of the par-

ticles show a symmetrically related dimer with the spiral domains in close contact. Only 13% of the data resulted in one flexibly detached spiral domain. The best resolved N-terminal structure with closed spiral domains was refined to a final resolution of 3.41 Å. In addition to the spiral–FATKIN contact described above, we identified a second interface between the spiral domains of the two protomers. The N-terminal inter-domain contact was not seen in other human structures, in which the kinase and FAT domains were exclusively

Table 1 | Cryo-EM data collection and refinement statistics

	#1 ATM (kinase, KU- 55933-bound state) (EMD-12343)	#2 ATM (hinge/ pincer, KU- 55933-bound state) (EMD-12345)	#3 ATM (N-term. spiral/ pincer, KU- 55933-bound state) (EMD-12346)	#4 ATM (focused N-term. spiral, KU- 55933-bound state) (EMD-12347)	#5 ATM (composite map, KU-55933-bound state) (EMD-12351, PDB 7NI5)	#6 ATM (kinase, M4076-bound state) (EMD- 12350, PDB 7NI4)	#7 ATM (kinase, ATP γ S-bound state) (EMD-12352, PDB 7NI6)
Data collection and processing							
Magnification	130,000	130,000	130,000	130,000	130,000	130,000	130,000
Voltage (kV)	300	300	300	300	300	300	300
Electron exposure (e ⁻ / Å ²)	45	45	45	45	45	45	43
Defocus range (μm)	-1.0 to -2.8	-1.0 to -2.8	-1.0 to -2.8	-1.0 to -2.8	-1.0 to -2.8	-1.0 to -2.8	-1.0 to -2.8
Pixel size (Å)	1.059	1.059	1.059	1.059	1.059	1.059	1.059
Symmetry imposed	C1	C1	C1	C1	C1	C2	C1
Initial particle images (no.)	2,679,787	2,679,787	2,679,787	2,679,787	2,679,787	2,346,822	709,013
Final particle images (no.)	826,510	807,127	1,035,906	977,752			
Map resolution (Å)	2.78	3.34	3.10	3.15	Composite Map (#1-4)	3.03	2.78
FSC threshold	0.143	0.143	0.143	0.143		0.143	0.143
Map resolution range (Å)	2.49-8.52	3.14-5.61	2.93-4.71	2.91-4.27		2.57-9.75	2.62-9.75
Refinement							
Initial model used					PDB 6K9L	PDB 7NI5	PDB 7NI5
Model resolution (Å)					2.79	3.3	2.9
FSC threshold					0.5	0.5	0.5
Model resolution range (Å)					2.49-4.27	2.57-4.80	2.62-3.90
Map sharpening B factor (Å ²)					0 (LAFTER filtered)	0 (LAFTER filtered)	0 (LAFTER filtered)
Model composition							
Nonhydrogen atoms					45,052	23,236	23,079
Protein residues					5,581	2,864	2,847
Ligands					4 Zn, 2 KU-55933	2 Zn, 2 M4076	2 Zn, 2 Mg, 2 AGS
B factors (Å ²)					22.49/138.51/70.38	59.66/184.03/ 106.29	24.39/131.44/65.67
Protein					39.77/167.58/48.67	74.15/205.96/ 78.84	50.79/143.71/69.28
Ligand							
R.m.s. deviations					0.003	0.005	0.003
Bond lengths (Å)					0.500	0.859	0.467
Bond angles (°)							
Validation							
MolProbity score					1.42	1.35	1.15
Clashscore					4.88	6.07	3.60
Poor rotamers (%)					0.02	0.08	0.08
Ramachandran plot							
Favored (%)					97.06	97.95	98.04
Allowed (%)					2.94	2.05	1.96
Disallowed (%)					0.00	0.00	0.00

Different datasets are described.

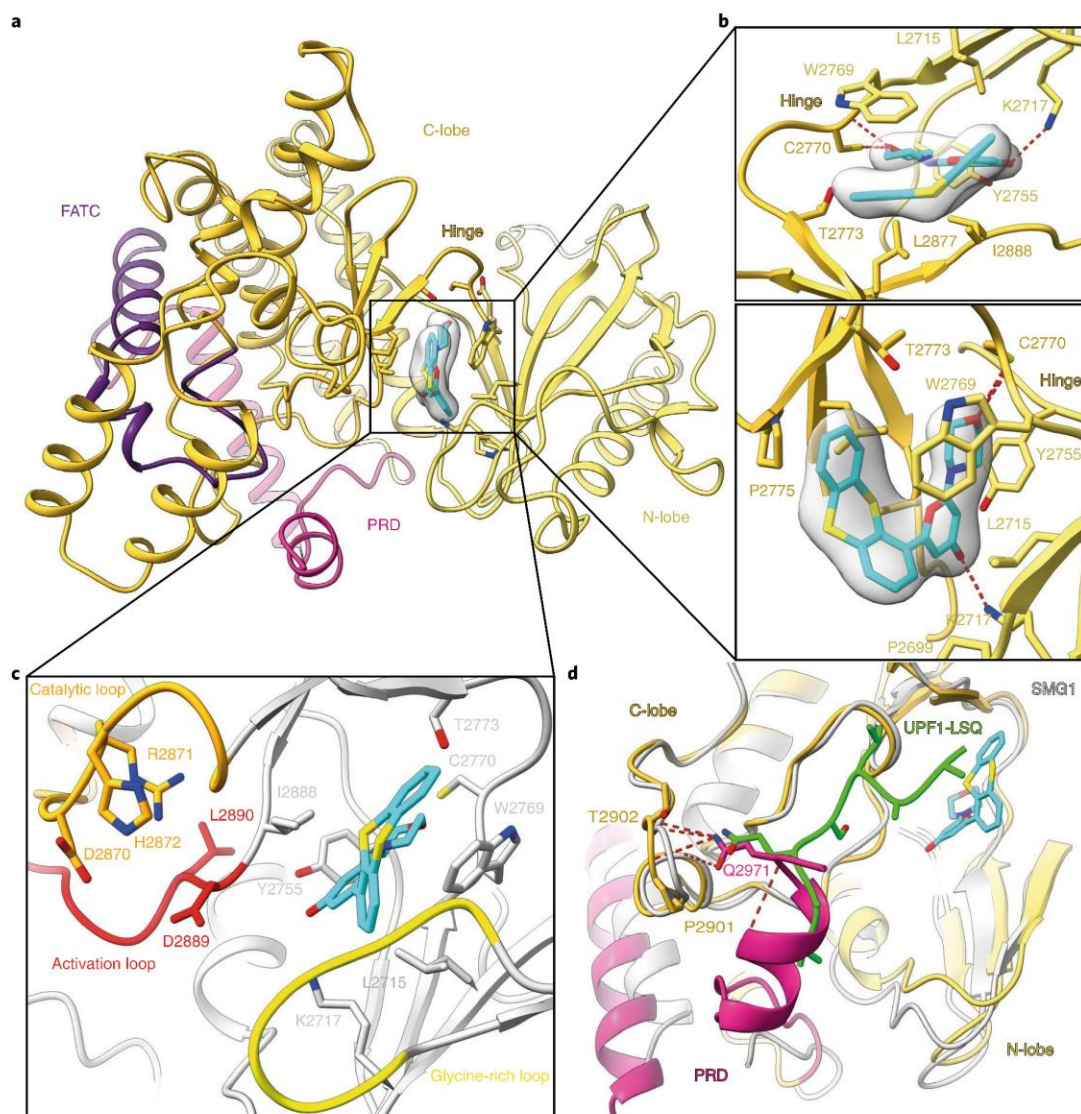


Fig. 2 | Human ATM active site conformation in the KU-55933 bound state. **a**, KU-55933 (cyan) in 2.8-Å density (contoured at 0.032) bound to the kinase active site. **b**, Detailed binding mode of KU-55933 inhibitor in side and top views. Side chains of inhibitor-proximal residues are shown. Interactions were calculated with ViewContacts and hydrogen bonds are indicated as red dotted lines⁵⁷. **c**, Conformations of the kinase catalytic loop (orange), activation loop (red) and glycine-rich loop (yellow) surrounding the bound inhibitor. **d**, Detailed view of the superimposed substrate-bound (UPF1 substrate in green) SMG1 (PDB ID 6Z3R; gray) and KU-55933-bound ATM (color) kinase domain. Substrate-mimicking Q2971 of PRD (magenta) and its hydrogen bonds (red dotted lines) to the kinase C-lobe residues T2902 and P2901 are indicated.

involved in dimerization²¹. This observation supports the assumption that the inhibitor-bound ATM structure is in a more stable dimeric state (Extended Data Fig. 1a,e). The resolution of the spiral-FATKIN interface loops does not permit unambiguous identification of the interacting residues, but the opposing loops carry charge complementarity, suggesting they may mediate salt bridge formation.

Cancer-associated human ATM mutations. The prevalence of mutations that result in ATM functional deficiency is generally below 5%, but is enhanced for colon adenocarcinoma (11%), cholangiocarcinoma (8.8%) and uterine corpus endometrial carcinoma (6.9%). Other mutations that do not compromise ATM kinase function represent the majority of ATM alterations. (The results

published here are in whole or part based upon data generated by the TCGA Research Network at <https://www.cancer.gov/tcga>.) We mapped the locations of common ATM mutations that were reported more than five times in the COSMIC database (Extended Data Fig. 3)⁵¹. Although mutations are distributed throughout the entire length of the protein, some mutations cluster in surface regions and may indicate important functional sites. For example, a highly conserved R23, frequently mutated to Q (count of 9), is located in the substrate-binding TAN motif. The very frequent F858L (count of 31) mutation maps to a loop that interacts with the TAN motif, supporting the functional role of this apical region in ATM signaling. R337C/H (count of 93), S707P and S333F (count of 9) mutations affect adjacent solvent-exposed loops of the spiral near the TAN motif, which may be an important interaction site.

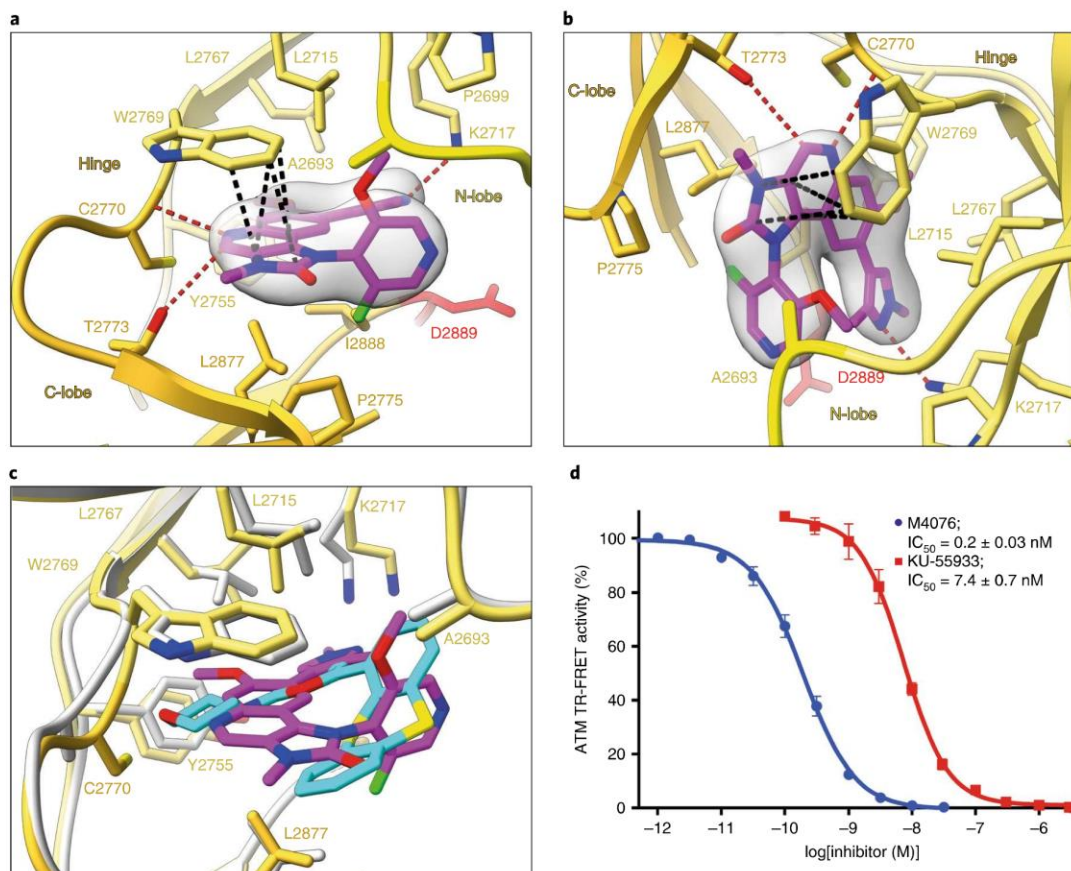


Fig. 3 | Human ATM active site conformation in the M4076-bound state. **a**, Detailed binding mode of the M4076 inhibitor at a resolution of 3.0 Å (contoured at 0.038). Side chains of inhibitor-proximal residues are shown. Interactions were calculated with ViewContacts⁵⁷. Hydrogen bonds are indicated by red dotted lines and π -stacking interactions are highlighted as black dotted lines. The kinase activation loop is shown in red. **b**, Same as in **a**, but as a side view. **c**, Superimposition of M4076 (magenta, colored model) and KU-55933 (cyan, gray model) bound ATM active sites. **d**, Dose-response curves of enzymatic ATM kinase inhibition by M4076 and KU-55933. Data represent the mean \pm s.e.m. from $n=15$ independent experiments performed in duplicate for M4076 ($IC_{50} = 0.20 \pm 0.03$ nM) and from one experiment performed in duplicate for KU-55933 ($IC_{50} = 7.4 \pm 0.7$ nM). Data for **d** are available as source data.

R337C/H was identified as a ‘hotspot’ cancer mutation common in colorectal cancer and associated with an ATM loss-of-function phenotype⁵². V410A (count of 20) forms an internal hydrophobic contact with I339 that may influence the stability of the spiral, or may lead to conformational changes. T1880R (count of 7) affects a loop stabilized by the pincer zinc-binding motif and thus could be a substrate/ligand interaction site. Q2442P (count of 7) and R2443Q (count of 21) are located in the helix of the TRD3 that contacts the PRD across a dimer interface. R3008H/C (count of 64) contributes to this interaction from the PRD side. This TRD3–PRD interaction would need to break to enable the conformational change into the open dimer, as reported by Baretic and colleagues¹⁶. It has been proposed that R3008H substitution impairs the conformational change of PRD-I required for substrate interactions with the catalytic loop⁵³. The following disease-associated mutations are located directly within the ATP-binding site: R2691C (count of 11), G2695S (count of 8), R2832C (count of 15), N2875S (count of 8), I2888T (count of 6) and L2890V (count of 7).

ATM active site and KU-55933 binding mode. The overall architecture of the FAT and kinase domains largely resembles the apoenzyme structure reported by Xiao et al. (Extended Data Fig. 4a,c)²²,

but the reduced structural flexibility of ATM due to inhibitor binding as compared with the apoenzyme structures allowed for model building of virtually all amino acid side chains in the active site (Extended Data Fig. 4d). Briefly, the catalytic cleft is formed by the N- and C-terminal lobes (N-lobe and C-lobe) which are connected via a hinge region (Fig. 2a). In general, the N-lobe of PIKKs is responsible for nucleotide binding and coordination, and contains the glycine-rich loop (P-loop). The C-lobe of ATM and related kinases includes the catalytic loop with the DRH residues (D2870, R2871, H2872) required for substrate phosphorylation. The catalytic loop is held in place by the activation loop, which contains a DLG motif composed of D2889, L2890 and G2891. This motif plays an important role in substrate recognition and Mg^{2+} coordination, and hence in the regulation of catalysis (Fig. 2c)²⁴. In the related kinases DNA-PK, mTOR, ATR and Mec1, the motif consists of DFG, DFN or DFD (see ‘Understanding of kinase inhibitor selectivity’ below). Recently, it was shown that the conserved phenylalanine residue is critical for autoinhibition and activation of Mec1⁵⁵. Mutation to leucine, the amino acid present in ATM and Tel1, leads to a constitutively active Mec1⁵⁵. Consequently, the F-to-L substitution in ATM/Tel1 may explain why no additional activator protein is needed for their basal phosphorylation activity. However, in the

Table 2 | Kinase selectivity of KU-55933 and M4076 inhibitors

Inhibitor	On-target	Primary downstream target		Kinase selectivity					
		ATM IC ₅₀ (nM) ^a	Cellular pCHK ^{Thr68} HCT116 IC ₅₀ (nM) ^b	DNA-PK IC ₅₀ (nM) ^a	mTOR IC ₅₀ (nM) ^c	ATR IC ₅₀ (nM) ^a	PI3K α IC ₅₀ (nM) ^a	PI3K β IC ₅₀ (nM) ^a	PI3K γ IC ₅₀ (nM) ^a
KU-55933	7.4	1,100 ^d	1,400	9,300 ^e	>100,000 ^a	2,000	1,900	14,000	1,500
M4076	0.2	10 ^f	600	>30,000 ^{c,g}	10,000 ^a	8,500 ^g	>30,000 ^g	>30,000 ^g	15,000 ^g

Shown are KU-55933 and M4076 biochemical IC₅₀ values against kinases ATM, DNA-PK, mTOR, ATR and PI3Ks and cellular IC₅₀ values for inhibition of bleomycin- or 2 Gy-induced phosphorylation of CHK2 (pThr68) in HCT116 cells. Source data for Table 2 are presented in Supplementary Data 1. ^aDetermined by time-resolved FRET assays with recombinant proteins. ^bIn vitro cell-based IC₅₀ for inhibition of bleomycin- or 2 Gy-induced phosphorylation of CHK2 (pThr68) in the human colon carcinoma cell line HCT116. ^cDetermined by enzymatic mTOR assay. ^dELISA, bleomycin-induced. ^eAs determined by Hicksson et al.⁴⁰. ^fLuminex assay, 2 Gy-induced (Methods). ^gIC₅₀ obtained for racemate of M4076.

KU-55933 complex structure, the PRD blocks active site access, as seen in other ATM/Tell structures, confirming the autoinhibitory function of the ATM PRD domain in the inhibitor-bound form^{19,21}. The PRD is firmly locked in position by interactions with the activation loop of the kinase via hydrogen-bond interactions of Q2971 with the backbone oxygens of P2901 and T2902 and hydrophobic contacts of L2970 (Fig. 2d). Superimposition with the substrate-bound SMG1-8-9 kinase UPF-1 complex structure shows that residue Q2971 occupies the substrate glutamine binding site of the kinase, thus mimicking the glutamine in the substrate SQ/TQ selectivity motifs and precluding substrate access to the catalytic center (Fig. 2d)^{19,21,56}. Sequence alignment of the PRD region indicates that the substrate-mimicking inhibitory mechanism is conserved among most ATM orthologs (Extended Data Fig. 4b). Combined structural and sequence analysis of the human ATM C terminus with other human PIKKs suggests that DNA-PK may use a similar substrate-mimicking mechanism. However, the map quality of the other kinases, as well as the low level of sequence conservation in this region, precludes more definitive statements regarding a conserved PRD inhibition mechanism for other PIKK family members (Extended Data Fig. 4b).

A more detailed comparison of the KU-55933-bound and apoenzyme structures reveals that the ATM kinase N-lobe is shifted outwards to accommodate the inhibitor (Extended Data Fig. 4c). KU-55933 is well ordered, which facilitates fitting of the small-molecule inhibitor and all interacting residues within this area (Fig. 2b and Extended Data Fig. 4d). The chemical description of the inhibitor is shown in Extended Data Fig. 4e. KU-55933 forms two distinct hydrogen bonds via the morpholine O atom with C2770 of the hinge region and via the pyran-4-one carbonyl O atom with the catalytically important residue K2717 in the N-lobe (Fig. 2b,c). The non-planar thianthrene ring is involved in extensive van der Waals (vdW) contacts with residues P2699 in the P-loop, L2715, L2767, W2769 in the N-lobe, P2775, L2877 and I2888 in the C-lobe and activation loop, respectively (Extended Data Fig. 4f). We next examined the binding and inhibitory mechanism of a second inhibitor, M4076, with a chemically distinct scaffold to KU-55933.

Towards a more selective and potent ATM inhibitor. KU-55933 is a potent ATM inhibitor (IC₅₀=7.4 nM) with selectivity towards ATR, mTOR (IC₅₀ values above 10 μ M) and other kinases, but with residual micromolar potencies on DNA-PK (IC₅₀=1.4 μ M), phosphoinositide 3-kinase (PIK3) isoforms α , β and δ (IC₅₀ values ~2 μ M) and PI3K γ (IC₅₀=14 μ M) corresponding to IC₅₀ splits above 180-fold towards ATM (Fig. 3d, Table 2 and Extended Data Figs. 5d and 6f)⁴⁰. The ATM inhibitor M4076 is a result of advanced optimization efforts that led to the identification of a candidate drug being evaluated in a phase I trial³¹. In comparison to KU-55933, M4076 is a potent, subnanomolar ATM kinase inhibitor (IC₅₀=0.2 nM) with strong enzymatic selectivity against ATM's close kinase family members, that is, ~3,000-fold selectivity towards DNA-PK (IC₅₀=600 nM) and more than 40,000-fold selectivity towards

ATR, mTOR and PIK3 isoforms α , β , γ and δ (IC₅₀ values above 8.5 μ M) (Fig. 3d, Table 2 and Extended Data Figs. 5d and 6c–e). Broader kinase profiling of M4076 revealed a strong overall human kinome selectivity. In a panel of 583 human kinases, no interaction had been observed below an IC₅₀ of ~700-fold compared to the on-target enzymatic ATM IC₅₀ of 0.2 nM for M4076 (Extended Data Fig. 6g,h and Supplementary Notes)^{42,43}. M4076 also showed low nanomolar cellular inhibition of checkpoint kinase 2 (CHK2) Thr68 phosphorylation in HCT116 cells (IC₅₀=10 nM) as the primary downstream target of ATM, while KU-55933 was only weakly potent (IC₅₀=1,100 nM) in this readout (Extended Data Fig. 6a,b).

To understand the enhanced biochemical ATM potency of M4076, we determined the cryo-EM structure of human ATM in complex with M4076 to 3.0 Å resolution in the kinase domain (Fig. 3a,b and Extended Data Fig. 5c). Before solving the structure, the inhibitory effect on the purified human ATM sample was verified by a CtIP kinase assay (Extended Data Fig. 5a). The EM density allowed clear binding mode assignment of the inhibitor in the ATM active site cleft. The chemical description of the inhibitor is provided in Extended Data Fig. 5b. The 1,3-dihydro-imidazo[4,5-c]quinolin-2-one moiety binds towards the hinge region, indicating a classical hydrogen bond between the N5 atom and C2770, as well as non-classical hydrogen bonds of the 4-CH group to C2770 and T2773 (Fig. 3a,b). Remarkably, the imidazolone ring forms extensive π - π and amide- π stacking interactions towards the W2769 side chain of the hinge region (Fig. 3a,b), as calculated from the atomic coordinates by the software tool ViewContacts⁵⁷. The 7-methoxy group attached to the quinoline ring interacts with the gatekeeper residue L2767 and with L2715 via vdW contacts (Extended Data Fig. 5c). The M4076 1,3-dimethyl-1H-pyrazole substituent is in vdW contact with I2888 next to the DLG motif of the activation loop and in hydrogen bond distance to K2717 via the unsubstituted N atom. Cryo-EM density fitting of the 3-fluoro-5-methoxypyridine ring was based on the S_a atropisomeric configuration of this moiety identified by small-molecule X-ray crystallography of M4076⁴⁶. In this orientation, the 3-fluoro-5-methoxypyridine ring indicates vdW contacts of the fluorine atom with P2775 and L2877 on one side and of the methoxy group towards W2769 and A2693 on the other side (Extended Data Fig. 5c).

Understanding of kinase inhibitor selectivity. To understand the inhibitory mechanism and to compare the inhibited structure with the catalytic states of ATM, we also determined the cryo-EM structure of human ATM bound to the non-hydrolysable ATP analog ATP γ S to a resolution of 2.8 Å (Extended Data Fig. 7c,d,h). Structural superimposition of all three human ATM structures in complex with compounds KU-55933, M4076 and ATP γ S indicate a similar overall ATM conformation, including N-terminal domains, and an almost identical active site cleft geometry (Supplementary Video 3 and Extended Data Figs. 7 and 8). However, one major conformational difference involves residue C2770 of the hinge region, which is shifted by 1.2 Å based on α C-atom distance

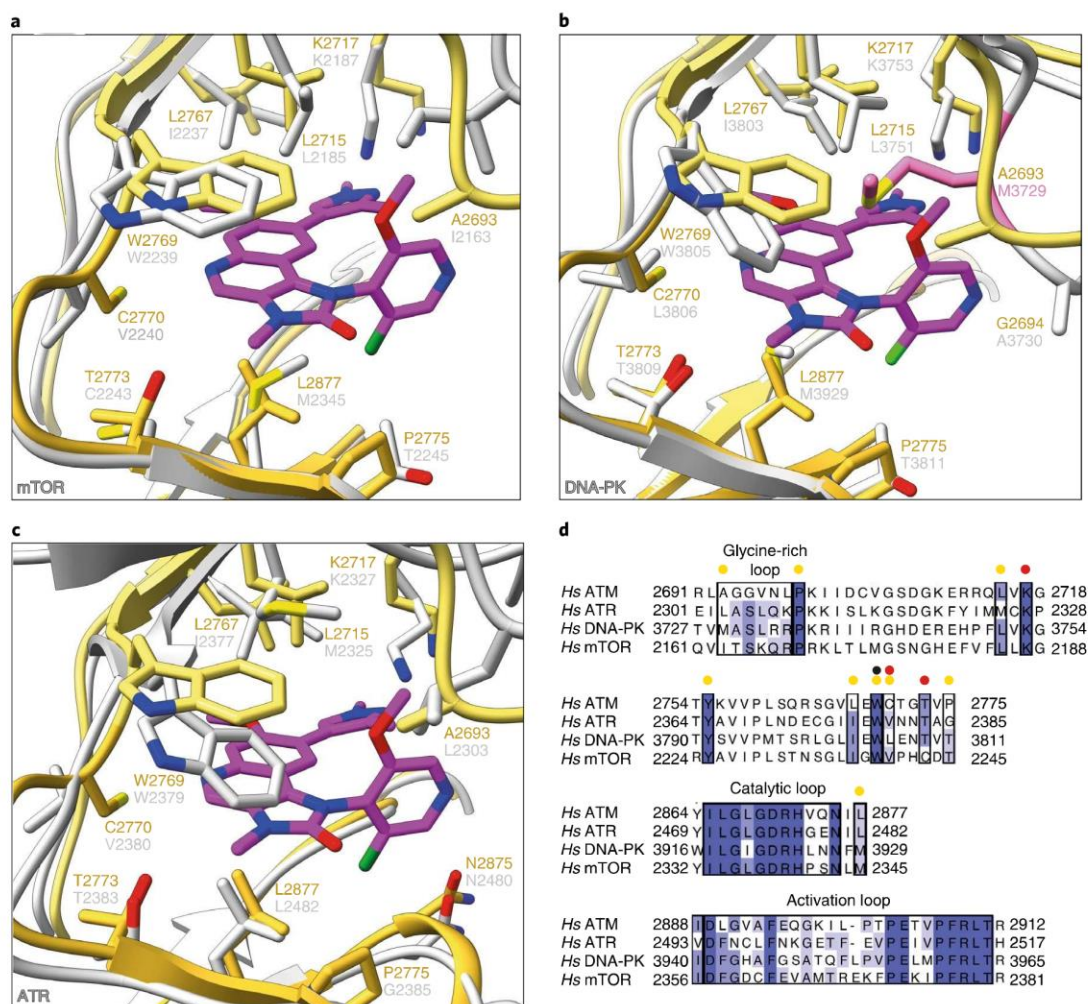


Fig. 4 | Specificity of the inhibitor M4076 towards human ATM kinase over other PI3Ks. a, Superimposition of the M4076-bound human ATM active site (color) and apo human mTOR (PDB 4J5N; gray). Residues surrounding the inhibitor are labeled accordingly. **b**, Same as in **a** but with apo DNA-PK (PDB 6ZFP; gray). DNA-PK M3729 is shown in pink. **c**, Same as in **a** but with apo ATR (PDB 5YZO; gray). **d**, Sequence alignment of the human (Hs) ATM, ATR, DNA-PK and mTOR active sites, colored by conservation. Glycine-rich, catalytic and activation loops are labeled. ATM residues forming hydrogen interactions with the inhibitor are marked with red circles, vdW interactions with yellow circles and π -stacking interactions with a black circle.

and 2.2 Å based on the S-atom distance towards the nucleotide binding site in the M4076 and ATP γ S structures. This shift is induced by hydrogen bond formation between the C2770 backbone amide NH donor and the 1,3-dihydro-imidazo[4,5-*c*]quinolin-2-one N5 atom of M4076 or with the ATP γ S N1 atom, respectively (Fig. 3a and Extended Data Fig. 7c,e,g). Furthermore, the 1,3-dihydro-imidazo[4,5-*c*]quinolin-2-one ring of M4076 overlaps well with the position of the purine ring in the ATP γ S structure, creating additional aromatic stacking interactions to the adjacent W2769. The induced fit observed for C2770 together with π - π and amide- π stacking interactions towards the hinge tryptophane might explain the ~35-fold improved biochemical ATM potency as well as the improved selectivity of M4076 towards DNA-PK compared with KU-55933 (Extended Data Fig. 5d). Thus, M4076 perfectly mimics the ATP γ S-bound pre-catalysis state of human ATM. Moreover, M4076 adopts additional vdW contacts to the C-lobe and the glycine-rich loop via both the 1,3-dimethyl-1*H*-pyrazole and 3-fluoro-5-methoxy-pyridine substituents, respectively. Another structural difference exclusively seen in the M4076-bound protein structure is an altered side

chain rotamer of residue L2767 to accommodate the 7-methoxy substituent (Fig. 3c).

Structural analysis together with sequence alignment revealed several residues involved in M4076 binding interactions, which are not conserved within the structurally most related kinases ATR, mTOR, DNA-PK and PI3K isoforms: A2693, L2715, L2767, C2770, T2773, P2775 and L2877 (Fig. 4a–d and Extended Data Fig. 6i). The superimposition of ATM cryo-EM structures in complex with KU-55933 and M4076 shows overall similar conformations of these non-conserved residues with few exceptions, including L2767 and C2770 (Fig. 3c). Structural comparison of the M4076-bound ATM with the apo-enzyme structures of mTOR, DNA-PK and ATR uncover a rational basis to understand the high selectivity of this inhibitor (Fig. 4a–c). These overlays highlight an important role of the M4076-specific 5-methoxy-pyridine group in selectivity, which is in vdW contact with A2693 in ATM⁵⁸. This alanine is replaced by the bulkier residues isoleucine, methionine and leucine in mTOR, DNA-PK/PI3Ks and ATR, respectively (Fig. 4a–d and Extended Data Fig. 6i). These larger amino acids might sterically hinder the scaffold of M4076 to obtain an optimal binding position towards

π - π stacking interactions with W2769 as well as hydrogen-bond interactions with C2770 in the hinge region. Sequence variations impairing optimal hinge-binding interactions are also in line with the observed M4076 selectivity against PI3K isoforms, because both W2769 and C2770 are replaced by valines (PIK3 α , β and δ) or isoleucine (PIK3 γ) and valine, respectively. Additional contributions towards DNA-PK, mTOR and ATR selectivity might be due to second shell residues in ATM (I2701, R2713 and T2771) influencing W2769 side chain flexibility, which are different in DNA-PK (R3737, P3749, E3807), mTOR (K2171, V2183, P2241) and ATR (K2311, I2323, N2381). Finally, residue L2877 below the inhibitor in the C-lobe region is in vdW contact with the imidazolone ring of M4076. This leucine is conserved in ATR but replaced with methionine in DNA-PK, mTOR and PI3Ks, leaving less space for the inhibitor in these kinases.

Discussion

As a key regulator, nuclear ATM kinase orchestrates cellular responses to DNA DSBs. Inhibition of ATM activity sensitizes different tumors to DNA DSB-inducing cancer treatments, such as chemo- and radiotherapy as well as targeted therapies (PARP or ATR inhibition), thereby impeding the ability of cancer cells to evade anticancer therapies^{25,32,35,37,59}. A compelling medical need thus exists for the development of ATM inhibitors for anticancer therapies, prompting us to focus on structural studies of ATM. We provide three cryo-EM structures of the human ATM kinase with bound inhibitors and ATP γ S. These structures reveal modes of action of small-molecule inhibition of ATM in therapeutic approaches, but also details of kinase active site autoinhibition, as well as an internal pseudo-substrate glutamine in human ATM. The increased conformational rigidity in the inhibited state allowed for atomic modeling of the nearly complete ATM protein. Careful evaluation of the spiral and pincer domain conformations of the KU-55933 inhibitor-bound ATM structure resulted in a cryo-EM density that allowed for a thorough model building of the entire solenoid region. This revealed—unexpectedly—two zinc-binding motifs in the spiral and pincer domains, respectively. These motifs are partially conserved in mammals and appear to either stabilize ATM or be involved in the interaction with other binding partners and/or DNA. Recently, a related zinc-finger motif was discovered in the N-terminal HEAT domain of Mec1^{ATR} checkpoint kinase, which is involved in stabilization of the interface area with the Mec1^{ATR} integral partner Ddc2^{ATRIP} (ref. 55). In all three structures, the PRD blocks the active site access, confirming the autoinhibitory function of this domain^{19,21}. Thereby, the PRD gatekeeper helix is locked in its position by interaction of Q2971 with the activation loop. Overall, the active site cleft geometry of the presented ATM structures is nearly identical except for the hinge region residue C2770 and minor changes in the glycine-rich loop (P-loop) region (Extended Data Fig. 7 and Supplementary Video 3). Together, structures with the bound small-molecule inhibitors uncover the binding mechanisms of two different ATM inhibitor classes and provide further insights into the understanding of their selectivity profiles.

High-resolution ATM structures were not available at the time of discovery of the ATM inhibitor M4076, detailed insights into the binding modalities as well as selectivity determinants towards closely related kinases remained hypothetical³¹. The presented high-resolution cryo-EM structure of ATM now allows detailed insights into the binding mode of M4076. In this regard, we identified extensive π - π and amide- π stacking interactions between the central 1,3-dihydro-imidazo[4,5-*c*]quinolin-2-one scaffold of M4076 towards W2769 in the hinge region of ATM, which are not present in the complex with KU-55933 (Fig. 3a–c). A second major difference between the ATM structures of both inhibitors is the position of C2770, also in the hinge region, which is shifted

towards the 1,3-dihydro-imidazo[4,5-*c*]quinolin-2-one moiety of M4076 with respect to the morpholine ring of KU-55933 (Fig. 3c and Supplementary Video 3). The same shifted position of C2770 was observed in the ATM structure with ATP γ S, which is considered to correspond to the pre-catalytic state of ATM (Extended Data Fig. 7g). In comparison to KU-55933, M4076 forms additional vdW contacts within the ATP site via its 7-methoxy group as well as with the 3-fluoro-5-methoxypyridine substituent. Together, these additional contacts explain the ~35-fold stronger enzymatic ATM potency of M4076 compared to KU-55933. The enhanced ATM inhibitory potency of M4076 observed in vitro translates well into the in cellulo inhibition of CHK2 phosphorylation at low nanomolar concentrations in HCT116 cells. We note that this inhibitory effect on cellular CHK2 phosphorylation is ~100-fold increased with M4076 compared with KU-55933. Additionally, we identified several non-conserved ATM residues involved in M4076 binding interactions by structural comparison with the DNA-PK, mTOR, ATR and PI3K isoforms. These sequence differences include residues in direct contact with M4076, such as A2693, and in the case of PI3K isoforms also W2769 and C2770. Further sequence differences involve residues in the second shell around W2769, thereby affecting its side chain flexibility to adopt optimal π -stacking interactions with the inhibitor (Fig. 4d and Extended Data Fig. 6i). In this respect, the substitution of A2693 in ATM by bulkier residues in DNA-PK, mTOR, ATR and PI3Ks is considered to be a crucial factor that explains the observed selectivity profile of M4076 towards these closely related kinase family proteins (Table 2).

Taken together, our atomic models of human ATM provide a framework for the evaluation and development of highly specific and potent therapeutics, as well as analyzing the central role and function of human ATM in healthy and cancerogenic cells through structure-informed approaches.

Online content

Any methods, additional references, Nature Research reporting summaries, source data, extended data, supplementary information, acknowledgements, peer review information; details of author contributions and competing interests; and statements of data and code availability are available at <https://doi.org/10.1038/s41594-021-00654-x>.

Received: 3 February 2021; Accepted: 30 July 2021;

Published online: 23 September 2021

References

- Hoeijmakers, J. H. Genome maintenance mechanisms for preventing cancer. *Nature* **411**, 366–374 (2001).
- Matsuoka, S. et al. ATM and ATR substrate analysis reveals extensive protein networks responsive to DNA damage. *Science* **316**, 1160–1166 (2007).
- Bartek, J. & Lukas, J. Chk1 and Chk2 kinases in checkpoint control and cancer. *Cancer Cell* **3**, 421–429 (2003).
- Burma, S., Chen, B. P., Murphy, M., Kurimasa, A. & Chen, D. J. ATM phosphorylates histone H2AX in response to DNA double-strand breaks. *J. Biol. Chem.* **276**, 42462–42467 (2001).
- Roos, W. P. & Kaina, B. DNA damage-induced cell death: from specific DNA lesions to the DNA damage response and apoptosis. *Cancer Lett.* **332**, 237–248 (2013).
- Mills, K. D., Ferguson, D. O. & Alt, F. W. The role of DNA breaks in genomic instability and tumorigenesis. *Immunol. Rev.* **194**, 77–95 (2003).
- Kastan, M. B. & Bartek, J. Cell-cycle checkpoints and cancer. *Nature* **432**, 316–323 (2004).
- Lovejoy, C. A. & Cortez, D. Common mechanisms of PIKK regulation. *DNA Repair (Amst.)* **8**, 1004–1008 (2009).
- Keith, C. T. & Schreiber, S. L. PIK-related kinases: DNA repair, recombination and cell cycle checkpoints. *Science* **270**, 50–51 (1995).
- Shiloh, Y. & Ziv, Y. The ATM protein kinase: regulating the cellular response to genotoxic stress, and more. *Nat. Rev. Mol. Cell Biol.* **14**, 197–210 (2013).
- Zou, L. & Elledge, S. J. Sensing DNA damage through ATRIP recognition of RPA–ssDNA complexes. *Science* **300**, 1542–1548 (2003).

12. Yamashita, A., Ohnishi, T., Kashima, I., Taya, Y. & Ohno, S. Human SMG-1, a novel phosphatidylinositol 3-kinase-related protein kinase, associates with components of the mRNA surveillance complex and is involved in the regulation of nonsense-mediated mRNA decay. *Genes Dev.* **15**, 2215–2228 (2001).
13. McMahon, S. B., Van Buskirk, H. A., Dugan, K. A., Copeland, T. D. & Cole, M. D. The novel ATM-related protein TRRAP is an essential cofactor for the c-Myc and E2F oncoproteins. *Cell* **94**, 363–374 (1998).
14. Yang, H. et al. mTOR kinase structure, mechanism and regulation. *Nature* **497**, 217–223 (2013).
15. Imseng, S., Aylett, C. H. & Maier, T. Architecture and activation of phosphatidylinositol 3-kinase related kinases. *Curr. Opin. Struct. Biol.* **49**, 177–189 (2018).
16. Baretic, D. et al. Structures of closed and open conformations of dimeric human ATM. *Sci. Adv.* **3**, e1700933 (2017).
17. Baretic, D. & Williams, R. L. PIKKs—the solenoid nest where partners and kinases meet. *Curr. Opin. Struct. Biol.* **29**, 134–142 (2014).
18. Sawicka, M. et al. The dimeric architecture of checkpoint kinases Mec1ATR and Tel1ATM reveal a common structural organization. *J. Biol. Chem.* **291**, 13436–13447 (2016).
19. Jansma, M. et al. Near-complete structure and model of Tel1ATM from *Chaetomium thermophilum* reveals a robust autoinhibited ATP state. *Structure* **28**, 83–95 (2020).
20. Xin, J. et al. Structural basis of allosteric regulation of Tel1/ATM kinase. *Cell Res.* **29**, 655–665 (2019).
21. Yates, L. A. et al. Cryo-EM structure of nucleotide-bound Tel1(ATM) unravels the molecular basis of inhibition and structural rationale for disease-associated mutations. *Structure* **28**, 96–104 (2020).
22. Xiao, J. et al. Structural insights into the activation of ATM kinase. *Cell Res.* **29**, 683–685 (2019).
23. Bakkenist, C. J. & Kastan, M. B. DNA damage activates ATM through intermolecular autophosphorylation and dimer dissociation. *Nature* **421**, 499–506 (2003).
24. Guo, Z., Kozlov, S., Lavin, M. F., Person, M. D. & Paull, T. T. ATM activation by oxidative stress. *Science* **330**, 517–521 (2010).
25. Lavin, M. F. & Yeo, A. J. Clinical potential of ATM inhibitors. *Mutat. Res.* **821**, 111695 (2020).
26. Jin, M. H. & Oh, D. Y. ATM in DNA repair in cancer. *Pharmacol. Ther.* **203**, 107391 (2019).
27. Weber, A. M. & Ryan, A. J. ATM and ATR as therapeutic targets in cancer. *Pharmacol. Ther.* **149**, 124–138 (2015).
28. Rainey, M. D., Charlton, M. E., Stanton, R. V. & Kastan, M. B. Transient inhibition of ATM kinase is sufficient to enhance cellular sensitivity to ionizing radiation. *Cancer Res.* **68**, 7466–7474 (2008).
29. Batey, M. A. et al. Preclinical evaluation of a novel ATM inhibitor, KU59403, in vitro and in vivo in p53 functional and dysfunctional models of human cancer. *Mol. Cancer Ther.* **12**, 959–967 (2013).
30. Riches, L. C. et al. Pharmacology of the ATM inhibitor AZD0156: potentiation of irradiation and olaparib responses preclinically. *Mol. Cancer Ther.* **19**, 13–25 (2020).
31. Fuchss, T. et al. Abstract 3500: highly potent and selective ATM kinase inhibitor M4076: a clinical candidate drug with strong anti-tumor activity in combination therapies. *Cancer Res.* **79**, 3500 (2019).
32. Choi, M., Kipps, T. & Kurzrock, R. ATM mutations in cancer: therapeutic implications. *Mol. Cancer Ther.* **15**, 1781–1791 (2016).
33. Dohmen, A. J. C. et al. Identification of a novel ATM inhibitor with cancer cell specific radiosensitization activity. *Oncotarget* **8**, 73925–73937 (2017).
34. Toledo-Sherman, L. et al. Optimization of potent and selective ataxia telangiectasia-mutated inhibitors suitable for a proof-of-concept study in Huntington's disease models. *J. Med. Chem.* **62**, 2988–3008 (2019).
35. Min, A. et al. AZD6738, a novel oral inhibitor of ATR, induces synthetic lethality with ATM deficiency in gastric cancer cells. *Mol. Cancer Ther.* **16**, 566–577 (2017).
36. Perkhof, L. et al. ATM deficiency generating genomic instability sensitizes pancreatic ductal adenocarcinoma cells to therapy-induced DNA damage. *Cancer Res.* **77**, 5576–5590 (2017).
37. Schmitt, A. et al. ATM deficiency is associated with sensitivity to PARP1- and ATR inhibitors in lung adenocarcinoma. *Cancer Res.* **77**, 3040–3056 (2017).
38. Weston, V. J. et al. The PARP inhibitor olaparib induces significant killing of ATM-deficient lymphoid tumor cells in vitro and in vivo. *Blood* **116**, 4578–4587 (2010).
39. Kantidze, O. L., Velichko, A. K., Luzhin, A. V., Petrova, N. V. & Razin, S. V. Synthetically lethal interactions of ATM, ATR and DNA-PKcs. *Trends Cancer* **4**, 755–768 (2018).
40. Hickson, I. et al. Identification and characterization of a novel and specific inhibitor of the ataxia-telangiectasia mutated kinase ATM. *Cancer Res.* **64**, 9152–9159 (2004).
41. Golding, S. E. et al. Improved ATM kinase inhibitor KU-60019 radiosensitizes glioma cells, compromises insulin, AKT and ERK prosurvival signaling, and inhibits migration and invasion. *Mol. Cancer Ther.* **8**, 2894–2902 (2009).
42. Karlin, J. et al. Orally bioavailable and blood-brain barrier-penetrating ATM inhibitor (AZ32) radiosensitizes intracranial gliomas in mice. *Mol. Cancer Ther.* **17**, 1637–1647 (2018).
43. Pike, K. G. et al. The identification of potent, selective and orally available inhibitors of ataxiatelangiectasia mutated (ATM) kinase: the discovery of AZD0156(8-[6-[3-(dimethylamino)propoxy]pyridin-3-yl]-3-methyl-1-(tetrahydro-2H-pyran-4-yl)-1,3-dihydro-2H-imidazo[4,5-c]quinolin-2-one). *J. Med. Chem.* **61**, 3823–3841 (2018).
44. Durant, S. T. et al. The brain-penetrant clinical ATM inhibitor AZD1390 radiosensitizes and improves survival of preclinical brain tumor models. *Sci. Adv.* **4**, eaat1719 (2018).
45. Morgado-Palacin, I. et al. Targeting the kinase activities of ATR and ATM exhibits antitumoral activity in mouse models of MLL-rearranged AML. *Sci. Signal.* **9**, ra91 (2016).
46. Fuchss, T., Becker, A., Kubas, H. & Graedler, U. Imidazolonylquinoline compounds and therapeutic uses thereof. WO patent 2020/193660 (2020).
47. Boland, A., Chang, L. & Barford, D. The potential of cryo-electron microscopy for structure-based drug design. *Essays Biochem.* **61**, 543–560 (2017).
48. Seidel, J. J., Anderson, C. M. & Blackburn, E. H. A novel Tel1/ATM N-terminal motif, TAN, is essential for telomere length maintenance and a DNA damage response. *Mol. Cell Biol.* **28**, 5736–5746 (2008).
49. Fernandes, N. et al. DNA damage-induced association of ATM with its target proteins requires a protein interaction domain in the N terminus of ATM. *J. Biol. Chem.* **280**, 15158–15164 (2005).
50. Falck, J., Coates, J. & Jackson, S. P. Conserved modes of recruitment of ATM, ATR and DNA-PKcs to sites of DNA damage. *Nature* **434**, 605–611 (2005).
51. Tate, J. G. et al. COSMIC: the Catalogue Of Somatic Mutations In Cancer. *Nucleic Acids Res.* **47**, D941–D947 (2019).
52. Weber, A. M. et al. Phenotypic consequences of somatic mutations in the ataxia-telangiectasia mutated gene in non-small cell lung cancer. *Oncotarget* **7**, 60807–60822 (2016).
53. Milanovic, M. et al. The cancer-associated ATM R3008H mutation reveals the link between ATM activation and its exchange. *Cancer Res.* **81**, 426–437 (2020).
54. Vivek, M., & Dunbrack, R. L. Defining a new nomenclature for the structures of active and inactive kinases. *Proc. Natl Acad. Sci. USA* **116**, 6818–6827 (2019).
55. Tannous, E. A., Yates, L. A., Zhang, X. & Burgers, P. M. Mechanism of auto-inhibition and activation of Mec1(ATR) checkpoint kinase. *Nat. Struct. Mol. Biol.* **28**, 50–61 (2021).
56. Langer, L. M., Gat, Y., Bonneau, F. & Conti, E. Structure of substrate-bound SMG1-8-9 kinase complex reveals molecular basis for phosphorylation specificity. *eLife* **9**, e57127 (2020).
57. Kuhn, B., Fuchs, J. E., Reutlinger, M., Stahl, M. & Taylor, N. R. Rationalizing tight ligand binding through cooperative interaction networks. *J. Chem. Inf. Model.* **51**, 3180–3198 (2011).
58. Chaplin, A. K. et al. Dimers of DNA-PK create a stage for DNA double-strand break repair. *Nat. Struct. Mol. Biol.* **28**, 13–19 (2021).
59. Armstrong, S. A., Schultz, C. W., Azimi-Sadjadi, A., Brody, J. R. & Pishvaian, M. J. ATM dysfunction in pancreatic adenocarcinoma and associated therapeutic implications. *Mol. Cancer Ther.* **18**, 1899–1908 (2019).

Publisher's note Springer Nature remains neutral with regard to jurisdictional claims in published maps and institutional affiliations.

© The Author(s), under exclusive licence to Springer Nature America, Inc. 2021

Methods

Expression of human ATM. The pCDNA3.1 vector containing the full-length (1–3056) human ATM gene was ordered from GenScript. Human ATM was designed to comprise an N-terminal FLAG tag (MDYKDDDDK) and codons optimized for protein expression in mammalian cells.

DNA required for transfections was obtained using GigaKit (Macherey-Nagel) and eluted in sterile deionized water. Human ATM was expressed in Expi293F cells (Thermo Fisher Scientific, A14527), as described previously¹⁶.

Human ATM purification. Cell pellet from 500 ml of transfected Expi293F culture was resuspended in 50 ml of pre-cooled buffer A (50 mM HEPES (pH 7.5, 23 °C), 150 mM NaCl, 100 mM L-arginine, 5% (vol/vol) glycerol) supplemented with one tablet of EDTA-free protease inhibitor cocktail (Sigma-Aldrich) and 10 U of TURBO DNase (Thermo Fisher Scientific). The cells were gently lysed using a Dounce homogenizer, followed by sonication for 70 s (50% duty cycle, five-output control) on ice. The cell lysate was cleared by centrifugation at 16,000 r.p.m. for 40 min using an SS-34 rotor. All of the following steps were performed at 8 °C. The soluble fraction of the lysate was filtered using 0.45- μ m PVDF membrane filters (Merck Millipore), then 3 ml of anti-FLAG affinity gel resin (Sigma-Aldrich) was equilibrated with buffer A. The cleared lysate was added to the equilibrated beads and incubated in a 2.5 cm \times 10 cm glass Econo-Column (Bio-Rad) on a rocking platform for 2 h. After removal of the flow-through, the resin was washed with 50 ml of buffer B (50 mM HEPES (pH 7.5, 23 °C), 150 mM NaCl, 5% (vol/vol) glycerol, 0.5 mM DTT), then 5 ml of buffer B supplemented with 2 mM ATP and 5 mM MgCl₂ was added to the resin and incubated for 30 min with rocking. The ATP wash was repeated four times. The resin was washed with 50 ml of buffer B. Elution buffer was prepared by diluting 3 \times FLAG peptide stock solution (5 mg ml⁻¹ 3 \times FLAG peptide in TBS (50 mM Tris-HCl at pH 7.4, 150 mM NaCl)) in buffer B to reach a final peptide concentration of 200 μ g ml⁻¹. The resin was gently resuspended in 3 ml of elution buffer and incubated for 30 min while slowly rocking. In total, 5 \times 3-ml elution fractions were obtained in this way. All elution fractions were combined and filtered through a 0.2- μ m filter (Merck Millipore) before anion exchange chromatography (AEC). AEC was performed on an AKTA Pure system using a 15-ml loop and a MonoQ 5/50 GL column equilibrated in MonoQ-A buffer (50 mM HEPES (pH 7.5, 23 °C), 150 mM NaCl, 5% (vol/vol) glycerol, 2 mM tris(2-carboxyethyl) phosphine (TCEP)). The column was washed with MonoQ-A buffer following sample application and eluted with a NaCl gradient from 150 mM (MonoQ-A buffer) to 1 M (MonoQ-B buffer (50 mM HEPES (pH 7.5, 23 °C), 1 M NaCl, 5% (vol/vol) glycerol, 2 mM TCEP)). Elution fractions of 0.2 ml were collected. Purified protein was stored at 4 °C and used for cryo-EM grid preparation within 48 h of purification.

Cryo-electron microscopy grid preparation. Freshly purified human ATM was diluted in compensation buffer to obtain a protein concentration of 0.26 mg ml⁻¹ in 20 mM HEPES (pH 7.5, 23 °C), 150 mM NaCl and 5 mM MgCl₂. The human ATM sample (4 μ l) was mixed with 1 μ l of 21 μ M inhibitor KU-55933 (Sigma-Aldrich) and incubated on ice for at least 5 min. Immediately before plunging, Tween-20 was added to the ATM sample to a final concentration of 0.01%. Grids were prepared using a Leica EM GP plunge freezer (Leica). Tween-20-containing sample (4.5 μ l) was deposited onto a plasma-cleaned (GloQube, Quorum) gold grid with a carbon support (Au 200, R2/2, 2 nm C, UltraAufoil). Samples were pre-incubated on the grids for 20 s at 15 °C and 95% humidity and blotted for 2.5 s before plunge-freezing the grid in liquid ethane.

Cryo-electron microscopy data acquisition. Two datasets of ATM-KU-55933 (8,519 and 4,139 micrographs) were acquired on a Titan Krios transmission electron microscope (Thermo Fisher Scientific) operated at 300 kV, with a K2 summit direct electron detector (Gatan) operated in counting mode and an energy filter (Gatan). Data acquisition was automated with the EPU (Thermo Fisher Scientific) software package. Images were recorded at a nominal magnification of \times 130,000 (1.059 Å per pixel) with a defocus range of 1.0 μ m to 2.8 μ m, and total dose of 45 e⁻/Å² over 40 frames. Four datasets of ATM-M4076 (5,287, 1,372, 3,745 and 2,269 micrographs) were acquired using the same set-up as described above. A dataset of ATM-ATPyS containing 5,619 micrographs was collected using the same set-up as described above. Representative micrographs are provided in Supplementary Fig. 7.

Cryo-electron microscopy image processing. Motion correction with MotionCor2 and CTF estimation with CTFind4 were performed on the fly for all datasets using an in-house-developed pipeline^{66,61}.

Further processing of ATM-KU-55933 data was carried out using RELION-3.0.7/3.1.0⁶². Particles were picked automatically using a previously obtained low-resolution map of human ATM filtered to 20 Å as a 3D reference (unpublished). A total of 5,333,298 particles were extracted using a box size of 320 \times 320 pixels and binned four times to speed up the initial processing. Extracted particles were subjected to a few rounds of 2D classification followed by a selection of 'clean' 2D classes. The resulting 2,679,787 particles were used in 3D classification and another round of 'cleanup' selection was done. The best 3D class with 891,295 particles was selected and used for two rounds of 3D refinement, followed by CTF

refinement and Bayesian polishing. A set of polished particles was cleaned by 2D classification. The remaining 826,510 particles were 3D-refined and post-processed with automatic *B*-factor determination. The final map showed an overall resolution of 2.78 Å according to the gold-standard Fourier shell correlation 0.143 criterion (used hereafter unless otherwise stated).

To better resolve the conformational flexibility of the N-terminal HEAT repeat region of ATM, we started by 3D-refining, CTF-refining and Bayesian-polishing all 2,679,787 particles. Polished particles were cleaned by 2D classification and further 3D-refined. The resulting 2,651,173 particles were subjected to a 3D classification, followed by a focused (N-terminal) 3D classification with fixed angles, selectively masking for the N-terminal domains. Masks for the regions of interest were created using UCSF Chimera⁶³. Three distinct 3D classes with different N-terminal solenoid confirmation emerged. All three classes were processed individually by focused 3D classification with fixed angles and 3D refinement (for details see the processing scheme in Supplementary Fig. 1). An analogous approach was used to resolve the conformational flexibility of the N-terminal region of M4076- and ATPyS-bound ATM (Extended Data Fig. 8).

To improve the resolution of the N terminus and pincer regions, subtracted maps were prepared. Using the 3D refinement of all 2,679,787 CTF-refined and polished particles, one complete monomer of the ATM dimer and the C-terminal portion of the other were subtracted. Two particle sets were prepared with the pincer region either included or subtracted. The particles were re-centered on the remaining N-terminal density and cropped to 200 \times 200 pixels. Maps from the subtracted particles were produced using *reliion_reconstruct*, and used to prepare masks and as references for 3D classifications with local angular searches. Dominant classes appeared containing 1,075,217 particles (excluding pincer) and 1,117,056 particles (including pincer). These classes were refined and post-processed to overall resolutions of 3.06 Å (excluding pincer) and 3.15 Å (including pincer). The 3D classifications with fixed angles were performed using masks for the pincer region and very N-terminal HEAT repeats, and the best classes refined with local searches using the same targeted masks. This resulted in a map of the N-terminal HEAT repeats from 1,035,906 particles to a resolution of 3.10 Å, and a map of the pincer region from 807,127 particles to a resolution of 3.34 Å (Supplementary Fig. 3).

Processing of the ATM-M4076 dataset was continued in CryoSPARC by using Topaz for automated particle picking on the motion-corrected micrographs^{64,65}. After four rounds of Topaz training and 2D classification cleaning, 455,866 particles were used for ab initio reconstruction and homogeneous refinement. Local refinement masking for the C-terminal half of ATM resulted in a final map with a resolution of 2.99 Å (the processing scheme is depicted in Supplementary Fig. 4).

ATM-ATPyS particles were picked in CryoSPARC by using Topaz (as described above) in combination with template-based automated particle picking performed in Relion using a previously obtained human ATM-KU-55933 map filtered to 20 Å as a 3D reference. Particle coordinates were transferred between CryoSPARC and Relion using UCSF pyEM, CryoSPARC and Relion picked particles were combined in Relion, removing duplicates, and cleaned by 2D classification. The resulting 709,013 particles were subjected to 3D refinement, CTF refinement and Bayesian polishing. Polished particles were cleaned by 2D classification and the selected 701,857 particles were 3D-refined and 3D-classified using fixed angles, then 690,548 particles from the best 3D class were 3D-refined, masking for the C-terminal half and using local search angles, and post-processed with automatic *B* factor determination (Supplementary Fig. 5). The final map showed an overall resolution of 2.78 Å (Supplementary Fig. 6).

Some maps were filtered using LAFTER in the CCPEM interface^{66,67}. Maps with different origins were aligned and resampled using UCSF Chimera where appropriate. Phenix combine-focused-maps was used to generate an overall map of ATM-KU-55933, combining the highest-resolution components of each focused map^{65,68}.

Model building and refinement. An existing model of *Hs*ATM (PDB 6K9L) was rigid-body-fitted to the ATM-KU-55933 map density using UCSF Chimera. Model building and refinement were performed using Coot^{69,69}. The existing *Hs*ATM model was used as a template for building of the C-terminal region, from which sequences were fitted, corrected and extended. However, all existing models were shown to be incorrect for the N-terminal and pincer regions, so these regions were built manually, assisted by secondary-structure predictions from JPred 4⁷⁰. The multiple maps with different focal positions were used to provide the highest resolution at each point in the protein sequence and ensure the model was built in the correct register, before fitting to individual maps. LAFTER filtered maps provided the clearest densities for model building⁶⁵. Loops with poor density were only built where well-defined anchor points and traceable density limited positioning errors. Some side chains were omitted in poorly resolved loops.

For modeling the lower-resolution N-terminal regions of the overall maps, the spiral and hinge models from the high-resolution subtracted maps were rigid-body-fitted into the density, followed by real-space refinement with local restraints. All structures were refined by iterative rounds of model building with Coot and refinement using Phenix real-space refine⁷¹. Models were validated using Phenix comprehensive validation (cryo-EM)⁶⁸. Figures were generated using UCSF ChimeraX⁷².

Sequence alignments of the C-terminal 236 amino acids of human ATM with other PIKK family members and ATM orthologs were carried out using the program clustalW2.

Human CtIP fragment expression and purification for kinase assays. A truncated version of human CtIP consisting of the C-terminal residues 650–897 and the phosphomimetic mutant T847E was cloned into a pET47b vector together with an N-terminal 6× His tag, followed by an MBP tag and an HRV3C protease cleavage site. Transfected *Escherichia coli* Rosetta cells (Novagen) were cultured in Turbo medium at 37 °C, 140 r.p.m. until reaching an optical density at 600 nm of ~1.2. Recombinant protein expression was induced with 0.2 mM IPTG and carried out at 18 °C, 140 r.p.m. for 16 h. Cells were collected by centrifugation at 4,000g, 10 min, 4 °C. The cell pellet from a 2-l culture was resuspended in 50 ml of pre-cooled lysis buffer (50 mM HEPES, pH 7.5, 300 mM NaCl, 10% (vol/vol) glycerol, 0.5 mM TCEP, 10 μM ZnCl₂, 10 mM imidazole, 0.5% NP-40) supplemented with one tablet of EDTA-free protease inhibitor cocktail (Sigma-Aldrich). Lysis was performed by three rounds of sonication for 5 min each (50% duty cycle, eight-output control) on ice. The cell lysate was cleared by centrifugation at 17,000 r.p.m. for 1 h using an SS-34 rotor. The supernatant was further filtered using 0.45-μm PVDF membrane filters (MERCCK Millipore). All of the following steps were performed at 8 °C. A 10 ml volume of Ni-NTA beads (Machery Nagel), equilibrated with buffer A (50 mM HEPES pH 7.5, 300 mM NaCl, 10% (vol/vol) glycerol, 0.5 mM TCEP, 10 μM ZnCl₂, 10 mM imidazole), was added to the cleared lysate and incubated in a 2.5 cm × 10 cm glass Econo-Column (Bio-Rad) on a rocking platform for 1 h. The flow-through was removed and the beads washed three times with buffer A, twice with 5% buffer B (buffer A, containing 500 mM imidazole), once with 10% buffer B and once with 15% buffer B. CtIP was eluted four times with 50% buffer B. The fractions were pooled and dialyzed against buffer containing 50 mM HEPES pH 7.5, 150 mM NaCl, 10% (vol/vol) glycerol, 0.5 mM TCEP, 10 μM ZnCl₂, and 5 mM imidazole overnight after self-made PreScission protease was added. The dialyzed sample was applied to the same amount of Ni-NTA beads, pre-equilibrated with dialysis buffer and incubated while rotating for 1 h. The flow-through, containing cleaved CtIP, was collected and excess protease removed with a glutathione bead (Thermo Scientific) pull-down. After concentrating the sample using a centrifugal filter (30-kDa molecular weight cutoff, Amicon) to ~8 mg ml⁻¹, 500 μl was injected onto a Superdex 75 10/300 column (GE Healthcare) connected to an ÄKTA Pure system, pre-equilibrated in SEC buffer (20 mM HEPES, pH 7.5, 150 mM NaCl, 10 μM ZnCl₂, 0.5 mM TCEP). CtIP was eluted at 1.5 mg ml⁻¹ with some minor degradation products, aliquoted, flash-frozen in liquid nitrogen and stored at –80 °C.

Gel-based kinase assay. The kinase activity of freshly purified full-length human ATM (50 mM HEPES (pH 7.5, 23 °C), 160 mM NaCl, 5% (vol/vol) glycerol, 2 mM TCEP) was assessed using human CtIP peptide substrate at a final concentration of 2.4 μM. The final concentration of human ATM used was 0.35 μM. The reactions were carried out in buffer containing 20 mM HEPES (pH 7.5, 23 °C), 150 mM NaCl, 5 mM MgCl₂, 1 mM MnCl₂, 0.01 mM ZnCl₂, 5% (vol/vol) glycerol and 0.5 mM TCEP at a final volume of 15 μl. The ATM-specific inhibitors KU-55933 (Sigma-Aldrich) and M4076 (Merck) were dissolved in dimethyl sulfoxide and used in a final concentration of 10 μM. The reactions were started by the addition of 1 mM adenosine 5'-triphosphate (ATP) followed by 30-min incubation at 30 °C. The reactions were stopped by adding 4× sodium dodecyl sulfate polyacrylamide gel electrophoresis (SDS–PAGE) loading buffer. An aliquot of 15 μl from each reaction was loaded on a 4–20× RunBlue SDS gel (Expedion) and resolved by SDS–PAGE. The gel was stained using Pro-Q Diamond Phosphoprotein gel stain (Thermo Fisher Scientific) and analyzed using a Typhoon FLA 9000 laser scanner (GE Healthcare). In addition, gel was stained with Coomassie (InstantBlue, Expedion) to assure consistent sample loading.

Thermal shift assay. 1,10-Phenanthroline, *N,N,N',N'*-tetrakis-(2-pyridylmethyl) ethylenediamine (TPEN) and EGTA (Sigma-Aldrich) were prepared by dissolving appropriate amounts of chelating agents in ethanol to reach 500 mM concentration, then further diluted with MonoQ-A buffer to generate 100 mM (100×) stock of chelating agents. The 100× stocks were further diluted with MonoQ-A buffer to 10× concentration before mixing chelating agents with protein.

A volume of 9 μl of freshly purified full-length human ATM at 0.6 μM concentration was mixed with 1 μl of 10× (10 mM) chelating agents. In the control reaction, the same amount of ATM was mixed with 1 μl of buffer prepared in the same way as chelating agents. Following a 10-min incubation of ATM with chelating agents, changes in the intrinsic fluorescence (at 330 nm and 350 nm) with respect to increasing temperature were measured using a Tycho NT.6 system (NanoTemper). The measurements were performed in standard capillaries (NanoTemper).

Recombinant proteins for biochemical kinase activity assays. The following recombinant proteins used in the biochemical kinase activity assays (except Fig. 1a and Extended Data Figs. 1c and 5a) were purchased from Eurofins: human full-length FLAG-tagged ATM (GenBank ID [NM_000051](#); item no. 14-933-K, lot no. 2447914) expressed in a mammalian cell line; human full-length FLAG-tagged

ATR (GenBank ID [NM_001184.3](#)) and human full-length ATRIP (GenBank ID [AF451323.1](#)) co-expressed in a mammalian cell line (item no. 14-953M, lot no. D14HP005NB); N-terminal FLAG-tagged human mTOR amino acids 1362–end (GenBank ID [NM_004958.2](#); item nos. 14-769, 14-769-K and 14-769M, lot no. 1607837) expressed by baculovirus in Sf21 insect cells; PI3K p110α/p85α (complex of N-terminal 6His-tagged full-length p110α and untagged full-length p85α; GenBank [U79143](#)(PI3Ka)/GenBank [XM_043865](#)(p85a)) (item nos. 14-602, 14-602-K and 14-602M, lot no. WAB0319), expressed by baculovirus in Sf21 insect cells; PI3K p110β/p85α (complex of N-terminal 6His-tagged full-length p110β and untagged full-length p85α; GenBank [NM_006219](#)(PI3Kb)/GenBank [XM_043865](#)(p85a)) (item nos. 14-603, 14-603-K and 14-603M, lot no. WAD0867), expressed by baculovirus in Sf21 insect cells; PI3K p120γ (N-terminal 6His-tagged full-length PI3-kinase (p120γ); GenBank [AF327656](#)) (item nos. 14-558, 14-558-K and 14-558M, lot no. 2298365) and PI3K p110δ/p85α (complex of N-terminal 6His-tagged full-length p110δ and untagged full-length p85α; GenBank [NM_005026](#)(PI3Kδ)/GenBank [XM_043865](#)(p85α)) (item nos. 14-604, 14-604-K and 14-604M, lot no. WAE0320), expressed by baculovirus in Sf21 insect cells.

DNA-PK was prepared from HeLa nuclear cell extract (Cilbiotech) by Merck KGaA, which was diluted to a final concentration of 40 mM KCl and applied to ion exchange chromatography (AIEEX Fractogel DEAE) in buffer A (40 mM KCl, 20 mM HEPES, 1 mM EDTA, 1 mM EGTA, 1 mM DTT, 10% glycerol, 0.02% Tween-20, pH 7.9). Increasing KCl concentrations were applied for a stepwise elution. Fractionation of active DNA-PK was achieved at 300 mM KCl. All steps were performed at 4 °C. Aliquots were frozen in liquid nitrogen and stored at –80 °C. Western blot analysis was used to confirm the DNA-PK catalytic subunit, Ku85 and Ku70. The final protein concentration was determined by Bradford assay (details are provided in the Supplementary Information).

Time-resolved FRET-based ATM kinase assay. The enzymatic ATM assay was carried out as a time-resolved FRET (TR-FRET; homogeneous time-resolved fluorescence (HTRF), Cisbio Bioassays) based 384-well assay. In the first step, purified human recombinant ATM (Eurofins) was incubated in assay buffer for 15 min with the ATM inhibitor at various concentrations and without test substance (as a negative or neutral control). The assay buffer comprised 25 mM HEPES pH 8.0, 10 mM Mg(CH₃COO)₂, 1 mM MnCl₂, 0.1% BSA, 0.01% Brij 35 and 5 mM DTT. The inhibitor solutions were dispensed into the microtiter plates using an ECHO 555 handler (Labcyte). In the second step, purified human recombinant c-myc-labeled p53 (human p53, full length, GenBank ID [BC003596](#), expressed in Sf21 insect cells, Eurofins) and ATP were added, and the reaction mixture was incubated at 22 °C for 35 min. The final concentrations in the assay during incubation of the reaction mixture were 0.3 nM ATM, 75 nM p53 and 10 μM ATP (final reaction volume of 5 μl). The enzymatic reaction was stopped by the addition of EDTA. The formation of phosphorylated p53 as the result of the ATM-mediated reaction in the presence of ATP was detected via specific antibodies (labeled with the fluorophore europium (Eu) as donor and d2 as acceptor (Cisbio Bioassays)), which enabled FRET. A volume of 2 μl of antibody-containing stop solution (12.5 mM HEPES pH 8.0, 125 mM EDTA, 30 mM NaCl, 300 mM KF, 0.006% Tween-20, 0.005% Brij 35, 0.21 nM anti-phospho-p53(ser15)-Eu antibody and 15 nM anti-cmyc-d2 antibody) was added to the reaction mixture. After 2 h of incubation for signal development, the plates were analyzed in a plate reader (EnVision, PerkinElmer or Pherastar, BMG Labtech) using the TRF mode (and with laser excitation). After excitation of the donor Eu at a wavelength of 340 nm, the emitted fluorescence light both of the acceptor d2 at 665 nm and of the donor Eu at 615 nm was measured. The amount of phosphorylated p53 was directly proportional to the quotient of the amounts of light emitted, that is, the relative fluorescence units at 665 nm and 615 nm. The measurement data were processed by means of GraphPad Prism software. IC₅₀ determinations were carried out by fitting a response curve to the data points by means of nonlinear regression analysis.

ATR–ATRIP kinase assay. The ATR–ATRIP enzymatic assay was performed as a TR-FRET (HTRF, Cisbio Bioassays) based 384-well assay. In a first step, purified human recombinant ATR–ATRIP (Eurofins) was incubated in assay buffer for 15 min at 22 °C with inhibitor at different concentrations or without test compound (as a negative control). The assay buffer contained 25 mM HEPES pH 8.0, 10 mM Mg(CH₃COO)₂, 1 mM MnCl₂, 0.1% BSA, 0.01% Brij 35 and 5 mM DTT. An ECHO 555 handler (Labcyte) was used to dispense compound solutions. In a second step, purified human recombinant cmyc-tagged p53 (human p53, full length, GenBank ID [BC003596](#), expressed in Sf21 insect cells, Eurofins) and ATP were added, and the reaction mixture was incubated for 25–35 min, typically 25 min, at 22 °C. The pharmacologically relevant assay volume was 5 μl. The final concentrations in the assay during incubation of the reaction mixture were 0.3–0.5 nM (typically 0.3 nM) ATR–ATRIP, 50 nM p53 and 0.5 μM ATP. The enzymatic reaction was stopped by the addition of EDTA. The generation of phosphorylated p53 as a result of the ATR-mediated reaction in the presence of ATP was detected by using specific antibodies (labeled with the fluorophores Eu as donor and d2 as acceptor (Cisbio Bioassays)), enabling FRET. For this purpose, 2 μl of antibody-containing stop solution (12.5 mM HEPES pH 8.0, 125 mM EDTA, 30 mM NaCl, 300 mM KF, 0.006% Tween-20, 0.005% Brij 35, 0.21 nM anti-phospho-p53(Ser15)-Eu antibody,

15 nM anti-cmyc-d2 antibody) were added to the reaction mixture. Following signal development for 2 h, the plates were analyzed in an EnVision (PerkinElmer) microplate reader using the TRF mode with laser excitation. Following excitation of the donor Eu at 340 nm, the emitted fluorescence light of the acceptor d2 at 665 nm as well as from the donor Eu at 615 nm was measured. The amount of phosphorylated p53 was directly proportional to the ratio of the amounts of emitted light, that is, the ratio of the relative fluorescence units at 665 nm and 615 nm. Data were processed using GraphPad Prism software. IC_{50} values were determined in the usual manner by fitting a dose-response curve to the data points using nonlinear regression analysis.

DNA-PK assay. The DNA-PK kinase assay was performed as an HTRF (Cisbio Bioassays) based 384-well assay. In a first step, DNA-PK protein complex from HeLa nuclear extract pre-incubated with DNA from calf thymus and staurosporine was incubated with or without test compound for 15–20 min at 22 °C. After addition of the STK-substrate 1-biotin (Cisbio Bioassays) and Mg-ATP, the reaction mixture was incubated for 60–70 min (depending on the activity of the DNA-PK protein complex) at 22 °C. An ECHO 555 handler (Labcyte) or a Biomek FX handler (Beckman Coulter) was used for dispensing of compound solutions. The assay buffer consisted of 25 mM HEPES pH 7.4, 11 mM $MgCl_2$, 80 mM KCl, 0.45 mM EDTA and 0.5 mM EGTA, and contained 1 mM DTT, 0.17% BSA and 0.01% Tween-20. The pharmacologically relevant volume was 5 or 5.5 μ l. The final concentrations in the assay during incubation of the reaction mixture were 100–235 ng DNA-PK protein complex per well (depending on the activity of the DNA-PK protein complex), 1 μ M STK substrate 1-biotin (Cisbio Bioassays), 10 or 20 μ M Mg-ATP, 80 ng DNA from calf thymus per well and 1 μ M staurosporine. The enzymatic reaction was stopped by the addition of EDTA. The generation of phosphorylated STK-substrate 1-biotin as a result of the DNA-PK-mediated reaction was detected via a specific anti-phospho STK-antibody (Cisbio Bioassays) labeled with Eu as donor and streptavidin labeled with XL665 (Cisbio Bioassays) as acceptor, allowing FRET. For this purpose, 4 μ l of antibody- and streptavidin-containing stop solution (50 mM HEPES pH 7.0, 800 mM KF, 20 mM EDTA, 0.1% BSA, 0.179 or 8.95 nM anti-phospho-STK antibody, 160 or 200 nM streptavidin-XL665) were added to the reaction mixture. Following signal development for 1 h, the plates were analyzed on a Rubystar or Pherastar (BMG Labtech) or on an Ultra Evolution (Tecan) microplate reader. The amount of phosphorylated substrate was directly proportional to the ratio of fluorescence units (excitation wavelength of 337 or 320 nm) at the emission wavelengths of 665 nm (phosphopeptide-sensitive wavelength/emission of XL665) to fluorescence units at 620 nm (reference wavelength Eu). IC_{50} values were calculated using GraphPad Prism software²³.

mTOR kinase assay. The DiscoverX KINOMEScan assay (Eurofins) was used for mTOR selectivity profiling of inhibitors. Recombinant human mTOR protein (Eurofins) was incubated in assay buffer containing 50 mM HEPES pH 7.5, 1 mM EGTA, 0.01% Tween-20, 2 mg ml⁻¹ substrate, 3 mM $MnCl_2$ and [γ -³²P-ATP] (specific activity ~500 c.p.m. pmol⁻¹, [ATP] = 70 μ M in the assay). The reaction was initiated by the addition of Mn-ATP solution. The reaction was stopped by the addition of 3% phosphoric acid after 40-min incubation at room temperature. A volume of 10 μ l of reaction solution was pipetted on P30 filters and washed three times for 5 min in 75 mM phosphoric acid and once in methanol, dried, and measured by scintillation counting. IC_{50} values were calculated using GraphPad Prism software.

PI3K HTRF-based assay. The DiscoverX KINOMEScan assay (Eurofins) was used for PI3K selectivity profiling of inhibitors. The following human recombinant proteins expressed by baculovirus in Sf21 insect cells (Eurofins) were used: PI3K p110 α /p85 α , PI3K p110 β /p85 α , PI3K p120 γ and PI3K p110 δ /p85 α . The following HTRF-based assay protocol was used for all PI3K isoforms with ATP concentrations at the respective K_m values (PI3K p110 α /p85 α , ATP K_m = 193 μ M, [ATP] = 200 μ M in assay; PI3K p110 β /p85 α ATP K_m = 235 μ M, [ATP] = 200 μ M in assay; PI3K p120 γ ATP K_m = 109 μ M, [ATP] = 100 μ M in assay; p110 δ /p85 α ATP K_m = 321 μ M, [ATP] = 200 μ M in assay). Recombinant human PI3K protein was incubated in assay buffer containing 10 μ M phosphatidylinositol-4,5-bisphosphate. The reaction was initiated by the addition of a Mg-ATP solution at K_m concentration (see above). After incubation for 30 min at room temperature, the reaction was stopped by the addition of EDTA and biotinylated phosphatidylinositol-3,4,5-trisphosphate. Finally, detection buffer was added, containing Eu-labeled anti-GST monoclonal antibody, GST-tagged GRP1 PH domain and streptavidin allophycocyanin. The plate was then read in time-resolved fluorescence mode and the HTRF signal was determined according to the formula $HTRF = 10,000 \times (Em\ 665\ nm/Em\ 620\ nm)$. Mg-ATP, magnesium 5'-O-[hydroxy[[[hydroxyphosphinato)oxy]-phosphinato]-oxy]-phosphoryl]adenosine; $MgCl_2$, magnesium dichloride; EGTA, ethyleneglycole-bis(aminoethylether)-N,N,N',N'-tetra acetic acid; Tween-20, Polysorbate 20. IC_{50} values were calculated using GraphPad Prism software.

In vitro kinase selectivity profiling assay for M4076. The Reaction Biology Corporation (RBC) HotSpot kinase profiling service (<http://www.reactionbiology.com>)

was used for in vitro selectivity profiling of M4076 in single-dose singlicate mode at a concentration of 1 μ M against 583 kinases. Dose-response curves of M4076 were determined for 10 kinases and their mutants (22 kinases in total), which showed activity values below 50% tested at 1 μ M M4076 in the in vitro kinase selectivity profile against 583 kinases. For IC_{50} determination, M4076 was tested in duplicate in a 10-dose IC_{50} mode with three-fold serial dilution starting at 10 μ M. Staurosporine was used as control compound and tested in 10-dose IC_{50} mode with four-fold serial dilution starting at 20 μ M. Reactions were carried out at K_m ATP concentrations of individual kinases according to the RBC K_m binning structure. Kinases inhibitory activities were assessed by the HotSpot assay platform, which contained specific kinase/substrate pairs along with the required cofactors. Base reaction buffer: 20 mM HEPES (pH 7.5), 10 mM $MgCl_2$, 1 mM EGTA, 0.02% Brij 35, 0.02 mg ml⁻¹ BSA, 0.1 mM Na_3VO_4 , 2 mM DTT and 1% DMSO. M4076 was dissolved in 100% DMSO to a specific concentration. The serial dilution was conducted by Integra Vialfo Assist in DMSO. The reaction mixture containing the examined compound M4076 and ³²P-ATP (specific activity 0.01 μ Ci μ l⁻¹ final) was incubated at room temperature for 2 h, and radioactivity was detected by the filter-binding method. In detail, reactions were spotted onto P81 ion exchange paper (Whatman cat. no. 3698-915) and filters were extensively washed in 0.75% phosphoric acid. Kinase activity data were expressed as the percent remaining kinase activity in test samples compared to vehicle (dimethyl sulfoxide) reactions. IC_{50} values and curve fits were obtained using GraphPad Prism software.

Cellular pCHK2 Thr68 Luminex. Cellular levels of pCHK2 were detected in a Luminex-based assay format. HCT116 cells (ATCC CCL-247, authenticated by STR analysis) were seeded in medium with 10% fetal calf serum (FCS) in 12-well plates. The next day, the medium was removed and 100 μ l of fresh medium including a serial dilution of inhibitor M4076 was added per well 1 h prior to the irradiation of 2 Gy by the CellRad irradiator. The irradiation was performed by adjusting the tube voltage to 120 kV_p; 5 mA and positioning the plates inside circle 2 at plate height position 2. A copper filter was used to reduce the intensity of particular wavelengths from the beam. At 1 h after irradiation, the cells were washed once with PBS, and cell lysates were prepared by using HGNT lysis buffer (20 mM HEPES pH 7.4, 150 mM NaCl, 2 mM EDTA, 25 mM NaF, 10% glycerol and 1% Triton X-100; plus 1% phosphatase inhibitor Cocktail Set II and 0.2% protease inhibitor Cocktail Set III) and analyzed for the level of pCHK2 Thr68 applying a Luminex-based assay. After adding the diluted bead suspension (3,000 beads in BR (Roche 11112589001 + 0.1% Tween)) with coupled antibodies against total CHK2 (Chk2 (D9C6) XP rabbit mAb; Cell Signaling Technology cat. no. 6334BF) to 25 μ g of total protein in HGNT, the plate was incubated overnight at 4 °C. The beads were washed three times with TBST (Pierce/Thermo 28358 + 0.05% Tween) and 25 μ l of BR as well as 25 μ l of antibody dilution of the detection antibody coupled to biotin were added in BR (tCHK2: Chk2 (IC12) mouse mAb; Cell Signaling Technology cat. no. 3440BF, pCHK2: pChk2 (Thr68) (C13C1) rabbit mAb; Cell Signaling Technology cat. no. 2197BF, final concentration 1.5 μ g ml⁻¹). After 1 h of incubation at room temperature, the beads were washed again with TBST and 25 μ l BR and the streptavidin-phycoerythrin dilution (25 μ l, Moss cat. no. 001NB, 1:1,000 diluted in BR) were added for 45 min at room temperature. After washing and adding 100 μ l of BR, the probes were analyzed in a Magpix instrument (Thermo Fisher Scientific) following the instruction manual. The instrument settings were as follows: sample volume, 35 μ l; count, 50; unit, MFI. To control the Luminex assay, different concentrations of recombinant CHK2 protein (R&D cat. no. 1358-KS) were used as standard and were analyzed in parallel. After background correction, the signals for the phosphorylated proteins were normalized to signals of the total protein. Basal levels were set to 0% and irradiated samples without compound were set to 100%. Samples were measured in singlicate and the experiment was repeated three times. IC_{50} values were calculated using GraphPad Prism software.

Cellular pCHK2 Thr68 enzyme-linked immunosorbent assay. HCT116 cells (ATCC CCL-247) were seeded in 100 μ l of culture medium (MEM Alpha, with 10% FCS) in the range of 5×10^4 cells per well in 96-well plates to achieve a defined cell density. The plates were then incubated for 24 h at 37 °C and 10% CO₂. The next day, the medium was removed and 100 μ l of fresh medium containing KU-55933 inhibitor in various concentrations (10 nM to 25 μ M) plus a constant concentration of 10 μ M bleomycin and without test substance as DMSO and bleomycin controls was added per well and incubation was continued for a further 6 h. The medium was removed and cells were lysed using HGNT lysis buffer (20 mM HEPES pH 7.4, 150 mM NaCl, 2 mM EDTA, 25 mM NaF, 10% glycerol and 1% Triton X-100; plus 1% phosphatase inhibitor Cocktail Set II and 0.2% protease inhibitor Cocktail Set III) and incubated at 4 °C overnight. Levels of pCHK2 were determined by ELISA (all reagents from Cell Signaling, cat. no. 7037; PathScan kit) with capture antibody specific for pCHK2 (Thr68) and detection antibody against total CHK2 protein. Anti-mouse immunoglobulin-G, horseradish peroxidase-linked antibody was then used to recognize the bound detection antibody. Horseradish peroxidase substrate (TMB) was added to develop color. The magnitude of the absorbance for the developed color is proportional to the amount of CHK2 phosphorylated at Thr68. Absorbance was measured at 450 nm for 4 s using a Tecan Sunrise reader. IC_{50} values were calculated using GraphPad Prism software.

Reporting Summary. Further information on research design is available in the Nature Research Reporting Summary linked to this Article.

Data availability

The 3D cryo-EM density maps reported in this Article have been deposited in the EMD under accession nos. EMD-12352 (ATM-ATPyS), EMD-12350 (ATM-M4076), EMD-12343 (ATM-KU-55933, Kinase), EMD-12347 (ATM-KU-55933, Spiral), EMD-12345 (ATM-KU-55933, Pincer) and EMD-12346 (ATM-KU-55933, Spiral-Pincer). The corresponding models have been deposited in the Protein Data Bank under IDs 7NI6 (ATM-ATPyS), 7NI4 (ATM-M4076) and 7NI5 (ATM-KU-55933). Raw micrographs are archived at the LRZ of the Bavarian Academy of Science and Humanities and can be accessed for legitimate research purposes upon reasonable request to K.P.H. (hopfner@genzentrum.lmu.de). Any requests for additional data by qualified scientific and medical researchers for legitimate research purposes will be subject to the Merck KGaA, Darmstadt, Germany Data Sharing Policy. All requests should be submitted in writing to the Merck KGaA, Darmstadt, Germany data-sharing portal (<https://www.emdgroup.com/en/research/our-approach-to-research-and-development/healthcare/clinical-trials/commitment-responsible-data-sharing.html>). When Merck KGaA, Darmstadt, Germany has a co-research, co-development, or co-marketing or co-promotion agreement, or when the product has been out-licensed, the responsibility for disclosure might be dependent on the agreement between parties. Under these circumstances, Merck KGaA, Darmstadt, Germany, will endeavor to gain agreement to share data in response to requests. Source data are provided with this paper.

References

60. Zheng, S. Q. et al. MotionCor2: anisotropic correction of beam-induced motion for improved cryo-electron microscopy. *Nat. Methods* **14**, 331–332 (2017).
61. Rohou, A. & Grigorieff, N. CTFFIND4: fast and accurate defocus estimation from electron micrographs. *J. Struct. Biol.* **192**, 216–221 (2015).
62. Zivanov, J. et al. New tools for automated high-resolution cryo-EM structure determination in RELION-3. *eLife* **7**, e42166 (2018).
63. Pettersen, E. F. et al. UCSF Chimera—a visualization system for exploratory research and analysis. *J. Comput. Chem.* **25**, 1605–1612 (2004).
64. Punjani, A., Rubinstein, J. L., Fleet, D. J. & Brubaker, M. A. cryoSPARC: algorithms for rapid unsupervised cryo-EM structure determination. *Nat. Methods* **14**, 290–296 (2017).
65. Bepler, T. et al. Positive-unlabeled convolutional neural networks for particle picking in cryo-electron micrographs. *Nat. Methods* **16**, 1153–1160 (2019).
66. Ramlal, K., Palmer, C. M. & Aylett, C. H. S. A local agreement filtering algorithm for transmission EM reconstructions. *J. Struct. Biol.* **205**, 30–40 (2019).
67. Wood, C. et al. Collaborative computational project for electron cryo-microscopy. *Acta Crystallogr. D Biol. Crystallogr.* **71**, 123–126 (2015).
68. Liebschner, D. et al. Macromolecular structure determination using X-rays, neutrons and electrons: recent developments in Phenix. *Acta Crystallogr. D Struct. Biol.* **75**, 861–877 (2019).
69. Emsley, P. & Cowtan, K. Coot: model-building tools for molecular graphics. *Acta Crystallogr. D Biol. Crystallogr.* **60**, 2126–2132 (2004).
70. Drozdetskiy, A., Cole, C., Procter, J. & Barton, G. J. JPred4: a protein secondary structure prediction server. *Nucleic Acids Res.* **43**, W389–W394 (2015).
71. Afonine, P. V. et al. Real-space refinement in PHENIX for cryo-EM and crystallography. *Acta Crystallogr. D Struct. Biol.* **74**, 531–544 (2018).
72. Pettersen, E. F. et al. UCSF ChimeraX: structure visualization for researchers, educators and developers. *Protein Sci.* **30**, 70–82 (2020).
73. Kashishian, A. et al. DNA-dependent protein kinase inhibitors as drug candidates for the treatment of cancer. *Mol. Cancer Ther.* **2**, 1257–1264 (2003).

Acknowledgements

EM data were collected at the Cryo-EM Core Facility of the Gene Center, Department of Biochemistry, LMU, Munich. B. Kessler, a technician at the Gene Center, LMU, provided support with cloning and protein purification. We are grateful for support from B. Blume and H. Dahmen, both employees of Merck KGaA, Darmstadt, Germany, for providing cellular pCHK2 results. Funding was provided by the Deutsche Forschungsgemeinschaft (CRC1054 to K.L.; CRC1361, CRC1064, Gottfried Wilhelm Leibniz-Prize and GRK1721 to K.P.H.) and a PhD fellowship from Boehringer Ingelheim Fonds (BIF) to E.v.d.L. This research was supported by the healthcare business of Merck KGaA, Darmstadt, Germany (CrossRef Funder ID 10.13039/100009945), which provided solid material of inhibitor M4076, free of charge.

Author contributions

J.D.B., K.S., M.R., A.A. and E.v.d.L. were involved in protein production and kinase assays. K.S., M.R., K.L. and J.D.B. carried out structural studies. T.F. was the project leader and principal inventor of M4076 at Merck KGaA, Darmstadt, Germany. U.G. was involved in the structure-based design of M4076 and cryo-EM structural refinement efforts. T.F. and U.P. contributed biochemical assay and kinase selectivity results and graphs. Together with K.L., K.S., M.R., J.D.B., T.F. and U.G. contributed to manuscript preparation. K.P.H. and all authors were involved in the interpretation of data, final manuscript preparation and approval.

Competing interests

K.S., M.R., K.L., J.D.B., E.v.d.L. and K.-P.H. declare no competing interests. A.A. contributed as an employee at the Gene Center, Department of Biochemistry, LMU at the time of the study and is currently an employee of Proteros Biostructures. U.G., T.F. and U.P. are employees of Merck KGaA, Darmstadt, Germany. Proteros Biostructures was contracted by Merck KGaA, Darmstadt, Germany, to determine the cryo-EM structure of ATM in complex with M4076.

Additional information

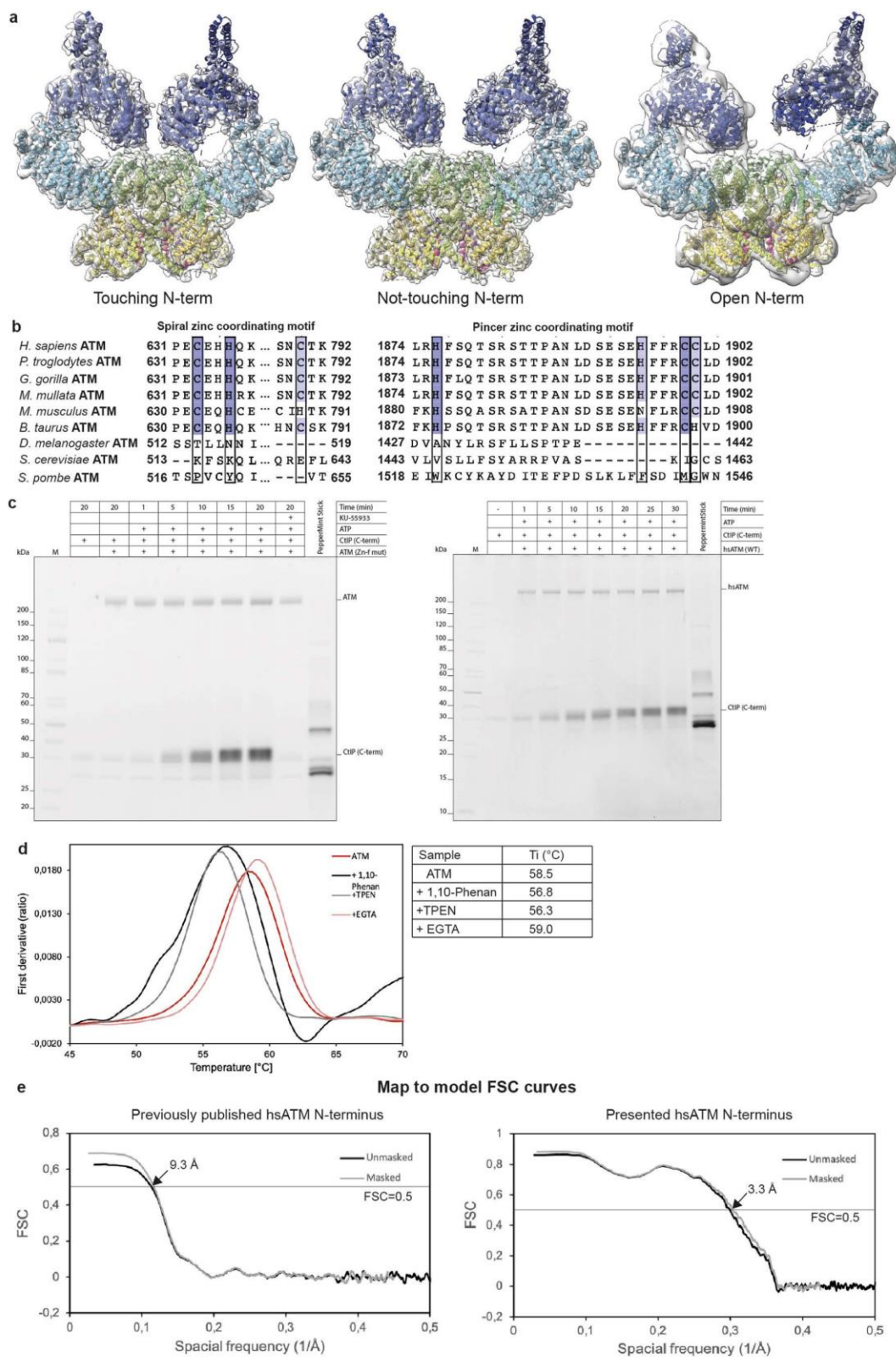
Extended data is available for this paper at <https://doi.org/10.1038/s41594-021-00654-x>.

Supplementary information The online version contains supplementary material available at <https://doi.org/10.1038/s41594-021-00654-x>.

Correspondence and requests for materials should be addressed to K. Lammens or K. P. Hopfner.

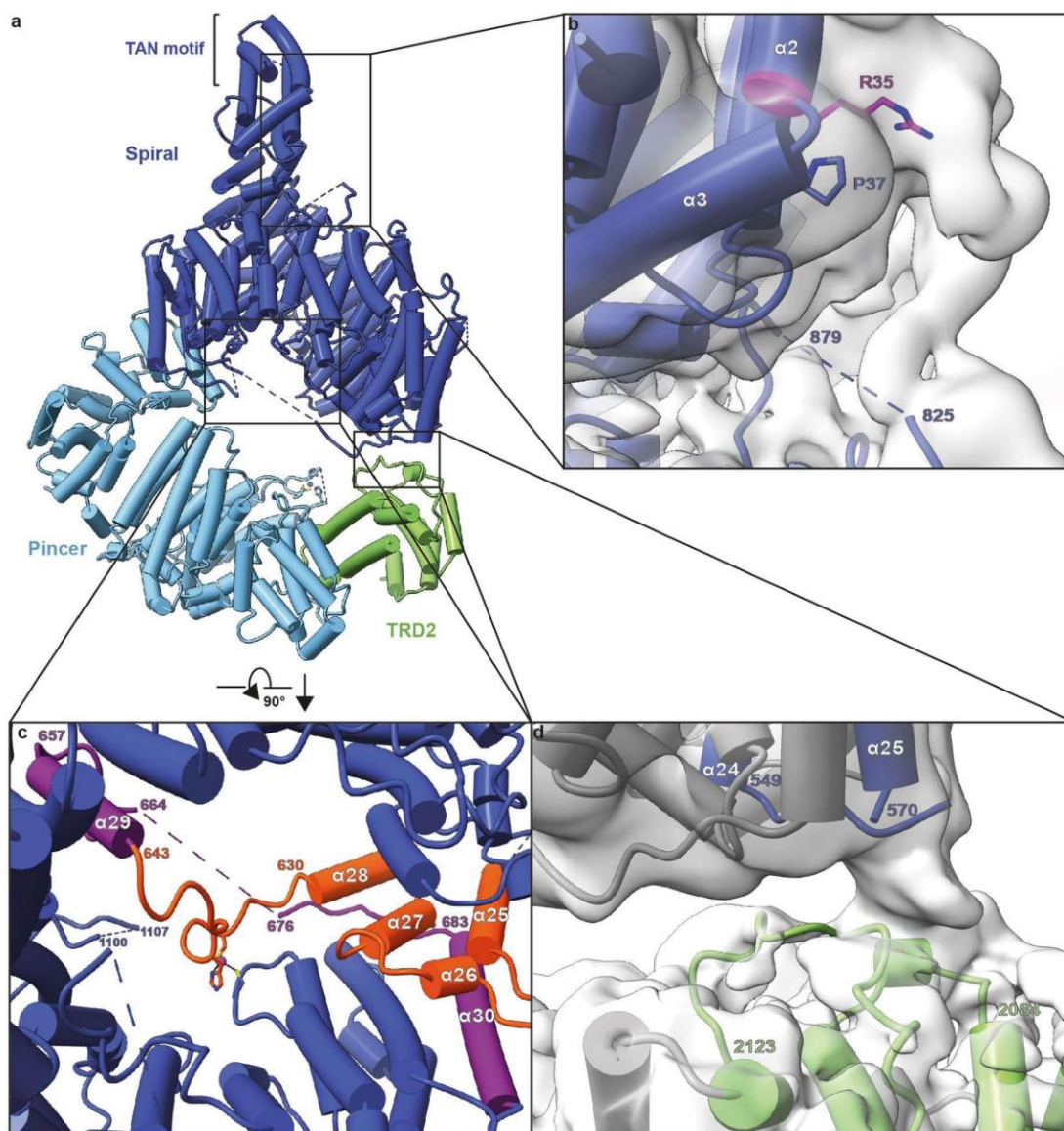
Peer review information *Nature Structural & Molecular Biology* thanks Xiaodong Zhang and the other, anonymous, reviewer(s) for their contribution to the peer review of this work. Peer reviewer reports are available. Anke Sparrmann and Beth Moorefield were the primary editors on this article and managed its editorial process and peer review in collaboration with the rest of the editorial team.

Reprints and permissions information is available at www.nature.com/reprints.

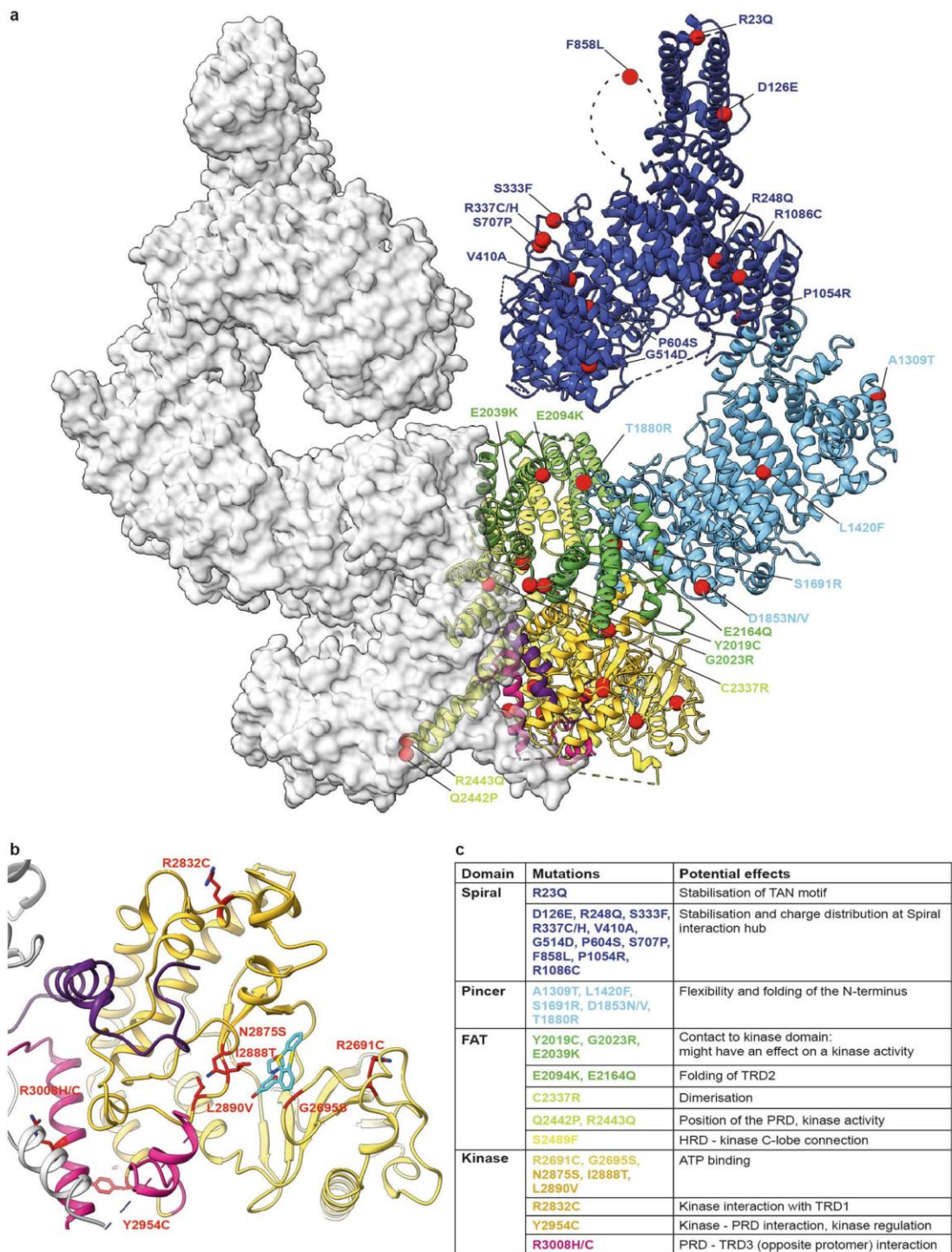


Extended Data Fig. 1 | See next page for caption.

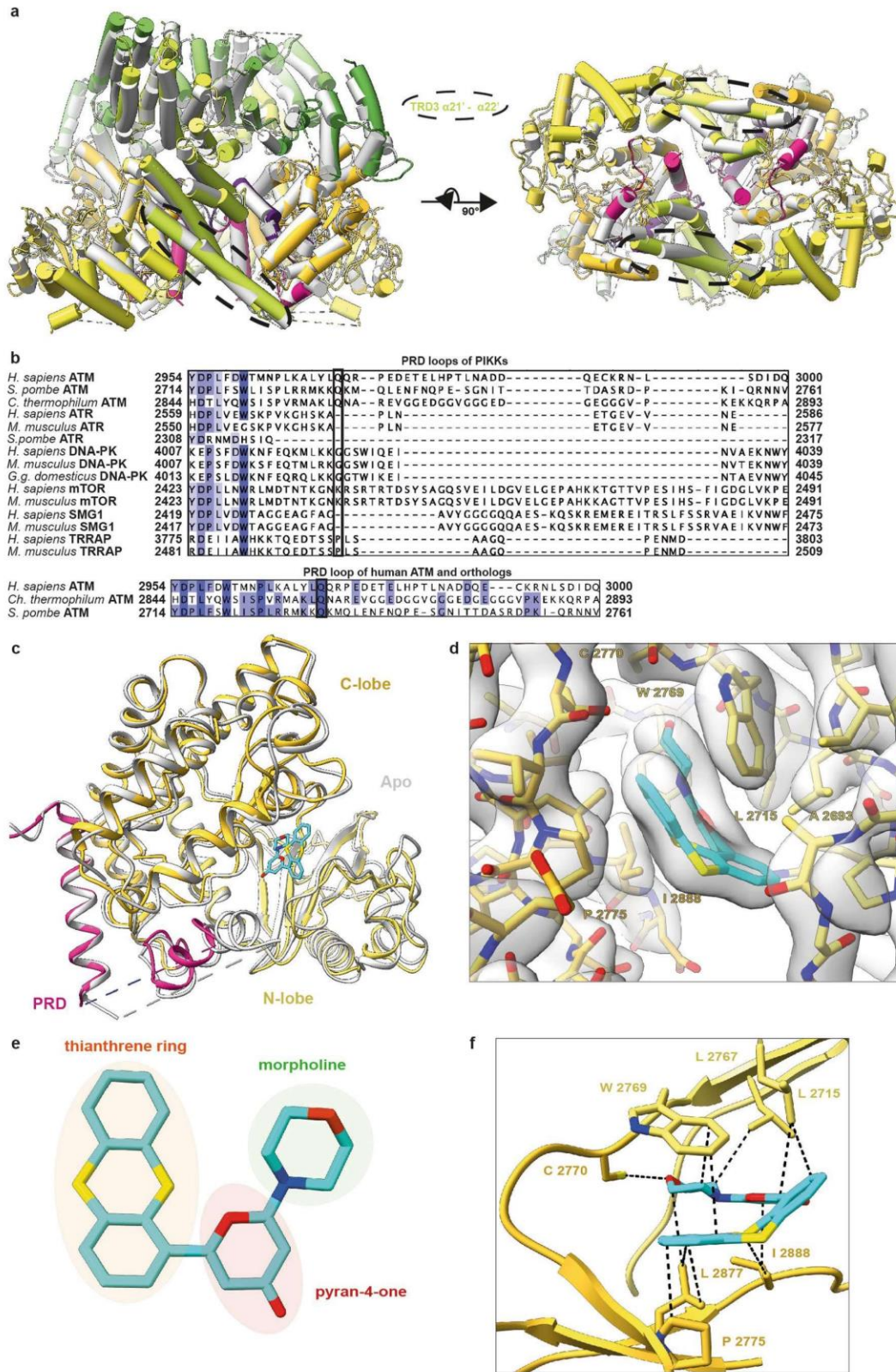
Extended Data Fig. 1 | Features of the N-terminal Spiral domain of human ATM. (a) Cryo-EM density maps and models representing three conformational states of N-terminal Spiral-Pincer domains. Left: N-terminal Spiral domains are touching. Middle: N-terminal Spiral domains are not touching. Right: One N-terminal Spiral domain is resolved, the other one is more flexible. (b) Sequence alignment of zinc-binding motifs of ATM from different species. ATM residues involved in zinc coordination are highlighted and coloured by conservation. (c) Kinase activity time-course of zinc-binding motif mutant (C1899A, C1900A, left) and WT (right) ATM. Kinase activity on CtIP C-terminus (650–897, phosphomimic mutation T847E) visualized by phosphoprotein SDS-PAGE staining. Uncropped gel image is available in Source Data: Extended Data Fig. 1. (d) Effects of chelating agents on the thermal stability of ATM. 1,10-phenanthroline (black) and TPEN (grey) are more specific to Zn²⁺. ATM only (red) and EGTA (pink) were used as controls. (e) Comparison of map to model FSC curves of previously published Spiral (PDB ID: 5NPO) and here presented Spiral domain model.



Extended Data Fig. 2 | N-terminal alpha-solenoid structure of human ATM. (a) Overview of organization of N-terminal spiral, pincer and TRD2 domains, helices depicted as cylinders. TAN motif labelled. (b) Interaction between unstructured loop 825–879 and R35 (helix 2). Density map contoured at 0.0034 and R35 colored in magenta. (c) Top view of spiral solenoid ring. Helices 25–28 and ring-crossing loop (630–643) colored in orange. Helices 29–30 and partially resolved loop (657–683) colored in purple. (d) Interaction between Spiral loop (549–570) joining helices 24 and 25 (blue), and TRD2 loops 2084–2092 and 2107–2123 (green). Density map contoured at 0.0032.

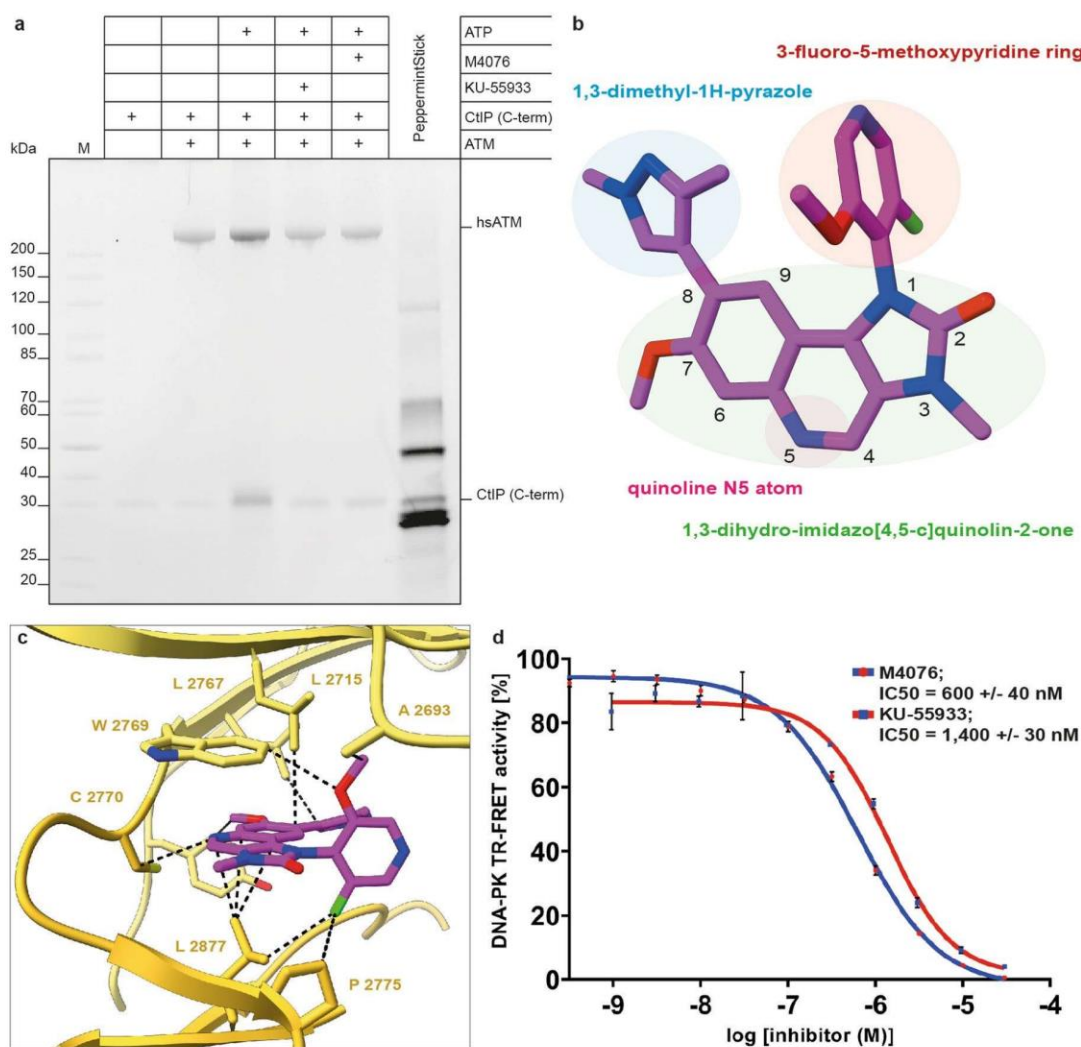


Extended Data Fig. 3 | Mapping of cancer-associated human ATM missense mutations. (a) Positions of commonly reported (count > 5) cancer mutations from COSMIC database depicted on to the ATM protomer. Approximate locations of F858L and T1880R mutations are shown based on unmodelled density. One ATM protomer coloured using domain colour-code, another—shown as a grey surface. Mutated residues are shown as red spheres with mutations indicated. **(b)** Model of KU-55933-bound ATM kinase with commonly (count > 5) mutated amino acid side chains coloured in red. Opposite protomer shown in grey. **(c)** Table summarising cancer-associated human ATM missense mutations. Mutations grouped based on their locations and coloured using domain colour-code.

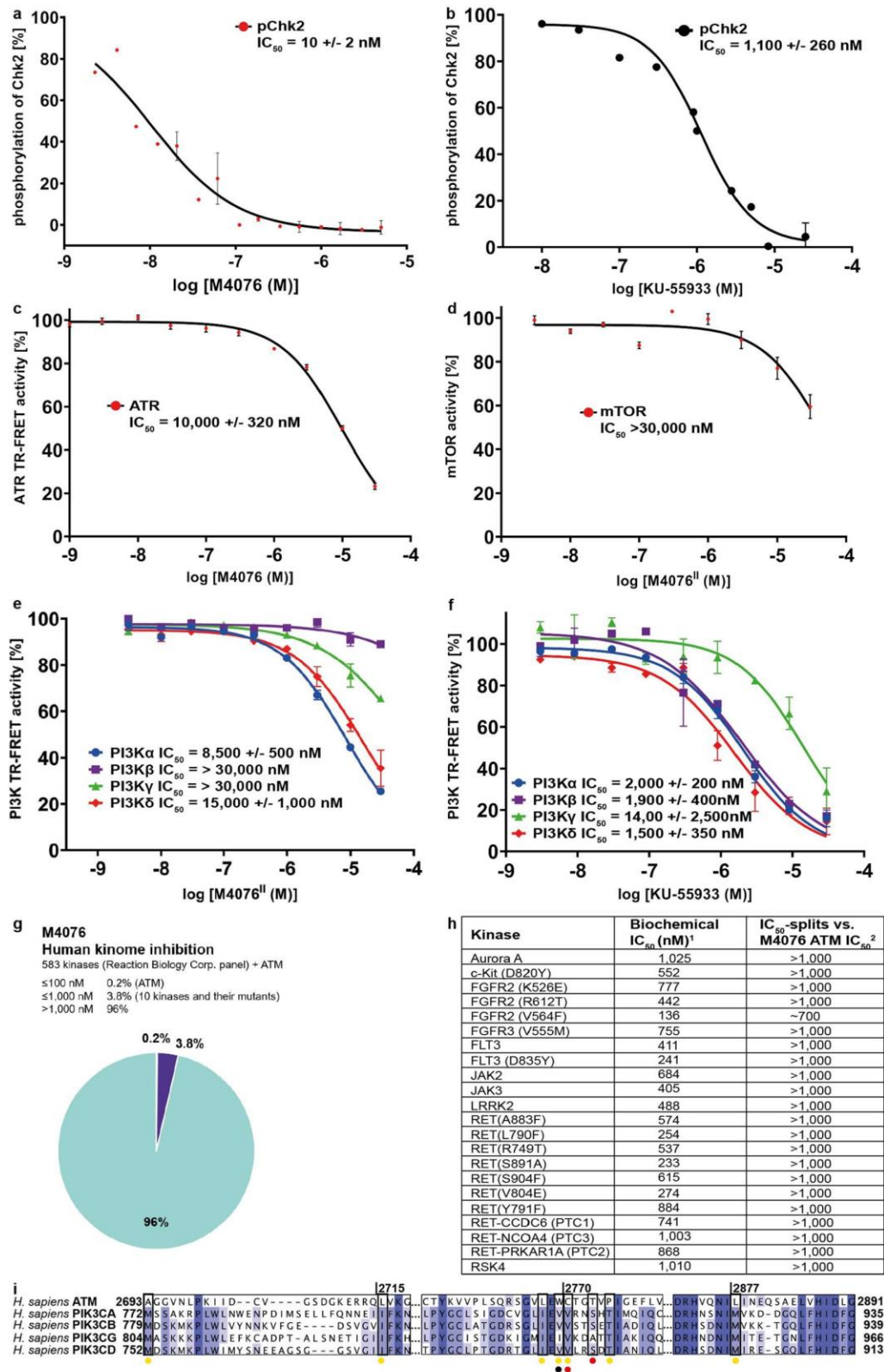


Extended Data Fig. 4 | See next page for caption.

Extended Data Fig. 4 | Conformation of KU-55933-bound human ATM. **(a)** Superimposition of KU-55933-bound human ATM dimer (color) and 'closed dimer' of human ATM (PDB ID: 5NP0; grey). Side and bottom views of C-terminal halves shown, helices depicted as cylinders. TRD3 α 21- α 22 indicated by black dotted line. **(b)** Sequence alignments of PRD loops from PIKKs from different organisms (top) and PRD loops of human ATM and its orthologs (bottom). PRD loops are colored by conservation and substrate-mimicking Q2971 of human PRD is highlighted. **(c)** Superimposition of kinase and PRD domains of inhibitor-bound (color) and apo human ATM (PDB ID: 6K9L; grey) models. **(d)** Cryo-EM density (grey, contoured at 0.0346) and model of the KU-55933 inhibited ATM active site. Clearly visible inhibitor proximal side chains labelled. **(e)** KU-55933 consists of three different ring systems: Thianthrene (orange), Pyran-4-one (red), Morpholine (green). **(f)** Detailed view of ATM active site with KU-55933. Van der Waals interactions indicated by dotted lines and interacting residues labelled.

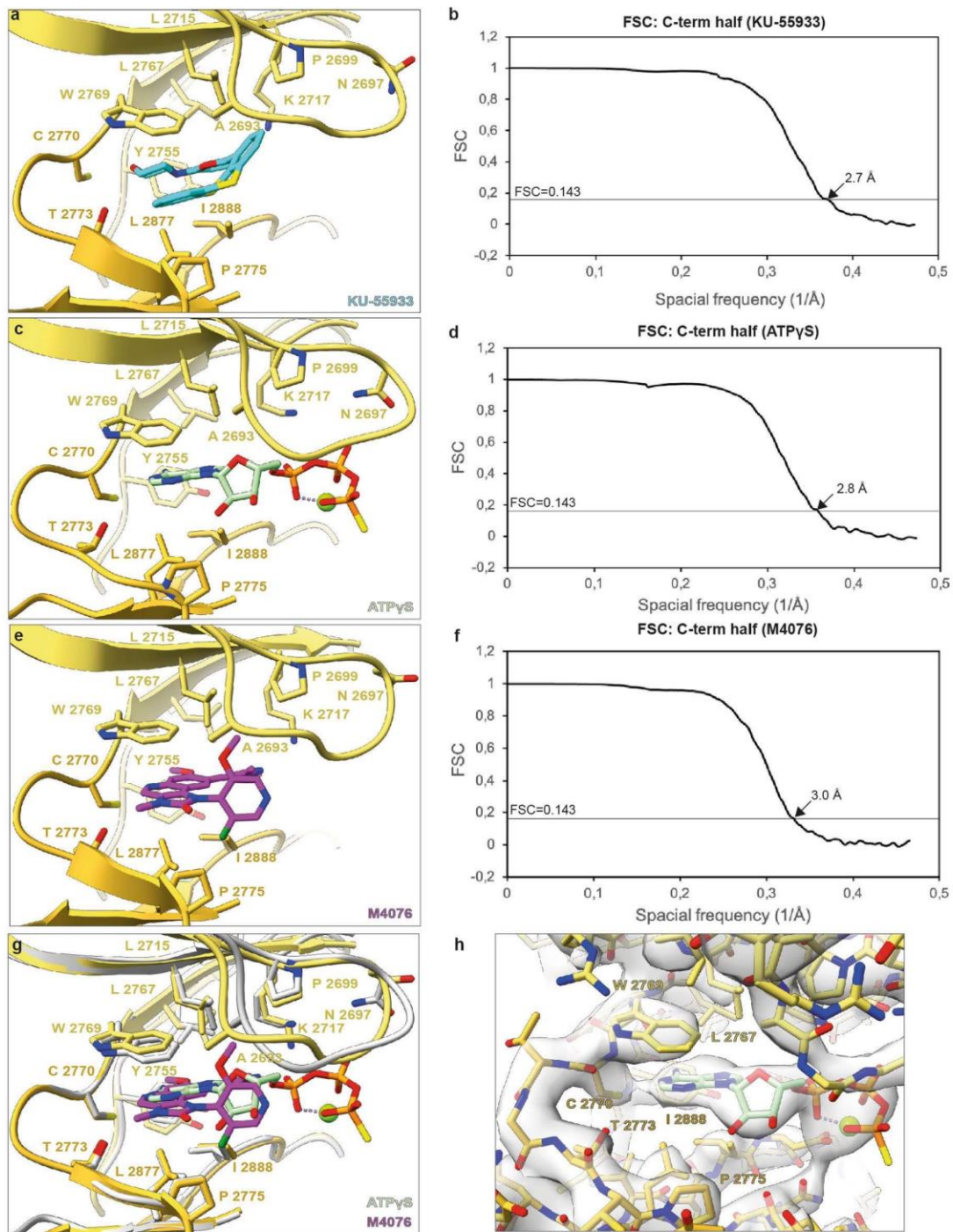


Extended Data Fig. 5 | Inhibition of ATM by M4076. (a) Inhibition of basal ATM kinase activity by M4076. Phosphorylation of CtIP C terminus (650–897, phosphomimetic mutation T847E) visualized by phosphoprotein SDS-PAGE staining, same gel as in Fig. 1a. The experiment was repeated twice with similar results. Uncropped gel image is presented in Source Data Fig. 1. (b) M4076 chemical structure and assignment of functional groups. (c) Detailed view of M4076 (magenta) bound ATM active site. Van der Waals interactions illustrated as black dotted lines and interacting residues labelled. (d) Dose-response curves of enzymatic DNA-PK kinase inhibition by M4076 and KU-55933. Data represent the mean \pm s.e.m. from $n = 16$ independent experiments performed in duplicates for M4076 ($IC_{50} = 600 \pm 40$ nM) and from one experiment performed in duplicates for KU-55933 ($IC_{50} = 1,400 \pm 30$ nM). Data behind graph in panel d are available in Source Data Extended Data Fig. 5d.

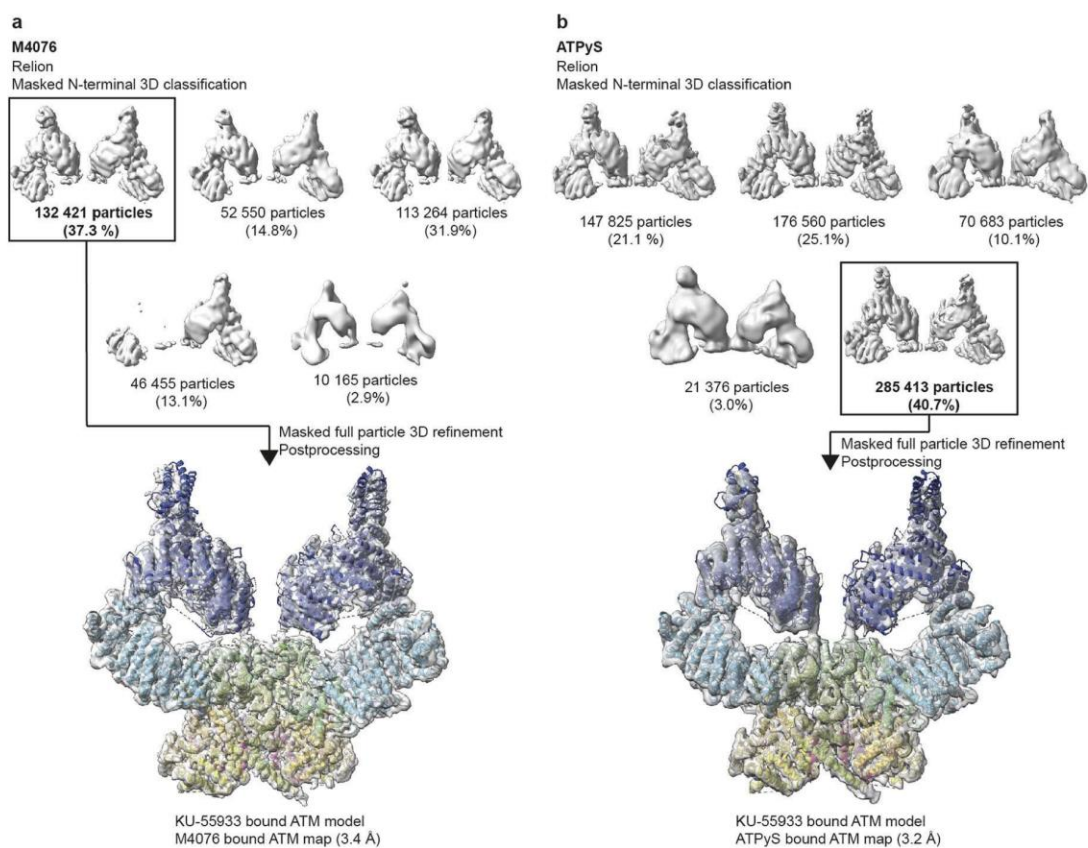


Extended Data Fig. 6 | See next page for caption.

Extended Data Fig. 6 | Kinase specificity of KU-55933 and M4076 inhibitors. (a) In vitro cell-based IC₅₀ for inhibition of 2 Gy-induced phosphorylation of CHK2 (pThr68) in the human colon carcinoma cell line HCT116 for M4076 (IC₅₀ = 10 ± 2 nM) from a Luminex assay. Data represent the mean ± s.e.m. from n = 3 independent experiments performed in singlicates. (b) In vitro cell-based IC₅₀ for inhibition of bleomycin-induced phosphorylation of CHK2 (pThr68) in the human colon carcinoma cell line HCT116 for KU-55933 (IC₅₀ = 1,100 ± 260 nM) from an ELISA. Data represent the mean ± s.e.m. from n = 2 independent experiments performed in singlicates. (c) Dose-response curves of enzymatic ATR kinase inhibition by M4076. Data represent the mean ± s.e.m. from n = 7 independent experiments performed in duplicates for M4076 (IC₅₀ = 10,000 ± 320 nM). (d) Dose-response curves of enzymatic mTOR kinase inhibition by the racemate of M4076. Data represent the mean ± s.e.m. from n = 1 experiment performed in duplicate for the racemate of M4076 (IC₅₀ > 30,000 nM). (e) Dose-response curves of enzymatic inhibition of recombinant PIK3 kinases p110α/p85α, p110β/p85α, p120γ, and p110δ/p85α by the racemate of M4076. Data represent the mean ± s.e.m. from n = 1 experiment performed in duplicates for the racemate of M4076 (IC₅₀ values above 8.5 μM). (f) Dose-response curves of enzymatic inhibition of recombinant PIK3 kinases p110α/p85α, p110β/p85α, p120γ, and p110δ/p85α by KU-55933. Data represent the mean ± s.e.m. from n = 1 experiment performed in duplicates (PIK3 isoforms α, β and δ: IC₅₀ values ~2 μM; PI3Kγ: IC₅₀ = 14 μM). (g) Reaction Biology Corporation (RBC) kinase selectivity profiles of 583 kinases for M4076 tested at 1 μM. Segment sizes of pie chart represent numbers of 583 kinases from RBC panel and ATM in addition with IC₅₀ ranges (cyan: 96% of the tested 583 kinases showed kinase activity values above 50% corresponding to IC₅₀ values above 1,000 nM; dark blue: 10 kinases and their mutants, 22 kinases in total (3.8% out of 583 kinases tested) showed kinase activity values below 50% corresponding to IC₅₀ values between 100–1000 nM). ATM is the only kinase with an IC₅₀ value below 100 nM (0.2%). (h) IC₅₀ values of M4076 determined for 10 kinases and their mutants, which showed kinase activity values below 50% tested at 1 μM M4076 in the RBC kinase selectivity profile against 583 kinases (22 kinases in total, corresponding to the dark blue segment in the Reaction Biology kinase selectivity pie chart in Extended Data Fig. 6g). 1: M4076 was tested in duplicate in a 10-dose IC₅₀ mode with 3-fold serial dilution starting at 10 μM. Reactions were carried out at K_m ATP concentrations of individual kinases according to the RBC K_m binning structure. 2: The biochemical ATM IC₅₀ value of 0.2 nM for M4076 was used for IC₅₀-split calculation of individual kinases. (i) Sequence alignment of human ATM and PIK3 kinases p110α/p85α, p110β/p85α, p120γ, and p110δ/p85α active sites, coloured by conservation. Glycine-rich, catalytic and activation loops labelled. ATM residues forming hydrogen interactions with the inhibitor are marked with red dots, van der Waals interactions - yellow dots, and π-stacking interactions - black dot. Data for panels a-h are available as Source Data (Source Data Extended Data Fig. 6a-h).



Extended Data Fig. 7 | Comparison of ATP γ S-bound to KU-55933 and M4076 inhibited ATM kinase active sites. (a) Active site of KU-55933 (cyan) bound ATM (yellow) with highlighted surrounding residues. **(b)** Gold-standard Fourier shell correlation (FSC) curve from RELION-3.0 of the KU-55933 full ATM map. **(c)** Same as (A) with ATP γ S (green, orange). **(d)** FSC curve from RELION-3.0 of the ATP γ S bound ATM FATKIN map. **(e)** Same as (A) with M4076 (magenta). **(f)** FSC curve from CryoSPARC-2.14 of the M4076-bound ATM FATKIN map. **(g)** Superimposition of ATP γ S (ATM in grey) and M4076 inhibitor (ATM in yellow) bound ATM active sites. **(h)** ATM active site density (grey, contoured at 0.0169) at 2.8 Å resolution with a fitted ATM model and ATP γ S (orange, green).



Extended Data Fig. 8 | N-terminal conformations of M4076 and ATP γ S bound ATM. (a) Masked N-terminal 3D classification of M4076-bound ATM followed by further processing of dominant class and comparison to KU-55933 bound ATM conformation. (b) Masked N-terminal 3D classification of ATP γ S bound ATM followed by further processing of dominant class and comparison to KU-55933 bound ATM conformation.

3. Discussion

3.1. Cryo-EM structure of the Mre11-Rad50-Nbs1 complex

The MRN complex acts as a central, multifunctional DSB repair factor to sense, process, tether DNA ends and to initiate the cellular DDR (via ATM recruitment and activation)^{50,57,117,179}. Further, the MRN complex functions in chromatin organization and telomere maintenance^{180–183}. Until now many mechanistical aspects regarding the activation and regulation of the MRN complex remain unclear. Especially, it was poorly understood how MRN combines both enzymatic activities and scaffolding functions.

3.1.1. The Mre11-Nbs1 interface

The presented structural data clarifies the stoichiometry of the MRN complex as $M_2R_2N_1$. This stoichiometry was robustly observed with different purification strategies (tag-free, Mre11-tagged, Nbs1-tagged) and species (human, *Chaetomium thermophilum*). In support of this finding, quantification of previously published recombinantly purified MRN complex from different labs and organisms (human, *Saccharomyces cerevisiae*) yielded a similar $M_2R_2N_1$ stoichiometry (Figure 12).

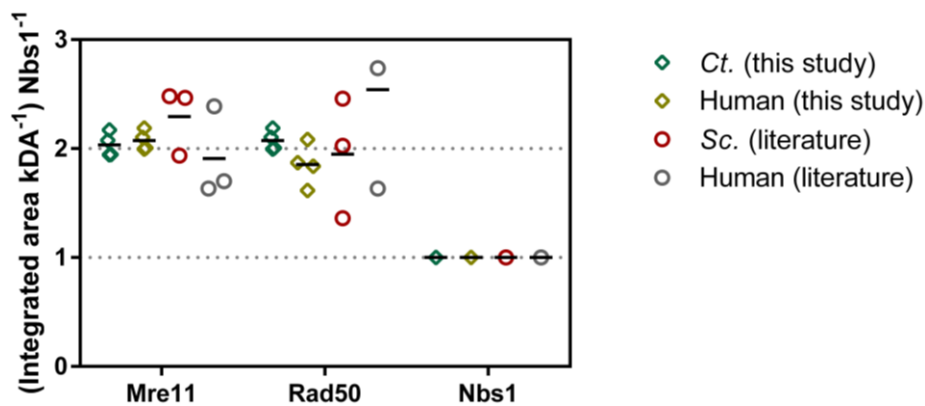


Figure 12: Comparison of MRN complex stoichiometry from this study and literature. Data was normalized by Nbs1. For quantification data from this study, gels (N=4) were quantified. For literature data for human and *Saccharomyces cerevisiae* (Sc) gels (N=3) from various publications were selected^{50,67,117,118,184,185}.

Previously, the stoichiometry of MRN was generally assumed to be $M_2R_2N_2$, even though some authors reported only one Nbs1 subunit bound¹⁸¹. A crystal structure of *Sp*Mre11-Nbs1 complex showed two Nbs1 subunits bind to the nuclease domain of the Mre11 dimer⁸². One Nbs1 subunit bridges the Mre11-dimer via a highly conserved NFKxFxK motif. The presented data reveals that in fact only one Nbs1 subunit wraps around the Mre11 nuclease domain as an elongated chain that binds to the same surfaces on the side of both Mre11 protomers via different regions (Figure 13). The presence of a small helical, species-specific structural feature in the CD of CtNbs1 facilitated the aligning of the otherwise highly symmetrical particles during cryo-EM processing. Thus, the CtMre11-Nbs1 interaction was resolved to a fairly decent resolution that fitted very well to the model obtained by AlphaFold2. The same wrapping mode was observed (both in AlphaFold2 and cryo-EM) for the HsMre11-Nbs1 interaction (Figure 13). However, for the human complex the resolution was significantly lower, possibly due to lack of a prominent structural feature in the CD. The conformation of the human Mre11 dimer obtained in this study was similar to other crystal

structures of eukaryotic Mre11. Recently, a structure of human Mre11 was published in which the protomers are rotated along the dimer interface, despite having a similar fold¹⁸⁶. The twisted conformation in the human Mre11-dimer is most likely caused by a not-conserved disulfide bond and also disrupts the central Nbs1 binding site. Taken the presented cryo-EM data and the conserved features on Nbs1 into account, it can be assumed that the overall architecture of the Mre11 dimer and the Nbs1 interaction is conserved from yeast to vertebrates.

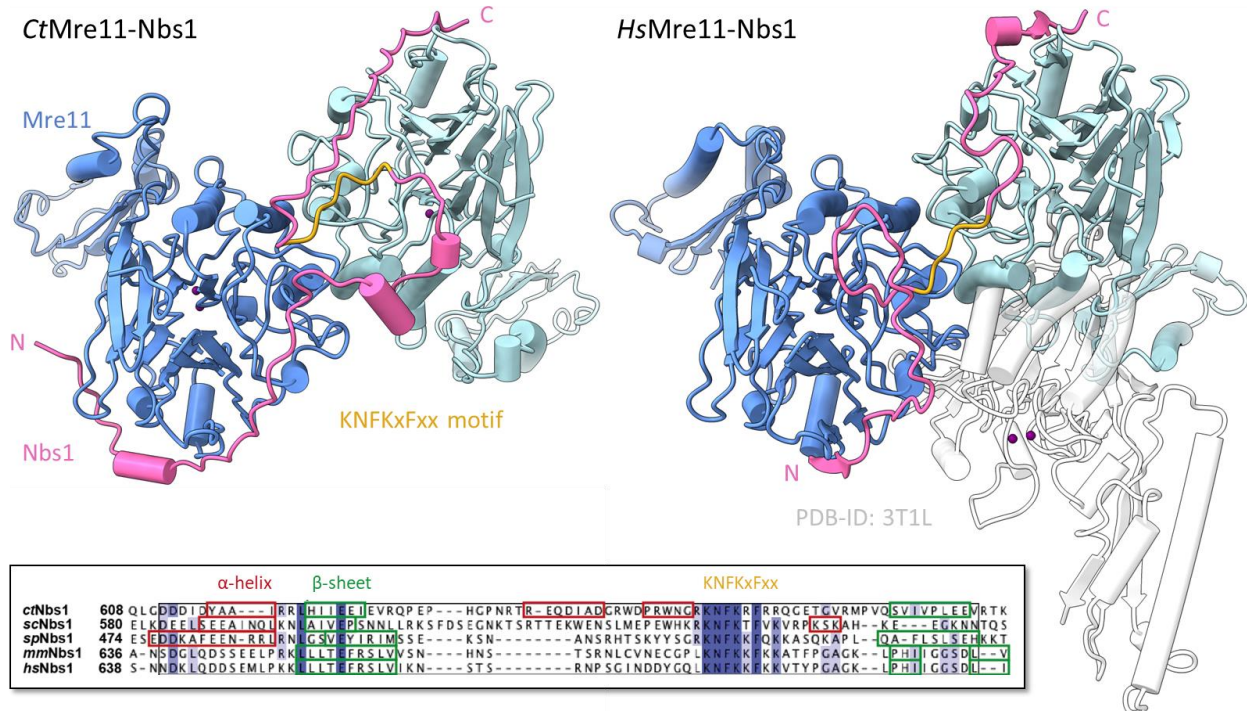


Figure 13: Nbs1 wraps around the Mre11 nuclease. CtMre11 (shades of blue) binds one Nbs1 (pink) that mainly interacts via a conserved KNFKxFxx motif (golden) and the N-/C-terminal sides. HsMre11 cryo-EM structure showed the same conformation, while a crystal structure (PDB-ID: 3T1L) adopted a twisted conformation (light grey) which would prevent Nbs1 binding¹⁸⁶.

Further classification revealed that the Nbs1-Mre11 interaction is rather weak and dynamic, which leads to heterogeneity within the MRN catalytic head. In most particles the CD was bound to Mre11 (92%) while the complete elongate Nbs1 fragment was only present in a smaller subset (25%). The reason for the observed heterogeneity is unclear, however it can be hypothesized that the strong interaction via the conserved NFKxFxK motif serves the stabilization of the Mre11 dimer and the catalytic head which might be critical for nuclear localization, ATM activation and other functions of the complex. In *S. cerevisiae* the Nbs1/Xrs2 provides nuclear localization and is required for ATM/Tel1 recruitment and end joining functions, while it is not required for the nuclease associated functions of MRN/X¹⁸⁷. In mice, a Nbs1 fragment that quite precisely correlates with the visualized Nbs1 fragment, was shown to restore viability and enable ATM activation⁸¹. It has been hypothesized that in order to function, the Mre11 dimer has to undergo dimer-monomer transition (bacterial and archaeal Mre11 are monomeric in absence of Rad50)^{65,66,85}. As eukaryotic MRN is activated via CtIP-Nbs1, a possible mode of activation could be suggested, in which CtIP-bound Nbs1 stops interacting via the CD to enable Mre11-dimer-monomer transition. Taken together, the visualized Nbs1 fragment most likely contains most residues that interact with Mre11 and the

observed wrapping of the Mre11 dimer could be particularly important for roles in DNA tethering and ATM activation.

3.1.2. The Nbs1 N-terminal domain and higher order oligomers

The N-terminal domain serves as a phosphopeptide binding scaffold, that recruits among others phosphorylated CtIP (section 1.2.3.5.1)⁵⁰. A crystal structure of the N-terminal FHA, tandem-BRCT domain was published with and without bound phosphopeptide¹⁰⁷. A refined density for the Nbs1 N-terminus was not obtained during cryo-EM processing, possibly because of its small size (<40 kDa) and flexibility.

However, XL/MS experiments with CtMRN generated some information even for the structurally unresolved areas. In general, the XL/MS restraints fitted very well to the cryo-EM data and were used to verify the model in lower resolution areas (e.g. CCs). The crosslinks agreed with an extended CC conformation which does not argue for elbow elements that appear in structurally similar SMC proteins¹⁸⁸. An AlphaFold2 model enabled us to visualize the crosslinks of the CtNbs1 N-terminal region to the catalytic head (Figure 14). Notably, there are multiple crosslinks of the FHA/tandem-BRCT domain to the side of the Rad50 β -sheets. The more flexible N-terminal linker region was not involved in crosslinking, however AlphaFold2 predicted a Nbs1 helix (577-604), directly prior to the visible Nbs1 region (605-689). Similar to the FHA/tandem-BRCT domain this helix was crosslinking to the Rad50 β -sheets (Figure 14). Intriguingly, a low resolution, unassigned cryo-EM density was located near exactly this putative interaction site (Figure 14). This density could be assigned to the N-terminal Nbs1 domain, the adjacent helix or the C-terminus of Mre11 that heavily crosslinks to the whole Rad50 NBDs.

The Rad50 β -sheets are an interesting interaction site that are reported to be involved in various functions and interactions. Mutation of exposed, hydrophobic residues at this site also reduced the oligomerization rate, DNA binding affinity and nuclease rate of the ScMR complex¹²⁰. It could be assumed that multiple MRN complexes interact via the Rad50 β -sheets in a rather unspecific, transient way and the density could possibly be assigned to neighboring complexes. Mutation of conserved β -sheet residues also led to a chronic ATM-checkpoint activation⁹⁸. ATM activation is dependent on DNA and notably the ATP-bound state of Rad50⁶⁷. In respect of these findings, it is plausible that either ATM interacts directly or indirectly with the Rad50 β -sheets, possibly mediated by multimerization and/or Nbs1. Lastly, several residues at the Rad50 β -sheets were identified as site of Rif2 interaction in yeast¹²⁹. Apart from the proposed destabilization of the DNA-bound state, Rif2 binding could also interfere with MRN regulation by Nbs1 and its interactors. Further research will be necessary to clarify how multiple proteins and domains interact with this important interaction site to modulate the function of MRN.

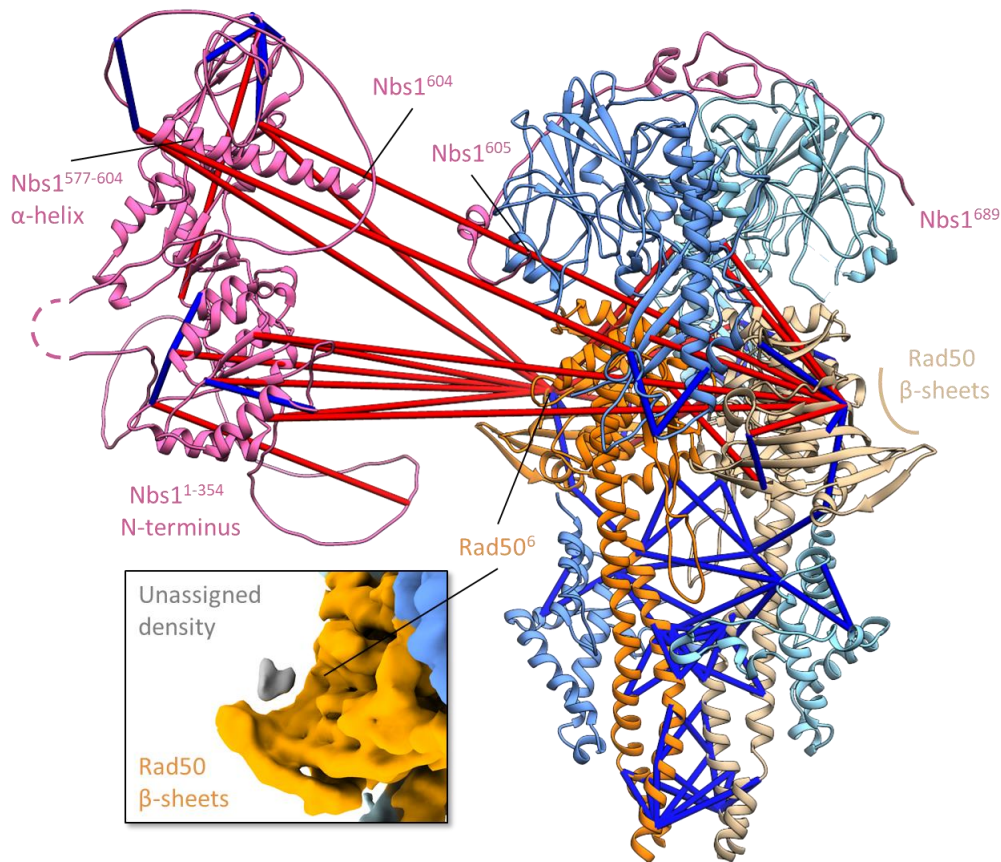


Figure 14: Nbs1 crosslinks to the MRN catalytic head. The N-terminal Nbs1 (pink) domain (1-345) crosslinks (blue, red distance restraints) to the side of the Rad50 (orange, tan) β -sheets. An unassigned, low resolution cryo-EM density was visible at this location. CtNbs1 model was calculated with AlphaFold2.

3.1.3. Dynamics within the MRN catalytic head

In this study, CtMRN bound to ATP γ S adopted a closed rod conformation different from the open ring conformation of EcMR-ATP γ S (Figure 15)⁶⁶. The open “resting state” in EcMR can be interpreted as scanning conformation that enables loading onto (blocked) DNA ends. However, the narrow gap between the CCs in the rod conformation would prevent loading of blocked DNA ends into the CtMRN complex. In biochemical studies we show that CtMRN-ATP γ S nevertheless binds linear DNA ends with very high affinity.

The rod conformation could indicate that eukaryotic MRN is in a more autoinhibited conformation than bacterial MR, which is also consistent with previously published data. The eukaryotic MRN complex showed only very weak endonuclease activity and required phosphorylated CtIP for its activation^{50,117}. As previously discussed, the binding of Nbs1 could promote an inactive state, possibly by stabilizing the Mre11 dimer configuration (section 3.1.1). Comparison with the CtRad50^{NBD}-CtMre11^{RBD}-ATP γ S complex revealed that full engagement of both Rad50 signature motifs with the γ -phosphate promotes opening of the CCs (Figure 15C)⁸⁸. In agreement with this data we found that, upon ATP addition, a small subset of particles (20%) had open CCs, similar to the EcMR resting state. In our structure we observed that only one signature motif was interacting with the γ -phosphate. Intriguingly, 3D variability analysis revealed

that the Rad50 protomer that does not interact with the signature motif of the other protomer is in a relatively flexible state (Figure 15B, orange Rad50 is flexible, tan Rad50 is rigid). The semi-engaged, asymmetric Rad50 NBDs could be induced by Nbs1 binding (compare Figure 15A). The Nbs1 residues located N-terminally of the CD (Nbs1⁶¹⁰⁻⁶¹⁵) interact with the Mre11²¹⁴⁻²²⁵ loop. This is different in the Nbs1 residues located C-terminally of the CD (Nbs1⁶⁸⁷⁻⁶⁸⁹), where this interaction is not present and the Mre11²¹⁶⁻²²⁵ loop of the other protomer that interacts with a Rad50 helix (Rad50¹²⁷⁹⁻¹²⁸⁶). The flexible Rad50 protomer is also the one in which the Mre11²¹⁴⁻²²⁵ loop interacts with Nbs1 and not with Rad50. It is very likely that the Nbs1 interaction with Mre11 induces asymmetry within the MRN catalytic head, which in turn promotes the more autoinhibited rod conformation.

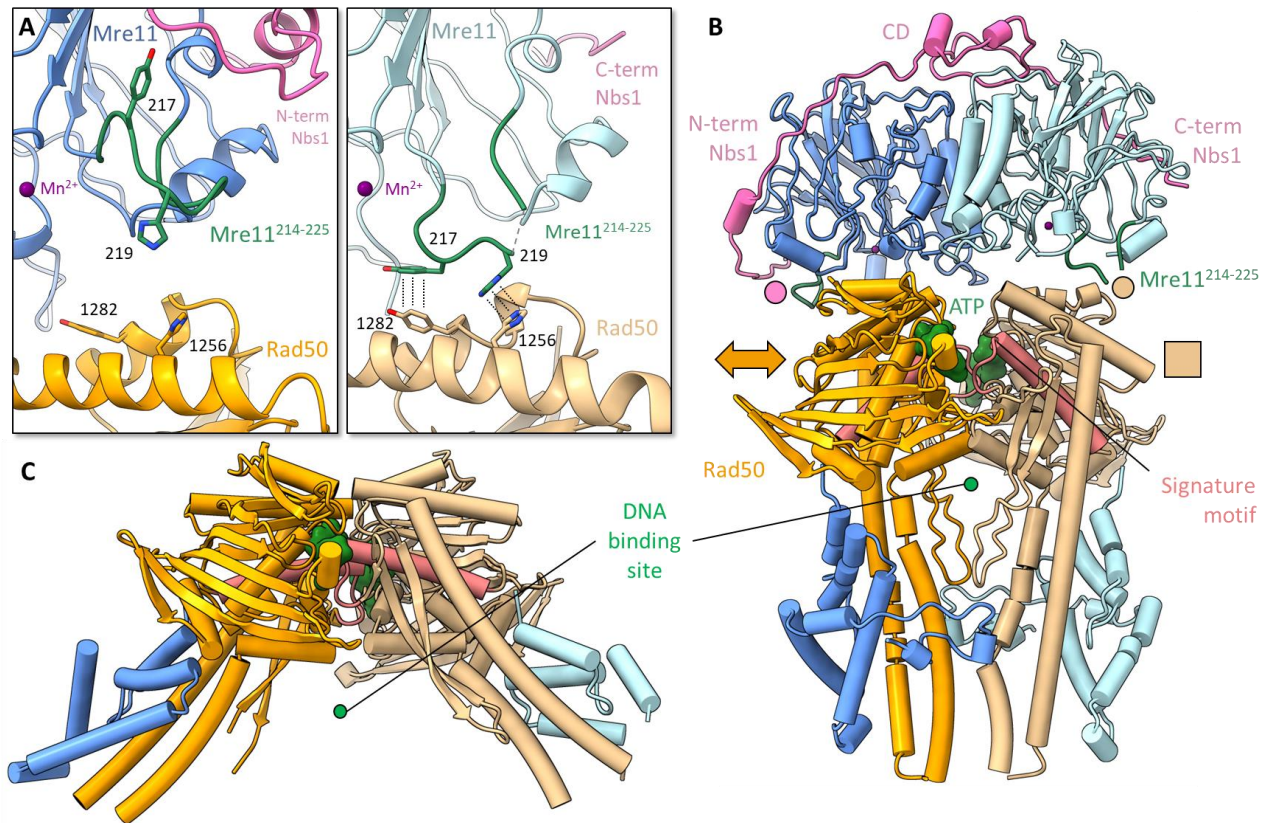


Figure 15: Dynamics within the MRN catalytic head. A: Asymmetric Nbs1 binding induces an asymmetric conformation of Rad50 and Mre11. Mre11²¹⁴⁻²²⁵ loop interacts with the N-terminal interaction region of Nbs1 (panel left), but not with the C-terminal interaction region (panel right), where it interacts with Rad50. **B: Binding of Nbs1 induces asymmetry and possibly flexibility within the catalytic head.** The Rad50 protomer (orange) that shows no interaction with the Mre11²¹⁴⁻²²⁵ loop (green) is more flexible (arrow symbol) than the other protomer (tan, square symbol). ATP is highlighted green and Rad50 signature motif (1206-1209) in red. The DNA binding site at the base of the Rad50 NBD is highlighted by a green circle. The Mre11 capping domain has been removed for visibility. **C: Symmetric engagement of the Rad50 signature motifs with ATP forces the CCs in an open conformation.** Crystal structure (PDB: 5DA9) shows an exposed DNA binding site⁸⁸.

Consequently, one could speculate that Nbs1 binding to CtIP promotes the more rigid, ring-shaped conformation of Rad50 to enable activation of the MRN complex. Dynamic switching between engaged (Rad50^{NBD} crystal structure) and semi-engaged (this study) states is in agreement with studies on archaeal MR that show open and partially open CCs¹⁸⁹. ATP and DNA binding could stabilize the open conformation

with fully engaged NBDs, since DNA ends enhance ATP hydrolysis rate by approx. 10x in human and *CtMRN*⁹⁶. Thus, it can be assumed that DNA interacts with MRN after ATP-dependent loading on DSBs at the DNA-binding site at the Rad50-NBDs, between the CCs. This is in consistency with crystallographic data on *CtRad50* and archaeal MR as well as cryo-EM data of prokaryotic MR^{66,88,90}. To summarize, Nbs1-binding could induce an asymmetric, semi-engaged state of the Rad50-NBDs. ATP binding and full-engagement of the NBDs would be required to pry the CCs open and to enable loading of DNA ends.

3.1.4. DNA-binding activities

As previously mentioned, the rod-state raised the question whether the canonical DNA binding site at the base of the Rad50 NBDs remained accessible and what role ATP/ATPyS plays in DNA binding. Intriguingly, it turned out that full-length *CtMRN* is able to bind DNA, even in absence of ATP/ATPyS, albeit with lower affinity. This finding was in contrast to previous work on bacterial and truncated eukaryotic MR complexes^{65,86,94,95}. Different FA plateau values in our analysis hinted towards binding of a second DNA molecule via a second DNA binding site. We identified the eukaryote-specific C-terminal extension as second binding site, removal of the Mre11 C-terminus resulted in strictly ATP-dependent DNA binding, similar to aforementioned results. Altogether, we show that the DNA-binding properties of eukaryotic MRN are more complex than in prokaryotic MR. We revealed that the canonical, conserved DNA binding site is strictly dependent on ATP-binding and has high specificity towards DNA ends. An additional, eukaryote-specific DNA binding site in the C-terminus of ScMre11 has been identified to be important for formation of meiotic breaks and chromatin organization¹⁹⁰. Our data revealed the function of the C-terminal DNA binding site is to bind circular DNA with lower affinity and independent of ATP. We envisioned a model with two DNA binding modes that facilitates understanding of the many functions of the eukaryotic MRN complex (Figure 16). It seems that MRN, similar to the prokaryotic MR, is loaded onto DNA ends to initiate DSB repair/DDR. However, the complex can also bind to internal, undamaged DNA via the Mre11 C-terminus. This, most likely enables the complex to scan intact DNA for DSBs and to function in poorly understood roles in chromatin organization or transcription^{191,192}.

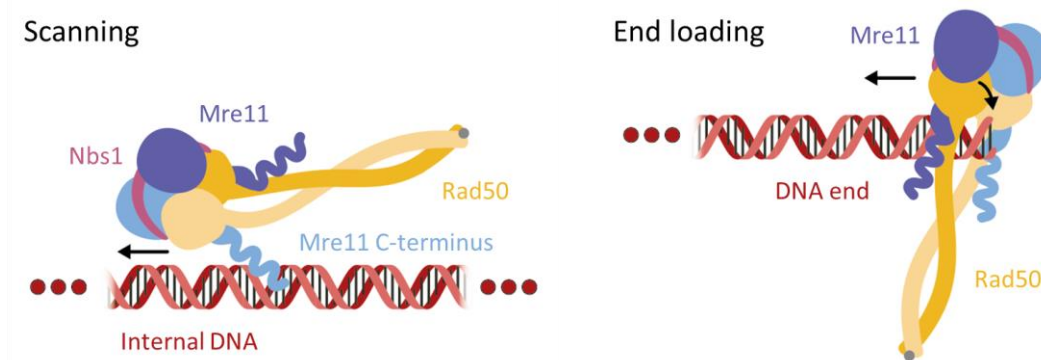


Figure 16: Two modes of DNA binding by the MRN complex. In ATP-independent scanning mode, MRN binds to internal DNA via the C-terminus of Mre11. Upon encounter of a DSB, the complex is loaded to the DNA end in an ATP-dependent mode to initiate DDR and resection.

Several recent studies can be interpreted using a model with separated DNA binding modes. In single-molecule DNA curtain experiments, MRN was shown to bind DNA ends where it cleaved off Ku70/80 and itself in a process that required ATP⁶⁴. This activity can be attributed to the canonical DNA binding site. However, prior to DNA end recognition, MRN was diffusing along internal DNA with ATP-independent diffusion coefficients, where it also managed to bypass protein obstacles⁶⁴. The internal DNA sliding activity can be attributed to the C-terminus of Mre11, due to the fact that we did not observe binding to linear DNA by MRN with truncated Mre11 C-terminus. Another study reported a physiologically occurring truncation of the *HsMre11* C-terminus in certain cancer cells that is similar to the truncated construct we analyzed⁹². The authors observed loss of DNA binding and nuclease activities of MRN *in vitro* and discussed beneficial effects of these MRN alterations for cancer cells. However, those activities were exclusively assessed in absence of ATP, which could indicate that ATP-dependent DNA end interaction might still be intact. Thus, the survival advantage caused by this truncation could maybe better attributed to MRN's DSB repair-independent roles.

3.1.5. MRN apex domain tethering

In various studies it has been established that MRN complexes can oligomerize via their apex domains to form long, DNA-end tethering assemblies^{101,103,104,120,180,193,194}. The apex domain was crystallized in rod and open conformations which fits very well to the ring-rod dynamics observed on the MRN head and CC domains (Figure 7). Previously, it was assumed that apex dimerization could be either between the CCs of a single MRN complex (intra-complex) or between the CCs from different MRN complexes (inter-complex)¹⁹⁴. The inter-complex assembly was thought to explain how two DNA ends are tethered by two MRN complexes. However, it remained unclear how the complexes would transition from intra- to inter-complexes and vice versa, a dynamic that has been observed in AFM^{99,104}. In fact, the emerging roles of the CCs as chemo-mechanical element as opposed to a mere head-apex linker and the stability of the CC interface made such inter-intra transition very unlikely. The most likely function of the apex domains is that of a stably associated hinge within an intra-complex that is able to switch dynamically between ring and rod state.

Cryo-EM processing led to a lower resolution density in which two MRN apices dimerized in a rod conformation to join two MRN complexes. This explains that MRN is an intra-complex that can further dimerize via the apex domain to form a 120 nm long assembly, able to tether two DNA ends (Figure 17). As the tethered apex domains adopt a rod conformation, it seems this allows a functional crosstalk between ATP-dependent head dynamics and tethering via the apex domain. In *Chaetomium thermophilum* the apex interacts, most likely quite transiently, via a small hydrophobic interface surrounded by salt bridges (Figure 17B). However, MRN forms large clusters on DNA that are also mediated via head-head interactions (Figure 17C), multiple protruding CC rods from different complexes could form multivalent interactions to enhance the tethering strength. This would even allow a regulation of tethering strength depending on the MRN cluster size. These clusters could also interact with MRN clusters on opposing sister chromatids which would explain observed sister chromatid cohesion at DSBs in *Saccharomyces cerevisiae*¹⁹².

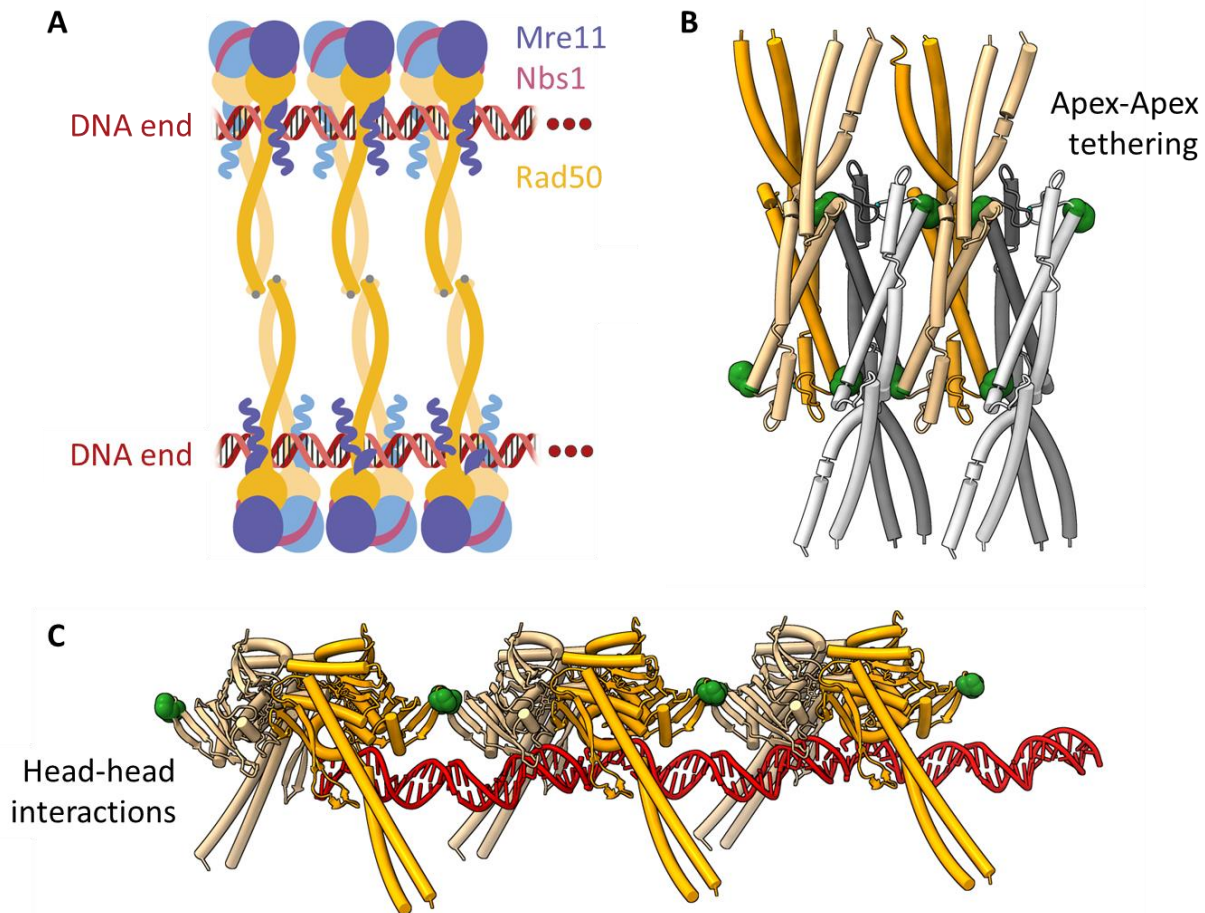


Figure 17: MRN oligomerizes via different parts of the complex. A: Schematic model to integrate multiple MRN oligomerization modes. Head-to-head oligomerization and Apex-Apex tethering could cooperate to enhance tethering strength. **B: Apex-Apex tethering via the Rad50 Apex domain.** The crystal lattice from *CtRad50^{apex}* in this study suggests a higher order oligomerization mode via hydrophobic (F688 highlighted green) and ionic interactions. **C: Head-head interactions on DNA-bound Rad50 NBD.** Conserved ionic interactions were shown to promote *Ct* and *ScRad50* oligomerization and nuclease activity^{88,120}.

Analysis of the *HsRad50* apex crystal structure revealed a similar tetrameric assembly, with mostly ionic interactions¹⁹⁴. Mutation of the apex tethering interface impaired repair of ROS induced DNA damage and homologous recombination in human cells, highlighting its functional significance. Intriguingly, an ATM and ATR phosphorylation site (S635, Q636) has been reported which is located in a loop insertion element that is part of the apex-apex interface^{158,159,195}. Mutation of this SQ-site affected DSB repair, checkpoint activation and survival and did not impair nuclease activity *in vitro*. Analysis of the apex crystal structure revealed that upon phosphorylation, the tethering stability could be increased through interaction with basic amino acids on the opposing apex protomer. These results indicate that tethering might even be regulated by ATM/ATR in human cells. However, research on *Saccharomyces pombe* MR found no increased sensitivity towards Camptothecin/Hydroxyurea in chimeric Rad50 protein where the apex domain was replaced with a bacterial dimerization domain¹⁰². These results and the different dimerization interfaces in human and *CtRad50* apex domains suggest the functional importance of apex-mediated tethering and regulation might differ between species.

3.2. Molecular basis of human ATM kinase inhibition

Upon activation by the MRN complex, ATM is the central signal kinase that initiates the DDR in response to DSBs¹³¹. ATM also functions outside the nucleus where it is activated in response to oxidative stress¹⁴⁹. Many mechanistical aspects regarding the activation of ATM and its DNA binding activity remain unclear. Previous structures of human ATM had a low resolution in the flexible N-terminal solenoid domain, which limits the understanding of this important protein interaction hub¹⁵⁰. DDR proteins are a promising target in cancer chemotherapy¹³¹. However previously no structures of ATM bound to inhibitor molecules were available for structure-based drug design.

3.2.1. The N-terminal solenoid domain

The N-terminal solenoid domain showed high conformational flexibility in multiple organisms studied, however this did not translate to structural rearrangement within the FATKIN domains^{111,152,154}. Binding of KU-55933 inhibitor increased the overall rigidity of ATM and thus enabled us to obtain a high-resolution EM-density that allowed thorough model building for the entire solenoid region. The high quality of the map revealed two previously undiscovered zinc-binding sites in the spiral and pincer domain. These motifs are conserved in higher eukaryotes and might serve to stabilize the solenoid domain and/or be involved in interaction with the multiple binding partners of ATM. A similar zinc-binding motif that involves cysteine and histidine residues was recently discovered in yeast ATR (Mec1), where it might stabilize the interaction with its activator ATRIP (Ddc2)¹⁹⁶. The zinc-binding motif in the pincer domain stabilizes a loop that harbors a residue (T1880R) which is a hotspot cancer mutation and a residue that was shown to be involved in ATM activation^{197,198}. This could hint binding of an interactor to or near this site.

Several studies showed that ATM has DNA binding properties, and biochemical assays revealed that fungal ATM solenoid domain alone has the ability to bind DNA^{67,111,152}. Similar to the whole ATM kinase, the solenoid domain had higher affinity towards longer DNA stretches and for ATM activation, no DNA ends were required^{67,111}. Taken together, the DNA binding activity might be needed to enable the formation of the MRN-ATM-DNA complex that promotes ATM activation, but most likely it is not needed to detect DNA structures (e.g. DNA ends, nicked DNA)¹⁵². A surface map, calculated from our atomic model, revealed positively charged patches at the N-terminal, conserved TAN motif (Figure 18). The TAN motif was shown to be involved in DNA damage signaling and telomere maintenance and is the only conserved region in the otherwise variable solenoid domain¹⁹⁹. Intriguingly, mutated TAN showed reduced recruitment of ATM to DSB lesions, this could hint an involvement in DNA dependent MRN-ATM interaction¹⁹⁹. The TAN motif also harbors an important cancer mutation (R23Q)²⁰⁰. This mutation reduces the positive surface charge which possibly influences DNA binding affinity.

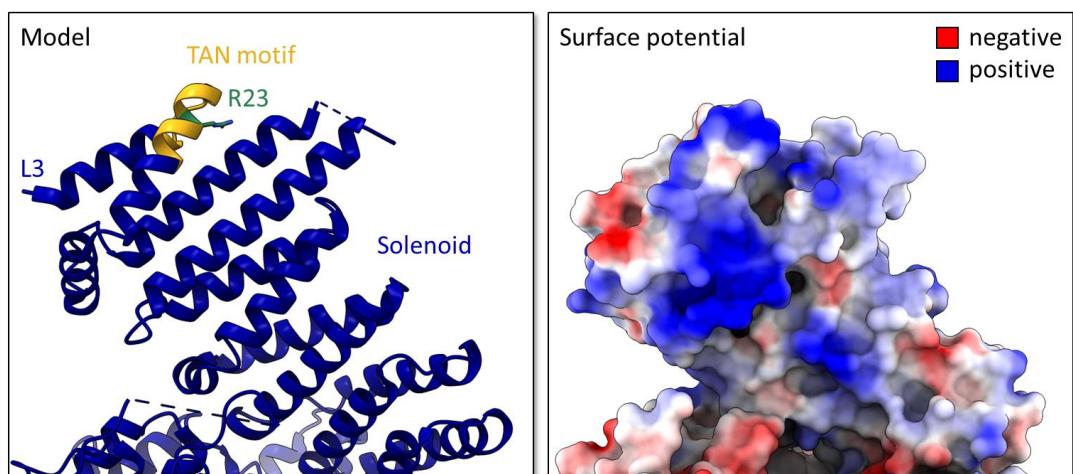


Figure 18: Model and calculated surface potential of N-solenoid and TAN motif. The N-terminal solenoid (blue) and the TAN motif (golden) show a positive surface charge (blue). The cancer mutation R23Q (green) reduces the positive surface charge.

3.2.2. The kinase domain and its regulation

Structures of ATM, including ours, showed the kinase to be in an autoinhibited dimeric form which is accordance to previous biochemical studies (Figure 19A)¹⁵⁰⁻¹⁵⁵. Similar to other high-resolution cryo-EM structures of the ATM kinase domain, our structure shows how access to the kinase active site is blocked by the PRD¹⁵⁰⁻¹⁵⁴. Apart from the restricted access by the PRD, the kinase active site seems to be in a catalytical competent conformation. Alignment of the inhibited ATM kinase active site with that of the SMG1-8-9 complex, bound to its activator UPF1, shows how Q2971 mimics the SQ/TQ substrate glutamine (Figure 19B)²⁰¹. The PRD is locked into position by the TRD3 CCs of the of the other protomer in all dimeric structures (Figure 19A, green). In a low resolution cryo-EM structure of monomeric ATM, this TRD3 is not present which would enable a downward shift of the PRD¹⁵⁶. Thus, the PRD blockage is removed which would explain how ATM is activated upon monomerization (Figure 19C). However, the structural evidence for this mode of activation is fairly weak, given the low resolution of the monomeric structure (7.8 Å). Dimeric ATM structures, especially from heat-tolerant model organisms, showed extensive hydrophobic interfaces at the TRD2-TRD2 dimer interface (Figure 19A)¹⁵². Even though biochemical evidence for dimer-monomer transition has been published, large structural rearrangements would be required to shield the hydrophobic patches²⁰².

Apart from the strong dimer-interface, two additional observations could indicate the activation of ATM does not require monomer-dimer transition. At first, the high conformational flexibility in the N-terminal solenoid domain. In some asymmetric dimer structures, the PRD was distorted which might indicate a more active conformation and explain the low basal kinase rate of ATM^{150,153}. It is also very likely that either PTMs or binding of interacting proteins (e.g. Nbs1) that modify the N-solenoid, translate to stabilization of an active kinase conformation. Secondly, the location of the PTMs that are required for ATM activation. Upon recruitment of ATM to DSBs by the MRN complex, the activation process requires auto-phosphorylation of at least five sites (S367, S1885, S1893, S1981, S2996) and Tip60-dependent acetylation at K3016¹⁹⁸. Intriguingly, all phosphorylation sites are located at flexible, exposed loops that were not

structured in our map (Figure 19A, red). As the phosphorylation sites are not located near the dimer interface or the PRD helices that phosphorylation most likely does not directly translate to dimer dissociation or other substantial conformational rearrangements. The effect of the phosphorylation could rather promote or regulate the binding of activating interactors. In contrast, the acetylation site at K3016 is located directly in a PRD helix where it possibly weakens ionic interactions to promote PRD removal.

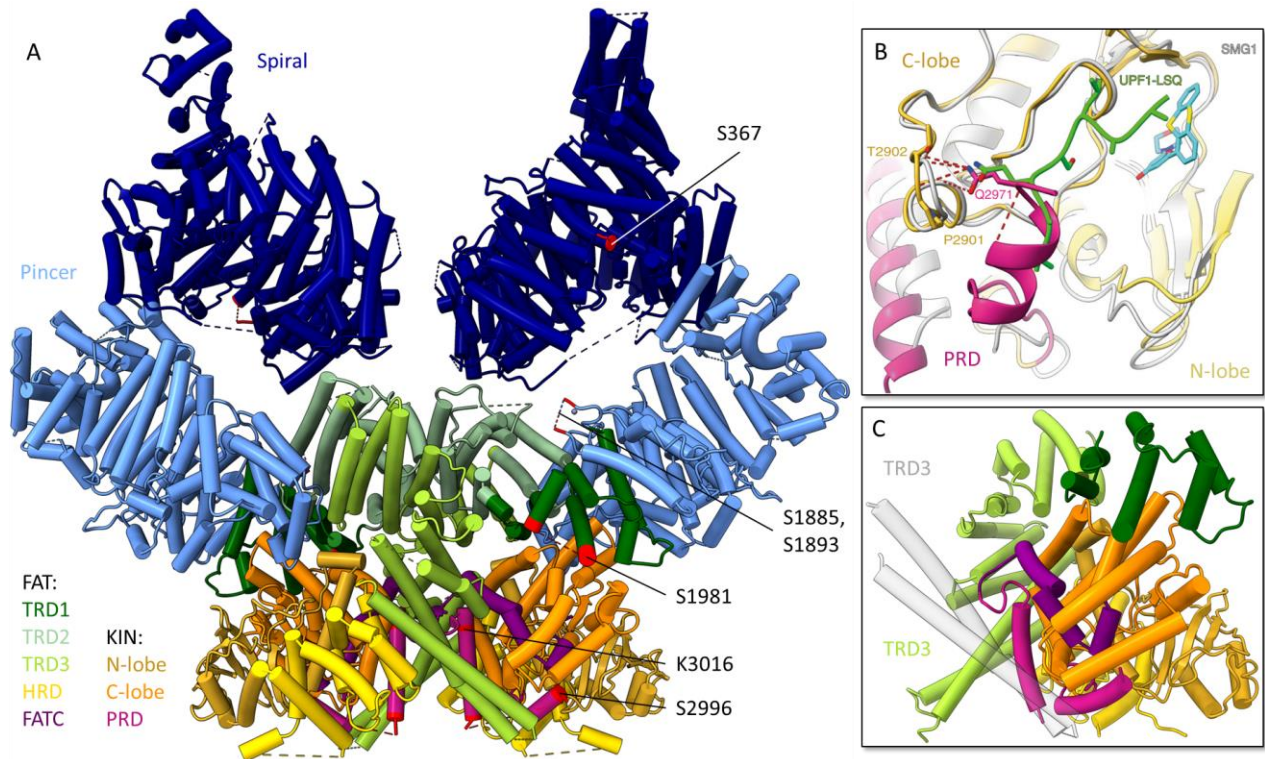


Figure 19: The ATM kinase and its regulation. **A:** Human ATM is an autoinhibited dimer with characteristic PIKK domain architecture. Auto-phosphorylation sites that promote ATM activation are located in flexible loops (red, S367, S1885, S1893, S1981, S2996), an acetylation site is located in the conserved PRD helix (red, K3016) and is modified by the Tip60 acetyltransferase. **B:** Q2971 located in PRD (pink) imitates substrate glutamine and interacts with the backbone of the kinase C-lobe (dotted lines). Superimposed substrate-bound (green, UPF1-substrate) SMG1 (grey, PDB-ID: 6Z3R) and KU-55933 bound ATM (colored) kinase active site. **C:** In monomeric ATM the TRD3 CCs (green) from the other protomer (grey) do not stabilize the PRD helices (pink) that restricts active site access.

Cryo-EM studies on mTOR1 revealed that binding of its activator RHEB to an area distant of the active site caused global conformational changes within the protein complex²⁰³. These conformational changes caused allosteric realignment of the active site residues to a more active conformation²⁰³. A structure of an Nbs1-peptide, bound to the ATM N-solenoid did not show significant active site changes (Figure 11)¹¹¹. However, biochemical analysis showed that for full activation Rad50, DNA and either Mre11 or Nbs1 are required⁶⁷. Up to date, the structural insights into ATM activation are limited and a full structure of ATM and MRN would be required to understand how this important cellular process is initiated.

3.2.3. Molecular basis of ATM-inhibitor potency and selectivity

ATM is a promising target for cancer therapy given its central role in DDR signaling (section 1.3.2). The rationale in targeting ATM is either to increase the cellular sensitivity towards IR or DNA-damaging agents, or to induce synthetic lethality by co-treating cells with PARP- or ATR-inhibitors (section 1.3.2.2). The first known PIKK-inhibitors Caffeine and Wortmannin are natural secondary metabolites with low potency (Caffeine) and specificity (Wortmannin)^{204,205}. Initial ATM-specific inhibitor (KU-55933) was identified only by compound library screens given the lack of structural data²⁰⁶. Although highly specific, the high lipophilicity of KU-55933 prevents therapeutic usage¹³¹. In subsequent research, this inhibitor has been used as lead structure and its pharmacokinetic properties were improved by functionalization^{172,207}. More recently, ATM-inhibitors based on new lead structures were developed (AZD0156, AZD1390)^{177,178}. We provide the first high-resolution structure of KU-55933 bound to the ATM kinase active site. In addition, we obtained high-resolution structures of the ATM kinase bound to ATPγS and the inhibitor M4076. The ATPγS-bound active site showed ATM in an ATP-state and revealed the binding modalities of two structurally diverging, ATP-competitive inhibitors.

M4076 was developed by Merck KGaA as a highly-potent and selective ATM inhibitor with a novel lead structure and is currently (24.05.2021-01.08.2022) in phase 1 clinical studies for treatment of advanced solid tumors (ClinicalTrials.gov Identifier: NCT04882917). In our study M4076 shows extremely high potency ($IC_{50} = 0.2$ nM), which is significantly higher than KU-55933 ($IC_{50} = 7.5$ nM) and also higher than that of other inhibitors in clinical phase 1 studies (AZD0156 $IC_{50} = 0.6$ nM, AZD1390 $IC_{50} = 0.8$ nM)^{177,178}. Comparison of the ATM kinase active site bound to ATPγS, KU-55933 and M4076 explains the molecular reasons for the increased potency of the latter inhibitor (Figure 20). While both inhibitors bind to the active site mostly via hydrophobic interactions, the M4076 inhibitor forms extensive aromatic stacking interactions with W2769. W2769 is the conserved residue that does a similar interaction with the aromatic purine ring system of the ATP cofactor. The KU-55933 inhibitor has a heterocyclic thianthrene moiety that is bent by a 128° angle which prevents comparable planar stacking interactions. Similar to M4076, the AZD0156 and AZD1390 have a central planar quinoline aromatic ring system which most likely enables the same stacking interactions. An interaction between C2770 and the KU-55933 morpholine oxygen atom leads to a slight outwards shift of the entire hinge region. The M4076 inhibitor does not cause this conformational change, thus the active site resembles more the ATP-bound state. Similarly, the methoxypyridine ring in M4076 imitates the ATP ribose.

Biochemical data confirms high selectivity of both inhibitors. The IC_{50} values of all PIKK members as well as downstream kinase CHK2 is at least 150x higher for both inhibitors. Comparison of the ATM active site with that of other PIKK family members reveals how the inhibitors selectively inhibit ATM. The PIKK family has a very highly conserved kinase domain, however several unconserved residues interact with the inhibitors and prevent binding to other PIKK members. Most importantly, residue A2693 is in direct van der Waals contacts with the M4076 methoxy functional group. This residue is replaced with bulkier, hydrophobic residues in other PIKKs.

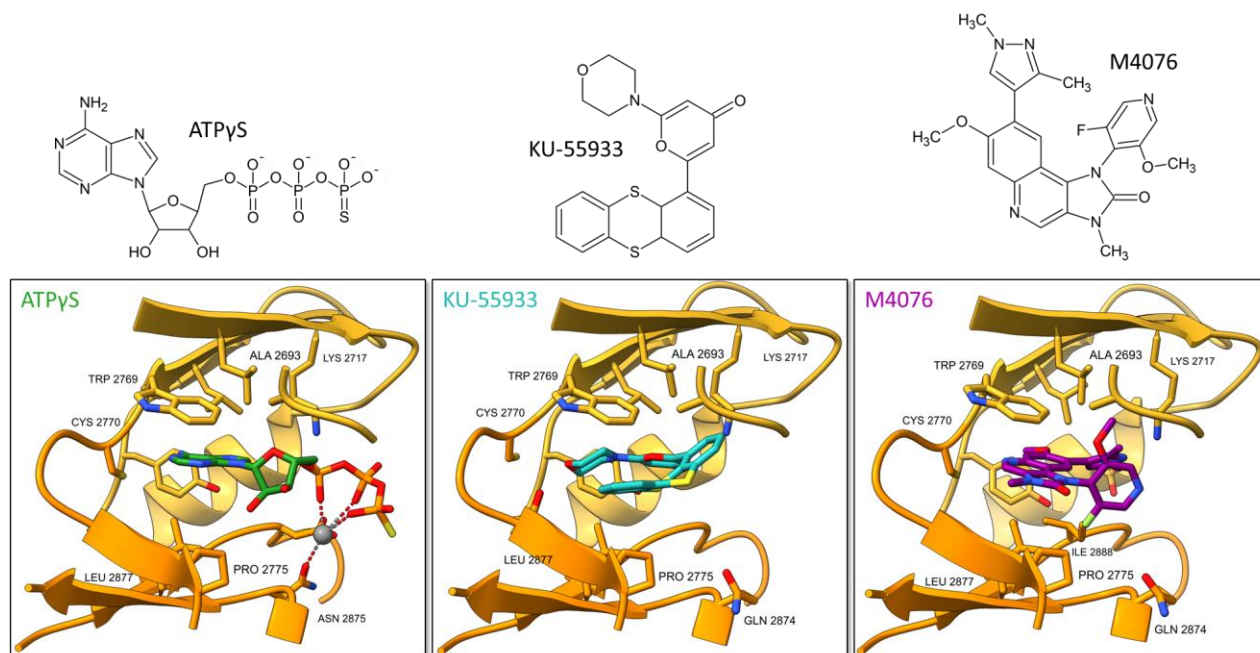


Figure 20: ATM kinase active site bound to ATP γ S, KU-55933, M4076. Residues in proximity and/or contact of inhibitors are labelled. Kinase domain N-lobe colored in golden, C-lobe in orange.

Literature

1. Crick, F. & Watson, J. © 1953 Nature Publishing Group. (1953).
2. Hoeijmakers, J. H. J. DNA Damage, Aging, and Cancer. (vol 361, pg 1475, 2009). *N. Engl. J. Med.* **361**, 1914 (2009).
3. Kirkwood, T. B. L. Understanding the odd science of aging. *Cell* **120**, 437–447 (2005).
4. Scully, R., Panday, A., Elango, R. & Willis, N. A. DNA double-strand break repair-pathway choice in somatic mammalian cells. *Nat. Rev. Mol. Cell Biol.* **20**, 698–714 (2019).
5. Ciccia, A. & Elledge, S. J. The DNA Damage Response: Making It Safe to Play with Knives. *Mol. Cell* **40**, 179–204 (2010).
6. Tubbs, A. & Nussenzweig, A. Endogenous DNA Damage as a Source of Genomic Instability in Cancer. *Cell* **168**, 644–656 (2017).
7. Friedberg, E. C. A brief history of the DNA repair field. *Cell Res.* **18**, 3–7 (2008).
8. Runger, T. M. & Kappes, U. P. Mechanisms of mutation formation with long-wave ultraviolet light (UVA). *Photodermatol. Photoimmunol. Photomed.* **24**, 2–10 (2008).
9. Srinivas, U. S., Tan, B. W. Q., Vellayappan, B. A. & Jeyasekharan, A. D. ROS and the DNA damage response in cancer. *Redox Biol.* **25**, 101084 (2019).
10. Chatterjee Nimrat; Walker Graham C. Mechanisms of DNA Damage, Repair, and Mutagenesis. *Environ. Mol. Mutagen.* **405**, 235–263 (2017).
11. Sample, A. & He, Y. Y. Mechanisms and prevention of UV-induced melanoma. *Photodermatol. Photoimmunol. Photomed.* **34**, 13–24 (2018).
12. Neidle, S. & Thurston, D. E. Chemical approaches to the discovery and development of cancer therapies. *Nat. Rev. Cancer* **5**, 285–296 (2005).
13. Kaina, B. & Christmann, M. DNA repair in personalized brain cancer therapy with temozolomide and nitrosoureas. *DNA Repair (Amst).* **78**, 128–141 (2019).
14. Bishop, J. B. & Wassom, J. S. Toxicological review of busulfan (Myleran). *Mutat. Res. Genet. Toxicol.* **168**, 15–45 (1986).
15. Brana, M. F., Cacho, M., Gradillas, A., de Pascual-Teresa, B. & Ramos, A. Intercalators as Anticancer Drugs. *Curr. Pharm. Des.* **7**, 1745–1780 (2005).
16. Eaton, D. L. & Gallagher, E. P. Mechanisms of aflatoxin carcinogenesis. *Annu. Rev. Pharmacol. Toxicol.* **34**, 135–172 (1994).

17. Weickert, P. & Stingele, J. DNA–Protein Crosslinks and Their Resolution. *Annu. Rev. Biochem.* **91**, 1–25 (2022).
18. Lindahl, T. Instability and decay of the primary structure of DNA. *Nature* **362**, 709–715 (1993).
19. Ziech, D., Franco, R., Pappa, A. & Panayiotidis, M. I. Reactive Oxygen Species (ROS)--Induced genetic and epigenetic alterations in human carcinogenesis. *Mutat. Res. - Fundam. Mol. Mech. Mutagen.* **711**, 167–173 (2011).
20. Rydberg, B. & Lindahl, T. Nonenzymatic methylation of DNA by the intracellular methyl group donor S-adenosyl-L-methionine is a potentially mutagenic reaction. *EMBO J.* **1**, 211–216 (1982).
21. Loeb, L. A. & Monnat, R. J. DNA polymerases and human disease. *Nat. Rev. Genet.* **9**, 594–604 (2008).
22. Stingele, J., Bellelli, R. & Boulton, S. J. Mechanisms of DNA-protein crosslink repair. *Nat. Rev. Mol. Cell Biol.* **18**, 563–573 (2017).
23. Caldecott, K. W. Single-strand break repair and genetic disease. *Nat. Rev. Genet.* **9**, 619–631 (2008).
24. Vilenchik, M. M. & Knudson, A. G. Endogenous DNA double-strand breaks: Production, fidelity of repair, and induction of cancer. *Proc. Natl. Acad. Sci. U. S. A.* **100**, 12871–12876 (2003).
25. Mehta, A. & Haber, J. E. Sources of DNA double-strand breaks and models of recombinational DNA repair. *Cold Spring Harb. Perspect. Biol.* **6**, 1–19 (2014).
26. Kim, M. S., Lapkouski, M., Yang, W. & Gellert, M. Crystal structure of the V(D)J recombinase RAG1-RAG2. *Nature* **518**, 507–511 (2015).
27. Panizza, S. *et al.* Spo11-accessory proteins link double-strand break sites to the chromosome axis in early meiotic recombination. *Cell* **146**, 372–383 (2011).
28. Beard, W. A., Horton, J. K., Prasad, R. & Wilson, S. H. Eukaryotic base excision repair: New approaches shine light on mechanism. *Annu. Rev. Biochem.* **88**, 137–162 (2019).
29. Marteiijn, J. A., Lans, H., Vermeulen, W. & Hoeijmakers, J. H. J. Understanding nucleotide excision repair and its roles in cancer and ageing. *Nat. Rev. Mol. Cell Biol.* **15**, 465–481 (2014).
30. Pegg, A. E., Dolan, M. E. & Moschel, R. C. Structure, Function, and Inhibition of O6-Alkylguanine-DNA Alkyltransferase. *Prog. Nucleic Acid Res. Mol. Biol.* **51**, 167–223 (1995).
31. Gerson, S. L. Clinical relevance of MGMT in the treatment of cancer. *J. Clin. Oncol.* **20**, 2388–2399 (2002).
32. Ray Chaudhuri, A. & Nussenzweig, A. The multifaceted roles of PARP1 in DNA repair and chromatin remodelling. *Nat. Rev. Mol. Cell Biol.* **18**, 610–621 (2017).

33. Beard, W. A. & Wilson, S. H. Structure and mechanism of DNA polymerase β . *Biochemistry* **53**, 2768–2780 (2014).
34. Hu, J., Lieb, J. D., Sancar, A. & Adar, S. Cisplatin DNA damage and repair maps of the human genome at single-nucleotide resolution. *Proc. Natl. Acad. Sci. U. S. A.* **113**, 11507–11512 (2016).
35. Sale, J. E. Mutagenesis in Eukaryotes. *Cold Spring Harb Perspect Biol* **5**:a012708, 1–22 (2013).
36. Li, G. M. Mechanisms and functions of DNA mismatch repair. *Cell Res.* **18**, 85–98 (2008).
37. Langelier, M., Adp-ribosyl, P., Planck, J. L., Roy, S. & Pascal, J. M. Structural Basis for DNA Damage–Dependent Poly(ADP-ribosyl)ation by Human PARP-1. *Structure* **728**, 728–733 (2012).
38. Feng, X. & Koh, D. W. Inhibition of poly(ADP-ribose) polymerase-1 or poly(ADP-ribose) glycohydrolase individually, but not in combination, leads to improved chemotherapeutic efficacy in HeLa cells. *Int. J. Oncol.* **42**, 749–756 (2013).
39. Smeenk, G. *et al.* Poly(ADP-ribosyl)ation links the chromatin remodeler SMARCA5/SNF2H to RNF168-dependent DNA damage signaling. *J. Cell Sci.* **126**, 889–903 (2013).
40. Ahel, D. *et al.* Poly(ADP-ribose)-dependent regulation of DNA repair by the chromatin remodeling enzyme ALC1. *Science (80-.)*. **325**, 1240–1243 (2009).
41. Van Gent, D. C. & Van Der Burg, M. Non-homologous end-joining, a sticky affair. *Oncogene* **26**, 7731–7740 (2007).
42. Walker, J. R., Corpina, R. A. & Goldberg, J. Structure of the Ku heterodimer bound to dna and its implications for double-strand break repair. *Nature* **412**, 607–614 (2001).
43. Chaplin, A. K. *et al.* Dimers of DNA-PK create a stage for DNA double-strand break repair. *Nat. Struct. Mol. Biol.* **28**, 13–19 (2021).
44. DeFazio, L. G., Stansel, R. M., Griffith, J. D. & Chu, G. Synapsis of DNA ends by DNA-dependent protein kinase. *EMBO J.* **21**, 3192–3200 (2002).
45. Jeggo, P. & O’Neill, P. The Greek Goddess, Artemis, reveals the secrets of her cleavage. *DNA Repair (Amst)*. **1**, 771–777 (2002).
46. Ma, Y., Pannicke, U., Schwarz, K. & Lieber, M. R. Hairpin opening and overhang processing by an Artemis/DNA-dependent protein kinase complex in nonhomologous end joining and V(D)J recombination. *Cell* **108**, 781–794 (2002).
47. Xie, A., Kwok, A. & Scully, R. Role of mammalian Mre11 in classical and alternative nonhomologous end joining. *Nat. Struct. Mol. Biol.* **16**, 814–818 (2009).
48. Wang, H. & Xu, X. Microhomology-mediated end joining: New players join the team. *Cell Biosci.* **7**, 4–9 (2017).

49. Sallmyr, A. & Tomkinson, A. E. Repair of DNA double-strand breaks by mammalian alternative end-joining pathways. *J. Biol. Chem.* **293**, 10536–10549 (2018).
50. Cannavo, E. & Cejka, P. Sae2 promotes dsDNA endonuclease activity within Mre11-Rad50-Xrs2 to resect DNA breaks. *Nature* **514**, 122–125 (2014).
51. Truong, L. N. *et al.* Microhomology-mediated End Joining and Homologous Recombination share the initial end resection step to repair DNA double-strand breaks in mammalian cells. *Proc. Natl. Acad. Sci. U. S. A.* **110**, 7720–7725 (2013).
52. Garcia, V., Phelps, S. E. L., Gray, S. & Neale, M. J. Bidirectional resection of DNA double-strand breaks by Mre11 and Exo1. *Nature* **479**, 241–244 (2011).
53. Rothenberg, E., Grimme, J. M., Spies, M. & Ha, T. Human Rad52-mediated homology search and annealing occurs by continuous interactions between overlapping nucleoprotein complexes. *Proc. Natl. Acad. Sci. U. S. A.* **105**, 20274–20279 (2008).
54. Paull, T. T. & Gellert, M. A mechanistic basis for Mre11-directed DNA joining at microhomologies. *Proc. Natl. Acad. Sci. U. S. A.* **97**, 6409–6414 (2000).
55. Audebert, M., Salles, B. & Calsou, P. Involvement of poly(ADP-ribose) polymerase-1 and XRCC1/DNA ligase III in an alternative route for DNA double-strand breaks rejoining. *J. Biol. Chem.* **279**, 55117–55126 (2004).
56. Ceccaldi, R. *et al.* Homologous-recombination-deficient tumours are dependent on Pol θ - mediated repair. *Nature* **518**, 258–262 (2015).
57. Cejka, P. DNA end resection: Nucleases team up with the right partners to initiate homologous recombination. *J. Biol. Chem.* **290**, 22931–22938 (2015).
58. Sun, Y., McCorvie, T. J., Yates, L. A. & Zhang, X. Structural basis of homologous recombination. *Cell. Mol. Life Sci.* **77**, 3–18 (2020).
59. Symington, L. S. & Gautier, J. Double-strand break end resection and repair pathway choice. *Annu. Rev. Genet.* **45**, 247–271 (2011).
60. Reginato, G., Cannavo, E. & Cejka, P. Physiological protein blocks direct the Mre11-Rad50-Xrs2 and Sae2 nuclease complex to initiate DNA end resection. *Genes Dev.* **31**, 2325–2330 (2017).
61. Isono, M. *et al.* BRCA1 Directs the Repair Pathway to Homologous Recombination by Promoting 53BP1 Dephosphorylation. *Cell Rep.* **18**, 520–532 (2017).
62. Mozaffari, N. L., Pagliarulo, F. & Sartori, A. A. Human CtIP: A ‘double agent’ in DNA repair and tumorigenesis. *Semin. Cell Dev. Biol.* **113**, 47–56 (2021).
63. Escribano-Díaz, C. *et al.* A Cell Cycle-Dependent Regulatory Circuit Composed of 53BP1-RIF1 and BRCA1-CtIP Controls DNA Repair Pathway Choice. *Mol. Cell* **49**, 872–883 (2013).

64. Myler, L. R. *et al.* Single-Molecule Imaging Reveals How Mre11-Rad50-Nbs1 Initiates DNA Break Repair. *Mol. Cell* **67**, 891-898.e4 (2017).
65. Saathoff, J. H., Käshammer, L., Lammens, K., Byrne, R. T. & Hopfner, K. P. The bacterial Mre11–Rad50 homolog SbcCD cleaves opposing strands of DNA by two chemically distinct nuclease reactions. *Nucleic Acids Res.* **46**, 11303–11314 (2018).
66. Käshammer, L. *et al.* Mechanism of DNA End Sensing and Processing by the Mre11-Rad50 Complex. *Mol. Cell* 1–13 (2019). doi:10.1016/j.molcel.2019.07.035
67. Hailemariam, S., Kumar, S. & Burgers, P. M. Activation of Tel1ATM kinase requires Rad50 ATPase and long nucleosome-free DNA but no DNA ends. *J. Biol. Chem.* **294**, 10120–10130 (2019).
68. Falck, J., Mailland, N., Syljuäsen, R., Bartek, J. & Lukas, J. The ATM±Chk2±Cdc25A checkpoint pathway guards against radioresistant DNA synthesis. **410**, 842–847 (2001).
69. Marsella, A., Cassani, C., Casari, E., Tisi, R. & Longhese, M. P. Structure–function relationships of the Mre11 protein in the control of DNA end bridging and processing. *Current Genetics* **65**, 11–16 (2019).
70. Mimori, T. & Hardin, J. A. Mechanism of interaction between Ku protein and DNA. *J. Biol. Chem.* **261**, 10375–10379 (1986).
71. Okayasu, R. & Iliakis, G. Ionizing radiation induces two forms of interphase chromosome breaks in Chinese hamster ovary cells that rejoin with different kinetics and show different sensitivity to treatment in hypertonic medium or β-araA. *Radiat. Res.* **136**, 262–270 (1993).
72. Postow, L. Destroying the ring: Freeing DNA from Ku with ubiquitin. *FEBS Lett.* **585**, 2876–2882 (2011).
73. Ira, G. *et al.* DNA end resection, homologous recombination and DNA damage checkpoint activation require CDK1. *Nature* **431**, 1011–1017 (2004).
74. Aylon, Y., Liefshitz, B. & Kupiec, M. The CDK regulates repair of double-strand breaks by homologous recombination during the cell cycle. *EMBO J.* **23**, 4868–4875 (2004).
75. Ceccaldi, R., Rondinelli, B. & D’Andrea, A. D. Repair Pathway Choices and Consequences at the Double-Strand Break. *Trends Cell Biol.* **26**, 52–64 (2016).
76. Hu, Y. *et al.* PARP1-driven poly-ADP-ribosylation regulates BRCA1 function in homologous recombination–mediated DNA repair. *Cancer Discov.* **4**, 1430–1447 (2014).
77. Hustedt, N. & Durocher, D. The control of DNA repair by the cell cycle. *Nat. Cell Biol.* **19**, 1–9 (2017).
78. Buis, J. *et al.* Mre11 Nuclease Activity Has Essential Roles in DNA Repair and Genomic Stability Distinct from ATM Activation. *Cell* **135**, 85–96 (2008).

79. Adelman, C. A., De, S. & Petrini, J. H. J. Rad50 Is Dispensable for the Maintenance and Viability of Postmitotic Tissues. *Mol. Cell. Biol.* **29**, 483–492 (2009).
80. Anand, R., Ranjha, L., Cannavo, E. & Cejka, P. Phosphorylated CtIP Functions as a Co-factor of the MRE11-RAD50-NBS1 Endonuclease in DNA End Resection. *Mol. Cell* **64**, 940–950 (2016).
81. Kim, J. H. *et al.* The Mre11-Nbs1 Interface Is Essential for Viability and Tumor Suppression. *Cell Rep.* **18**, 496–507 (2017).
82. Schiller, C. B. *et al.* Structure of Mre11-Nbs1 complex yields insights into ataxia-telangiectasia-like disease mutations and DNA damage signaling. *Nat. Struct. Mol. Biol.* **19**, 693–700 (2012).
83. Williams, R. Scott, Jessica S. Williams, John A. Tainer. Mre11–Rad50–Nbs1 is a keystone complex connecting DNA repair machinery, double-strand break signaling, and the chromatin template. *Biochem. Cell Biol.* (2007).
84. Paull, T. T. & Gellert, M. The 3' to 5' exonuclease activity of Mre11 facilitates repair of DNA double-strand breaks. *Mol. Cell* **1**, 969–979 (1998).
85. Hopfner, K. P. *et al.* Structural biochemistry and interaction architecture of the DNA double-strand break repair Mre11 nuclease and Rad50-ATPase. *Cell* **105**, 473–485 (2001).
86. Lammens, K. *et al.* The Mre11:Rad50 structure shows an ATP-dependent molecular clamp in DNA double-strand break repair. *Cell* **145**, 54–66 (2011).
87. Shibata, A. *et al.* DNA Double-Strand Break Repair Pathway Choice Is Directed by Distinct MRE11 Nuclease Activities. *Mol. Cell* **53**, 7–18 (2014).
88. Seifert, F. U., Lammens, K., Stoehr, G., Kessler, B. & Hopfner, K.-P. Structural mechanism of ATP-dependent DNA binding and DNA end bridging by eukaryotic Rad50. *EMBO J.* **35**, 759–772 (2016).
89. Williams, G. J. *et al.* ABC ATPase signature helices in Rad50 link nucleotide state to Mre11 interface for DNA repair. *Nat. Struct. Mol. Biol.* **18**, 423–432 (2011).
90. Liu, Y. *et al.* ATP -dependent DNA binding, unwinding, and resection by the Mre11/Rad50 complex . *EMBO J.* **35**, 743–758 (2016).
91. Usui, T. *et al.* Complex formation and functional versatility of Mre11 of budding yeast in recombination. *Cell* **95**, 705–716 (1998).
92. Na, J. *et al.* SPRTN protease-cleaved MRE11 decreases DNA repair and radiosensitises cancer cells. *Cell Death Dis.* (2021). doi:10.1038/s41419-021-03437-w
93. Williams, R. S. *et al.* Mre11 Dimers Coordinate DNA End Bridging and Nuclease Processing in Double-Strand-Break Repair. *Cell* **135**, 97–109 (2008).
94. Hopfner, K. P. *et al.* Structural biology of Rad50 ATPase: ATP-driven conformational control in

- DNA double-strand break repair and the ABC-ATPase superfamily. *Cell* **101**, 789–800 (2000).
95. Rojowska, A. *et al.* Structure of the Rad50 DNA double-strand break repair protein in complex with DNA. *EMBO J.* **33**, 2847–2859 (2014).
 96. Deshpande, R. A., Lee, J. H. & Paull, T. T. Rad50 ATPase activity is regulated by DNA ends and requires coordination of both active sites. *Nucleic Acids Res.* **45**, 5255–5268 (2017).
 97. Chen, L. *et al.* Effect of amino acid substitutions in the Rad50 ATP binding domain on DNA double strand break repair in yeast. *J. Biol. Chem.* **280**, 2620–2627 (2005).
 98. Alani, E., Padmore, R. & Kleckner, N. Analysis of wild-type and rad50 mutants of yeast suggests an intimate relationship between meiotic chromosome synapsis and recombination. *Cell* **61**, 419–436 (1990).
 99. Zabolotnaya, E., Mela, I., Henderson, R. M. & Robinson, N. P. Turning the Mre11/Rad50 DNA repair complex on its head: Lessons from SMC protein hinges, dynamic coiled-coil movements and DNA loop-extrusion? *Biochem. Soc. Trans.* **48**, 2359–2376 (2020).
 100. Hohl, M. *et al.* The Rad50 coiled-coil domain is indispensable for Mre11 complex functions. *Nat. Struct. Mol. Biol.* **18**, 1124–1131 (2010).
 101. Hopfner, K. P. *et al.* The Rad50 zinc-hook is a structure joining Mre11 complexes in DNA recombination and repair. *Nature* **418**, 562–566 (2002).
 102. Tatebe, H. *et al.* Rad50 zinc hook functions as a constitutive dimerization module interchangeable with SMC hinge. *Nat. Commun.* **11**, 1–11 (2020).
 103. Zabolotnaya, E. *et al.* Modes of action of the archaeal Mre11/Rad50 DNA-repair complex revealed by fast-scan atomic force microscopy. *Proc. Natl. Acad. Sci.* 201915598 (2020). doi:10.1073/pnas.1915598117
 104. Moreno-Herrero, F. *et al.* Mesoscale conformational changes in the DNA-repair complex Rad50/Mre11/Nbs1 upon binding DNA. *Nature* **437**, 440–443 (2005).
 105. Park, Y. B. *et al.* Eukaryotic Rad50 functions as a rod-shaped dimer. *Nat. Struct. Mol. Biol.* **24**, 248–257 (2017).
 106. Lloyd, J. *et al.* A Supramodular FHA/BRCT-Repeat Architecture Mediates Nbs1 Adaptor Function in Response to DNA Damage. *Cell* **139**, 100–111 (2009).
 107. Williams, R. S. *et al.* Nbs1 Flexibly Tethers Ctp1 and Mre11-Rad50 to Coordinate DNA Double-Strand Break Processing and Repair. *Cell* **139**, 87–99 (2009).
 108. Stracker, T. H. & Petrini, J. H. J. The MRE11 complex: Starting from the ends. *Nat. Rev. Mol. Cell Biol.* **12**, 90–103 (2011).

109. Chapman, J. R. & Jackson, S. P. Phospho-dependent interactions between NBS1 and MDC1 mediate chromatin retention of the MRN complex at sites of DNA damage. *EMBO Rep.* **9**, 795–801 (2008).
110. Chen, L., Nievera, C. J., Lee, A. Y. L. & Wu, X. Cell cycle-dependent complex formation of BRCA1·CtIP·MRN is important for DNA double-strand break repair. *J. Biol. Chem.* **283**, 7713–7720 (2008).
111. Warren, C. & Pavletich, N. P. Structure of the human ATM kinase and mechanism of Nbs1 binding. *Elife* **11**, 1–23 (2022).
112. Rass, E. *et al.* Role of Mre11 in chromosomal nonhomologous end joining in mammalian cells. *Nat. Struct. Mol. Biol.* **16**, 819–824 (2009).
113. Zhang, X. & Paull, T. T. The Mre11/Rad50/Xrs2 complex and non-homologous end-joining of incompatible ends in *S. cerevisiae*. *DNA Repair (Amst)*. **4**, 1281–1294 (2005).
114. Helmink, B. A. *et al.* MRN complex function in the repair of chromosomal Rag-mediated DNA double-strand breaks. *J. Exp. Med.* **206**, 669–679 (2009).
115. Tseng, S. F., Chang, C. Y., Wu, K. J. & Teng, S. C. Importin KPNA2 is required for proper nuclear localization and multiple functions of NBS1. *J. Biol. Chem.* **280**, 39594–39600 (2005).
116. Anand, R. *et al.* NBS1 promotes the endonuclease activity of the MRE11-RAD50 complex by sensing CtIP phosphorylation. *EMBO J.* **38**, 1–16 (2019).
117. Deshpande, R. A., Lee, J. H., Arora, S. & Paull, T. T. Nbs1 Converts the Human Mre11/Rad50 Nuclease Complex into an Endo/Exonuclease Machine Specific for Protein-DNA Adducts. *Mol. Cell* **64**, 593–606 (2016).
118. Wang, W., Daley, J. M., Kwon, Y., Krasner, D. S. & Sung, P. Plasticity of the Mre11-Rad50-Xrs2-Sae2 nuclease ensemble in the processing of DNA-bound obstacles. *Genes Dev.* **31**, 2331–2336 (2017).
119. Mirzoeva, O. K. & Petrini, J. H. J. DNA replication-dependent nuclear dynamics of the Mre11 complex. *Mol. Cancer Res.* **1**, 207–218 (2003).
120. Kissling, V. M. *et al.* Mre11-Rad50 oligomerization promotes DNA double-strand break repair. *Nat. Commun.* **13**, 1–16 (2022).
121. Duursma, A. M., Driscoll, R., Elias, J. E. & Cimprich, K. A. A Role for the MRN Complex in ATR Activation via TOPBP1 Recruitment. *Mol. Cell* **50**, 116–122 (2013).
122. Shay, J. W. & Wright, W. E. Telomeres and telomerase: three decades of progress. *Nat. Rev. Genet.* **20**, 299–309 (2019).
123. Longhese, M. P. DNA damage response at functional and dysfunctional telomeres. *Genes Dev.* **22**,

- 125–140 (2008).
124. Mary Kironmai, K. & Muniyappa, K. Alteration of telomeric sequences and senescence caused by mutations in RAD50 of *Saccharomyces cerevisiae*. *Genes to Cells* **2**, 443–455 (1997).
 125. Chamankhah, M. & Xiao, W. Formation of the yeast Mre11-Rad50-Xrs2 complex is correlated with DNA repair and telomere maintenance. *Nucleic Acids Res.* **27**, 2072–2079 (1999).
 126. Takata, H., Tanaka, Y. & Matsuura, A. Late S phase-specific recruitment of Mre11 complex triggers hierarchical assembly of telomere replication proteins in *Saccharomyces cerevisiae*. *Mol. Cell* **17**, 573–583 (2005).
 127. Karlseder, J. *et al.* The telomeric protein TRF2 binds the ATM Kinase and Can Inhibit the ATM-dependent DNA damage response. *PLoS Biol.* **2**, (2004).
 128. Rai, R. *et al.* NBS1 Phosphorylation Status Dictates Repair Choice of Dysfunctional Telomeres. *Mol. Cell* **65**, 801-817.e4 (2017).
 129. Roisné-Hamelin, F. *et al.* Mechanism of MRX inhibition by Rif2 at telomeres. *Nat. Commun.* **12**, 1–16 (2021).
 130. Bartek, J. & Lukas, J. Chk1 and Chk2 kinases in checkpoint control and cancer. *Cancer Cell* **3**, 421–429 (2003).
 131. Weber, A. M. & Ryan, A. J. ATM and ATR as therapeutic targets in cancer. *Pharmacol. Ther.* **149**, 124–138 (2015).
 132. Zou, L. & Elledge, S. J. Sensing DNA damage through ATRIP recognition of RPA-ssDNA complexes. *Science (80-.)*. **300**, 1542–1548 (2003).
 133. Gatei, M. *et al.* Ataxia-telangiectasia-mutated (ATM) and NBS1-dependent phosphorylation of Chk1 on Ser-317 in response to ionizing radiation. *J. Biol. Chem.* **278**, 14806–14811 (2003).
 134. Banin, S. *et al.* Enhanced phosphorylation of p53 by ATM in response to DNA damage. *Science (80-.)*. **281**, 1674–1677 (1998).
 135. Khosravi, R. *et al.* Rapid ATM-dependent phosphorylation of MDM2 precedes p53 accumulation in response to DNA damage. *Proc. Natl. Acad. Sci. U. S. A.* **96**, 14973–14977 (1999).
 136. Yang, H. *et al.* MTOR kinase structure, mechanism and regulation. *Nature* **497**, 217–223 (2013).
 137. Yamashita, A., Ohnishi, T., Kashima, I., Taya, Y. & Ohno, S. Human SMG-1, a novel phosphatidylinositol 3-kinase-related protein kinase, associates with components of the mRNA surveillance complex and is involved in the regulation of nonsense-mediated mRNA decay. *Genes Dev.* **15**, 2215–2228 (2001).
 138. Baretić, D. & Williams, R. L. PIKKs - the solenoid nest where partners and kinases meet. *Curr.*

- Opin. Struct. Biol.* **29**, 134–142 (2014).
139. Imseng, S., Aylett, C. H. & Maier, T. Architecture and activation of phosphatidylinositol 3-kinase related kinases. *Curr. Opin. Struct. Biol.* **49**, 177–189 (2018).
 140. Banaszynski, L. & Liu, C. Characterization of the FKBP, Rapamycin, FRB Ternary Complex. *J. Am. Chem. Soc.* 4715–4721 (2006).
 141. Yoshimura, S. H. & Hirano, T. HEAT repeats - versatile arrays of amphiphilic helices working in crowded environments? *J. Cell Sci.* **129**, 3963–3970 (2016).
 142. Lavin, M. F. & Kozlov, S. ATM activation and DNA damage response. *Cell Cycle* **6**, 931–942 (2007).
 143. So, S., Davis, A. J. & Chen, D. J. Autophosphorylation at serine 1981 stabilizes ATM at DNA damage sites. *J. Cell Biol.* **187**, 977–990 (2009).
 144. Hailemariam, S., Kumar, S. & Burgers, P. M. Activation of Tel1ATM kinase requires Rad50 ATPase and long nucleosome-free DNA but no DNA ends. *J. Biol. Chem.* **294**, 10120–10130 (2019).
 145. Xiao, J. *et al.* Structural insights into the activation of ATM kinase. *Cell Res.* **29**, 683–685 (2019).
 146. Tanaka, T., Halicka, H. D., Huang, X., Traganos, F. & Darzynkiewicz, Z. Constitutive histone H2AX phosphorylation and ATM activation, the reporters of DNA damage by endogenous oxidants. *Cell Cycle* **5**, 1940–1945 (2006).
 147. Lau, W. C. Y. *et al.* Structure of the human dimeric ATM kinase. *Cell Cycle* **15**, 1117–1124 (2016).
 148. Lavin, M. F. & Yeo, A. J. Clinical potential of ATM inhibitors. *Mutat. Res. - Fundam. Mol. Mech. Mutagen.* **821**, 111695 (2020).
 149. Guo, Z., Kozlov, S., Lavin, M. F., Person, M. D. & Paull, T. T. ATM activation by oxidative stress. *Science (80-.).* **330**, 517–521 (2010).
 150. Bareti, D. *et al.* Structures of closed and open conformations of dimeric human ATM. **2**, (2017).
 151. Sawicka, M. *et al.* The dimeric architecture of checkpoint kinases Mec1ATR and Tel1ATM reveal a common structural organization. *J. Biol. Chem.* **291**, 13436–13447 (2016).
 152. Jansma, M. *et al.* Near-Complete Structure and Model of Tel1ATM from *Chaetomium thermophilum* Reveals a Robust Autoinhibited ATP State. *Structure* **28**, 83-95.e5 (2020).
 153. Xin, J. *et al.* Structural basis of allosteric regulation of Tel1/ATM kinase. *Cell Res.* (2019). doi:10.1038/s41422-019-0176-1
 154. Yates, L. A. *et al.* Cryo-EM Structure of Nucleotide-Bound Tel1ATM Unravels the Molecular Basis of Inhibition and Structural Rationale for Disease-Associated Mutations. *Structure* **28**, 96-104.e3 (2020).

155. Du, F. *et al.* Dimer monomer transition and dimer re-formation play important role for ATM cellular function during DNA repair. *Biochem. Biophys. Res. Commun.* **452**, 1034–1039 (2014).
156. Xiao, J. *et al.* Structural insights into the activation of ATM kinase. *Cell Res.* **29**, 683–685 (2019).
157. Kijas, A. W. *et al.* ATM-dependent phosphorylation of MRE11 controls extent of resection during homology directed repair by signalling through Exonuclease 1. *Nucleic Acids Res.* **43**, 8352–8367 (2015).
158. Lavin, M. F., Kozlov, S., Gatei, M. & Kijas, A. W. ATM-dependent phosphorylation of all three members of the MRN complex: From sensor to adaptor. *Biomolecules* **5**, 2877–2902 (2015).
159. Gatei, M. *et al.* ATM protein-dependent phosphorylation of Rad50 protein Regulates DNA repair and cell cycle control. *J. Biol. Chem.* **286**, 31542–31556 (2011).
160. Wechsler, T. *et al.* DNA-PKcs function regulated specifically by protein phosphatase 5. *Proc. Natl. Acad. Sci. U. S. A.* **101**, 1247–1252 (2004).
161. Harding, S. M., Coackley, C. & Bristow, R. G. ATM-dependent phosphorylation of 53BP1 in response to genomic stress in oxic and hypoxic cells. *Radiother. Oncol.* **99**, 307–312 (2011).
162. Wu-Baer, F. & Baer, R. Effect of DNA damage on a BRCA1 complex. *Nature* **414**, 36 (2001).
163. Gatei, M. *et al.* Ataxia-telangiectasia-mutated (ATM) and NBS1-dependent phosphorylation of Chk1 on Ser-317 in response to ionizing radiation. *J. Biol. Chem.* **278**, 14806–14811 (2003).
164. Buscemi, G. *et al.* DNA Damage-Induced Cell Cycle Regulation and Function of Novel Chk2 Phosphoresidues. *Mol. Cell. Biol.* **26**, 7832–7845 (2006).
165. Matsuoka, S. *et al.* Ataxia telangiectasia-mutated phosphorylates Chk2 in vivo and in vitro. *Proc. Natl. Acad. Sci. U. S. A.* **97**, 10389–10394 (2000).
166. Chen, L., Gilkes, D. M., Pan, Y., Lane, W. S. & Chen, J. ATM and Chk2-dependent phosphorylation of MDMX contribute to p53 activation after DNA damage. *EMBO J.* **24**, 3411–3422 (2005).
167. Kim, S. T., Xu, B. & Kastan, M. B. Involvement of the cohesin protein, Smc1, in Atm-dependent and independent responses to DNA damage. *Genes Dev.* **16**, 560–570 (2002).
168. Hoeijmakers, J. H. J. Genome maintenance mechanisms for preventing cancer. *Nature* **411**, 366–374 (2001).
169. Hanahan, D. & Weinberg, R. A. The Hallmarks of Cancer Review. *Acta Crystallogr. Sect. D Struct. Biol.* **100**, 57–70 (2000).
170. Hanahan, D. & Weinberg, R. A. Hallmarks of cancer: The next generation. *Cell* **144**, 646–674 (2011).

171. Rainey, M. D., Charlton, M. E., Stanton, R. V. & Kastan, M. B. Transient inhibition of ATM kinase is sufficient to enhance cellular sensitivity to ionizing radiation. *Cancer Res.* **68**, 7466–7474 (2008).
172. Batey, M. A. *et al.* Preclinical evaluation of a novel ATM inhibitor, KU59403, In Vitro and In Vivo in p53 functional and dysfunctional models of human cancer. *Mol. Cancer Ther.* **12**, 959–967 (2013).
173. Rouleau, M., Patel, A., Hendzel, M. J., Kaufmann, S. H. & Poirier, G. G. PARP inhibition: PARP1 and beyond. *Nat. Rev. Cancer* **10**, 293–301 (2010).
174. Schmitt, A. *et al.* ATM deficiency is associated with sensitivity to PARP1- and ATR inhibitors in lung adenocarcinoma. *Cancer Res.* **77**, 3040–3056 (2017).
175. Perkhofer, L. *et al.* ATM deficiency generating genomic instability sensitizes pancreatic ductal adenocarcinoma cells to therapy-induced DNA damage. *Cancer Res.* **77**, 5576–5590 (2017).
176. Weston, V. J. *et al.* The PARP inhibitor olaparib induces significant killing of ATM-deficient lymphoid tumor cells in vitro and in vivo. *Blood* **116**, 4578–4587 (2010).
177. Pike, K. G. *et al.* The Identification of Potent, Selective, and Orally Available Inhibitors of Ataxia Telangiectasia Mutated (ATM) Kinase: The Discovery of AZD0156 (8-{6-[3-(Dimethylamino)propoxy]pyridin-3-yl}-3-methyl-1-(tetrahydro-2 H-pyran-4-yl)-1,3-dihydro-2 H-imidazo[4. *J. Med. Chem.* **61**, 3823–3841 (2018).
178. Durant, S. T. *et al.* The brain-penetrant clinical ATM inhibitor AZD1390 radiosensitizes and improves survival of preclinical brain tumor models. *Sci. Adv.* **4**, (2018).
179. Syed, A. & Tainer, J. A. The MRE11-RAD50-NBS1 Complex Conducts the Orchestration of Damage Signaling and Outcomes to Stress in DNA Replication and Repair. *Annu. Rev. Biochem.* **87**, 263–294 (2018).
180. De Jager, M. *et al.* Human Rad50/Mre11 is a flexible complex that can tether DNA ends. *Mol. Cell* **8**, 1129–1135 (2001).
181. Lamarche, B. J., Orazio, N. I. & Weitzman, M. D. The MRN complex in double-strand break repair and telomere maintenance. *FEBS Lett.* **584**, 3682–3695 (2010).
182. Lee, J. H. & Paull, T. T. Activation and regulation of ATM kinase activity in response to DNA double-strand breaks. *Oncogene* **26**, 7741–7748 (2007).
183. You, Z., Chahwan, C., Bailis, J., Hunter, T. & Russell, P. ATM Activation and Its Recruitment to Damaged DNA Require Binding to the C Terminus of Nbs1. *Mol. Cell. Biol.* **25**, 5363–5379 (2005).
184. Anand, R., Pinto, C. & Cejka, P. *Methods to Study DNA End Resection I: Recombinant Protein Purification. Methods in Enzymology* **600**, (Elsevier Inc., 2018).
185. Lee, J. H. *et al.* Ataxia Telangiectasia-Mutated (ATM) kinase activity is regulated by ATP-driven conformational changes in the Mre11/Rad50/Nbs1 (MRN) complex. *J. Biol. Chem.* **288**, 12840–

- 12851 (2013).
186. Park, Y. B., Chae, J., Kim, Y. C. & Cho, Y. Crystal structure of human Mre11: Understanding tumorigenic mutations. *Structure* **19**, 1591–1602 (2011).
 187. Oh, J., Al-Zain, A., Cannavo, E., Cejka, P. & Symington, L. S. Xrs2 Dependent and Independent Functions of the Mre11-Rad50 Complex. *Mol. Cell* **64**, 405–415 (2016).
 188. Bürmann, F. *et al.* A folded conformation of MukBEF and cohesin. *Nat. Struct. Mol. Biol.* **26**, 227–236 (2019).
 189. Canny, M. D. & Latham, M. P. LRET-derived HADDOCK structural models describe the conformational heterogeneity required for DNA cleavage by the Mre11-Rad50 DNA damage repair complex. *Elife* **11**, 1–22 (2022).
 190. Furuse, M. *et al.* Distinct roles of two separable in vitro activities of yeast Mre11 in mitotic and meiotic recombination. *EMBO J.* **17**, 6412–6425 (1998).
 191. Salifou, K. *et al.* Chromatin-associated MRN complex protects highly transcribing genes from genomic instability. *Sci. Adv.* **7**, 1–15 (2021).
 192. Forey, R. *et al.* A Role for the Mre11-Rad50-Xrs2 Complex in Gene Expression and Chromosome Organization. *Mol. Cell* **81**, 183-197.e6 (2021).
 193. He, J. *et al.* Rad50 zinc hook is important for the Mre11 complex to bind chromosomal DNA double-stranded breaks and initiate various DNA damage responses. *J. Biol. Chem.* **287**, 31747–31756 (2012).
 194. Park, Y. B. *et al.* Eukaryotic Rad50 functions as a rod-shaped dimer. *Nat. Struct. Mol. Biol.* **24**, 248–257 (2017).
 195. Gatei, M., Kijas, A. W., Biard, D., Dörk, T. & Lavin, M. F. RAD50 phosphorylation promotes ATR downstream signaling and DNA restart following replication stress. *Hum. Mol. Genet.* **23**, 4232–4248 (2014).
 196. Tannous, E. A., Yates, L. A., Zhang, X. & Burgers, P. M. Mechanism of auto-inhibition and activation of Mec1ATR checkpoint kinase. *Nat. Struct. Mol. Biol.* **28**, 50–61 (2021).
 197. Martin, D. *et al.* The head and neck cancer cell oncogenome: A platform for the development of precision molecular therapies. *Oncotarget* **5**, 8906–8923 (2014).
 198. Kozlov, S. V. *et al.* Autophosphorylation and ATM activation: Additional sites add to the complexity. *J. Biol. Chem.* **286**, 9107–9119 (2011).
 199. Seidel, J. J., Anderson, C. M. & Blackburn, E. H. A Novel Tel1/ATM N-Terminal Motif, TAN, Is Essential for Telomere Length Maintenance and a DNA Damage Response. *Mol. Cell. Biol.* **28**, 5736–5746 (2008).

200. Bell, D. *et al.* Integrated genomic analyses of ovarian carcinoma. *Nature* **474**, 609–615 (2011).
201. Langer, L. M., Gat, Y., Bonneau, F. & Conti, E. Structure of substrate-bound SMG1-8-9 kinase complex reveals molecular basis for phosphorylation specificity. *Elife* **9**, 1–14 (2020).
202. Du, F. *et al.* Dimer monomer transition and dimer re-formation play important role for ATM cellular function during DNA repair. *Biochem. Biophys. Res. Commun.* **452**, 1034–1039 (2014).
203. Yang, H. *et al.* Mechanisms of mTORC1 activation by RHEB and inhibition by PRAS40. *Nature* **552**, 368–373 (2017).
204. Price, B. D. & Youmell, M. B. The phosphatidylinositol 3-kinase inhibitor wortmannin sensitizes murine fibroblasts and human tumor cells to radiation and blocks induction of p53 following DNA damage. *Cancer Res.* **56**, 246–250 (1996).
205. Sarkaria, J. N. *et al.* Inhibition of ATM and ATR kinase activities by the radiosensitizing agent, caffeine. *Cancer Res.* **59**, 4375–4382 (1999).
206. Hickson, I. *et al.* Identification and characterization of a novel and specific inhibitor of the ataxia-telangiectasia mutated kinase ATM. *Cancer Res.* **64**, 9152–9159 (2004).
207. Biddlestone-Thorpe, L. *et al.* ATM kinase inhibition preferentially sensitizes p53-mutant glioma to ionizing radiation. *Clin. Cancer Res.* **19**, 3189–3200 (2013).
208. Williamson, D. The curious history of yeast mitochondrial DNA. *Nat. Rev. Genet.* **3**, 475–481 (2002).
209. Allentoft, M. E. *et al.* The half-life of DNA in bone: Measuring decay kinetics in 158 dated fossils. *Proc. R. Soc. B Biol. Sci.* **279**, 4724–4733 (2012).
210. Orlando, L. *et al.* Recalibrating equus evolution using the genome sequence of an early Middle Pleistocene horse. *Nature* **499**, 74–78 (2013).
211. van der Valk, T. *et al.* Million-year-old DNA sheds light on the genomic history of mammoths. *Nature* **591**, 265–269 (2021).
212. Kim, M. & Costello, J. DNA methylation: An epigenetic mark of cellular memory. *Exp. Mol. Med.* **49**, (2017).
213. Nurk Sergey, Sergey Koren, P. A. M. The complete sequence of a human genome. *Science (80-.).* **327**, 44–53 (2022).
214. Shoaib, M. *et al.* Histone H4 lysine 20 mono-methylation directly facilitates chromatin openness and promotes transcription of housekeeping genes. *Nat. Commun.* **12**, 1–16 (2021).
215. Huang, H. *et al.* Physiological levels of ATP negatively regulate proteasome function. *Cell Res.* **20**, 1372–1385 (2010).

216. Majka, J., Alford, B., Ausio, J., Finn, R. M. & McMurray, C. T. ATP hydrolysis by RAD50 protein switches MRE11 enzyme from endonuclease to exonuclease. *J. Biol. Chem.* **287**, 2328–2341 (2012).

Danksagung

Ausdrücklich danken möchte ich meinem Doktorvater Prof. Dr. Karl-Peter Hopfner für seine hervorragende Betreuung, sein großes Vertrauen und die Möglichkeit in seiner Gruppe zu forschen. Durch seine professionelle, kompetente und nahbare Unterstützung ist er mir ein wichtiges Vorbild geworden.

Erfolgreiche Forschung ist für mich nur im Team vorstellbar und ich bin sehr glücklich während meiner Doktorarbeit an der Seite von hilfsbereiten und kooperativen Kollegen arbeiten zu dürfen. Besonderer Dank gilt Kristina Stakyte, ihre Kooperation und Organisationsfähigkeit war entscheidend für den Erfolg unserer Forschungsprojekte und ich bin sehr dankbar für unsere vertrauensvolle und enge Zusammenarbeit. Katja Lammens war eine sehr gute Ratgeberin, ich durfte von ihr nicht nur Kryo-EM und Kristallographie lernen, ihre Ratschläge und ihre Hilfe bei der Zielsetzung und Kollaborationsvermittlung waren für mich unverzichtbar. Von Joe Bartho durfte ich wertvolles Wissen über Proteinstrukturbau, Elektronenmikroskopie, Datenprozessierung und Geopolitik lernen, ich bin ihm sehr dankbar für anschauliche Erklärungen und spannende Diskussionen. Aaron Alt hat mich besonders zu Beginn meiner Promotion unterstützt und mir beigebracht mehrere Projekte zu managen und zielgerichtet zu arbeiten. Bei Brigitte Keßler bedanke ich mich für ihre geduldige Hilfe bei praktischen Fragen jeder Art, ihre zuverlässige Mitarbeit war ausschlaggebend für meinen Erfolg. Schließlich gilt mein Dank allen Kollegen, die das Labor zu einem besonderen Ort gemacht haben und die ich jederzeit um Hilfe, Rat oder Kaffeepausen bitten durfte. In meinen Forschungsprojekten durfte ich außerdem viele wissenschaftliche Kollaborationen schließen und mit Experten aus verschiedensten Feldern zusammenarbeiten, dafür bin ich sehr dankbar.

Von ganzem Herzen möchte ich mich bei meiner Ehefrau Katharina, meiner Familie und meinen Freunden bedanken, die mir zu jeder Zeit geduldig zur Seite standen und mich so annehmen wie ich bin.